Determining controls on aeolian dust emissions: analysis of dynamic processes at Etosha Pan, Namibia.

Natasha S. Wallum

Supervisors:

Professor Giles F.S. Wiggs

School of Geography and the Environment, University of Oxford, UK

Dr Robert G. Bryant

Department of Geography, University of Sheffield, UK

A thesis submitted for the degree of

Doctor of Philosophy

at the University of Oxford



Abstract

Ephemeral lake beds are prominent sources of atmospheric mineral dust aerosols globally, but emissions from these landforms are characterised by considerable spatial and temporal variability. It has proven extremely difficult to resolve the complex relationships between the climatic and surface drivers that control aeolian emissivity. Such complexity introduces uncertainty in model predictions of atmospheric dust loading with subsequent imprecision in estimates of its impacts and interactions with other global scale processes in the Earth system, which have far-reaching implications for climate, ocean fertilisation, nutrient transport, air quality and human health.

A key challenge remains to collect high resolution, field-based measurements of the local scale controls and processes of aeolian entrainment from specific emitting surfaces and relating these to remote sensing observations of basin scale environmental drivers and surface erodibility dynamics, despite the promising potential for the generation and testing of dust emission models. This thesis presents a combined approach utilising in-situ field experimentation and remote sensing analysis techniques to determine the local and regional controls on the emission of mineral dust from Etosha Pan in Namibia, a major southern-hemisphere dust source.

A range of satellite-retrieved (e.g., MODIS, MSG-SEVIRI and Landsat) measurements of lake inundation, mineral aerosols, surface geochemistry, and climate data (from meteorological stations and model reanalysis data sources) for the period 2000–2022 were used to determine the hydrological contexts, salt crust mineralogy, and climatic environments modulating dust emission dynamics from the pan. A discrete and sensitive set of significant associations were established between annual and seasonal variations in basin scale precipitation, ephemeral pan surface inundation, and the frequency and magnitude of dust emissions across the analysis period. In addition, a significant proportion of the observed variability in the dust and hydrological cycle of this source could also be attributed to El Niño-Southern Oscillation (ENSO) and Indian Ocean sea surface temperature (SST) anomalies.

A twenty-year record of dust point source locations enabled the identification of clusters of dust sources ('hot-spots') on the pan surface. These were found to correspond to dynamic changes in sediment availability (i.e., surface erodibility) associated with variations in surface crust characteristics and moisture conditions, rather than a function of sediment supply driven by ephemeral inundation. Validated linear spectral unmixing analysis of the pan surface mineralogical composition from satellite image time-series revealed the varying development of evaporite mineral crusts through the process of salt efflorescence, influenced by the timing of seasonal precipitation and recession of surface flooding. It was established that the emergence of highly emissive dust 'hot-spots' on the pan surface were associated with the intermittent degradation of the evaporite crust by high winds in the dry season, which exposed a large supply of fine textured and highly erodible clay and rock-forming silicate subsurface sediments that were extremely susceptible to aeolian entrainment. Field-based investigations using a portable wind tunnel confirmed that such differences in surface crust morphology and geochemistry, dependent on antecedent hydrological and climatic conditions, offer a first-order control on sediment availability for dust emission from Etosha Pan.

Evidence from the research presented in this thesis suggests that dynamic shifts in erodibility conditions associated with the development and degradation of an evaporite (salt) crust, as a function of seasonal surface moisture regimes, play a significant part in determining the spatiotemporal variability of dust emissions. Attempts to better represent the controls and seasonal variations in surface moisture dynamics and subsequent moisture-related effects on surface salt crust properties and sediment availability therefore represent a key endeavour towards improving large-scale model simulations of dust emissions from globally significant ephemeral lake bed sources.

Acknowledgements

First, I am especially grateful to my supervisors, Professor Giles Wiggs and Dr Rob Bryant, for their unparalleled wisdom, patience, guidance and kindness; and their effortless ability to impart them on the likes of me.

Funding for this research was generously provided by the UK Research and Innovation (UKRI) Natural Environment Research Council's Doctoral Training Programme (NERC-DTP) and Hertford College. In addition to this financial support, the compilation of this thesis has greatly benefitted from the kind support of many people and organisations.

Acknowledgements are due to all the staff at the Etosha Ecological Institute and Etosha National Park for their access permissions and help with fieldwork campaigns at Etosha Pan, with special thanks to Claudine Cloete for her invaluable assistance; The Ministry of Environment and Tourism and the National Commission on Research, Science and Technology for their support and permission to undertake this research; the Namibia Meteorological Service and Namibia Statistics Agency. The value of satellite data made available for free use by the National Aeronautics and Space Administration (NASA), the European Organisation for the Exploitation of Meteorological Satellites (EUMETSAT) and the European Space Agency (ESA) deserves particular acknowledgement. Thank you also to Jaime Azain, Matt Baddock, George Breit, Sebastian Engelstaedter, Harland Goldstein, Brent Holben, Rosie Huck, Ray Kokaly, Jen Leidelmeijer, John Mendelsohn, Jon Murray, Jo Nield, Rich Reynolds, Mikhail Sorokin, Dave Thomas, and Wilferd Versfeld.

Last but by no means least, I am indebted to all of my close friends and loved ones – you know who you are – whose relentless love, encouragement, and inspiration, which at times came from close by and further afar, have made this '*pan*-demic' research an extremely positive, unforgettable experience.

Table of Contents

Abstract i

Acknowledgements iii

Abbreviations viii

Glossary of Terms x

List of Figures xii

List of Tables xviii

Chapter 1 Introduction 1

1.1. Research Context 2

1.2. Aims and Objectives 7

1.3. Thesis Structure 13

Chapter 2 Literature Review 14

2.1. Atmospheric Mineral Dust 15

2.2. Ephemeral lake beds as a dust emissions source 24

2.3. Sub-landform scale emission 'hot-spots' 26

2.4. Controls on dust emissions 28

2.4.1. Sediment Supply 30

2.4.2. Aeolian Transport Capacity 34

2.4.3. Sediment Availability 38

2.5. Summary 45

Chapter 3 Research Approach and Methods 46

3.1. Study Site 47

3.2. Data Sources and Methods 49

3.2.1. Remote Sensing 50

3.2.2. Climate Data 51

3.2.3. Fieldwork and Laboratory Analysis 54

Chapter 4 Hydrological context of the Cuvelai-Etosha Basin **56**

4.1. Introduction 57

4.2. Data Sources and Methods 60

4.2.1. Catchment precipitation data sources 60

4.2.2. Pan surface flooding data sources 64

4.2.3. Detection of pan surface flooding extents 66

4.2.4. Identification of surface flooding sources 68

4.2.5. The influence of regional catchment precipitation on pan surface flooding dynamics 69

4.2.6. The influence of global climate cycles on catchment precipitation and pan surface flooding dynamics 69

4.3. Results and Discussion 71

4.3.1. Spatiotemporal dynamics of catchment precipitation 71

4.3.2. Spatiotemporal dynamics of pan surface flooding 83

4.3.3. Sources of pan surface flooding 91

4.3.4. The influence of regional catchment precipitation on pan surface flooding dynamics 94

4.3.5. The influence of global climate cycles on catchment precipitation and pan surface flooding dynamics 97

4.4. Conclusion 103

Chapter 5 Determining the hydrological controls on dust emissions **107**

5.1. Introduction 108

5.2. Data Sources and Methods 110

5.2.1. Dust emission event detection 110

5.2.2. Meteorological context for dust emissions 127

5.2.3. Hydrological controls and dust emissions 128

5.3. Results and Discussion 129

5.3.1. Dust emission event detection 129

5.3.2. Meteorological context for dust emissions 139

5.3.3. Hydrological controls and dust emissions 143

5.4. Conclusion 154

Chapter 6 Controls on sediment availability in the formation of dust emission 'hot-spots' on Etosha Pan 158

6.1. Introduction 159

6.2. Data Sources and Methods 163

6.2.1. Identification of 'hot-spot' emissive surfaces 163

6.2.2. Geochemical analysis of 'hot-spot' emissive surfaces 164

6.2.3. Determining the hydrological and climatological conditions on emissive and non-emissive surfaces 181

6.3. Results and Discussion 183

6.3.1. Identification of 'hot-spot' emissive surfaces 183

6.3.2. Geochemistry of 'hot-spot' emissive surfaces 190

6.3.3. Determining the hydrological and climatological conditions on emissive and non-emissive surfaces 197

6.4. Conclusion 205

Chapter 7 Surface controls of sediment availability for dust emissions from Etosha Pan 209

7.1. Introduction 210

7.2. Data Sources and Methods 215

7.2.1. Field site selection 215

7.2.2. On-site measurements 219

7.2.3. Laboratory Analyses 228

7.3. Results and Discussion 229

7.3.1. PM_{10} emissions 229

7.3.2. Surface characterisation 235

7.3.3. Surface erodibility controls on PM_{10} emissions 245

7.4. Conclusion 255

Chapter 8 Conclusions **259**

Reference List **276**

Appendices **356**

A.1. Supplementary Information for Chapter 4 357

A.2. Supplementary Information for Chapter 6 360

Abbreviations

ABI	Advanced Baseline Imager
AI	Aerosol Index
ALI	Advanced Land Imager
AOD	Aerosol Optical Depth
ASD	Analytical Spectral Devices
ASTER	Advanced Spaceborne Thermal Emission and Reflectance Radiometer
AVHRR	Advanced Very High Resolution Radiometer
AVIRIS	Airborne Visible/Infrared Imaging Spectrometer
BTD	Brightness Temperature Difference
CHIME	Copernicus Hyperspectral Imaging Mission
CSD	Clear Sky Differencing
ECMWF	European Centre for Medium Range Weather Forecasts
EMIT	Earth Surface Mineral Dust Source Investigation
EO-1	Earth Observing-1
ERA5	ECMWF Global Climate Reanalysis
ESA	European Space Agency
EUMETSAT	The European Organisation for the Exploitation of Meteorological Satellites
FIRMS	Fire Information for Resource Management System
GIS	Geographic Information System
GPM-IMERG	Integrated Multi-satellite Retrievals for Global Precipitation Measurement
ISS	International Space Station
LAADS DAAC	Level-1 and Atmospheric Archive & Distribution System Distributed Active Archive Center

MNDWI	Modified Normalized Difference Water Index
MODIS	Moderate Resolution Imaging Spectroradiometer
MSG-SEVIRI	Meteosat Second Generation Spinning Enhanced Visible and InfraRed Imager
NASA	National Aeronautics and Space Administration
NDVI	Normalized Difference Vegetation Index
NIR	Near-Infrared
OLI	Operational Land Imager
OMI	Ozone Mapping Instrument
PI-SWERL	Portable In-Situ Wind ERosion Laboratory
PRISMA	Precursore IperSpettrale della Missione Applicativa
RGB	Red-Green-Blue
RPM	Rotations Per Minute
RST	Robust Satellite Technique
SEM-EDX	Energy-dispersive X-ray analysis with a Scanning Electron Microscope
SLC	Scan Line Corrector
SWIR	Shortwave Infrared
TIR	Thermal Infrared
TM	Thematic Mapper
TOMS	Total Ozone Mapping Spectrometer
TRMM	Tropical Rainfall Measuring Mission
USGS	United States Geological Survey
VIR	Visible and Infrared
VNIR	Visible Near-Infrared
XRD	X-Ray Diffraction

Glossary of Terms

Parameter	Description	Units
A_{eff}	Effective area underneath the PI-SWERL annular ring	m^2
B_λ	Spectral radiance	mW m^{-2} sr^{-1} $(cm^{-1})^{-1}$
C	PM_{10} concentration	mg m^{-3}
E_i	PM_{10} emission flux at PI-SWERL step level i	mg m^{-2} s^{-1}
ESD	Earth-Sun distance	au
F	Blower flow rate for fresh air entering the PI-SWERL chamber	m^3 s^{-1}
$F_0(\lambda)$	Extra-terrestrial solar flux	mW m^{-2} sr^{-1} $(cm^{-1})^{-1}$
$\overline{F_0(\lambda)}$,	Extra-terrestrial solar flux at equinox	mW m^{-2} sr^{-1} $(cm^{-1})^{-1}$
i	PI-SWERL step level	RPM
m	Number of days in the clear sky average	–
$\rho_{0.6}^{d}$	The 0.6 μm lower baseline (third lowest) reflectance for an MSG-SEVIRI pixel for a given time over a n-day rolling window used to calculate the clear sky average	%
$\rho_{0.6}^{k}$	The 0.6 μm reflectance on day for an MSG-SEVIRI pixel for a given time and day within a n-day rolling window used to calculate the clear sky average	%
$\rho_{0.6}^{csn}$	Clear sky 0.6 μm reflectance for an MSG-SEVIRI pixel for a given time and day within a n-day rolling window	%
R_λ	Solar reflectance	%
RH	Relative humidity	%

t	Surface air temperature	° C
t_d	Dew point temperature	° C
$T_B,\ BT$	Brightness temperature	K
$t_{begin,i}$	Test time at the beginning of a PI-SWERL step level i	s
$t_{end,i}$	Test time at the end of a PI-SWERL step level i	s
t_0	PI-SWERL nephelometer sampling time	s
μ_0	Cosine of the solar zenith angle	°
u_*	Wind shear velocity	m s^{-1}
u_{*t}	Threshold wind shear velocity for PM_{10} emission	m s^{-1}
u_{*eff}	Wind shear velocity exerted by the PI-SWERL to the effective area	m s^{-1}
$u,\ U$	The eastward component of the 10 m wind. The horizontal speed of air moving towards the east at a height of ten metres above the surface of the Earth	m s^{-1}
$v,\ V$	The northward component of the 10 m wind. The horizontal speed of air moving towards the north at a height of ten metres above the surface of the Earth	m s^{-1}
ws	The speed of the horizontal 10 m wind. Calculated as the square root of the sum of the squared u and v components of the wind at a height of ten metres above the surface of the Earth	m s^{-1}
z_0	Aerodynamic roughness length	m

List of Figures

Main body

Figure 2.1. The global distribution of major dust sources based upon mean measured daily Total Ozone Mapping Spectrometer (TOMS) Aerosol Index values.

Figure 2.2. Dust plume frequency and timings for southern African sources.

Figure 2.3. Dust emission 'hot-spots' on Etosha Pan.

Figure 2.4. The principal components of aeolian transport and controlling factors.

Figure 2.5. Comparisons of TOMS AI data and inundation extents on Etosha Pan during 1996–2000.

Figure 2.6. Surface measurements of aerosol concentration and boundary layer climate at Etosha Pan during (a) a low level jet-driven dust emission event on 2 August 2015 and (b) a cold pool outflow-driven dust emission event on 30 December 2015.

Figure 3.1. The geographic location of Etosha Pan in Namibia.

Figure 4.1. The location of Etosha Pan within the Cuvelai-Etosha Basin in Namibia.

Figure 4.2. Time-series of observed monthly precipitation from meteorological stations and pixel value estimates from the TRMM and GPM-IMERG satellite rainfall products within the Cuvelai-Etosha Basin.

Figure 4.3. Annual trends in observed precipitation from meteorological stations and satellite-retrieved mean catchment precipitation for the 2000–2022 period in the Cuvelai-Etosha Basin.

Figure 4.4. Spatial distribution of mean annual precipitation in the Cuvelai-Etosha Basin from 2000 to 2022.

Figure 4.5. Mean monthly precipitation in the Cuvelai-Etosha Basin from 2000 to 2022.

Figure 4.6. Mean monthly precipitation recorded at meteorological stations in the Cuvelai-Etosha Basin from 2000 to 2022.

Figure 4.7. Spatiotemporal distributions of mean monthly precipitation derived from satellite-retrieved (TRMM/GPM-IMERG) gridded precipitation data in the Cuvelai-Etosha Basin from 2000 to 2022.

Figure 4.8. Spatiotemporal distributions of annual precipitation frequencies by month derived from satellite-retrieved (TRMM/GPM-IMERG) gridded precipitation data in the Cuvelai-Etosha Basin from 2000 to 2022.

Figure 4.9. Annual mean lake surface inundation extents and total frequency of flooding at Etosha Pan from 2000 to 2022.

Figure 4.10. Spatiotemporal distributions of annual lake surface inundation frequencies at Etosha Pan from 2000 to 2022.

Figure 4.11. Mean monthly lake surface inundation extents and frequency of flooding at Etosha Pan from 2000 to 2022.

Figure 4.12. Spatiotemporal distributions of annual lake surface inundation frequencies by month from 2000 to 2022.

Figure 4.13. Frequency of flooding at Etosha Pan contributed from fluvial inputs, direct precipitation, and groundwater from 2000 to 2022.

Figure 4.14. Mean monthly lake surface inundation extents at Etosha Pan and mean monthly precipitation in the Cuvelai-Etosha Basin from 2000 to 2022.

Figure 4.15. Monthly time-series of (a) lake surface inundation extents at Etosha Pan, (b) precipitation totals for the Cuvelai-Etosha Basin, and (c) El Niño-Southern Oscillation Sea Surface Temperature (ENSO 3.4 SST) and subtropical Indian Ocean Dipole Index (SIOD) anomalies for the period July 1999 – July 2022.

Figure 5.1. Rendered images highlighting a dust plume over Etosha Pan captured at 0800 UTC by MSG-SEVIRI on 7 September 2019.

Figure 5.2. Rendered images highlighting a dust plume over Etosha Pan at two-hourly time-steps captured by MSG-SEVIRI on 2 August 2015.

Figure 5.3. Annual frequency of dust plume events at Etosha Pan detected from MODIS true-colour imagery, MSG-SEVIRI CSD composites, and both sensors from 2000 to 2022.

Figure 5.4. Annual frequency of dust days at Etosha Pan detected from MODIS true-colour imagery, MSG-SEVIRI CSD composites, and both sensors from 2000 to 2022.

Figure 5.5. Box and whisker plots showing dust events detected from MSG-SEVIRI CSD time-series discriminated by measured time of uplift and event duration.

Figure 5.6. Annual values of mean daily AOD and total number of dust plume events and dust days at Etosha Pan from 2000 to 2022.

Figure 5.7. Monthly values of mean daily AOD and total number of dust plume events and dust days at Etosha Pan from 2000 to 2022.

Figure 5.8. ERA5-Land 10 m wind speeds and directions associated with the activation of dust plume events at Etosha Pan from 2000 to 2022.

Figure 5.9. Annual frequency of 10 m wind speed thresholds for dust plume events observed at Etosha Pan from 2000 to 2022.

Figure 5.10. Frequency distributions of ERA5-Land (a) daily mean wind speeds and (b) daily mean wind gusts associated with the active dust emission season.

Figure 5.11. Monthly time-series of (a) MODIS aerosol optical depth (AOD) and cubed surface wind speed (W^3) anomalies, (b) lake surface inundation extents at Etosha Pan, (c) precipitation totals for the Cuvelai-Etosha Basin, and (d) El Niño-Southern Oscillation Sea Surface Temperature (ENSO 3.4 SST) and subtropical Indian Ocean Dipole Index (SIOD) anomalies for the period July 1999 – December 2022.

Figure 5.12. Spatiotemporal distributions of annual dust emission events and lake surface inundation frequencies at Etosha Pan from 2000 to 2022.

Figure 5.13. Frequency distributions of (a) the number of days since wetting and (b) wetting occurrences of dust source surfaces preceding emission events at Etosha Pan from 2000 to 2022.

Figure 6.1. VNIR – SWIR reflectance spectra for the nine mineral phase spectral endmembers identified from field samples at Etosha Pan correlated with the spectral resolution and wavelengths of the Landsat 8-9 OLI sensors.

Figure 6.2. Workflow diagram illustrating the processing pathway for the production of mineral proportion maps and RGB images using a fully constrained linear spectral unmixing method on Landsat 8–9 OLI satellite time-series data.

Figure 6.3. Scatterplots of predicted mineral abundances based on pixel values from linear spectral unmixing of image data and the measured (XRD) mineral content (weight %) of ground samples collected in September 2022.

Figure 6.4. Landsat 8-9 OLI false-colour image composites of Etosha Pan showing (a) the occurrence and distribution of dust plumes sourced from emission 'hot-spots' during emissive dry seasons in 2018, 2019 and 2022 compared with (b) non-emissive (control) dry seasons in 2020 and 2021.

Figure 6.5. Landsat 8-9 OLI false-colour image composite time-series of surface change at Etosha Pan following the end of the austral summer wet seasons and across the austral winter dry seasons (March to October) of (a) 2018, (b) 2019, (c) 2020, (d) 2021 and (e) 2022.

Figure 6.6. Landsat 8-9 OLI false-colour image composites of Etosha Pan showing an increase in the extent of 'hot-spot' surfaces following major dust emission events during the 2018 dry season.

Figure 6.7. Field photo taken from the border of an emissive 'hot-spot' sample site located in the centre of Etosha Pan at the end of the dust season in September 2018.

Figure 6.8. Temporal comparisons of Landsat 8-9 OLI false-colour composite images of surface change at Etosha Pan across the 2018 austral winter dry season showing the development of emissive 'hot-spot' surfaces and linear spectral unmixing model output RGB image composite maps for corresponding image dates.

Figure 6.9. Temporal comparisons of Landsat 8-9 OLI false-colour composite images of surface change at Etosha Pan across the 2021 austral winter dry season and linear spectral unmixing model output RGB image composite maps for corresponding image dates.

Figure 6.10. Daily time-series of (a) abraded surface crust and subsequent dust emission 'hot-spot' extents with dust day occurrences, (b) flooding event occurrences and precipitation totals derived from satellite estimates, in addition to (c) surface temperature, (d) relative humidity and (e) wind speeds extracted from the ERA5–Land climate reanalysis dataset for the period November 2017–2022.

Figure 7.1. Field site locations in the south of Etosha Pan as part of the research campaign conducted in September 2022.

Figure 7.2. Field sites and key surface features examined in September 2022.

Figure 7.3. The Portable In-Situ Wind Erosion Laboratory (PI-SWERL) device and its portable buggy.

Figure 7.4. PI-SWERL test sequence configurations and examples of dust emissions response observed for the (a) ramp test and (b) step test.

Figure 7.5. Measurements of surface and sediment properties recorded at 10 cm intervals along the 10 m transect at each field site.

Figure 7.6. Average wind shear velocity (u_*) and the log-transform of potential PM_{10} dust emissions measured by the PI-SWERL at each site.

Figure 7.7. Average dust emissions response from surfaces at each field site for PI-SWERL test sequences for the (a) ramp test and (b) step test.

Figure 7.8. Field photos taken from Site 1 showing broken crust fragments (white) and ripple features (a) across the 10 m measurement transect and (b) close-up at the surface.

Figure 7.9. Field photos showing heterogeneity in crust thickness between sites.

Figure 7.10. Ternary plot depicting textures (percent sand, silt and clay) of surface crust and near-surface sediments (top 5 cm) of field sample sites.

Appendices

Figure A1.1. Scatterplot of observed monthly precipitation at meteorological stations and corresponding pixel values of TRMM/GPM-IMERG satellite-derived precipitation totals within the Cuvelai-Etosha Basin.

Figure A1.2. Comparison of surface flooding at Etosha Pan on 15 May 2020 derived from MODIS and Landsat data.

Figure A2.1. Temporal comparisons of Landsat 8-9 OLI false-colour composite images of surface change at Etosha Pan across the 2019 austral winter dry season showing the development of emissive 'hot-spot' surfaces and linear spectral unmixing model output RGB image composite maps for corresponding image dates.

Figure A2.2. Temporal comparisons of Landsat 8-9 OLI false-colour composite images of surface change at Etosha Pan across the 2020 austral winter dry season and linear spectral unmixing model output RGB image composite maps for corresponding image dates.

Figure A2.3. Temporal comparisons of Landsat 8-9 OLI false-colour composite images of surface change at Etosha Pan across the 2022 austral winter dry season showing the development of emissive 'hot-spot' surfaces and linear spectral unmixing model output RGB image composite maps for corresponding image dates.

List of Tables

Main body

Table 4.1. Global climate indices of sea surface temperature (SST) anomalies used in correlation analyses for the 2000–2022 period.

Table 4.2. Pearson correlation coefficients between satellite-derived catchment precipitation totals in the Cuvelai-Etosha Basin and lake surface inundation extents and frequency of flooding at Etosha Pan across annual, monthly (+1 and +2 month lags), and daily timescales from 2000 to 2022.

Table 4.3. Quarterly Pearson correlation coefficients between wet season (DJF) rainfall anomalies in the Cuvelai-Etosha Basin and tropical Pacific El Niño-Southern Oscillation SST (ENSO 3.4), subtropical Indian Ocean Dipole Index (SIOD), Indian Ocean (West IO and East IO), Tropical Southern Atlantic Index (TSA), Multivariate ENSO Index (MEI V2) and Dipole Mode Index (DMI) anomalies from 2000 to 2022.

Table 5.1. Dust event metrics used at varying temporal scales of analysis derived from MSG-SEVIRI and MODIS satellite sensors over Etosha Pan from 2000 to 2022.

Table 5.2. Pearson correlation coefficients between satellite-derived lake surface inundation extents and frequency of flooding at Etosha Pan, catchment precipitation totals in the Cuvelai-Etosha Basin and dust emission magnitudes (AOD) and frequency at Etosha Pan across annual (+1, +2 and +3 year lags), monthly (+1, +2 and +3 month lags), and daily timescales from 2000 to 2022.

Table 6.1. X-ray diffraction (XRD) results for Etosha sediment samples obtained in July and September 2018.

Table 7.1. Field site locations and descriptions, as informed by satellite remote sensing observations of dust emissions and pan surface characteristics and wetting regimes.

Table 7.2. Mean and standard deviation of measured threshold friction velocities for PM_{10} emission (m s^{-1}) and potential PM_{10} emissions (mg m^2 s^{-1}) measured at a shear velocity of 0.56 m s^{-1} from replicate tests given for each site.

Table 7.3. X-ray diffractometry (XRD) results for surface crust and sediment samples acquired from each of the five sample sites at Etosha Pan in September 2022.

Table 7.4. Physical characteristics of the five sample sites at Etosha Pan in September 2022.

Appendices

Table A1.1. The user's, producer's and overall accuracies of water body detection from MODIS time-series data.

CHAPTER ONE

Introduction

Introduction

1.1. Research Context

The emission, transport, and deposition of windblown mineral dust from desert regions represents a critical component in the Earth's land-atmosphere-ocean-biosphere system (Ravi *et al.,* 2011; Knippertz and Todd, 2012; Middleton and Kang, 2017; Adebiyi *et al.,* 2023); impacting climate (Kok *et al.,* 2018, 2023; Schepanski, 2018; Francis *et al.,* 2022), ocean fertilisation (Dansie *et al.,* 2017a,b, 2022; Mahowald *et al.,* 2018; Meng *et al.,* 2022), nutrient transport (Mahowald *et al.,* 2008; Kumar *et al.,* 2022; Formenti*,* 2023), and air quality and human health (Goudie, 2014; Middleton, 2017; Querol *et al.,* 2019; Tobías and Stafoggia, 2020; Prospero *et al.,* 2021; Tong *et al.,* 2023).

Numerical models offer the principal means of forecasting future global atmospheric dust loading and transport pathways of nutrient-laden dust plumes (Raupach and Lu, 2004; Mann *et al.,* 2010; Tegen and Schulz, 2014; Zhao *et al.,* 2022; Kok *et al.,* 2023). The relative impact of dust depends on the mineralogical and geochemical composition of the particles, which are primarily determined by the terrestrial sources from which they are initially entrained, and on the relative magnitude and timing of emission events from dust source regions (Shao *et al.,* 2011; Abell *et al.,* 2020; Gonçalves Ageitos *et al.,* 2023). Accordingly, an accurate knowledge of the origin of erodible material, the identification of emission source areas, and data on the drivers governing eroding

processes are a prerequisite for global dust emissions modelling (Shi *et al.,* 2012; Cui *et al.,* 2019a; Chappell *et al.,* 2023a,b; Mona *et al.,* 2023; Hennen *et al.,* 2024).

Geomorphological studies dedicated to the detection and mapping of large-scale desert dust source areas using remote sensing data have identified ephemeral lake beds in their dry phases (pans or playas) as regionally and globally significant dust sources (Prospero *et al.,* 2002; Washington *et al.,* 2003; Bullard *et al.,* 2011; Baddock *et al.,* 2016, 2021; Zucca *et al.,* 2021; Bryant and Baddock, 2021; Papi *et al.,* 2022). Within these regions, stores of fine sediment can be replenished during flooding periods which, on drying, may become susceptible to aeolian erosion (Bryant, 2003; Mahowald *et al.,* 2003). However, the relative sophistication of existing numerical models remains limited in representing dust emissions from these significant source regions (Bryant *et al.,* 2015; Karami *et al.,* 2021). This is due in part to uncertainty surrounding the nature, source and regimes of the supply of sediment to emissive sources (often associated with ephemeral flooding events), and the specific controls on surface erodibility in the post-depositional environment (e.g., the production/disruption of evaporite mineral crusts) (Reynolds *et al.,* 2007; Parajuli *et al.,* 2014; Sweeney *et al.,* 2022; Dickey *et al.,* 2023).

Whilst research to date has provided a general understanding of the windblown dust system (e.g., Allen and Washington, 2014; Marticorena, 2014; Knippertz, 2017; Caton Harrison *et al.,* 2019), the processes by which sediment is eroded from a playa surface

by wind are inherently complex (Bryant *et al.,* 2007; Nield *et al.,* 2015, 2016a,b; Goldstein *et al.,* 2017; Clements and Washington, 2021, 2023; Wiggs *et al.,* 2022). This is due to dynamic variability in the environmental drivers that control the availability of sediment for aeolian entrainment in response to variations in sediment geochemistry and atmospheric conditions (Sweeney *et al.,* 2016; De Deckker, 2019). Inherent complexities in dynamic sediment availability generate high spatial (sub-model grid) and temporal (seasonal and inter-annual) heterogeneity in emission sources (Haustein *et al.,* 2015; Marticorena *et al.,* 2017; Bergametti *et al.,* 2018, 2022), which are poorly depicted in model parametrisations owing to uncertainties associated with interpretation of coarse-scale remotely sensed data and a general lack of field verification data from source regions (Bryant, 2013; Klose *et al.,* 2019; Mei *et al.,* 2020; Baddock *et al.,* 2021; Bryant and Baddock, 2021; Wiggs *et al.,* 2022).

In recent decades, an increasing number of field observation and experimentation studies have sought to examine the specific controls and processes of aeolian entrainment from playa surfaces (e.g., Nield *et al.,* 2016a,b; Sweeney *et al.,* 2016, 2022; Klose *et al.,* 2019; Van Pelt *et al.,* 2020; Clements and Washington, 2021; Webb *et al.,* 2021). While others have examined the basin/sub-basin scale emissions drivers and sediment availability dynamics from remote sensing observations in different geographic regions (e.g., Bryant, 2003; Mahowald *et al.,* 2003; Bryant *et al.,* 2007; Baddock *et al.,* 2016, 2021; Urban *et al.,* 2018; Cheng *et al.,* 2022; Clements and Washington, 2023). Yet few studies have related the two approaches for the case of

ephemeral lakes (Reynolds *et al.,* 2007; Bryant, 2013; von Holdt *et al.,* 2019; Wiggs *et al.,* 2022), despite the promising potential for the generation and testing of dust emission models (Haustein *et al.,* 2015; Baddock *et al.,* 2021; Connelly *et al.,* 2021; Zhang, J. *et al.,* 2021).

This underlines the need to conduct source-based investigations that examine the surface controls and processes of aeolian entrainment, and to relate these to observations of broader scale environmental drivers and sediment availability dynamics. Such analyses would help to determine the effects of both local and regional environmental drivers on the emission and transport of mineral dust from ephemeral lake beds and thus improve assessments of the dynamics of emissions in response to changing environmental conditions in the future (Shao *et al.,* 2011; Kok *et al.,* 2018, 2021a, 2023; Cui *et al.,* 2019a).

Etosha Pan, in the semi-arid north of Namibia, represents a suitable case study region to facilitate research into the complex controls and dynamics of mineral dust emissions from ephemeral lake beds. Relative to its surface area, Etosha Pan represents one of the largest sources of aeolian dust emissions in the southern hemisphere (Vickery *et al.,* 2013; Baddock *et al.*, 2016; Formenti *et al.,* 2019). It also constitutes a large playa environment that is relatively accessible for field-based investigation of the drivers and fluxes of dust emission and the atmospheric and land surface dynamics that control dust uplift at-source (Clements and Washington, 2021; Wiggs *et al.,* 2022). Yet,

research into the dynamics of sediment availability specifically at this ephemeral lake basin, and the potential impacts this may have on dust emissions, has remained limited compared to other similar source regions, such as Kati Thanda-Lake Eyre, Australia (Bullard *et al.,* 2008; Baddock *et al.,* 2009, 2015; Strong *et al.,* 2011), Owens (dry) Lake and Franklin Lake Playa, USA (Reynolds *et al.,* 2007, 2009), and the Makgadikgadi Pans, Botswana (Bryant *et al.,* 2007; Vickery *et al.,* 2013).

With continued advances in remote sensing technologies and the subsequent launch of a host of new global satellite platforms and data products in recent decades, a novel opportunity exists to identify specific dust emission sources at the sub-landform scale and to characterise the spatiotemporal dynamics of controls on sediment availability for aeolian erosion at these locations. Combined with in-situ measurements of surface emissivity and analysis of windblown sediment at-source, this will provide an evidence base that could be applied across other similarly significant but poorly understood playa dust source regions for improvements in constraining control parameters of dust production in order to enhance our assessments of future dust emissions (Kok *et al.,* 2018, 2021a, 2023; Cui *et al.,* 2019a).

1.2. Aims and Objectives

The purpose of this research is to investigate the complex environmental controls on aeolian erosion and dust emissions in a major ephemeral lake basin. To achieve this aim, a detailed examination of soil erodibility and dust emission dynamics and controls will be conducted at Etosha Pan, Namibia.

The investigation will be divided into four parts, which seek to analyse the influence and interconnections between hydrological and climatological conditions, surface crust geochemistry and sediment properties on dust emissions from the ephemeral playa across multiple spatial and temporal scales, ranging from the basin landform scale (i.e., operating on seasonal time scales of months to years and length scales of several thousands of kilometres) down to the experimental surface "plot" scale (i.e., operating at time scales of seconds to days and length scales of 10^1 m). This will, in turn, provide a potentially useful evidence base for understanding and improving model representations of dust emission from playa landforms.

The rationale and specific aims and objectives pertaining to the four individual parts of the research are summarised briefly in the following sections.

Part 1 – Hydrological context of the Cuvelai-Etosha Basin

In order to establish the association between regional hydrological drivers and aeolian dust emissions from Etosha Pan, the first part of research seeks to investigate the spatiotemporal dynamics of catchment-scale precipitation and associated pan surface inundation events within the Cuvelai-Etosha Basin. Analyses of contemporary satellite image time-series data from the region across a twenty-year period (2000–2022) will determine the annual trends and seasonal variability in catchment precipitation and ephemeral flooding of Etosha Pan. In addition, statistical analyses will explore their potential connection with broader-scale global climate cycles and sea surface temperature (SST) anomalies. Together, these will provide the necessary hydrological context for investigations into the dynamics and controls of dust emissions in succeeding chapters.

The specific aim and objectives for Part 1 are:

Aim: To quantify the temporal and spatial dynamics of precipitation events across the Cuvelai-Etosha Basin and subsequent flooding of Etosha Pan and place them in context with global scale climate cycles for the period from 2000 to 2022.

Research Objectives:

1) To determine the annual and seasonal trends in precipitation across the Cuvelai–Etosha Basin;

2) To determine the annual and seasonal trends in ephemeral flooding events on Etosha Pan;

3) To identify the sources of ephemeral flooding on the pan surface;

4) To establish any association between flooding of Etosha Pan and catchment-scale precipitation;

5) To explore the potential relationship between precipitation and flooding dynamics at Etosha Pan with large-scale global climate cycles and sea surface temperature (SST) anomalies.

Part 2 – Determining the hydrological controls on dust emissions

This chapter considerably develops previous remote sensing research (e.g., Bryant, 2003; Mahowald *et al.,* 2003) to investigate the basin-scale drivers of aeolian dust emission at Etosha Pan. Satellite-based detection of dust plume events for the period 2000–2022 will be performed to discern the spatiotemporal dynamics of dust emissions from the pan surface. By investigating the interconnections between dust emission events and catchment-scale precipitation and pan surface flooding dynamics identified in the preceding chapter, this second part of the research will determine the influence of hydrological controls on the supply and availability of sediment for erosion and quantify their relative contribution compared with wind speed and erosivity conditions on governing dust emission events.

The specific aim and objectives for Part 2 are:

Aim: To identify the temporal and spatial variability in dust emissions from the pan surface and quantify the extent to which dust entrainment is controlled by regional hydrology and ephemeral surface inundation dynamics for the period from 2000 to 2022.

Research Objectives:

1) To determine the annual and seasonal trends in dust emission events detected using multi-sensor satellite platforms;
2) To identify the erosivity conditions associated with dust emission events from the pan;
3) To establish whether the frequency, timing and magnitude of dust emissions are associated with catchment-scale precipitation and ephemeral pan surface flooding.

Part 3 – Controls on sediment availability in the formation of dust emission 'hot-spots' on Etosha Pan

The focus of the third part of the thesis is to determine the influence of surface crust mineralogy and morphology (and associated environmental controls) on sediment availability for dust emission at Etosha Pan. Multispectral Landsat OLI satellite image time-series, together with ground-truth spectroscopic and mineralogical data, will be

used to investigate the development of highly emissive dust source regions ('hot-spots') on the pan surface for the period from 2018 to 2022. Analyses of surface crust geochemistry, hydrological dynamics, and local climate conditions at the sub-basin scale will determine the precise controls and mechanisms that govern spatiotemporal variations in sediment erodibility and cause specific surfaces to become highly susceptible to aeolian erosion and dust emission.

The specific aim and objectives for Part 3 are:

Aim: To determine the sub-basin level controls on sediment availability (erodibility) that make specific surfaces on Etosha Pan prone to enhanced dust emissions.

Research Objectives:

1) To identify the specific locations and surface properties (i.e., the appearance, colour and texture) of dust emission 'hot-spots' compared with non-emissive surfaces on the pan;
2) To resolve the geochemical properties of emissive 'hot-spots' through spectral signature analysis of the pan surface;
3) To examine the surface moisture dynamics, crust and climatological conditions surrounding the development and activation of emissive 'hot-spots'.

Part 4 – Surface controls on sediment availability for dust emissions

While the research conducted in Parts 1 to 3 will identify the broader-scale sediment availability drivers and dynamics of dust emissions from Etosha Pan, these analyses depend on proxy estimates of atmospheric conditions, surface crust and sediment properties established from remote sensing data at moderate spatial and temporal resolutions, which do not easily facilitate examination of the surface erodibility conditions and sediment properties that govern the potential for dust emission at-source. In Part 4, field-based analyses and laboratory investigations of surface crust and subsurface sediment properties will be performed to determine the surface controls on the nature and magnitude of windblown dust emissions measured from various representative surfaces on the ephemeral playa using a small portable field wind tunnel (PI-SWERL). These data, allied with remote sensing measurements collected in Parts 1 to 3, can help towards resolving the complex interconnections between basin-scale hydrological and climatological conditions, and their influence on local-scale surface salt crust and subsurface properties (e.g., crust thickness, soil profile, and mineralogical composition) that determine the potential for dust emission.

The specific aim and objectives for Part 4 are:

Aim: To quantify the local-scale surface erodibility conditions and sediment properties that govern the potential for dust emission from Etosha Pan.

Research Objectives:

1) To measure the erosivity threshold for dust emission and potential dust flux at increasing shear velocity from dust emission 'hot-spot' surfaces and other surface types across the pan;
2) To determine the physical and mineralogical properties of the pan surface and near-surface, especially where surface crusts are present, for sites of varying emissivity on the pan surface;
3) To identify the key surface properties and erodibility characteristics that influence the susceptibility of the pan surface to aeolian entrainment and dust emission.

1.3. Thesis Structure

The DPhil research is presented as a chapter-based thesis, which comprises a review of the literature to date (Chapter 2) and a preliminary discussion of the study region and summary of the research methods (Chapter 3), followed by four individual chapter sections (Chapters 4 to 7) describing the distinctive research methods and results pertaining to the four principal aims of research identified above (see section 1.2). The outcomes of the individual research parts are discussed together in relation to the overall aim of the research as well as the consequent implications and potential opportunities for further investigation in the eighth and final concluding chapter.

CHAPTER TWO

Literature Review

Literature Review

2.1. Atmospheric Mineral Dust

Mineral dust aerosols are a suspension of small rock-derived particles in the atmosphere (Shao, 2001, 2008; Kok *et al.,* 2012). Representing the initial stage of the mineral dust cycle, the emission of dust into the atmosphere is governed by complex interactions between the wind and the land surface (Schepanski, 2018; Chen *et al.,* 2022). Field observations and laboratory wind tunnel experiments have helped to explain the physical processes of wind erosion that remove fine sediment particles from land surfaces and thus generate dust (Gillette *et al.,* 1974; Shao *et al.,* 1993; Ginoux *et al.,* 2001; Sow *et al.,* 2009; Parajuli *et al.,* 2016). It is generally considered to be a threshold concept, where high wind velocities and turbulent fluxes exceeding a local surface-dependent threshold are necessary to mobilize sediment particles (Raupach *et al.,* 1993; Marticorena and Bergametti, 1995; Shao, 2008).

The amount of dust that can be raised into the atmosphere by wind varies across different soil types, owing to different characteristic particle size distributions and particle binding energies (Shao *et al.,* 1996; Kok and Renno, 2009; Kok, 2011; Webb *et al.,* 2021). Arid and semi-arid regions, in particular, are susceptible to wind erosion due to typically dry conditions and sparse or absent vegetation cover exposing bare soil to the atmosphere (Schepanski, 2018). Mineral dust particles are typically small in size (usually < 100 μm in diameter) and light in density (Shao, 2008). They can

therefore remain suspended in the atmosphere at altitudes of up to 6 km for hours to days and can be transported over distances of several thousand kilometres (Mahowald *et al.,* 2014; Adebiyi *et al.,* 2023).

Since the 1990s, scholars have recognised that it is inaccurate to classify mineral dust exclusively as a "natural aerosol" (Penner *et al.,* 1994; Tegen and Fung, 1995; Tegen *et al.,* 2004; Huang *et al.,* 2015; Munkhtsetseg *et al.,* 2017). Rather, according to differences in dust sources and emission mechanisms, mineral dust aerosols have been categorised as 'natural dust' or 'anthropogenic dust', where natural dust is produced from wind erosion of natural land surfaces (namely deserts) and anthropogenic mineral dust (or fugitive dust) is generated by wind erosion of human-disturbed land surfaces (e.g., farmlands and grasslands) or suspended into the air by human activities (e.g., off-road vehicles, mineral extraction and processing, and commercial and industrial sites) (Gill *et al.,* 2006; Ginoux *et al.,* 2012; Chen *et al.,* 2013, 2018).

However, this distinction remains contentious given the inherent anthropogenic influence on many of the Earth's natural (desert) dust sources. For example, the Aralkum (Aral Sands) desert on the border between Kazakhstan and Uzbekistan in Central Asia has become a pre-eminent contemporary source of desert dust following the severe desiccation of the former Aral Sea since the 1960s (Groll *et al.,* 2013; Nobakht *et al.,* 2021). Yet, due to the cause of its formation, the Aralkum may be regarded as one of the world's most significant anthropogenic dust sources (Banks *et*

al., 2022). Hence, while natural (desert) dust accounts for the majority of the atmospheric aerosol burden by mass, loading the atmosphere with ~26 million tonnes of dust year^{-1} (Kok *et al.,* 2017, 2021b; Gliß *et al.,* 2021), the significant anthropogenic contribution to global mineral dust emissions cannot be ignored (Webb and Pierre, 2018; Wang *et al.,* 2022).

Due to its abundance and long-range transport in the atmosphere, windblown mineral dust has important effects on a wide variety of natural processes in the Earth system (Shao *et al.,* 2011; Kok *et al.,* 2023) and is commonly cited to have adverse effects on human health, air quality and visibility (Goudie, 2014; Middleton, 2020; Ukhov *et al.,* 2020; Prospero *et al.,* 2021). Mineral dust aerosols impact the energy budget of Earth through interactions with solar (shortwave) and terrestrial (longwave) radiation (Washington *et al.,* 2003; Yoshioka *et al.,* 2007; Saidou Chaibou *et al.,* 2020), cloud properties and precipitation (Karydis *et al.,* 2017; Storelvmo, 2017; Abediyi *et al.,* 2023), atmospheric chemistry (Bauer *et al.,* 2007; Klingmuller *et al.,* 2019, 2020), the cryosphere (Skiles et *al.,* 2018; Tuccella *et al.,* 2021), and both marine and terrestrial biogeochemistry (Okin *et al.,* 2004; Jickells *et al.,* 2005; Maher *et al.,* 2010; Mahowald *et al.*, 2011; Dansie *et al.,* 2017a,b, 2018, 2022; Hamilton *et al.,* 2022).

As dust activity is sensitive to many environmental parameters, it is a variable system that is not entirely predictable in terms of how it may change, or the effects it may have on other systems, particularly in response to climate and land-use change

(Stanelle *et al.,* 2014; Xi and Sokolik, 2016; Kok *et al.,* 2018). The inclusion of an accurate dust cycle in climate and weather models is therefore critical to understanding future climate and environmental conditions (Middleton and Kang, 2017; Klose *et al.,* 2021; Kok *et al.,* 2023; Hennen *et al.,* 2024).

Over the past three decades, dust models have benefitted from the rapid growth of satellite remote sensing and ground-based observations, advances in model physics, and substantial developments in computational capability (Parajuli *et al.,* 2019). Existing model parameterizations presently range from simplified formulations based on topography or elevation (e.g., Ginoux *et al.,* 2001; Koven and Fung, 2008; Zender *et al.,* 2003) to those that aim to represent the physics of the emission processes (e.g., Shao, 2004; Klose *et al.,* 2014, 2021; Kok *et al.,* 2014, 2021a).

However, several sources of uncertainty remain in all commonly used regional and global dust models (Shao *et al.,* 2011; Evan *et al.,* 2014; Klose *et al.,* 2014). Due to scaling issues and difficulties with obtaining measurement data for parameters known to affect dust emission (e.g., sediment texture, soil moisture, and land-surface properties), in particular globally (Bryant, 2013), the current generation of dust modules show considerable disagreements with observations for several critical aspects of the global dust cycle, including dust size distribution, surface concentration, and deposition flux (Cakmur *et al.,* 2006; Albani *et al.,* 2014; Evan *et al.,* 2014; Ansmann *et al.,* 2017; Adebiyi *et al.,* 2020). Correspondingly, estimates of atmospheric dust

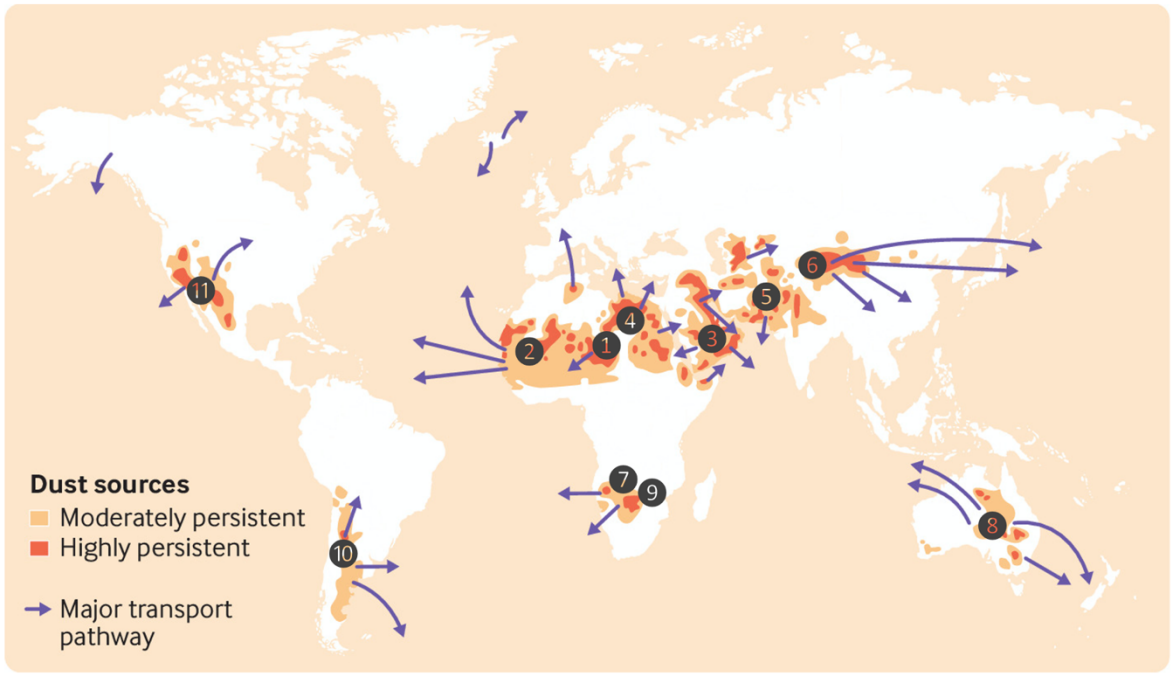
loading can vary by up to an order of magnitude between different regional and global model simulations (Huneeus *et al.,* 2011; Wu *et al.,* 2020).

Several fundamental properties of dust that govern its potential environmental impacts (i.e., particle size, mineralogy and chemical composition) are influenced by its region of origin (Claquin *et al.,* 1999; Grousset and Biscaye, 2005; Journet *et al.,* 2014). Accordingly, more simplified dust emission schemes that are commonly used in global and regional dust models are constrained by a semi-empirical "preferential" dust source function (Tegen *et al.,* 2002; Kim *et al.,* 2017). It is widely accepted that the use of a "preferential" dust source function improves the estimation of dust emission fluxes in models by approximately locating and enhancing dust emissions from prolific large-scale dust sources (Schepanski *et al.,* 2009; Kok *et al.,* 2014; Parajuli *et al.,* 2019). Such schemes are typically established from observed atmospheric dust loading or plume event frequency statistics traced back to their source locations (e.g., Grini *et al.,* 2005; Ginoux *et al.,* 2012; Parajuli *et al.,* 2014; Anisimov *et al.,* 2017; Chappell *et al.,* 2023a).

The use of Earth-orbiting satellite data has been instrumental in allowing the spatial distribution and temporal variability of dust sources to be identified at a global scale (Bryant, 2013; Muhs *et al.,* 2014; Baddock *et al.,* 2021). The Total Ozone Mapping Spectrometer (TOMS) has created significant breakthroughs in identifying major dust sources since the early 2000s. The first global multi-temporal remote sensing studies

of atmospheric dust loading using the TOMS Absorbing Aerosol Index (AAI) established broad source regions for dust, revealing the importance of closed hydrological basins as dust sources (Figure 2.1) (Middleton and Goudie, 2001; Prospero *et al.,* 2002; Washington *et al.,* 2003).

Continued monitoring using TOMS and other sensors has further revealed the intermittency and inter-annual variability of dust-emitting topographic basins, particularly those situated outside of the dominant Saharan Dust Belt (Mahowald *et al.,* 2003; Zender *et al.,* 2003; Engelstaedter *et al.,* 2006; Bryant *et al.,* 2007; Engelstaedter and Washington, 2007a,b; Varga, 2012).



	Location	Mean AAI Value
1	Bodélé Depression of south central Sahara	> 3.0
2	West Sahara in Mali and Mauritania	> 2.4
3	Arabia (southern Oman/Saudi border)	> 2.1
4	Eastern Sahara (Libya)	> 1.5
5	Southwest Asia (Makran coast)	> 1.2
6	Taklamakan/Tarim Basin	> 1.1
7	Etosha Pan (Namibia)	> 1.1
8	Lake Eyre Basin (Australia)	> 1.1
9	Makgadikgadi Basin (Botswana)	> 0.8
10	Salar de Uyuni (Bolivia)	> 0.7
11	Great Basin of the United States	> 0.5

Figure 2.1. Map of major global sources of desert dust and pathways of long distance transport. Dust source distributions are derived from frequency of occurrence (number of days) where monthly mean TOMS Absorbing Aerosol Index (AAI) is greater than 0.7 (significant amounts of dust) or 1.0 (abundant dust). Orange shading indicates moderately persistent dust sources with AAI values > 0.7 for 7–21 days; red shading indicates highly persistent dust sources with AAI values > 0.7 for 21–31 days. Purple arrows indicate typical dust transport pathways, based on interpretation of MODIS imagery from Terra and Aqua satellites. Numbered labels represent locations of major global dust sources with the highest mean AAI values listed in the accompanying table. (Figure adapted from: Middleton, 2020; Data sources: Prospero *et al.,* 2002; Washington *et al.,* 2003; Muhs *et al.,* 2014).

Following the initial identification of topographic basins as key dust sources, ensuing remote sensing investigations have focused on determining the specific source locations and dynamics of dust emissions from these regions (a detailed review is given by Baddock *et al.,* 2021). This has been facilitated by the emergence of different satellite platforms, data products, and detection algorithms for dust assessment (Li J. *et al.,* 2021), which have allowed researchers to better resolve spatial and temporal variations in dust emissivity (Parajuli *et al.,* 2014; Baddock *et al.,* 2016).

Extensive research efforts have since shown that topographic basins are not single entities with uniform emissions of dust. Rather, dust plume sources are preferentially linked to certain geomorphology and land surface types at the sub-basin scale (Wang *et al.,* 2006; Schepanski *et al.,* 2007, 2009; Bullard *et al.,* 2008; Lee *et al.,* 2009).

Geomorphology-based landform mapping has subsequently been used to represent dust emission potential in preferential dust schemes across local and regional scales (e.g., Bullard *et al.,* 2011; Parajuli *et al.,* 2014, Baddock *et al.,* 2016) and globally (Parajuli and Zender, 2017) to improve the quality of existing dust source functions (erodibility maps) used in dust models. These are continually being developed and refined based on a growing number of field and satellite observations linking dust source emission frequencies and dynamics to surface properties and geomorphology (Hennen *et al.,* 2022, 2024).

It has become clear from such work that dust emissions can be associated with a range of geomorphological environments, including river valleys and terraces (Dansie *et al.,* 2017a,b; von Holdt *et al.,* 2017, 2019), sand dunes (Crouvi *et al.,* 2012; Sweeney *et al.,* 2016), and alluvial fans (Crouvi *et al.,* 2017; Nobakht *et al.,* 2021). However, pre-eminence has long been given to ephemeral lake beds (i.e., pans or playas) (Prospero *et al.,* 2002; Schepanski *et al.,* 2007, 2009; Bullard *et al.,* 2008, 2011; Baddock *et al.,* 2011a,b; Lee *et al.,* 2012; Goudie, 2018). For example, Ginoux *et al.* (2012) determined the geomorphology of natural and anthropogenic dust sources using Level-2 Aerosol Optical Depth (AOD) data from the Moderate Resolution Imaging Spectroradiometer (MODIS) and found that 31% of global dust emissions originated from terrains associated with ephemeral water bodies. Parajuli and Zender (2017) also conducted a global analysis of dust activity in relation to landform types and found a consistent association of substantial dust storm generation with playas and dry ephemeral lake beds.

Numerous other studies have since examined dust source geomorphology using high-resolution satellite data (e.g., Schepanski *et al.,* 2012; Tegen *et al.,* 2013; Hahnenberger and Nicoll, 2014; Parajuli *et al.*, 2016; Evan *et al.,* 2015; Kandakji *et al.,* 2020). These studies have all commonly identified ephemeral lake beds in their dry phases as dominant dust emission source areas.

2.2. Ephemeral lake beds as a dust emissions source

Ephemeral lake beds (a term often used synonymously with pans, playas, salinas, salt pans or flats) are common landscape features of hydrologically-closed topographic depressions in arid and semi-arid areas (Shaw and Bryant, 2011). These flat, mostly barren, periodically flooded and often salt-crusted features occupy the lowest areas of endorheic basins, where evaporation significantly exceeds water inflows (Fookes and Lee, 2018). Such internally-draining environments are conducive to the deposition of fine-grained alluvial sediments (Bryant, 2003; Goudie, 2018). The regular cycle of flooding and desiccation typically result in the build-up of salt-rich sediment layers, which contain a significant proportion of evaporite minerals (Eugster and Hardie, 1978; Lowenstein and Hardie, 1985; Reynolds *et al.,* 2007; Buck *et al.,* 2011). This hydrological and sediment recharge behaviour both contributes to the overall highly emissive nature of playa surfaces and modulates their activity as sources of dust (Reynolds *et al.,* 2007; Baddock *et al.,* 2021).

Having been recognised as significant sources of global dust emissions (Prospero *et al.,* 2002; Washington *et al.,* 2003; Bullard *et al.,* 2011; Baddock *et al.,* 2016; Zucca *et al.,* 2021), a large body of empirical evidence has shown many ephemeral lakes are associated with substantial dust storm generation and activity in several geographic regions, including Australia (Bullard *et al.,* 2008; McGowan and Clark, 2008a,b; Baddock *et al.,* 2009; De Deckker *et al.*, 2014), North Africa (Mahowald *et al.,* 2003; Warren *et al.,* 2007; Gherboudj *et al.,* 2015), southern Africa (Eckardt *et al.,* 2001; Bryant *et al.,* 2007; Vickery *et al.,* 2013), Asia (Rashki *et al.,* 2012, 2013; Zhang *et al.,*

2015), the Middle East (Vishkaee *et al.,* 2011, 2012; Indoitu *et al.,* 2015; Rashki *et al.,* 2017, 2021; Ahmadi-Molaverdi *et al.,* 2022), North America (Lee *et al.,* 2009; Rivera Rivera *et al.,* 2010; Baddock *et al.,* 2011a,b; Goldstein *et al.,* 2017), and South America (Gaiero *et al.,* 2013; Gholampour *et al.,* 2015; Bucher and Stein, 2016).

In the Kati Thanda-Lake Eyre basin of Australia, Bullard *et al.* (2008) reported that for the period 2003–2006, ephemeral lakes (playas) dominated in terms of number of dust sources per unit area, with 11 times as many dust plumes originating from ephemeral lake beds compared with aeolian deposits, and 6 times as many per unit area compared with alluvial deposits. While Baddock *et al.* (2011a) observed that despite representing only 4% of total surface area, ephemeral lake beds were the source of 48% of observed dust plumes from the Chihuahuan Desert. Likewise, research in the Bodélé Depression in north-central Africa has shown its predominance in world dust generation (Washington *et al.,* 2006; Warren *et al.,* 2007). However, Crouvi *et al.* (2012) note that in parts of the Sahara, the association of dust emissions with playas is not as significant as other source regions.

In southern Africa, Vickery *et al.* (2013) found more than half (64%) of all detected dust plumes originated from pans – principally the Etosha Pan in Namibia and the Makgadikgadi Pans in Botswana (Figure 2.2). Though, the authors note that the entire geomorphological feature does not act as a homogenous source. Rather, persistent clusters of point sources were responsible for emissions within these large pans (Vickery *et al.,* 2013).

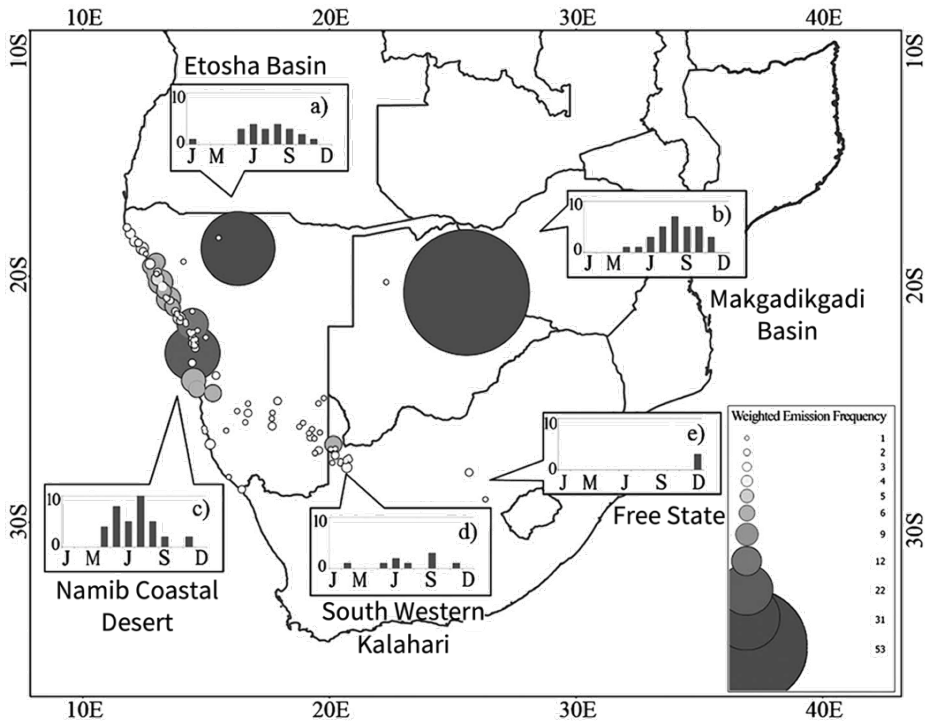


Figure 2.2. Dust plume frequency and timings for southern African sources, indicating the dominance of the Etosha and Makgadikgadi Pans (Adapted from: Vickery *et al.,* 2013).

2.3. Sub-landform scale emission 'hot-spots'

Preliminary research utilising high-resolution satellite imagery and field data at Etosha Pan has shown dust emissions originate from a multitude of point sources measuring 1 to 10 km in diameter within the ephemeral playa (Figure 2.3) (Wiggs *et al.*, 2018). These intense localized dust production areas, commonly referred to as 'hot-spots' (Gillette, 1999), constitute only a small fraction of a playa surface, with each hot-spot producing individual point source plumes (Goudie, 2008). Nevertheless, Walker *et al.* (2009) observed that multiple point source plumes merge to form considerable overall dust loadings at a regional and synoptic scale.

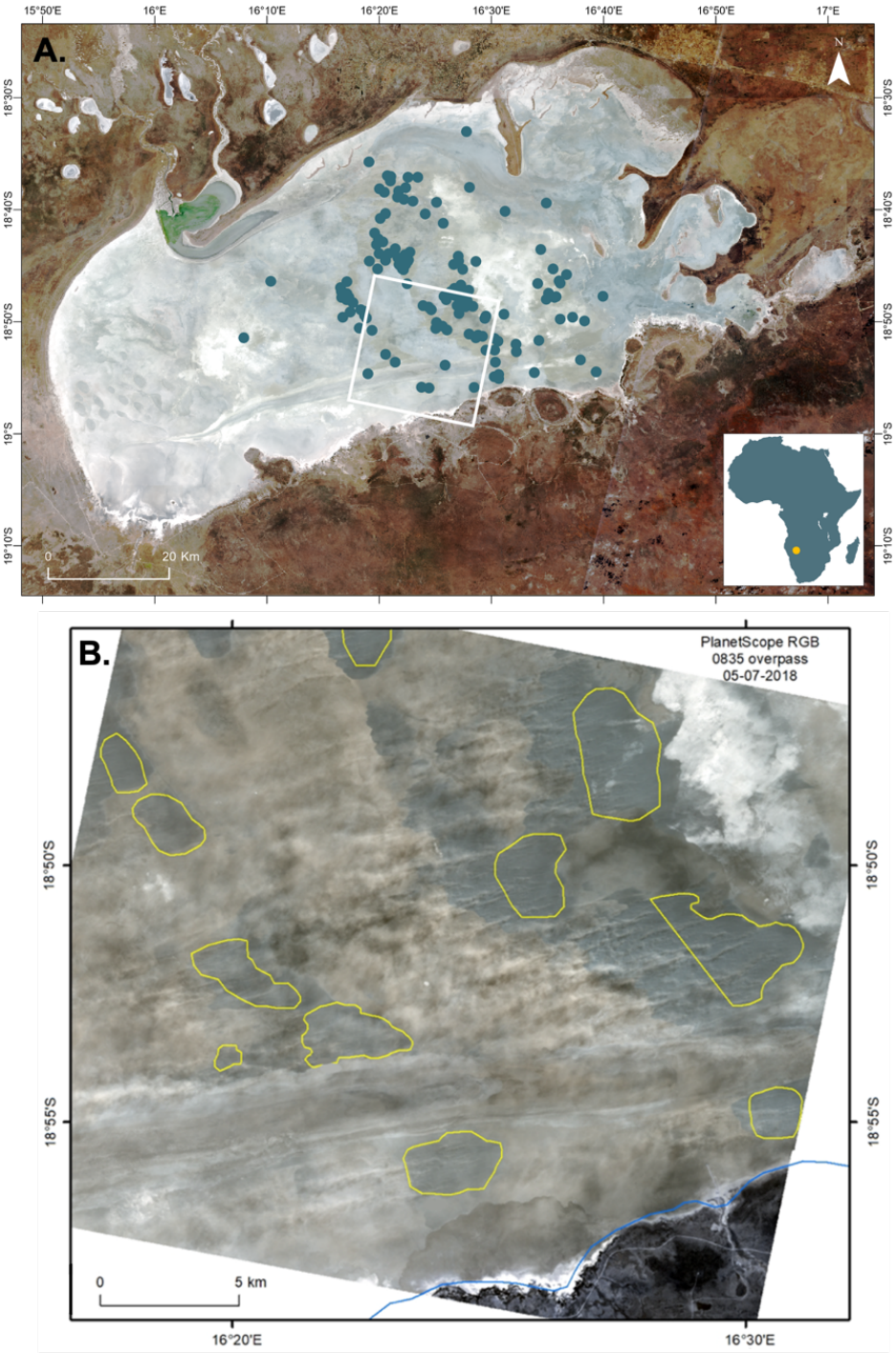


Figure 2.3. Dust emission 'hot-spots' on Etosha Pan identified (a) at the sub-basin scale using MODIS and MSG-SEVIRI satellite sensors for the 2018 dust season and (b) at the point source-level using *PlanetScope* imagery for July 2018. True-colour image composites were captured by (a) Sentinel-2 and (b) *PlanetScope* satellite sensors on 5 July 2018.

Reynolds *et al.* (2007) argue that discrete dust plume production 'hot-spots' are not static phenomenon; rather, their occurrence is a function of complex interactions between multiple controlling factors (e.g., playa hydrology and surface sediments) that determine the type and amount of dust emitted from the surface by wind erosion across varying spatial and temporal scales. This results in significant spatiotemporal variability in regional dust loadings associated with ephemeral lake sources (Ono *et al.,* 2011) and Etosha Pan in particular (Bryant, 2003; Mahowald *et al.,* 2003; Bryant *et al.,* 2015).

Hence, a thorough understanding of the dynamics and interactions between various environmental factors controlling dust production at 'hot-spot' point sources is vital to the accurate parameterization of coarse resolution dust plumes in regional and global scale wind erosion models (Walker *et al.,* 2009; Shao *et al.,* 2011; Webb and Strong, 2011; Kandakji *et al.,* 2020; Baddock *et al.,* 2021).

2.4. Controls on dust emissions

The timing and magnitude of dust emissions in playa environments can be considered as a function of three separate components: sediment supply, aeolian transport capacity, and sediment availability (Figure 2.4). This conceptual framework was originally developed by Kocurek and Lancaster (1999) to describe aeolian system behaviour in desert environments; where sediment supply serves as the source material for aeolian entrainment, transport capacity is the potential for sediment transport by

the wind, and sediment availability refers to the susceptibility of surface grains to aeolian entrainment.

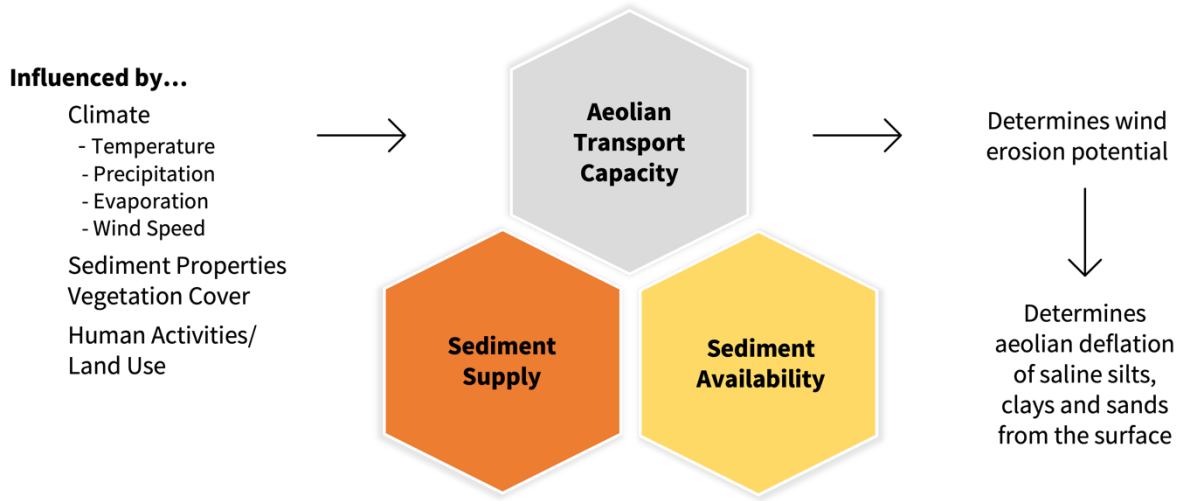


Figure 2.4. The principal components of aeolian transport and controlling factors (Based on: Kocurek and Lancaster, 1999).

Bullard *et al.* (2011) suggest that consideration of the separate issues of sediment supply, sediment availability and transport capacity of the wind allows for connections to be made between our understanding of spatial trends in the dust emission potential of surfaces and concepts of their known time-varying attributes, such as being either supply-limited (i.e., relating to the provision of sediment of a suitable grain size for emission) or transport-capacity-limited (i.e., relating to the sediment-carrying capacity of the wind at any given time).

In this regard, the majority of emission point sources produce dust on an intermittent basis, when supply of appropriate sediment is available for deflation and wind energy is sufficient to entrain the sediment (Bullard *et al.,* 2008; von Holdt *et al.*, 2017). It is

recognised that the conceptual model posed by Kocurek and Lancaster (1999) for dune systems does not have direct applicability to ephemeral playa environments, owing to differences in the environmental contexts and sediment supply regimes that influence both the evolution of the distinctive landform features and the dynamics of aeolian entrainment from within them. Nevertheless, identifying the environmental factors which influence each component in Figure 2.4 and identifying the relationships between them does offer a systematic means by which the spatiotemporal dynamics of dust production from emissive 'hot-spot' point sources within ephemeral lake beds might be determined.

2.4.1. Sediment Supply

Ephemeral lake beds in dryland basins commonly contain a large supply of fine-grained sediments; either as a legacy of past conditions (e.g., sediment accumulation in former pluvial lakes) or as a result of present-day inputs (Goudie, 2018). Among these inputs are fluvial alluvium, alluvial fans, aeolian sand, dust, biological material (e.g., diatoms), precipitates of salts, and bedrock that has been broken down by salt attack (Muhs *et al.,* 2014). As noted by Prospero *et al.* (2002, p. 23), 'The playa is the ultimate receptacle of almost all the fine-grained sediments eroded within a basin over a geological time period; thus they are storehouses of fine, dry, unconsolidated (and thus wind-erodible) sediments often in amounts far in excess of production rates in the present climate.'

One exceptional source of erodible sediment is the material that has accumulated in lake basins during past pluvials. This material may be fine-grained sediment composed of silt and fine sand, or, as in the case of the Bodélé depression in the Sahara Desert (a pre-eminent example of a dust-producing dry lakebed) may consist of friable, non-dense diatoms, which are eroded into yardangs and emitted in dust storms (Washington *et al.,* 2006; Todd *et al.,* 2007).

Many studies have shown that an association exists between areas subjected to frequent or past flooding and increased dust production, from local-scale individual plume point source areas (Crusius *et al.,* 2011), the sub-basin scale of playa landforms (Reheis, 2006; Elmore *et al.,* 2008; Sweeney *et al.,* 2016), up to regional and global-scale observations (Prospero *et al.,* 2002; Washington *et al.,* 2003). For contemporary ephemeral lakes, sediment delivery typically occurs due to endorheic draining during periods of heavy seasonal precipitation (Bryant, 2003). Dry conditions, coupled with wind events that follow the accretion of fluvial sediment, may result in aeolian output of the deposited material (Urban *et al.,* 2009).

Belnap *et al.* (2011) suggest that while the magnitude of wind and precipitation events may vary by season, shifts between dry periods of primarily aeolian activity and wet periods of primarily alluvial activity can occur across annual and sometimes up to decadal time scales as a result of climatic variability. In the Sistan region of eastern Iran and southwestern Afghanistan, Rashki *et al.* (2012) observed that dust outputs

from the Hamoun Lakes respond to wetting and drying cycles caused by fluctuations in water inputs from the Helmand River. The authors note that during wet years, increased river inflow and subsequent surface flooding intuitively lead to the suppression of dust activity, while complete desiccation of the lake complex under drought conditions caused dust storms to increase in both frequency and severity, as fresh deposits of fine material delivered via fluvial input during flooding events were easily uplifted by intense local winds (Rashki *et al.,* 2012).

Similar trends have been observed at Etosha Pan. During related studies in 1996–2000, Bryant (2003) and Mahowald *et al.* (2003) identified two major flooding episodes on the pan surface. These were sourced from ephemeral channel inputs draining the surrounding basin during heavy rainfall periods in 1997 and 2000, which were subsequently related to El Niño-Southern Oscillation (ENSO) and Indian Ocean sea surface temperature anomalies (Bryant *et al.,* 2007). Assessments of lake areas detected by the Advanced Very High Resolution Radiometer (AVHRR) with TOMS Aerosol Index (AI) values showed that the two inundation events of 1997 and 2000 corresponded with an initial reduction in dust emissions (Figure 2.5; Bryant, 2003; Mahowald *et al.,* 2003). It was found that AI values were lower than average for a more protracted period during the austral summer wet season (November to April) in both 1997 and 2000, which imposed on the winter dry seasons (May to October) that followed (Figure 2.5). However, anomalously high AI values were recorded in late 1998 and 2000 compared with other years during the study period (Figure 2.5).

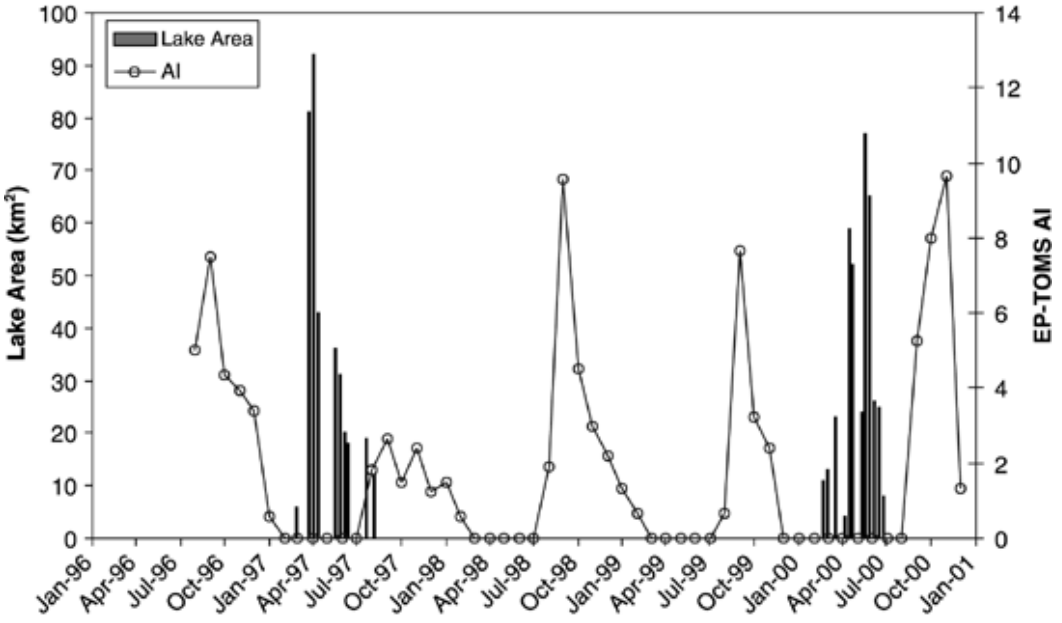


Figure 2.5. Comparisons of TOMS AI data and inundation extents on Etosha Pan during 1996 – 2000 (Source: Bryant, 2003).

Comparisons with meteorological station data showed that trends in AI values were not associated with wind speed anomalies, suggesting that natural surface inundation played an influential role on the timing and magnitude of aeolian emissions at Etosha Pan, potentially as a consequence of supply dynamics driven by the deposition of sediment from surrounding ephemeral river channels into Etosha Pan (Mahowald *et al.,* 2003). However, noting the almost two-year lag between the 1997 inundation event and observed increased in dust emissions, the authors hypothesised that further factors (i.e., soil moisture and groundwater dynamics) likely modulated the availability of sediment to aeolian entrainment from the pan surface, but did not investigate further.

2.4.2. Aeolian Transport Capacity

The transport capacity of the wind is considered a main driver for dust emission (Lu and Shao, 2001; Csavina *et al.,* 2014). Yet, even since Bryant (2013) underlined a persistent knowledge gap concerning the interconnections between emissions event dynamics and aeolian transport capacity (erosivity characteristics) from large-scale dry lake beds, it has remained a great challenge to research owing to difficulties in collecting relevant ground-based data from highly emissive source areas in relatively inaccessible locations. Recent innovative applications of field monitoring equipment and sampling strategies, together with significant advances in dust remote sensing and dust modelling, have sought to address this data gap and improved our understanding of the role of multi-scale meteorological processes involved in dust emission from ephemeral lake sources (Washington *et al.,* 2006; Schepanski *et al.,* 2007, 2009; Heinold *et al.,* 2013; Goudie, 2018; Clements and Washington, 2021, 2023; Wiggs *et al.,* 2022).

While each dust source region has its own particular local characteristics, the passage of low-pressure fronts with intense baroclinic gradients accompanied by very high velocity winds has been observed to be a dominant dust-generating mechanism within dry lake beds in many dust source regions (Rivera Rivera *et al.,* 2009; Strong *et al.,* 2011; Vishkaee *et al.,* 2012; Rashki *et al.,* 2013). Primarily controlled by synoptic-scale weather systems, these mechanisms generate strong seasonal variations in dust emissions (Knippertz, 2014).

A large body of work discusses the importance of nocturnal low-level jets (LLJs) for dust emissions (Washington and Todd, 2005; Knippertz, 2008; Todd *et al.,* 2008a,b; Allen *et al.,* 2013, 2015; Fiedler *et al.,* 2013; Heinold *et al.,* 2013; Allen and Washington, 2014; Caton Harrison *et al.,* 2019; Wiggs *et al.,* 2022). After sunrise, the boundary layer mixes momentum from the jet level to the surface, which leads to gusty winds and potential dust emission (Engelstaedter and Washington, 2007a,b).

The current state of knowledge regarding these emission mechanisms comes largely from work conducted in the central Sahara and west Africa, where major dust source areas show morning peaks in emissions related to the breakdown of the LLJ, particularly in winter and spring (Washington *et al.,* 2006; Rajot *et al.,* 2008; Schepanski *et al.,* 2009; Allen and Washington, 2014; Kaly *et al.,* 2015), while summer has an important contribution from afternoon convective storms (cold pool outflows) (Marticorena *et al.,* 2010; Marsham *et al.,* 2008, 2013; Allen *et al.,* 2015; Caton Harrison *et al.,* 2019, 2021).

A number of field-based studies have identified similar erosivity dynamics associated with dust emissions from Etosha Pan (Zunckel *et al.,* 1996a,b; Clements and Washington, 2021, 2023; Wiggs *et al.,* 2022). Observational data from the SAFARI field campaign in September – October 1992 have shown a diurnal oscillation in winds over Etosha Pan, with synoptically-forced E-NE winds during the day and lower velocity southerly winds resulting from a more local thermos-topographic forcing at

night (Preston-Whyte *et al.,* 1994). Using data from the same field campaign, Zunckel *et al.* (1996a,b) observed the persistent development of a nocturnal LLJ in the boundary layer, however its role in generating dust was not investigated.

Recent work by Clements and Washington (2021) using Doppler lidar confirmed the presence of a nocturnal LLJ at Etosha in the austral winter dry season. In addition, the research identified the mixing-down of momentum during the morning breakdown of the jet (producing peak surface winds between 0900 and 1100 local time) as the primary driver of dust emission from the pan surface between the months of August and September (Clements and Washington, 2021).

In a comprehensive investigation of aeolian dust emission dynamics at Etosha Pan by Wiggs *et al.* (2022), remotely-sensed dust event frequencies and field-based measurements of dust concentrations and associated meteorological conditions recorded from July 2015 to July 2016 showed that morning emission events related to the breakdown of the LLJ during austral winter months (June – September) were longer in duration but smaller in magnitude than dust emission events observed in the late afternoon to evening associated with downdrafts from convective storms (cold pool outflows) during austral summer (December – March) (Figure 2.6).

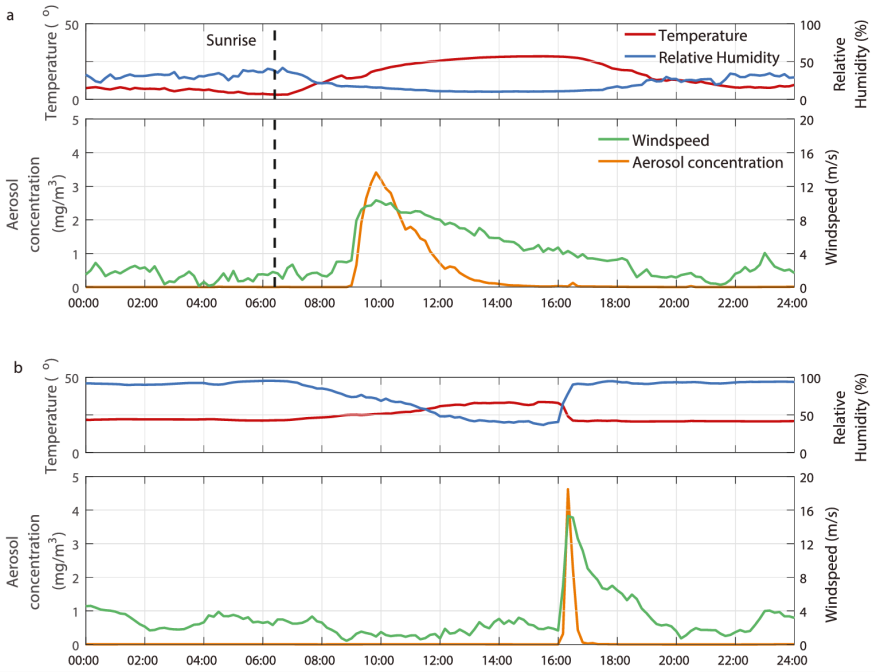


Figure 2.6. Surface measurements of aerosol concentration and boundary layer climate at Etosha Pan during (a) a low level jet-driven dust emission event on 2 August 2015 and (b) a cold pool outflow-driven dust emission event on 30 December 2015 (Source: Wiggs *et al.,* 2022).

Satellite remote sensing observations of dust event frequencies for the same period suggest that austral winter emission events occur more frequently than austral summer events (Wiggs *et al.*, 2022), corresponding to findings from previous remote sensing studies in the region (Mahowald *et al.,* 2003; Bryant *et al.,* 2007; Vickery *et al.,* 2013; Murray *et al.,* 2016). However, it should be noted that satellite retrievals struggle to detect very shallow dust layers, dust over bright surfaces or dust beneath clouds, leading to some important biases (Kocha *et al.,* 2013). Comparisons with field observations showed that short, convective emission events in summer months were poorly documented in event frequencies derived from satellite remote sensing data (Wiggs *et al.,* 2022). An observation which confirms the inherent underestimation by

satellite remote sensing studies of the smaller but not insignificant contribution of austral summertime emissions in the annual dust loading cycle of Etosha Pan (Clements and Washington, 2023). Such findings emphasise the advantages of an approach that employs both remote sensing and spatially comprehensive field measurement for investigating aeolian dust emissions from desert playa source areas (Wiggs *et al.,* 2022).

Nevertheless, both field-based and remote sensing observations showed a very clear peak in mass sediment transport in November, with an increase in not only frequency of events but also a near doubling of event flux to 571 g/m^2 from the average winter value of 279 g/m^2 (Wiggs *et al.*, 2022). This has been suggested to be controlled by a changing pattern of erosivity and erodibility conditions during a transition period from the dry winter to wetter summer, where desiccating conditions are known to lead to reductions in critical wind velocity thresholds as pan surface crusts crack and degrade (Wiggs *et al.*, 2022). However, such dynamics have yet to be observed in detail or quantified.

2.4.3. Sediment Availability

In most coarse-resolution regional and global scale dust models, dust emission is parameterised as a function of the cube of surface wind speed above a specified threshold in shear velocity (u_*, a measure of momentum transfer from the wind to the surface) that exceeds the cohesive force of the surface particles (Knippertz and Todd,

2012; Kok *et al.,* 2012). Realistic simulation of the emission process is therefore dependent on the accurate representation of the susceptibility of the surface to aeolian erosion (i.e., surface erodibility) (Zender *et al.,* 2003; Shao, 2008; Klose *et al.,* 2019). Surface erodibility represents an important factor contributing to the spatiotemporal variability of playa dust emissions (Bullard *et al.,* 2011; Ono *et al.,* 2011; Bryant, 2013; Nield *et al.,* 2015, 2016b). Yet, it remains a poorly constrained parameter within regional and global scale model representations of these highly dynamic dust source regions (Cui *et al.,* 2019a; Kok *et al.,* 2021a).

A number of factors have been established as important for controlling the erodibility of playa surfaces (see review in Webb and Strong, 2011), which include (but are not limited to): the presence of moisture as determined by precipitation events and groundwater conditions (Reheis and Urban, 2011; Dai *et al.,* 2020; Cheng *et al.,* 2022), surface cohesiveness depending on clay content and salt cementation (Langston and McKenna Neuman, 2005; Nachshon *et al.,* 2011; Goldstein *et al.,* 2017), surface roughness (Chappell *et al.,* 2003; 2010; Nield *et al.,* 2013, 2015), the geochemical composition (i.e., salt type) and distribution of surface crusts (Reynolds *et al.,* 2007, 2009; Bucher and Stein, 2016; Dai *et al.,* 2022), natural and anthropogenic disturbance of surface crusts (Baddock *et al.,* 2011b; Brungard *et al.,* 2015; Munkhtsetseg *et al.,* 2017; Moayeri *et al.,* 2023), the presence and distribution of vegetation (Zhao *et al.,* 2011; Van Pelt *et al.,* 2020; Zucca *et al.,* 2021; Cheng *et al.,* 2022), and the availability

of loose sediments and surface aggregates for saltation activity (Cahill *et al.,* 1996; Ono *et al.,* 2011; Nield *et al.,* 2016b; Sweeney *et al.,* 2023; Zhang *et al.,* 2023).

Notably, the combination of seasonal rainfall, ephemeral flooding and high evaporation rates within closed drainage basins favours the development of crusted surfaces by efflorescence of evaporite (salt) minerals, which can exert a profound influence on both the amount of fine material available for aeolian erosion and on the spatial and temporal distribution of dust emissions (Bowler, 1986; Cahill *et al.,* 1996; Gill, 1996; Goldstein *et al.,* 2017; Zhang, G. *et al.,* 2021). As precipitation ceases and, in years with pan inundation, the recession of surface flooding occurs during seasonal dry periods, the on-going evaporation of near-surface groundwater results in the precipitation of salt minerals at the surface, of which the specific mineralogy is controlled by the composition of the evaporating solutes (Buck *et al.,* 2011; Milewski *et al.,* 2019; Dai *et al.,* 2022).

Differences in the morphology and mechanical properties of surface crusts have been found to vary depending on the different types of evaporite minerals that precipitate at the surface. Field investigations have shown that under certain climatic conditions, salt minerals may precipitate to form soft "puffy" crusts with loose unconsolidated individual crystals at and near the surface that can be directly entrained by wind (Gillette *et al.,* 1980; Reynolds *et al.,* 2007, 2009; Buck *et al.,* 2011; Bucher and Stein, 2016; Nield *et al.,* 2016a; De Deckker, 2019), or they can form hard crusts composed

of interlocking crystals (Nickling and Ecclestone, 1981; Langston and McKenna Neuman, 2005; Bullard *et al.,* 2011; Goldstein *et al.,* 2017). Hence, the presence or absence of salt crusts as well as the mineralogical composition and interlocking nature of the precipitated crystals play a significant role in determining sediment erodibility by wind and thus dust emission from playa source regions (Bowler, 1986; Gillette *et al.,* 2001; Nachshon *et al.,* 2011; Lee and Kurtis, 2017; Zhang, Z. *et al.,* 2018; Zhang *et al.,* 2021).

Combined, the processes governing playa surface erodibility and the interactions between them, are highly dynamic; further modified directly and indirectly by several physical and chemical soil parameters (i.e., particle size, soil texture, moisture and organic content) and varying climatic conditions (i.e., temperature, precipitation and humidity), which generate extreme variability in the availability of sediment for aeolian erosion from surfaces within playas across a range of spatial and temporal scales (Webb and McGowan, 2009; Sweeney *et al.,* 2016). This causes significant uncertainty in representing the highly heterogenous nature of dust emissions from playas in dust models (Darmenova *et al.,* 2009; Haustein *et al.,* 2015; Mei *et al.,* 2020).

Accordingly, investigation of the factors and processes controlling erodibility on emissive surfaces, and how shifts in erodibility over time and space can affect dust fluxes, offers the potential to elucidate the complex spatial and temporal dynamics of aeolian erosion on playa surfaces (Bullard *et al.,* 2011; Tollerud and Fantle, 2014), which may lead to increased accuracy of dust models (Kok *et al.,* 2021a).

The experimental use of field and laboratory wind tunnels has been, and continues to be, central to our understanding of the relationships between surface erodibility and dust emission processes from playa environments (Bryant, 2013; Goudie, 2018). Large stationary laboratory wind tunnels allow control over the mechanical dust generation process and experimental environments (i.e., wind and soil factors), and have thus enabled researchers to determine the range and magnitude of dust emissions for different surface conditions (e.g., stable vs. disturbed surface crusts) to support the development of predictive models (Gill *et al.,* 2006; Domingo *et al.,* 2010; Madden *et al.,* 2010; Nield *et al.,* 2016b; McKenna Neuman, 2024). However, such laboratory-based experimentation is limited to testing soil surfaces that have been removed from their natural setting to precisely controlled surroundings (Van Pelt and Zobeck, 2013), which pose challenges in drawing accurate comparisons to processes occurring under natural environmental conditions (Bhattachan *et al.,* 2012).

The development and use of portable wind tunnels for field-based experimentation have been instrumental in measuring the effects of surface characteristics on sediment erodibility and wind velocity thresholds for dust emissions. Portable field-wind tunnels allow a controlled wind field to be applied to the surface whilst keeping surface conditions intact, thus permitting genuine in-situ observations of playa surface erodibility (Macpherson *et al.,* 2008; Van Pelt *et al.,* 2010; Bryant, 2013). The Portable In-Situ Wind Erosion Laboratory (PI-SWERL; Etyemezian *et al.,* 2007; Sweeney *et al.,* 2008) is one such field-portable wind tunnel system used to generate erodibility

estimates from different surfaces within natural playa dust source regions (Baddock *et al.,* 2011b; Sweeney *et al.,* 2011, 2016; Cui *et al.,* 2019a,b; Van Pelt *et al.,* 2020, 2023; Dickey *et al.,* 2023).

By combining field and wind tunnel investigations with concurrent analyses of sediment properties directly from emissive surfaces, researchers have further explored fundamental aspects of the biological, mineralogical and textural components of dust from within playa sources (King *et al.,* 2011; Buck *et al.,* 2011; Cui *et al.,* 2019a). Together, these data allow us to begin to understand and quantify the complex spatial and temporal relationships that can exist between factors controlling the availability of sediment and the transport capacity of the wind for specific dust 'hot-spot' point sources.

Nevertheless, while their impact on our understanding of the emissive nature of playa surfaces is significant, these data exist for only a very limited range of dust source locations, and over relatively restricted timescales (Bryant, 2013; Klose *et al.,* 2019; Baddock *et al.,* 2021). A key research priority must therefore include an expansion of these sampling approaches to other dust 'hot-spot' surfaces (Bullard, 2010; Bullard *et al.,* 2011) and to draw connections between field-observed erodibility dynamics with the space and time scales of remote sensing observations of playa dust sources (Haustein *et al.,* 2015; von Holdt *et al.,* 2019; Wiggs *et al.,* 2022) to provide a useful

basis for the parameterisation and validation of a range of model components within the dust cycle.

Though challenging, field-based investigation into the processes and controls of dust emission at-source is possible at Etosha Pan. However, while remote sensing and fieldwork studies have explored the spatiotemporal dynamics of dust emissions from the ephemeral playa (Bryant *et al.,* 2007; Vickery *et al.,* 2013), both in relation to factors controlling sediment supply (Bryant, 2003; Mahowald *et al.,* 2003) and aeolian transport capacity (Clements and Washington, 2021, 2023; Wiggs *et al.*, 2022), the role of surface erodibility dynamics has yet to be examined.

Research into the geochemical properties of Etosha Pan has pointed to the presence of evaporite (salt) minerals from surface crust sediment and groundwater samples obtained from the ephemeral playa (Herdtfelder, 1984; Buch and Rose, 1996; Rahm and Buch, 1997; Li *et al.,* 2018). Two field studies have sampled sediments from the surface to determine the potential influence of dust plume geochemistry and nutrient content on regional terrestrial and marine ecosystems downwind of the pan (Bhattachan *et al.,* 2015; Dansie *et al.,* 2017b). However, no other sediment or surface erodibility measurements relevant to aeolian dust emission from Etosha Pan are available in the literature.

This offers an opportunity for research to explore what processes and conditions determine the availability of sediment for aeolian erosion and how surface erodibility

affects the nature and magnitude of dust emissions from this globally significant source of atmospheric mineral aerosols. This will, in turn, provide an evidence base for understanding and improving model representations of dust emission from these significant source regions.

2.5. Summary

Regionally and globally significant dust emissions from ephemeral lake beds (playas) occur via localized dust production 'hot-spot' sources. The emissivity of 'hot-spot' surfaces can vary over space and time as a function of three components: sediment supply, sediment availability (erodibility) and aeolian transport capacity (erosivity) factors. Research efforts have utilised remote sensing and field observations to seek to identify and quantify the various environmental factors controlling each component, in order to determine the key drivers and processes of dust emissions from ephemeral lake beds, at the surface up to basin-scale. The availability of sediment for aeolian erosion, as a function of surface erodibility, is arguably the lesser well-understood control owing to the complex interplay of controlling factors and interactions with sediment supply and erosivity dynamics across varying spatial and temporal scales. Novel investigation into surface erodibility dynamics at Etosha Pan, in conjunction with existing knowledge of sediment supply and aeolian transport capacity from previous studies, would provide a useful evidence basis for improving our understanding of what defines the local-scale emissivity of ephemeral lake sources to better constrain dust emission model estimates.

CHAPTER THREE

Research Approach and Methods

Research Approach and Methods

3.1. Study Site

Etosha Pan is a 4,800 km^2 hydrologically-ephemeral basin situated in the semi-arid north of Namibia (Figure 3.1). The pan lies at 1,080 m asl and is an endorheic depression at the terminus of the Cuvelai-Etosha drainage system covering southern Angola and northern Namibia (Miller, 1997; Figure 3.1a).

Mean annual precipitation in the region varies from 400 to 600 mm, with the majority falling in the austral summer months from November to April (Hamunyela *et al.,* 2022). Rainfall drives the ephemeral drainage system to the north of Etosha, which consists of an extensive network of ephemeral channels (locally termed *iishana* [plural] or *oshana* [singular]) thought to supply fine-grained fluvial sediment to the pan during periods of shallow inundation (Bryant, 2003; Mahowald *et al.,* 2003; Pickford *et al.,* 2009; Figure 3.1b).

In the dry austral winter months (July to October) the groundwater table lowers and the surface of the pan, rich in fine clay and silt-sized sediments that have been attributed to the Andoni formation (Buch and Rose, 1996; Hipondoka *et al.,* 2014; Bhattachan *et al.,* 2015), becomes susceptible to erosion by the predominant E-NE regional winds, which can result in significant dust emission events (Wiggs *et al.,* 2022; Figure 3.1c).

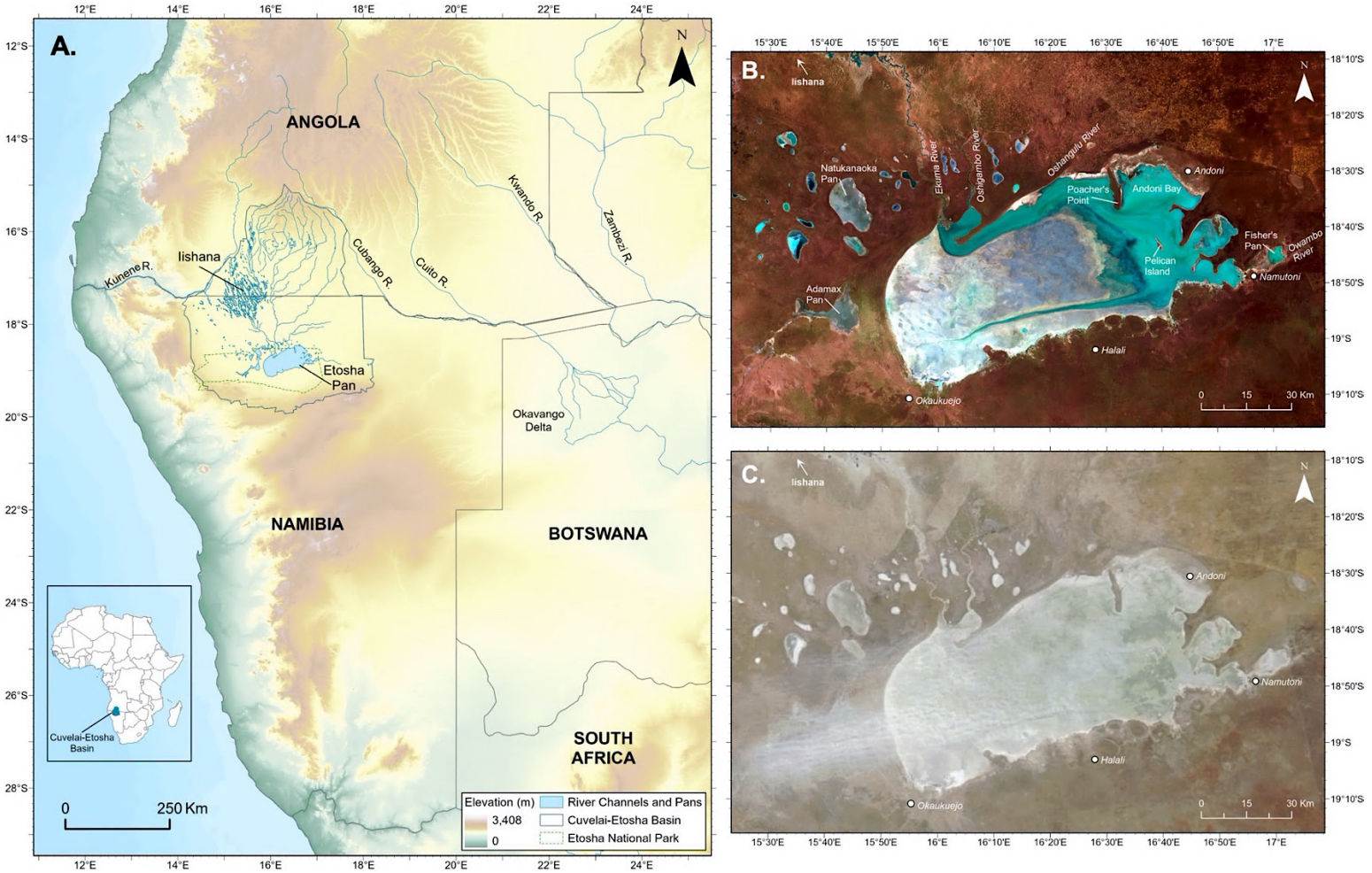


Figure 3.1. The geographic location of Etosha Pan in Namibia, highlighting (a) the catchment boundary of the Cuvelai-Etosha Basin, key river networks and surface elevation based on the Shuttle Radar Topography Mission (SRTM) 30m digital elevation model (Farr *et al.*, 2007; Lehner *et al.*, 2008). Geospatial boundary data were obtained from the Namibia Statistics Agency (nsa.org). (b) Landsat 8 OLI false colour composite (bands 7, 4, 1) image captured on 7 May 2020 showing ephemeral flooding of Etosha Pan and key hydrological features. (c) MODIS Terra true colour composite (bands 1, 4, 3) image captured at 1030 UTC on 7 September 2019 showing a dust emission event blowing towards the west.

Accordingly, numerous remote sensing investigations have recognised Etosha Pan as being a prime dust source area in the southern hemisphere (Bryant, 2003; Bryant *et al.,* 2007; Vickery *et al.,* 2013; Formenti *et al.,* 2019) and one of the most significant dust sources globally (Prospero *et al.,* 2002; Washington *et al.,* 2003; Ginoux *et al.,* 2012).

3.2. Data Sources and Methods

A combination of satellite remote sensing, model reanalysis, fieldwork and laboratory methods were employed to fulfil the four principal aims and associated objectives of the research (see section 1.2). This approach enabled investigation of the complex environmental controls on aeolian erosion and dust emissions at Etosha Pan across multiple spatial and temporal scales; offering a means to bridge the gap in understanding between smaller-scale processes occurring at the pan surface and larger-scale process dynamics represented in regional process-based wind erosion models.

The data sources and collection methods used, as well as their relevance to individual research chapters, are summarised briefly in the following sections. Detailed descriptions of the data sources and analysis techniques employed to meet the specific aims and objectives of Parts 1 to 4 of the research are given in the corresponding thesis chapters.

3.2.1. Remote Sensing

Satellite remote sensing formed the principle means of data collection and analysis in this research. With the capability of synoptic view and repeated coverage of the Earth's surface, satellite remote sensing provided a continuous measurement record of atmospheric and land surface characteristics across the Cuvelai-Etosha Basin. Improvements in the development and availability of remote sensing data at increasingly high spatial and temporal resolutions offered a novel opportunity for detailed investigation of the specific controls and dynamics of dust emission 'hot-spot' surfaces at Etosha Pan. This enabled connections to be drawn between remote observations of the major drivers and processes of dust emission at the basin-scale with discrete in-situ field observations of local-scale processes and conditions that determine the potential for aeolian erosion at the surface. Hence, the collection, processing and interpretation of image scenes and data products from several different satellite sensors contributed, to a greater or lesser extent, towards meeting the aims and objectives of all research chapters.

Satellite-derived precipitation observations from the Integrated Multi-satellite Retrievals for Global Precipitation Measurement (GPM-IMERG) and the Tropical Rainfall Measuring Mission (TRMM) as well as optical image data from the Moderate Resolution Imaging Spectroradiometer (MODIS), Landsat 5 Thematic Mapper (TM) and Landsat 8 Operational Land Imager (OLI) sensors facilitated assessment of catchment-scale precipitation, ephemeral pan surface inundation and fluvial inflow

sources at Etosha Pan in Part 1 of the research (see section 4.2) and Meteosat Second Generation Spinning Enhanced Visible and InfraRed Imager (MSG-SEVIRI) and MODIS image composites and aerosol data products for the detection of dust emission events and magnitudes from the pan surface in Part 2 of the research (see section 5.2.1) for the period from 2000 to 2022.

Image scenes from Landsat 8 OLI and Landsat 9 OLI-2 sensors provided the means to investigate the development of highly emissive surfaces and determine the potential controls of sediment availability for aeolian erosion in Part 3 of the research by enabling the identification of dust plume 'hot-spots' (see section 6.2.1) and the derivation of proxy measurements for surface geochemistry (see section 6.2.2).

Lastly, the findings from analyses of remotely-sensed datasets conducted in Parts 1, 2 and 3 were used to inform the site selection for fieldwork observations and sediment sampling for laboratory analysis in Part 4 of the research (see section 7.2).

3.2.2. Climate Data

Assessment of the atmospheric and surface environments at Etosha Pan and surrounding Cuvelai-Etosha Basin was necessary for understanding the specific climatological conditions that govern the spatial and temporal dynamics of dust emissions from the pan surface. While in-situ measurements provide a more detailed assessment of climate conditions at-source (Bryant, 2013), establishing sufficient coverage of high resolution observations necessary to assess dynamic relationships between basin-scale climatological drivers, local-scale erosivity and surface erodibility

characteristics, and dust emissions requires an extended large-scale field study (e.g., Wiggs *et al.* 2022), which was not feasible for this research investigation. Consequently, time series data for several climate parameters were derived from a combination of meteorological station records and model reanalysis data sources.

Ground-based precipitation observations utilised throughout this research were acquired from daily climate data records for the period 2000–2022 from 11 local meteorological stations positioned within the Cuvelai-Etosha Basin by the Southern African Science Service Centre for Climate Change and Adaptive Land Management (SASSCAL). The SASSCAL meteorological station network provides some observations for a limited number of additional relevant climate variables, including air and soil temperature, relative humidity, and wind speed. However, vast gaps in data records for meteorological stations within the Cuvelai-Etosha Basin meant that observations were insufficient in both spatial and temporal coverage and resolution for the purpose of this research.

Due to a lack of observed meteorological parameters in the vicinity of the study region, modelled climatic parameters derived from the European Centre for Medium-Range Weather Forecasts (ECMWF) reanalysis (ERA5-Land) climate model were used to identify the atmospheric processes and land surface conditions contributing to dust emission at Etosha Pan in Parts 2 and 3. ERA5-Land is a state-of-the-art reanalysis dataset for the land components of the fifth generation of European ReAnalysis (ERA5) of the global climate (Muñoz-Sabater *et al.,* 2021, 2023). The dataset provides

up to 70 years (1950 – present day) of hourly estimates for a large number of atmospheric and land surface climate variables that are available from the Copernicus Climate Change Service Data Store (https://cds.climate.copernicus.eu/). A key advantage of the ERA5-Land dataset is that it offers an enhanced horizontal resolution of 9 km compared to previous ECMWF reanalyses ERA5 (31 km) and ERA-Interim (80 km) (Muñoz-Sabater *et al.,* 2021). Climatic parameters extracted from the ERA5-Land dataset for analysis include surface air temperature (2 m), dew point temperature (2 m) and horizontal (u) and vertical (v) components of wind (10 m), with a spatial domain restricted to ± 2° from the approximate centre of Etosha Pan (18°47'53"S 16°19'57"E). Calculated u and v vector components were corrected with relevant off-set and scaling factors, from which wind speed, wind direction and wind gusts were computed.

ERA5-Land reanalysis climate variables have been routinely used for assessing atmospheric and land surface conditions in arid and semi-arid regions where meteorological data is spatially and temporally sparse (Forootan *et al.,* 2017; Jury, 2021; Hou *et al.,* 2022). Evaluation against independent in-situ observations and satellite-based reference datasets has demonstrated the added value of ERA5-Land in the description of atmospheric system processes (Muñoz-Sabater *et al.,* 2021). Moreover, the ERA5-Land climate reanalysis dataset has been established as a valid representation of local atmospheric conditions at Etosha Pan, specifically. A comprehensive evaluation of surface wind regimes performed by Gadal *et al.* (2022)

found predictions of the ERA5-Land climate reanalysis to be in close agreement with continuous direct measurements of local wind speed and direction from stations situated in the south-west of Etosha Pan for multiple seasonal cycles in 2015–2018. Further technical details of the ERA5-Land reanalysis, including an overview of performance can be found in Muñoz-Sabater *et al.* (2021).

3.2.3. Fieldwork and Laboratory Analysis

In order to characterise the physical and geochemical characteristics of emissive surfaces and quantify the smaller-scale controls on sediment availability and processes for dust emissions from the pan in Parts 3 and 4 of the research, a fieldwork campaign was conducted at Etosha Pan in September 2022. Field studies were performed across five strategic sample sites situated in the southern portion of Etosha Pan, which represented surfaces of varying emissivity (ranging from non-emissive to highly emissive 'hot-spot' surfaces) identified from the satellite remote sensing observations of dust emissions in Parts 2 and 3.

The Portable In-Situ Wind ERosion Laboratory (PI-SWERL; Etyemezian *et al.,* 2007, 2014; Sweeney *et al.,* 2008) was employed to measure erosion thresholds and emissions flux from each sample site (see section 7.2). The PI-SWERL allows for relatively fast, repeatable measurements, and has been successfully used to produce erodibility estimates on various playa surfaces in numerous geomorphic studies (Baddock *et al.,* 2011; Buck *et al.,* 2011; King *et al.,* 2011; Sweeney *et al.,* 2011, 2016, 2023; Cui *et al.,* 2019a,b; von Holdt *et al.,* 2019; Dickey *et al.,* 2023).

To identify the surface erodibility characteristics that determine the relative emissivity of surfaces, ground-based measurements of various land surface properties (i.e., crust depth and strength, and subsurface volumetric soil moisture content) were simultaneously obtained alongside PI-SWERL tests (see section 7.2.2). Surface crust and near-surface (top 5 cm) sediment samples were collected from each field site for laboratory analyses of particle grain size and geochemistry. Grain size analyses of sediment samples were performed by laser diffraction to determine sample particle size ranges and identify the proportion of fine sediment susceptible to aeolian erosion at each site (see section 7.2.3) (Gillette *et al.,* 1997; Qiang *et al.,* 2007; Vandenberghe, 2013). The mineralogical compositions of sediment samples were examined by X-ray diffraction (XRD) analyses (see sections 6.2.2 and 7.2.3) and comparisons of spectral profiles obtained using an Analytical Spectral Devices (ASD) FieldSpec 4 Pro portable spectroradiometer (see section 6.2.2).

Comparisons of field and laboratory measurements in relation to PI-SWERL erosion thresholds and emission fluxes at each site were performed to determine the relative influence of post-depositional processes and sediment properties that differentiate dust producing and non-dust producing surfaces at the sub-landform scale. The outcomes of those analyses were subsequently contextualised against broader-scale hydrological and climatological conditions, erosivity drivers, and surface characteristics derived from remote sensing analyses performed in Parts 1, 2 and 3 to further clarify the processes and controls that lead to the development of dust 'hot-spot' emissive surfaces and their thresholds for erosion at Etosha Pan.

CHAPTER FOUR

Part 1

Hydrological context of the Cuvelai-Etosha Basin

Hydrological context of the Cuvelai-Etosha Basin

4.1. Introduction

Given the potential influence on both sediment supply (through pan surface inundation) and availability (through surface crusting and moisture dynamics), changes in the timing, frequency and amount of precipitation occurring in the Cuvelai-Etosha Basin have the potential to generate significant variability in the magnitude, distribution and timing of windblown dust emissions from Etosha Pan on a seasonal and inter-annual basis (Bryant *et al.,* 2003; Mahowald *et al.,* 2003). Yet, studies of precipitation and hydrological dynamics in the Cuvelai-Etosha Basin are uncommon and preliminary in their analyses.

Several previous investigations have noted that precipitation and surface flooding events in the region are characterised by high spatial and temporal variability (Bryant, 2003; Hipondoka *et al.,* 2006, 2018; Mendelsohn *et al.,* 2013; Hamunyela *et al.,* 2022). At the continental scale, observational and modelling studies have produced evidence of a link between rainfall variability in southern Africa with El Niño-Southern Oscillation (ENSO) phases and related sea surface temperature (SST) anomalies over the Indian and South Atlantic Oceans (Nicholson and Kim, 1997; Nicholson and Selato, 2000; Reason and Rouault, 2002; Reason and Jagadheesha, 2005; Bryant *et al.,* 2007; Meque and Abiodun, 2015; Gaughan *et al.,* 2016; Gore *et al.,* 2020).

Yet, there remains a gap in research to date that examines the specific spatiotemporal dynamics of rainfall within the Cuvelai-Etosha catchment (particularly in the context of global climate cycles), ephemeral flooding of Etosha Pan, the possible links between them and their potential to control windblown dust emissions from the pan surface.

Remote sensing investigations by Bryant (2003) and Mahowald *et al.* (2003) have linked rainfall-driven ephemeral flooding events with aeolian dust emissions on Etosha Pan. However, these analyses were conducted using a limited time-series of climate and remote sensing data (1996–2000). The number and intensity of observed pan surface inundation events (< 3 events) was not sufficient to fully comprehend the observed variability in dust emissions (Bryant *et al.,* 2007). Moreover, such observations did not consider the broader influence of regional hydrological and climatological controls on flooding and dust dynamics. Improvements in the development and availability of open-access satellite remote sensing products in recent decades has offered the capability for continuous global-scale estimates of atmospheric and land surface characteristics with increased spatial and temporal resolution (Dash and Ogutu, 2016; Huang *et al.,* 2018; Li, W. *et al.,* 2020; Duan *et al.,* 2021).

A novel opportunity therefore exists to considerably expand upon the previous research conducted at Etosha Pan in 1996–2000 (Bryant, 2003; Mahowald *et al.,* 2003). By extending the time-series of remote sensing data and analysis to the most recent twenty-year period, this research seeks to establish a comprehensive hydrological

context of the Cuvelai-Etosha Basin, which is necessary to ultimately determine the potential hydrological controls on aeolian dust emissions at Etosha Pan.

This chapter details the first part of the remote sensing-based research, which aims to quantify the temporal and spatial dynamics of precipitation events across the Cuvelai-Etosha Basin and subsequent flooding of Etosha Pan, and place them in context with global scale climate cycles for the period 2000 to 2022.

The specific research objectives are to:

1) Determine the annual and seasonal trends in precipitation across the Cuvelai–Etosha Basin;
2) Determine the annual and seasonal trends in ephemeral flooding events on Etosha Pan;
3) Identify the sources of ephemeral flooding on the pan surface;
4) Establish any association between flooding of Etosha Pan and catchment-scale precipitation;
5) Explore the potential relationship between precipitation and flooding dynamics at Etosha Pan with large-scale global climate cycles and sea surface temperature (SST) anomalies.

4.2. Data Sources and Methods

4.2.1. Catchment precipitation data sources

Precipitation observations used in this research were acquired from 11 meteorological stations located within the Cuvelai-Etosha Basin. Monthly observed precipitation totals were derived from available climate data records with varying temporal coverage across 10 local weather stations (Mahenene, Ondjiva, Namacunde, Oshaambelo, Ogongo, Ondangwa, Okashana, Okapya, Okaukuejo, and Mannheim) provided by the Southern African Science Service Centre for Climate Change and Adaptive Land Management (SASSCAL; https://sasscal.org/) and continuous rain gauge measurements recorded at Windpoort (data provided by W. Versfeld, M.G. Sorokin and B. Holben [NASA]) (see Figure 4.1 for locations).

Precipitation records were extracted and pre-processed by removing anomalous wet season zero values (i.e., data gaps caused by malfunctioning meteorological stations) to develop monthly, seasonal and annual (July – June hydrological year) time series for the 2000–2022 research period. The precipitation time-series based upon meteorological station observations are limited in their representation of rainfall variability in terms of both spatial coverage, with an inherent bias towards the southern and western regions of the catchment area (Figure 4.1), and temporal coverage, with numerous gaps in observations for the period of analysis (Figure 4.2).

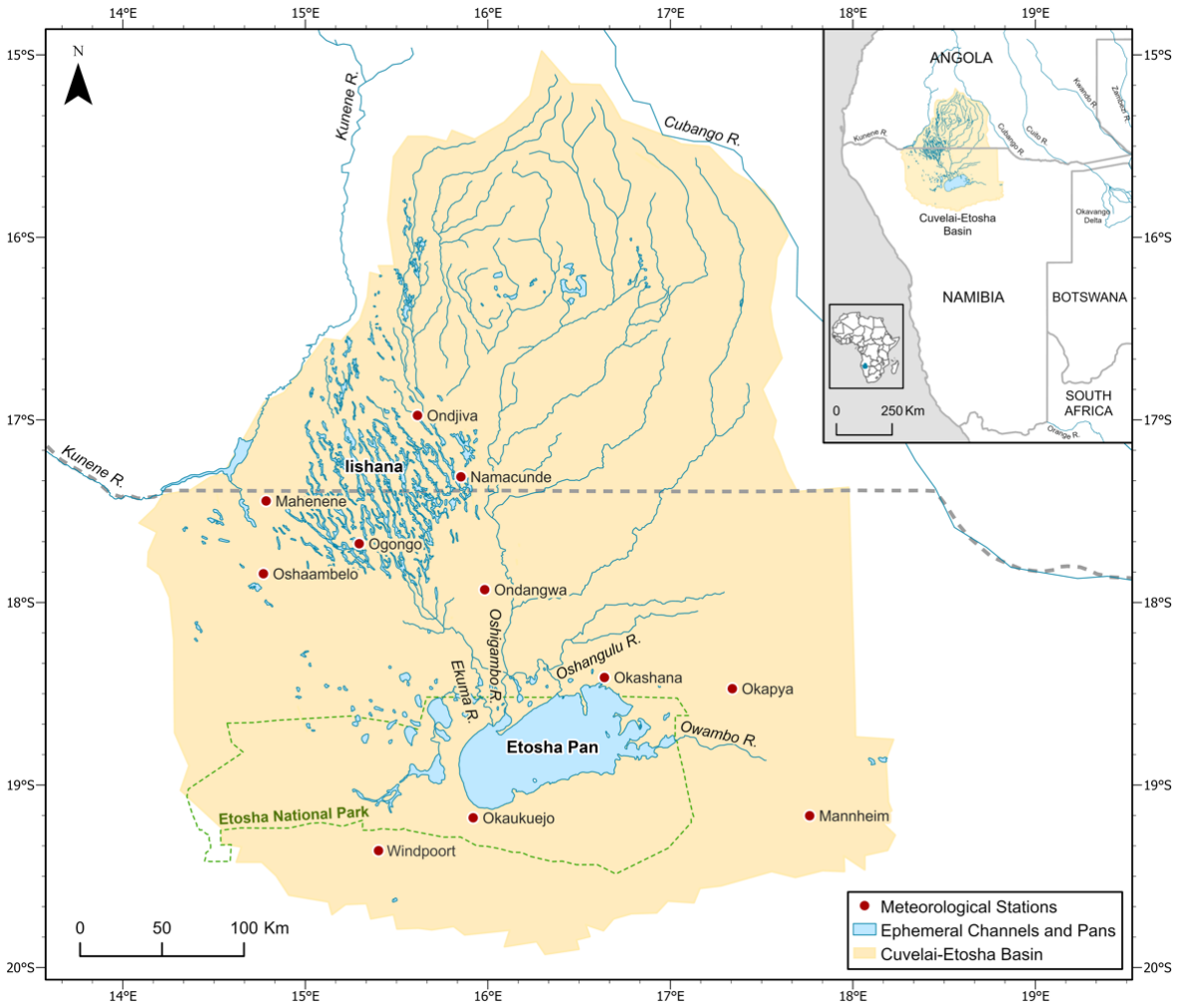


Figure 4.1. The location of Etosha Pan within the Cuvelai-Etosha Basin in Namibia, highlighting key river channels and the principal meteorological stations used in this study. Geospatial boundary data were obtained from the Namibia Statistics Agency (nsa.org). Hydrographic vector shapefiles were obtained from the HydroSHEDS database (Lehner *et al.*, 2008). Meteorological station data (with the exception of Windpoort) were obtained from the Southern African Science Service Centre for Climate Change and Adaptive Land Management (SASSCAL).

Accordingly, these data were augmented with satellite-retrieved daily, monthly and annual precipitation estimates for the Cuvelai-Etosha Basin using The Integrated Multi-Satellite Retrievals for GPM (GPM-IMERG) and The Tropical Rainfall Measuring Mission (TRMM) gridded precipitation products, available from the Goddard Earth Science Data and Information Services Center (http://disc.gsfc.nasa.gov/).

The GPM-IMERG post-processed product, which provides up to hourly precipitation estimates at 0.1° x 0.1° spatial resolution, has been shown to provide optimal estimates of precipitation when compared against other satellite-retrieved and reanalysis rainfall products (e.g., CHIRPS and TRMM) and ground-based rain gauge data (Shawky *et al.,* 2019; Tang *et al.,* 2020; Peng *et al.,* 2021; Kazamias *et al.,* 2022; Pradhan *et al.,* 2022). However, since GPM-IMERG data are available from June 2000 – present day, precipitation estimates were supplemented with TRMM data (available from 1998–2019 at 0.25° x 0.25° spatial resolution) for July 1999 – June 2000 to ensure complete coverage of the research period. The accuracy of the satellite-retrieved precipitation data was evaluated by statistical comparison (Pearson Correlation) against the ground-based observations data from the meteorological stations (Figure 4.2; see also Appendix 1.1).

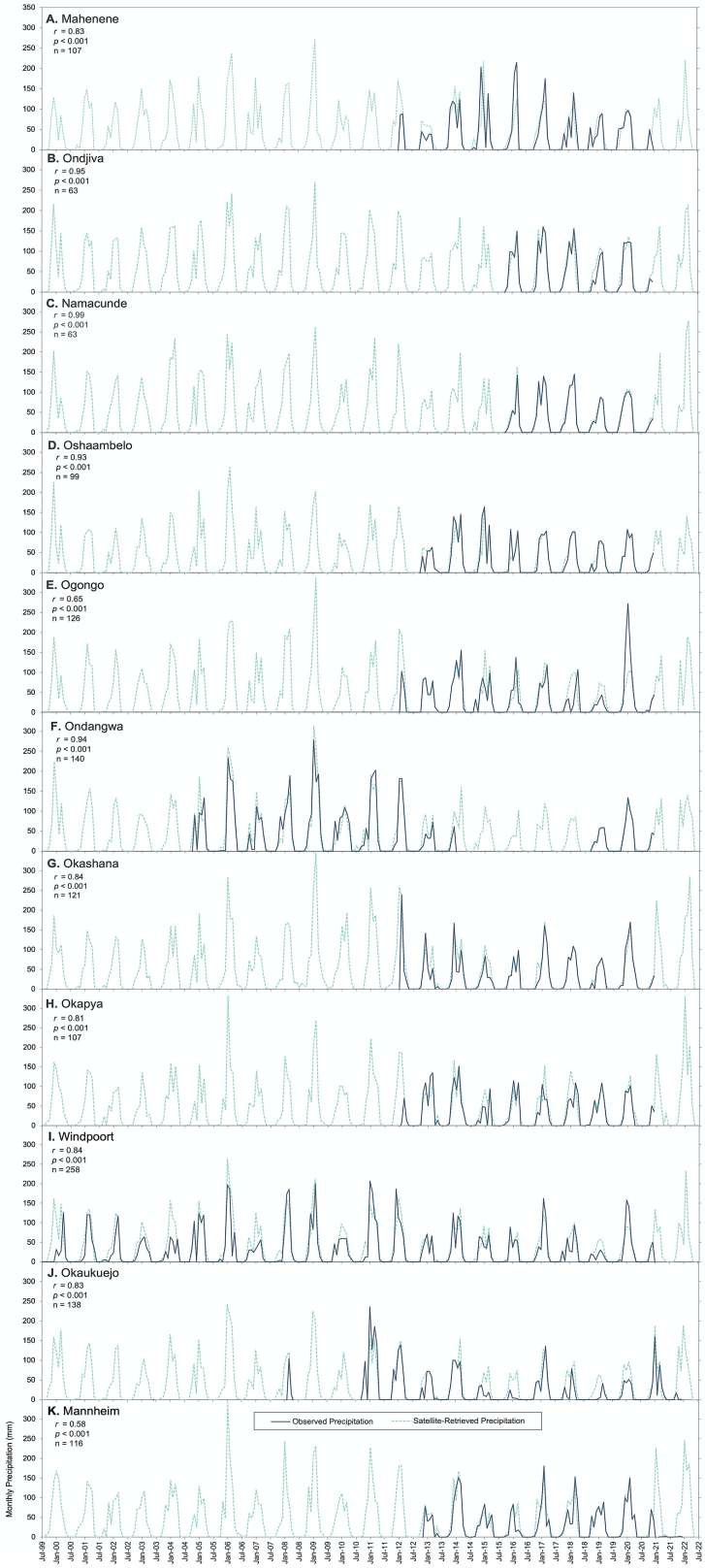


Figure 4.2. Time-series of observed monthly precipitation from meteorological stations (shown in blue; see Figure 4.1, Chapter 4 for locations) and pixel value estimates from the TRMM (July 1999 – June 2000) and GPM-IMERG (July 2000 – June 2022) satellite rainfall products (shown in green) in corresponding locations within the Cuvelai-Etosha Basin.

4.2.2. Pan surface flooding data sources

With the capability of synoptic view and repeated coverage of the Earth's surface, satellite remote sensing is an effective and well-established approach for monitoring ephemeral water bodies across a range of spatial and temporal scales (Haas *et al.,* 2009; Li *et al.,* 2015; Huang *et al.,* 2018; Herndon *et al.,* 2020). Optical satellite imagery platforms such as the Moderate Resolution Imaging Spectroradiometer (MODIS) and Landsat have been widely used to map surface water dynamics in many arid and semi-arid regions (Bryant and Rainey, 2002; Soti *et al.,* 2009; Haas *et al.,* 2011; Deus and Gloaguen, 2013; Sun *et al.,* 2014; Acharya *et al.,* 2016; Mohammadi *et al.,* 2017; d'Andrimont and Defourny, 2018; Che *et al.,* 2019).

Images acquired from the MODIS sensor aboard NASA's Terra satellite were selected as the principal data source for analysing the spatiotemporal dynamics of lake surface area at Etosha Pan. The MODIS Surface Reflectance dataset (MOD09GA.006), which provides surface reflectance values at 250 m (bands 1 – 2) and 500 m (bands 3 – 7) spatial resolutions, was selected on the basis of availability and coverage of daily image time-series at Etosha Pan since 2000 to the present day. The dataset therefore offers the opportunity to considerably expand and develop upon previous studies on the hydrology of Etosha Pan in 1996–2000 (Bryant, 2003; Mahowald *et al.,* 2003) and to thoroughly examine the seasonal and inter-annual trends in surface inundation across the longer-term (i.e., 2000–2022) (Klein *et al.,* 2014; Baddock *et al.,* 2021).

A total of 7,594 MODIS images from February 2000 to December 2022 were procured from NASA's LAADS DAAC data portal (ladsweb.modaps.eosdis.nasa.gov/) to build a daily image time-series for water body detection and analysis. As the presence of clouds can lead to confusion in the identification of water bodies using near-infrared remote sensing imagery (Ogilvie *et al.,* 2018; Wang *et al.,* 2019; Yao *et al.,* 2019), associated quality assessment information for each MODIS image scene was used to mask pixels labelled as cloudy from the time-series prior to the extraction of water bodies.

The moderate spatial resolution of MODIS imagery (250 – 500 m) limits its discrimination ability over small lakes and rivers (Che *et al.,* 2015). Landsat sensors offer the capability to delineate small water bodies and features (e.g., ephemeral river channels) characteristic of arid and semi-arid environments from its medium-high spatial resolution (30 m) imagery (Mishra *et al.,* 2020). However, the narrow swath and long (8- to 16-day) revisit intervals pose limitations for effectively capturing dynamic changes in lake areas due to seasonal or extreme weather events (e.g., heavy rainfall) across large spatial scales (Li *et al.,* 2015). Accordingly, Landsat data of 30 m resolution was used to assess the accuracy of water body detection and to identify sources of flooding to the pan from surrounding river channels.

A total of 185 cloud-free images collected from Landsat 5 TM (1984–2012) and Landsat 8 OLI (2013 – present day) sensors were used to validate the results of water body

detection from MODIS data. Level-2 Landsat TM and OLI data were acquired through the USGS Earth Explorer data portal (www.earthexplorer.com). Due to the pixel errors in Landsat 7 ETM+ (1999 – present day) imagery resulting from the scan-line corrector (SLC) failure (Chen *et al.*, 2011), Landsat 7 ETM+ data were not used in this study.

4.2.3. Detection of pan surface flooding extents

The simple method of density thresholding the MODIS daily time-series of band 2 (NIR; 0.84 – 0.88 μm; 250 m) surface reflectance images (2000–2022) was employed to identify and interrogate water body pixels in this study. A detailed description of the technique is given by Harris and Mason (1989). The density thresholding technique has proven to be a relatively rapid, reliable, and easily repeatable approach for extracting ephemeral lake area data from image time-series (Bryant and Rainey, 2002) and has been successfully applied in previous research applications at Etosha Pan (Bryant, 2003; Mahowald *et al.,* 2003).

Single NIR band thresholding techniques have been found to detect water bodies more effectively than multi-band spectral indices in arid and semi-arid areas (Frazier and Page, 2000; Fisher *et al.,* 2016; Herndon *et al.,* 2020). While multi-band spectral indices, such as the Normalized Difference Water Index (NDWI) (McFeeters, 1996), Modified NDWI (MNDWI) (Xu, 2006), Normalized Difference Moisture Index (NDMI) (Gao, 1996), the Normalized Difference Pond Index (NDPI) (Lacaux *et al.,* 2007), and

the Automated Water Extraction Index (AWEI) (Feyisa *et al.,* 2014), have been widely used in mapping water bodies (Watson *et al.,* 2018; Cooley *et al.,* 2019; Yue *et al.,* 2020), they are less suitable for detecting ephemeral water bodies in arid and semi-arid regions, where the characteristic shallow depths and turbidity of saline lakes cause these multi-band indices to misclassify their waters as built-up areas or sand (Mishra *et al.,* 2020).

Atmospheric conditions, water depth and turbidity all influence the spectral features of ephemeral water bodies (Mishra *et al.,* 2020). As a result, a standard threshold value derived from one image could not be applied for the whole study period. Rather, the separation, or density thresholding, of land and water peaks from image histograms was performed for each daily image time-step. A semi-automated thresholding approach was applied by curve fitting the interval between peaks in image histograms and then using the first differential of this curve to determine the boundary separating the peaks, and thus water and land. This enabled extraction of water pixels to generate Boolean masks of lake area extents for each daily time-step in the MODIS image series.

The dynamic threshold density method was additionally applied to segment water bodies from Landsat 5 TM and 8 OLI image time-series for the corresponding period, which served as a validation source to evaluate the accuracy of MODIS-based surface water classifications (see Appendix 1.2). An overall accuracy of 0.96 was obtained for this study (Table A1.1), which is adequate for the dynamic analysis of lake surface area (Li *et al.,* 2015).

A time-series of 7,594 daily water masks were developed by dynamic threshold selection of MODIS band 2 data acquired from 2000 to 2022. A total of 3,406 daily image masks contained water bodies based on the water classification analysis; indicating that some part of Etosha Pan experienced flooding for approximately 42% of the study period. Daily, seasonal and annual flooding frequencies and lake area statistics (km^2 and % of the pan) were quantified to examine both inter-annual and seasonal trends in surface water dynamics at Etosha Pan.

4.2.4. Identification of surface flooding sources

It was necessary to identify the sources of fluvial input from surrounding river channels draining the Cuvelai-Etosha catchment in order to elucidate the spatiotemporal dynamics of flooding events on Etosha Pan and to recognise any potential sources of sediment supply deposited on the pan surface during flooding periods.

Owing to a lack of available gauged flow data within the catchment, Landsat imagery was used to detect surface water as a proxy for water inflow entering the pan from surrounding ephemeral river channels. A total of 303 Landsat 5 TM and 8 OLI image scenes spanning the 2000–2022 research period were employed for the detection of contributory river channel sources for surface inundation events identified from MODIS data at corresponding acquisition times. The dynamic threshold density method was used to segment water bodies within ephemeral river channels from

Landsat 5 TM and 8 OLI NIR data (bands 4 and 5, respectively). In the instances where pan surface inundation occurred but a contributory river channel source could not be identified from the Landsat imagery, the sources of ephemeral flooding events were attributed to direct precipitation (provided non-negligible precipitation totals were recorded over Etosha Pan) or groundwater fluctuations (if no precipitation was observed) based upon TRMM/GPM-IMERG gridded precipitation data for corresponding periods.

4.2.5. The influence of regional catchment precipitation on pan surface flooding dynamics

The potential associations between pan surface flooding events with annual and seasonal rainfall in the Cuvelai-Etosha Basin were examined by statistical comparisons (Pearson Correlation) of daily, monthly, and annual flooding frequencies and extents against corresponding satellite-derived catchment precipitation totals over the 2000–2022 period.

4.2.6. The influence of global climate cycles on catchment precipitation and pan surface flooding dynamics

Summer rainfall variability in southern Africa has previously been linked with El Niño-Southern Oscillation (ENSO) cycles (e.g., Nicholson and Kim, 1997; Nicholson and Selato, 2000; Reason and Rouault, 2002; Kane, 2009; Philippon *et al.,* 2012), Indian Ocean sea surface temperature (SST) anomalies (e.g., Landman and Mason,

1999; Washington and Preston, 2006), and changes in the Indian Ocean Dipole (e.g., Bryant *et al.,* 2007; Gaughan *et al.,* 2016; Hoell and Cheng, 2018). In line with these observations, the potential associations between precipitation anomalies in the Cuvelai-Etosha Basin with global scale climate cycles and sea surface temperature (SST) anomalies (Table 4.1) were examined by statistical analysis (Pearson Correlation).

Table 4.1. Global climate indices of sea surface temperature (SST) anomalies used in correlation analyses for the 2000 – 2022 period.

Climate Index	Description	References
ENSO 3.4	Tropical Pacific El Niño–Southern Oscillation SST anomalies in the Niño 3.4 region (5°N–5°S and 120°W–170°W).	Rayner *et al.* (2003)
SIOD	Subtropical Indian Ocean Dipole Index computed from the difference between western (55°E–65°E and 37°S–27°S) and eastern (90°E–100°E and 28°S–18°S) Indian Ocean SST anomalies.	Behera and Yamagata (2001)
West IO	SST anomalies from the western Indian Ocean (37°S–27°S and 55°E–65°E).	Saji *et al.* (1999); Iizuka *et al.* (2000)
East IO	SST anomalies from the eastern Indian Ocean (28°S–18°S and 90°E–100°E).	Saji *et al.* (1999); Iizuka *et al.* (2000)
TSA	Tropical Southern Atlantic Index computed from SST anomalies in the eastern tropical South Atlantic Ocean (0°S–20°S and 10°E–30°W).	Enfield *et al.* (1999)
MEI V2	The Multivariate El Niño–Southern Oscillation (ENSO) index computed from the Empirical Orthogonal Function (EOF) of five different variables (sea level pressure, sea surface temperature, zonal and meridional components of the surface wind, and outgoing longwave radiation) over the tropical Pacific basin (30°S–30°N and 100°E–70°W).	Wolter and Timlin (2011); Kobayashi *et al.* (2015)
DMI	Dipole Mode Index computed from SST anomalies between the western equatorial Indian Ocean (10°S–10°N and 50°E–70°E) and the south-eastern equatorial Indian Ocean (10°S–0°N and 90°E–110°E).	Saji and Yamagata (2003a, b)

A time-series of standardised quarterly (Dec/Jan/Feb [DJF]; Mar/Apr/May [MAM]; Jun/Jul/Aug [JJA]; Sep/Oct/Nov [SON]) rainfall anomalies for 2000–2022 were formed by spatially averaging the satellite-derived monthly gridded precipitation totals over the catchment area for each period. Sea surface temperature anomalies listed in Table 4.1 were extracted from the Climate Diagnostics Centre (CDC) online archives (http://psl.noaa.gov/data/climateindices) and the Indian Ocean dipole (IOD) site maintained by the Frontier Research System for Global Change (FRSGC)/Japan Agency for Marine-Earth Science and Technology (JAMSTEC) Climate Variations Research Program (http://www.jamstec.go.jp).

4.3. Results and Discussion

4.3.1. Spatiotemporal dynamics of catchment precipitation

Annual Trends

The inter-annual variations in precipitation in the Cuvelai-Etosha Basin from 2000 to 2022 are displayed in Figure 4.3. While the overall trends are consistent between the ground-based observed and satellite-retrieved precipitation data sources, results indicate that mean annual precipitation observed from meteorological stations was systematically lower than the catchment-wide mean annual precipitation derived from spatially averaged satellite gridded precipitation products. This is emphasised by the 37% difference in the twenty-year mean annual precipitation values of 394 mm (field-observed) and 572 mm (satellite-derived) (Figure 4.3). This suggests that a

greater proportion of rainfall in the Cuvelai-Etosha Basin occurs in other regions apart from the central and southern areas of the catchment where the meteorological stations are situated (see Figure 4.1 for locations).

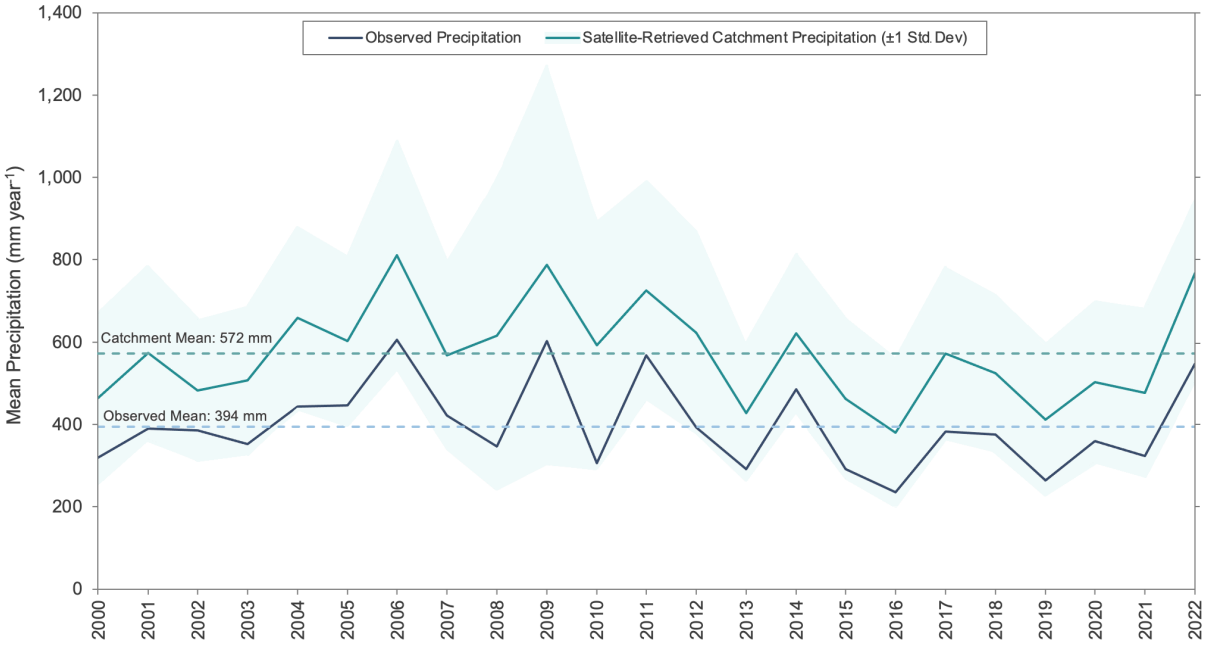


Figure 4.3. Annual trends in observed precipitation from meteorological stations (dark blue) and satellite-retrieved mean catchment precipitation (±1 standard deviation) (green) from 2000 to 2022 in the Cuvelai-Etosha Basin.

Indeed, Mendelsohn *et al.* (2013) have shown that a seasonal north-east to south-west rainfall gradient exists across the Cuvelai-Etosha Basin as a result of moist air being fed in from the north and north-east during the wet season. In line with these observations, it is likely that the overall catchment-wide mean annual precipitation estimates are increased by higher rainfall totals received in northern regions of the Cuvelai-Etosha Basin (Hamunyela *et al.*, 2022).

Therefore, given the inherent bias in spatial coverage of meteorological station records across the catchment, the use of available observed records will always underestimate catchment-scale precipitation. This emphasises the value of utilising satellite-retrieved gridded estimates to quantify precipitation across the entire catchment, provided that estimates have sufficient accuracy upon ground-truthing (Pradhan *et al.,* 2022).

Shown in Figure 4.3, rainfall in the Cuvelai-Etosha Basin has increased steadily from 2000 to a peak in 2006, reaching a value of 811 mm across the entire catchment based upon satellite-retrieved estimates. A gradual declining trend followed, where below average catchment-scale precipitation was recorded in particularly dry years of 2013 (428 mm ±164 mm), 2015 (462 mm ±193 mm), 2016 (379 mm ±178 mm) and 2019 (411 mm ±184 mm) during the study period (Figure 11). However, this declining trend was disrupted by increased values measured during the particularly wet years of 2009 (787 mm ±604 mm), 2011 (725 mm ±265 mm) and 2022 (768 mm ±174 mm) (Figure 4.3).

In addition to having some of the highest mean annual precipitation totals recorded during the study period, the years 2006, 2009, and 2011 also experienced the greatest variability in rainfall across the catchment, as indicated by the satellite-retrieved estimates (±1 standard deviation; Figure 4.3). This was a result of extreme rainfall values recorded across the catchment during the austral summer wet season months (November – April) in comparison to the dry season precipitation totals. For instance,

mean catchment precipitation in February 2009 was 250 mm, a significant increase compared to the average of 74 mm for that month recorded across the study period, contributing to the increase in the mean annual total and variability for that year.

Figure 4.4 illustrates the spatial variability in the mean annual precipitation derived from the satellite gridded precipitation estimates across the Cuvelai-Etosha Basin. The existence of a north-east to south-west rainfall gradient in the catchment is evident, where mean annual precipitation was much higher (~700 – 820 mm $year^{-1}$) in the upper reaches of the catchment, declining towards the south-west, where mean annual rainfall was much lower (~240 – 300 mm $year^{-1}$) for the 2000 to 2022 research period (Figure 4.4).

The graph in Figure 4.4, which shows pixel estimates of the twenty-three year mean annual precipitation along a N–S transect, indicates that rainfall declined at a steady rate from 819 mm (± 214 mm) in the northernmost part of the catchment. However, the rate of decline decreased towards a stable annual precipitation total of around 310 mm between 350 km and 550 km south along the N–S transect (where the majority of meteorological stations are situated), with the exception of a small rise in measured rainfall of ~330 – 350 mm $year^{-1}$ over Etosha Pan itself (Figure 4.4).

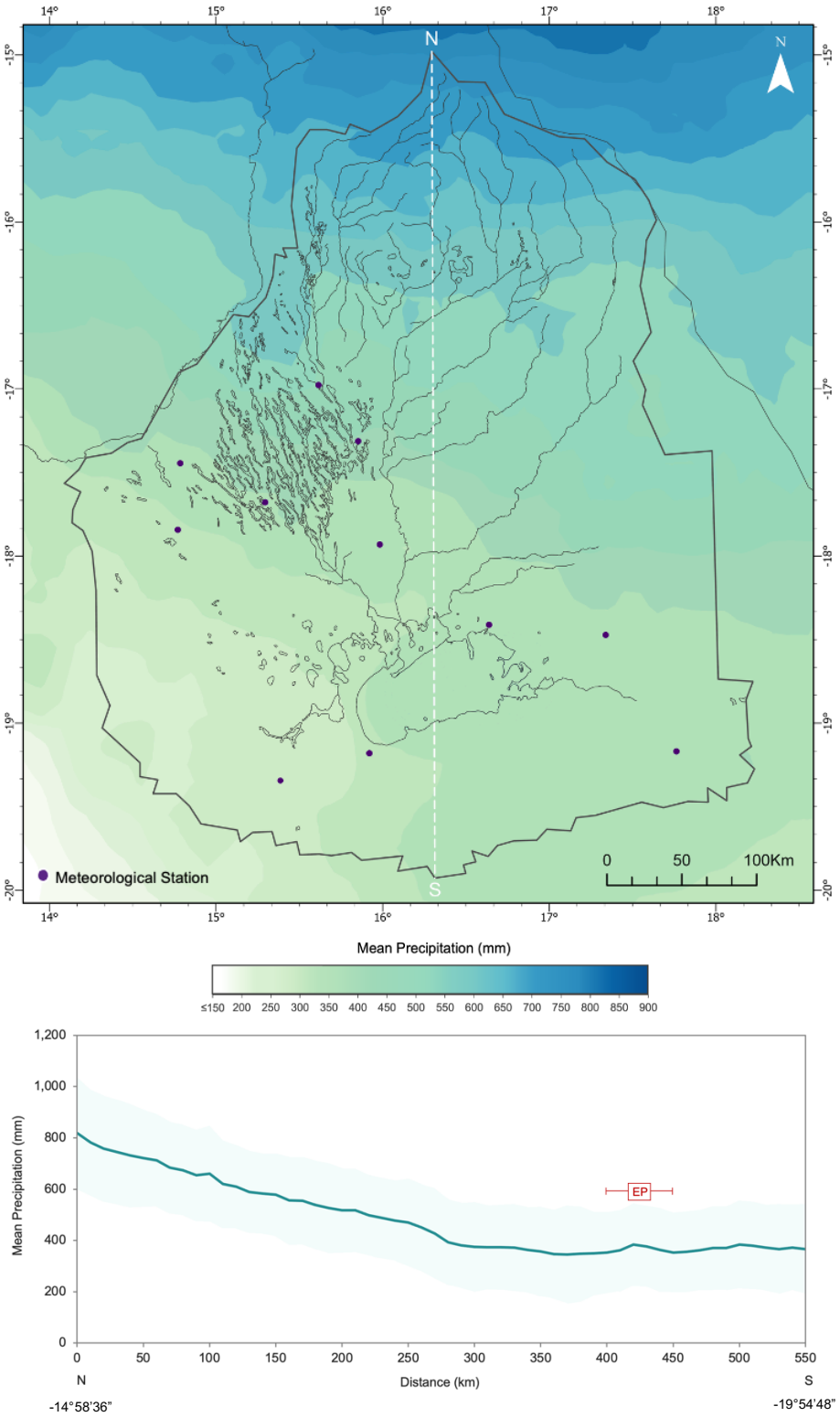


Figure 4.4. Spatial distribution of mean annual precipitation in the Cuvelai-Etosha Basin from 2000 to 2022. The contour map shows that mean annual precipitation decreases along a NE – SW gradient, emphasised by the corresponding N – S transect displayed in the graph, where the solid line represents mean values (±1 standard deviation). Purple points indicate the principal meteorological stations utilised in this study. EP indicates the location and extent of Etosha Pan along the N – S transect.

Seasonal Cycle

A seasonal rainfall cycle at the catchment scale is displayed in Figure 4.5, derived from satellite-retrieved monthly accumulations in the Cuvelai-Etosha Basin for 2000–2022. Figure 4.5 shows periods of increased rainfall in the catchment during the austral summer wet season (November – April), which decline into the austral winter dry season (May – October).

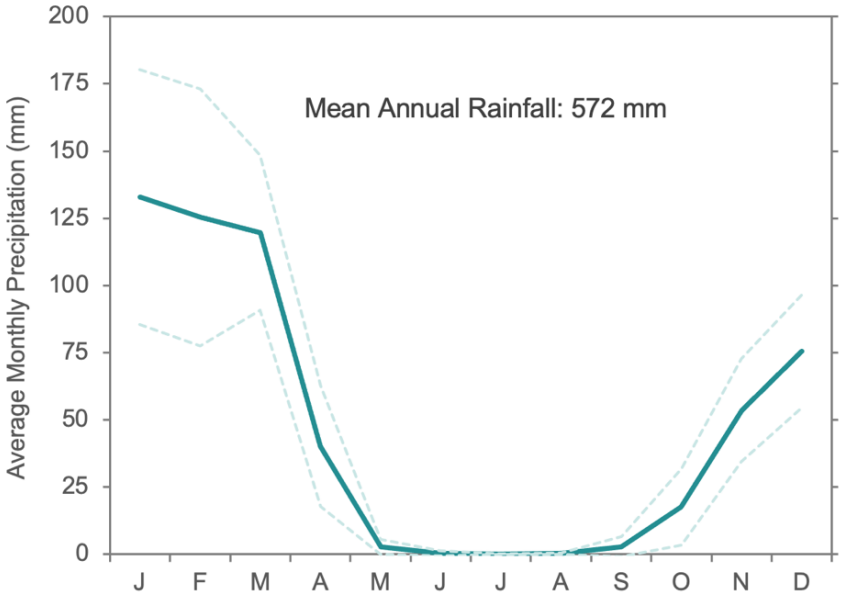


Figure 4.5. Mean monthly precipitation in the Cuvelai-Etosha Basin from 2000 to 2022 derived from satellite-retrieved (TRMM/GPM-IMERG) gridded precipitation data, where solid lines represent mean values and dashed lines represent ±1 standard deviation.

Both the highest mean values of monthly precipitation and greatest inter-annual variability were recorded towards the latter half of the wet season (November – April), during the months of January (132.82 mm ±47.39 mm), February (125.39 mm ±47.79 mm) and March (119.65 mm ±28.78 mm) (Figure 4.5). Mean precipitation was lowest and showed the least inter-annual variability in the austral winter dry season (May – October), with negligible rainfall (<0.5 mm) recorded during the months of June (0.49

mm ±0.88 mm), July (0.07 mm ±0.10 mm), and August (0.35 mm ±0.33 mm) (Figure 4.5).

Seasonal rainfall cycles derived from the meteorological stations are displayed in Figure 4.6, which correspond to the north-east to south-west rainfall gradient observed in the region (see also Figure 4.4; Mendelsohn *et al.,* 2013; Hamunyela *et al.,* 2022). The highest mean annual rainfall was recorded at stations located furthest north in the catchment (Ondjiva: 527 mm [Figure 4.6b] and Namacunde: 516 mm [Figure 4.6c]) compared to the lowest mean annual rainfall recorded at stations located in the south-west (Windpoort: 316 mm [Figure 4.6i] and Okaukuejo: 333 mm [Figure 4.6j]). This was the result of differences in the extent of wet season rainfall across the catchment, where higher average monthly precipitation totals were recorded in the wettest months (January – March) at stations located furthest north in the catchment (e.g., Ondjiva: ~130 mm; Figure 4.6b) compared to the lowest recorded at stations situated in the southern regions surrounding Etosha Pan (e.g., Windpoort: ~80 mm; Figure 4.6i).

During the austral winter dry season, negligible ($<$ 0.5 mm) mean monthly precipitation was observed by almost all of the meteorological stations (Figure 4.6a–k), with the exception of Ondangwa, which recorded anomalous precipitation in June and July (Figure 4.6f).

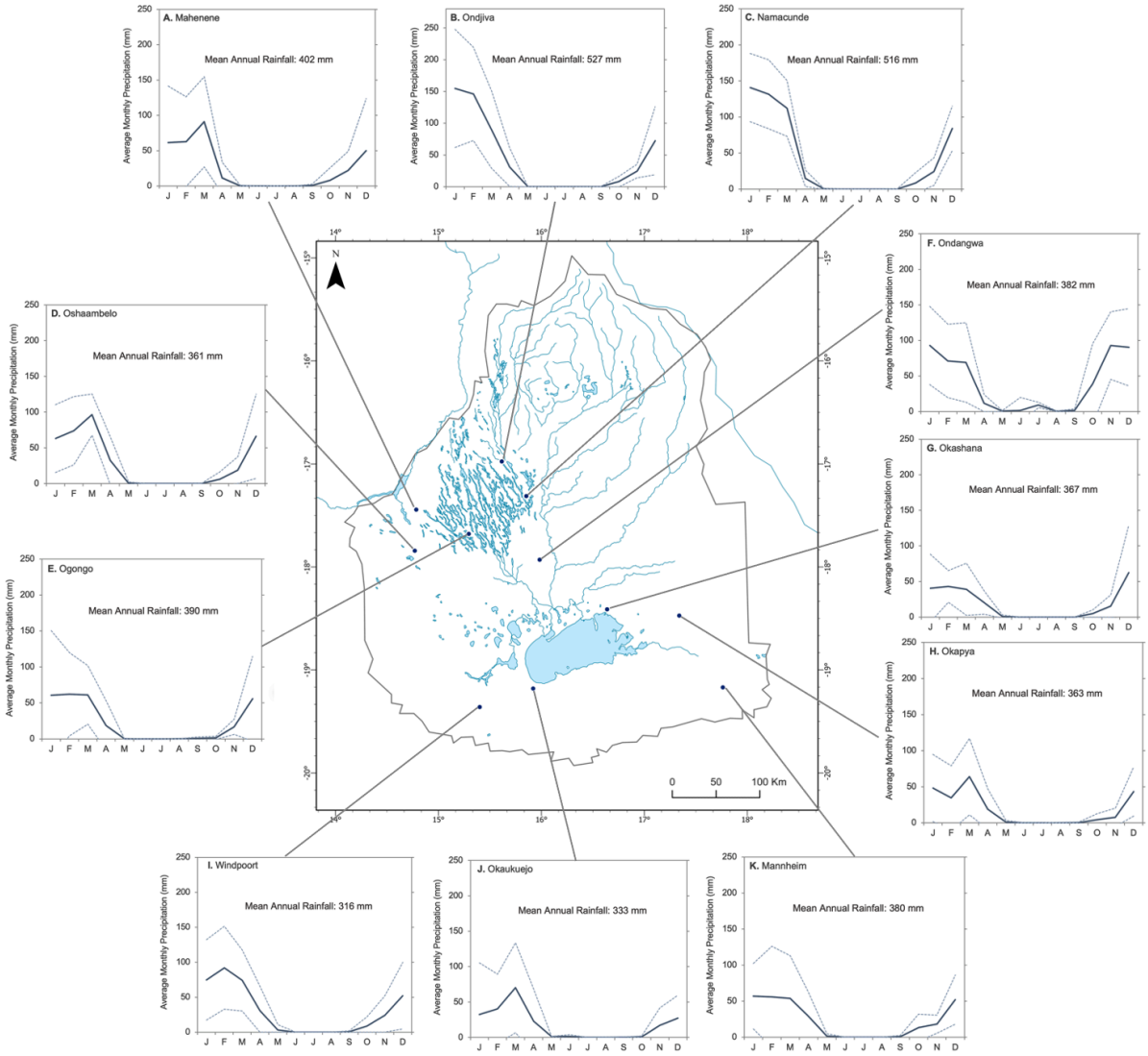


Figure 4.6. Mean monthly precipitation in the Cuvelai-Etosha Basin for the period 2000 – 2022 recorded at the following meteorological stations: (a) Mahenene, (b) Ondjiva, (c) Namacunde, (d) Oshaambelo, (e) Ogongo, (f) Ondangwa, (g) Okashana, (h) Okapya, (i) Windpoort, (j) Okaukuejo, and (k) Mannheim. All data are characterised by high inter-annual variability and a clear wet/dry season. Solid lines represent mean values and dashed lines represent ±1 standard deviation.

The spatiotemporal trends in seasonal rainfall suggested in Figure 4.6 are further supported by Figure 4.7, which shows average monthly rainfall distributions across the whole Cuvelai-Etosha Basin derived from satellite-retrieved gridded precipitation estimates for the 2000–2022 study period.

In Figure 4.7, the catchment-scale wet and dry seasons are clearly divisible. However, as the dry season transitioned to the wet season in October, there was a slight increase in mean monthly precipitation in the northern regions of the catchment (up to 30 mm) while much of the south-west remained dry (Figure 4.7j). Similarly, January to March are shown to be the wettest months on average, where regions in the north and east of the catchment experienced the highest rainfall totals (160 to 230 mm) (Figures 4.7a–c).

In contrast, during the dry season (May – September) the majority of the catchment received < 0.5 mm rainfall (Figures 4.7e–i). However, Figure 4.7 shows that, with the exception of July, anomalous precipitation (up to 20 mm) fell directly onto the eastern part of Etosha Pan compared to negligible (< 0.5 mm) mean monthly precipitation in the surrounding catchment during the dry season months of May to September (Figures 4.7e–i).

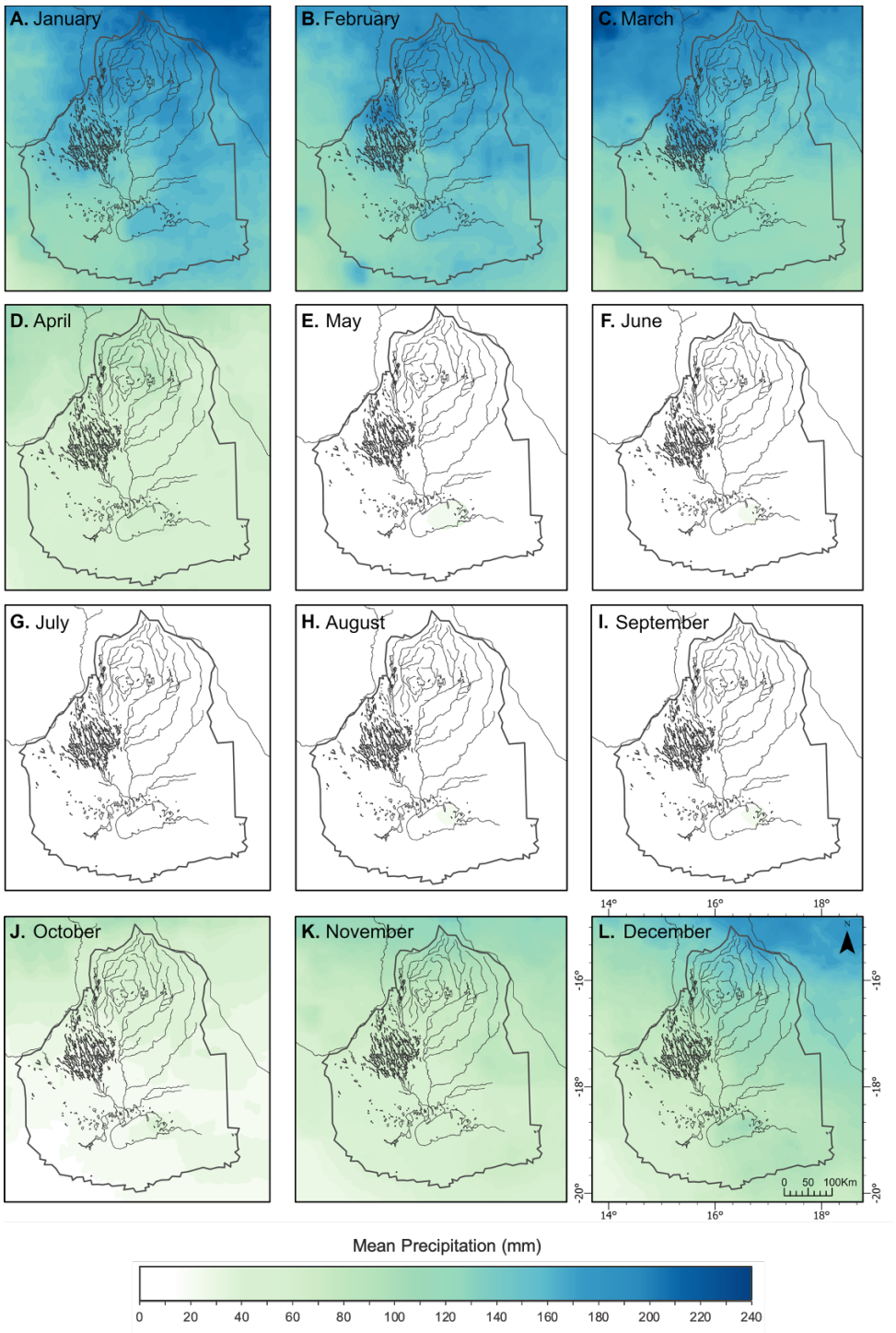


Figure 4.7. Spatiotemporal distributions of mean monthly precipitation for (a) January to (l) December derived from satellite-retrieved (TRMM/GPM-IMERG) gridded precipitation data in the Cuvelai-Etosha Basin from 2000 to 2022.

While Figure 4.7 illustrates the clear spatial variability in seasonal rainfall, it does not reflect the high inter-annual variability in rainfall indicated in Figures 4.3 and 4.5. Accordingly, frequency composites were also developed to illustrate the spatiotemporal variability of precipitation in the Cuvelai-Etosha catchment for each month in 2000–2022 (Figure 4.8), where 0.1° x 0.1° pixel values indicate the frequency (in years) that each individual pixel experienced precipitation during the study period.

As expected, the majority of precipitation events occurred during the wet season, with the highest wetted pixel frequencies (23 years) recorded across the majority of the catchment in the months of October – April (Figures 4.8a–d and j–l). While the months of May (Figure 4.8e) and September (Figure 4.8i) experienced the greatest variability in wetted pixel frequencies during the study period. This may be because they mark the transitions between the wet-to-dry and dry-to-wet seasons, respectively (Figures 4.5 and 4.6).

Correspondingly, the lowest wetted pixel frequencies (up to 5 years) were recorded in the dry season months of June – August (Figures 4.8f–h). However, July (Figure 4.8g) was the only month where the vast majority of the catchment received less than 0.5 mm of rainfall for all years of the study period.

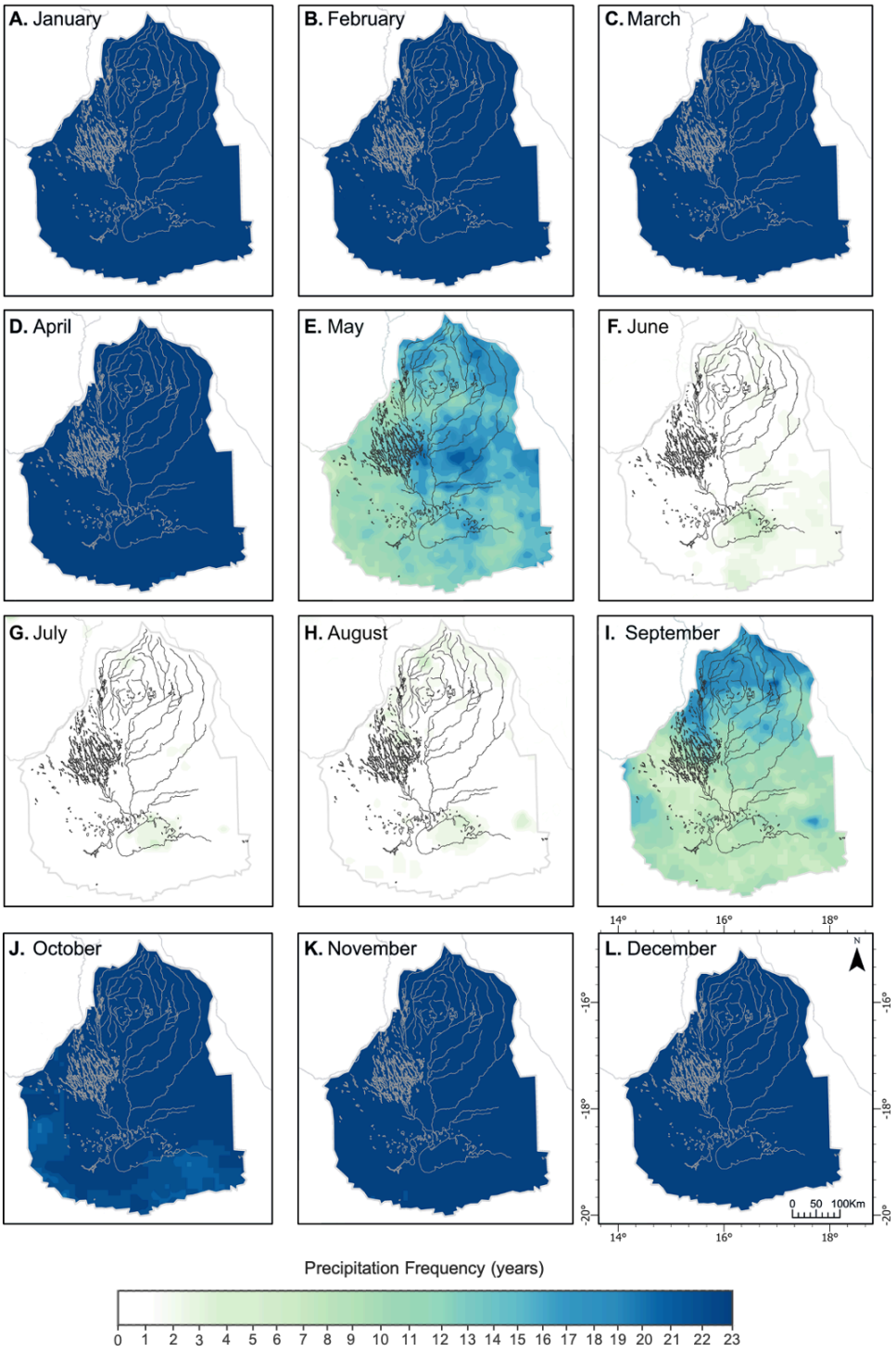


Figure 4.8. Spatiotemporal distributions of annual precipitation frequencies for (a) January to (l) December derived from satellite-retrieved (TRMM/GPM-IMERG) gridded precipitation data in the Cuvelai-Etosha Basin from 2000 to 2022. **Note:** the numbers at each pixel indicate the frequency in years that it has experienced > 0.5 mm precipitation in 2000 to 2022.

At the seasonal scale, it can be seen from Figures 4.7 and 4.8 that the majority of widespread precipitation on Etosha Pan occurred during the austral summer wet season months of November to April (~90 mm month^{-1} on average). Notably, however, at the height of the the dry season (June to August) clusters of light rainfall events (~5 mm month^{-1} on average) were concentrated in the central and eastern regions of Etosha Pan (Figures 4.7f–h and 4.8f–h). In the driest months of June (Figure 4.8f), July (Figure 4.8g), and August (Figure 4.8h), the satellite estimates suggest that some direct precipitation on those areas of the pan surface occurred in some of the wettest years (up to seven years) of the study period. This observation is supported by records of winter dry season precipitation (up to 27 mm month^{-1}) during the wettest years according to observed data from meteorological stations surrounding Etosha Pan (e.g., Okaukuejo and Okashana; Figure 4.2).

4.3.2. Spatiotemporal dynamics of pan surface flooding

Annual Trends

The inter-annual variations in lake surface inundation extents and flooding frequencies at Etosha Pan for hydrological years (July – June) from 2000 to 2022 are displayed in Figure 4.9. Results indicate that, to some degree, surface flooding of the pan occurred every year during 2000–2022. However, it has neither shown a general increasing or decreasing trend. Rather, both mean inundation extents and flooding frequencies have fluctuated considerably across the research period (Figure 4.9).

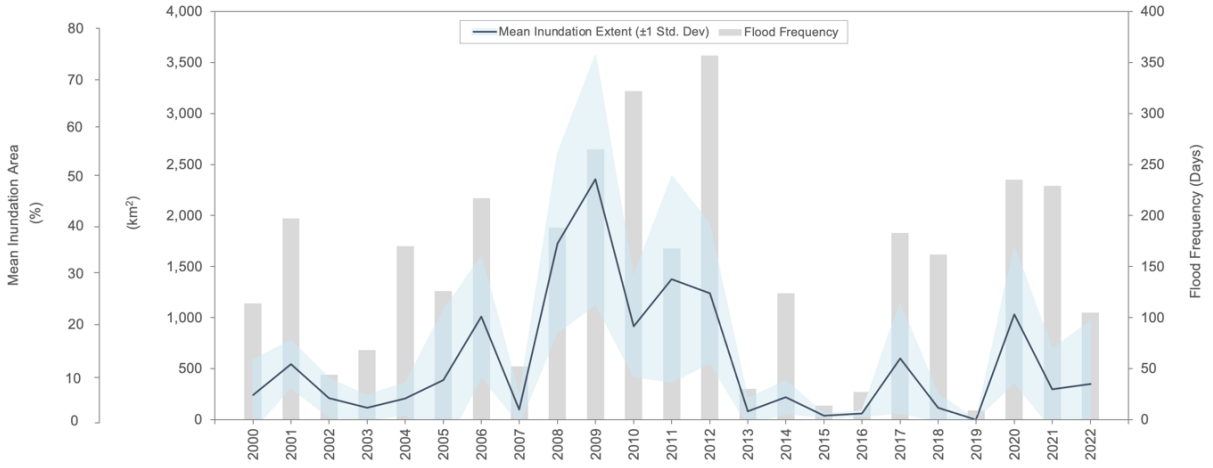


Figure 4.9. Annual mean lake surface inundation extents and total frequency of flooding at Etosha Pan for hydrological years (July – June) from 2000 to 2022.

It is also apparent from Figure 4.9 that mean lake surface inundation extents and flooding frequencies did not necessarily closely correspond. Greater average inundation extents were recorded in 2008 (1,725 km^2; 35.9% of total pan area), reaching a peak in 2009 (2,354 km^2; 49% of total pan area), and 2011 (1,378 km^2; 28.7% of total pan area). While annual flooding durations indicate that Etosha Pan was most frequently flooded in 2009 (265 days; 72.6% of the hydrological year), 2010 (322 days; 88.2% of the hydrological year), and 2012 (357 days; 97.5% of the hydrological year) (Figure 4.9). This suggests that extensive inundation of the pan surface is not always synonymous with prolonged flooding periods, where periods of frequent flooding did not necessarily generate the largest areal extents of pan surface inundation, and the most extensive flooding events were not the most frequent or prolonged in duration.

Frequency composites of daily flooding extents for each year of the research period displayed in Figure 4.10 illustrate the discrepancy between lake inundation extents and flooding frequency. For instance, the frequency maps for hydrological years 2008

and 2011 show extensive inundation across the pan surface. However, the corresponding flooding frequencies of these regions are lower (up to 200 days) than some of the smaller inundation extents recorded in 2010 and 2012 ($>$200 days) (Figure 4.10). Conversely, the frequency map for 2009 (Figure 4.10) contains one of the largest, most frequently flooded extents across the pan surface of all the years in the research period, corresponding to both its high annual mean lake surface inundation extent and flooding frequency (Figure 4.9).

The spatiotemporal distributions of flooding frequencies displayed in Figure 4.10 further emphasise the considerable variability in lake surface flooding that is not well reflected by mean surface inundation extent values recorded in Figure 4.9. At the individual flooding event scale, inundation of the pan surface ranged across considerably smaller and larger extents than mean values suggest for all years during the research period. However, it was during those hydrological years between 2008 and 2012, in which the most frequent and extensive flooding of the pan surface occurred, that there was the greatest variability in pan surface flooding extent (±1 standard deviation; Figure 4.9). For example, pan surface inundation areas fluctuated considerably around the annual average (1,378 km^2; 28.7% of total pan area) in 2011, ranging from 9.2 km^2 (0.2% total pan area) up to 4,051 km^2 (84.3% total pan area) for discrete ephemeral flooding events.

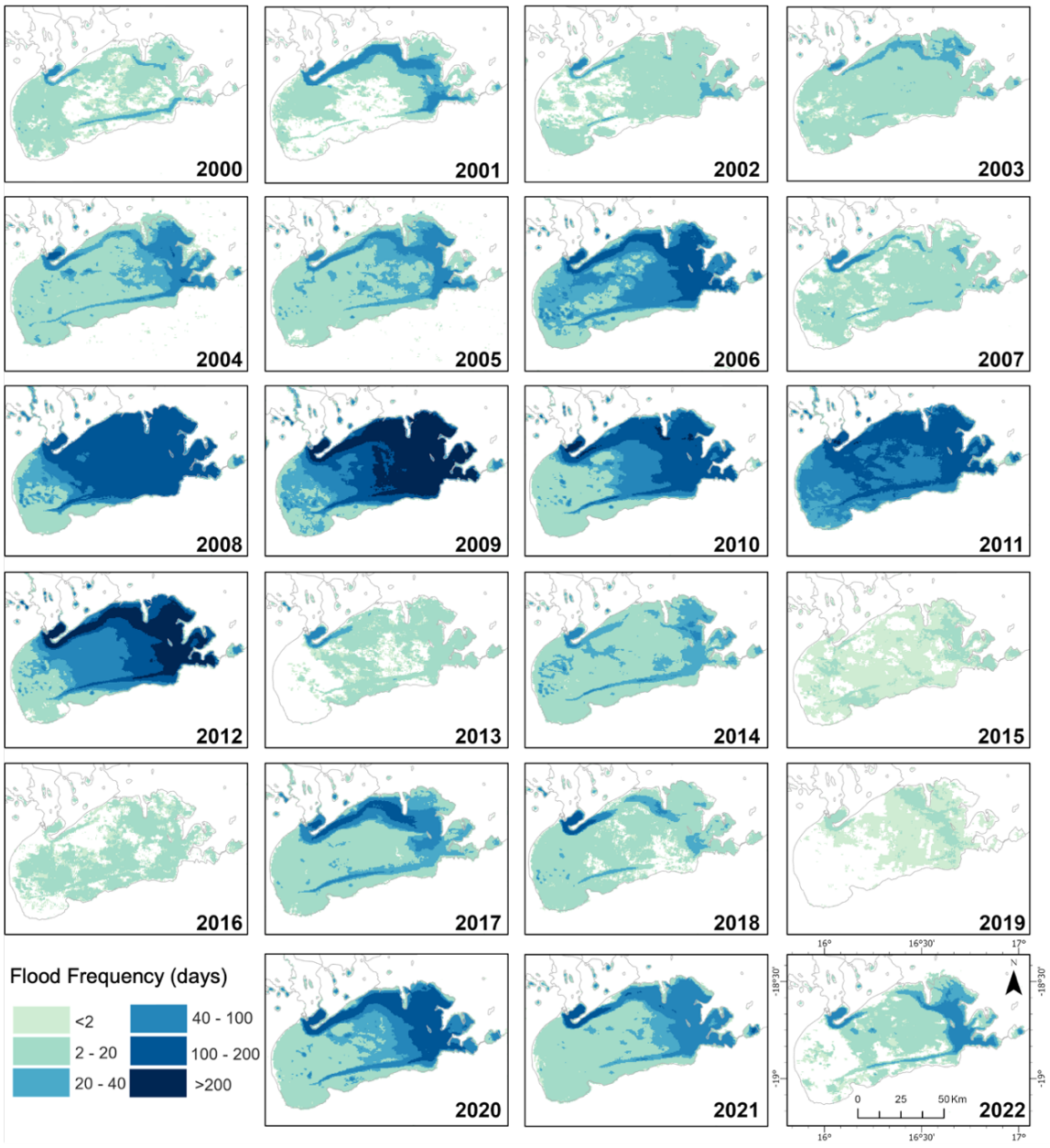


Figure 4.10. Spatiotemporal distributions of annual lake surface inundation frequencies at Etosha Pan from 2000 to 2022, where the value of each pixel indicates the frequency in days that it has experienced flooding for hydrological years (July – June) from 2000 to 2022.

Despite this inherent variability, the period of most frequent and extensive flooding of the pan surface in 2008–2012 corresponds to a period of above average rainfall in the Cuvelai-Etosha Basin (Figure 4.3). Indeed, Mendelsohn *et al.* (2013) and Cuthbert *et al.* (2019) observed that heavy rains in 2009 (787 mm) and 2011 (725 mm) (Figure 4.3) caused substantial flooding and increased groundwater recharge across the entire catchment. While both the annual lake surface inundation extents and flooding frequencies were consistently lower for hydrological years 2015 (40.7 km^2; 14 days flooded), 2016 (58.2 km^2; 27 days flooded), and 2019 (17.3 km^2; 9 days flooded). These observations are consistent with records of below average catchment-scale precipitation for corresponding years (Figure 4.3), which have been noted for causing some of the most extreme droughts in Namibia in the last century (Shikangalah, 2020; Liu and Zhou, 2021; van Rensburg and Tortajada, 2021).

Seasonal Cycle

Figure 4.11 illustrates the seasonal variations in average lake surface inundation extents and flooding frequencies at Etosha Pan from 2000 to 2022. Results indicate the most extensive and frequent flooding of the pan surface occurred during the latter end of the wet season (November – April) in the region, with consistently greater average inundation extents and flooding frequencies recorded in the months of March (1,094 km^2; 22 days flooded), April (1,052 km^2; 22 days flooded), and May (974 km^2; 26 days flooded).

This is followed by a decline throughout the dry season months that followed (June to October) to the lowest average inundation extents and flooding frequencies observed in November (365 km^2; 9 days flooded) and December (371 km^2; 8 days flooded), respectively (Figure 4.11). Note, however the inherent variability in both the extent and frequency of flooding (±1 standard deviation) in Figure 4.11, caused by extremes in lake surface inundation that were considerably higher than monthly average values during 2008–2012 and lower than monthly average values during 2015, 2016 and 2019, in accordance with inter-annual trends (Figure 4.9).

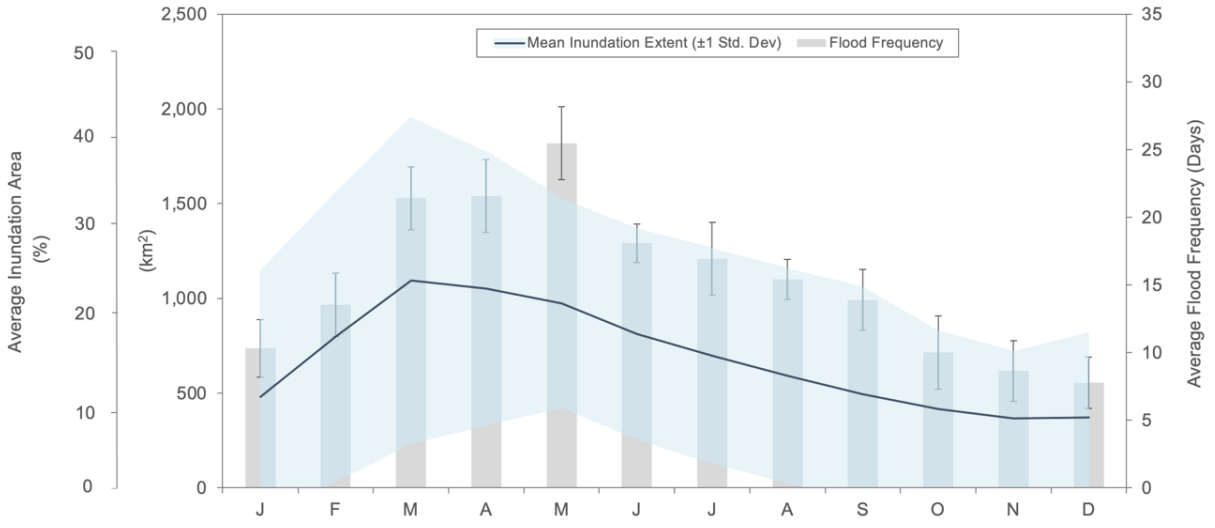


Figure 4.11. Mean monthly lake surface inundation extents and frequency of flooding at Etosha Pan from 2000 to 2022.

Displayed in Figure 4.12, frequency composites illustrate the spatial variations in lake surface flooding for each month during the 2000–2022 research period, which corroborate both the seasonal trends and inherent variability of inundation extents and flooding frequencies at Etosha Pan in Figure 4.11. The spatiotemporal

distributions show the majority of extensive flooding events occurred in January to May (Figures 4.12a–e), with the highest flood pixel frequencies (23 years) recorded in March (Figure 4.12c) and April (Figure 4.12d). Whereas lake surface flooding generally declined in extent and frequency during the following months of June to December (Figures 4.12f–l).

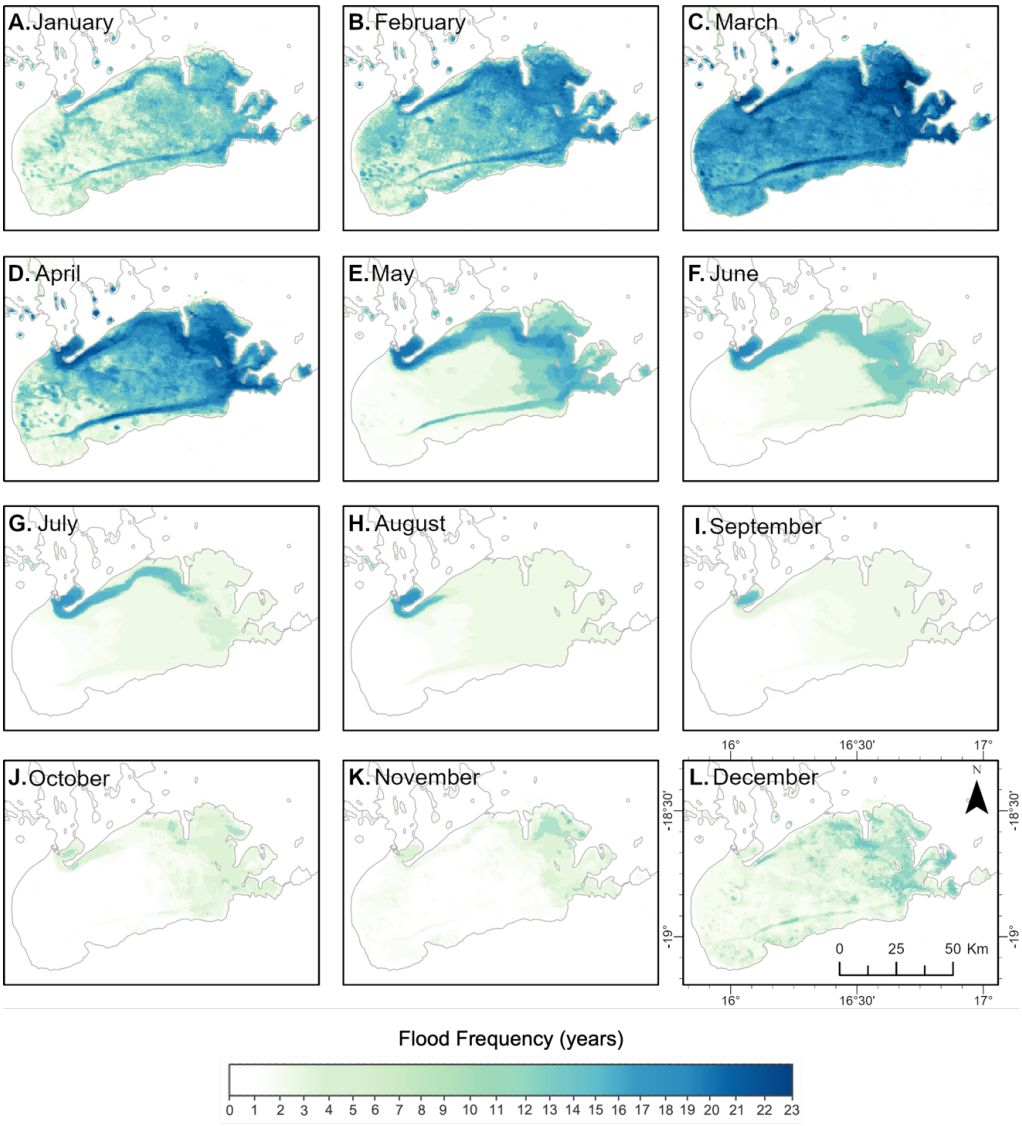


Figure 4.12. Spatiotemporal distributions of annual lake surface inundation frequencies for (a) January to (l) December from 2000 to 2022, where the value of each pixel indicates the frequency in years that it has experienced flooding for a given month in 2000 – 2022.

The seasonal patterns of pan surface inundation are largely consistent with those observed at Etosha Pan in previous related remote sensing studies in 1996–2000 (Bryant, 2003; Mahowald *et al.,* 2003). Using 1.1 km resolution AVHRR Ch-2 (NIR) data, both Bryant (2003) and Mahowald *et al.* (2003) recorded periods of inundation of the pan surface from March to July in 1997 and 2000, with lake areas peaking in April – May. These were sourced from ephemeral channel inputs draining the surrounding basin during heavy rainfall periods in 1997 and 2000 (Bryant, 2003). However, surface flooding was not observed in the region for all other years during the 1996–2000 period. Furthermore, the maximum monthly inundation extents for the two flooding events were 92 km^2 (1.9% of total pan area) in April 1997 and 79 km^2 (1.6% of total pan area) in May 2000, respectively (Bryant, 2003; Mahowald *et al.,* 2003), which were considerably smaller in area than those observed in this research for corresponding months during 2000–2022 (Figure 4.12).

Such variations may reflect the differing spectral and spatial resolutions of AVHRR and MODIS data (Liu *et al.,* 2019). However, a further validation exercise comparing water body masks derived using AVHRR Ch-2 (NIR) data with MODIS-derived water masks for 50 randomly selected corresponding acquisition dates during 2000–2022 revealed an overall agreement of 0.97 between the datasets. This suggests that the considerable differences between surface inundation extents observed in this research compared with those of Bryant (2003) and Mahowald *et al.* (2003) are likely a

consequence of natural variations in flooding events, rather than discrepancies in data collection techniques.

This is supported by the observed reduction in mean annual precipitation totals during the 1990s using long-term satellite-retrieved and ground-based meteorological station data (Mendelsohn *et al.,* 2013; Hamunyela *et al.,* 2022). It is, therefore, possible that the variations in flooding extent may reflect the inherent variability in catchment-scale hydrology in the Etosha-Cuvelai Basin (see section 4.3.1). Accordingly, the temporal dynamics of surface inundation observed from 2000 to 2022 provide a useful context to the shorter-term trends observed from 1996 to 2000 by Bryant (2003) and Mahowald *et al.* (2003) at Etosha Pan.

4.3.3. Sources of pan surface flooding

A spatial trend in ephemeral flooding dynamics may be inferred from both the annual and seasonal flooding frequency composites displayed in Figures 4.10 and 4.12. Generally, the most frequently flooded pixels are located in a small area in the north-western region of Etosha Pan, situated south of the Ekuma and Oshigambo rivers (Figures 4.10 and 4.12; see also Figure 4.1). In the instances where inundation of the pan surface extends beyond this region, floodwaters are channelled in an eastward direction along the northern fringe, accentuating the subtle natural slope of the pan surface (where the eastern portion is ~5 m lower in elevation than the west; Mendelsohn *et al.,* 2013), to cause extensive inundation of the eastern portion of Etosha

Pan. Where inundation of the pan surface is more extensive, floodwaters generally spread from the eastern portion in a westward direction, principally via a shallow channel running along the southern region of the pan (Figures 4.10 and 4.12; see also Figure 3.1, Chapter 3).

Such spatial trends are consistent with the north-east to south-west rainfall gradient that exists across the Cuvelai-Etosha Basin (Figure 4.4; Mendelsohn *et al.,* 2013; Hamunyela *et al.,* 2022). Floodwaters from the northern regions of the catchment are thus transported southwards via ephemeral river channels (iishana), which converge into the Ekuma and Oshigambo rivers that drain into the north-west of Etosha Pan (Figure 4.1; Bryant, 2003; Miller *et al.,* 2010; Hipondoka *et al.,* 2018).

Correspondingly, the detection of river channel sources from Landsat false-colour image scenes revealed that the Ekuma and Oshigambo rivers were the principal sources of lake surface inundation at Etosha Pan in 2000–2022. Shown in Figure 4.13, both individual and simultaneous fluvial inputs from the Ekuma and Oshigambo rivers were observed for 77% and 69% of flooding days, respectively.

Fluvial input from the Oshangulu river was observed for 12% of flooding days (Figure 13). However, this was not exclusive from flooding events where fluvial inputs were also observed from the Ekuma and Oshigambo rivers. Contrary to previous research which identified the Owambo river as a major source of floodwater input to Etosha Pan (Bryant, 2003; Mahowald *et al.,* 2003; Mendelsohn *et al.,* 2013), floodwaters

sourced from the Owambo river were identified for only 4% of flooding days in this research (Figure 4.13).

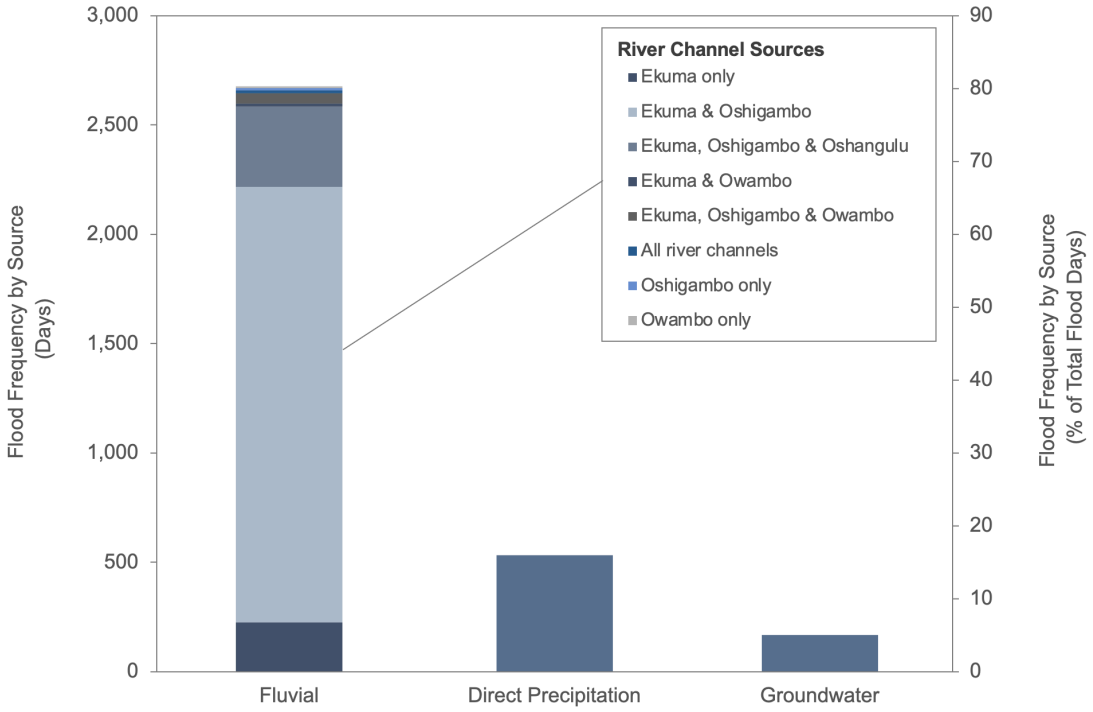


Figure 4.13. Frequency of flooding (count of days flooded and % of total days flooded) at Etosha Pan contributed from fluvial inputs, direct precipitation, and groundwater from 2000 to 2022. **Note:** For fluvial sources, flood frequencies refer to the number of days a given river channel contributed as both a single source and one of several river sources simultaneously flooding the pan surface.

Notably, for 21% of flooding days during the 2000–2022 period, no river channel surrounding the pan was detected as a source of fluvial input. Rather, surface flooding was attributed to direct precipitation for 16% of those flooding days, based upon satellite observations of rainfall directly over the pan surface for corresponding periods. Water table fluctuations were identified as the contributory source of surface inundation for the remaining 5% of flooding days where no fluvial inputs were observed (Figure 4.13). In these instances, surface water bodies were detected in the group of

springs situated in the south-west region of the pan (see Figure 3.1b, Chapter 3) and precipitation was not observed across the pan surface for corresponding periods.

It should be noted, however, the contributions of both direct precipitation and water table fluctuations to surface water presence on the pan may be considerably underestimated, given that the approach employed in this study could not differentiate the relative contributions of these non-fluvial sources from river channel inputs when surface flooding events occurred from several sources simultaneously.

4.3.4. The influence of regional catchment precipitation on pan surface flooding dynamics

It can be seen from the analyses conducted in this research that spatiotemporal connections exist between rainfall variability across the Cuvelai-Etosha Basin and the dynamics of surface flooding at Etosha Pan across both annual and seasonal scales. Shown in Table 4.2, Pearson correlation coefficients establish the quantitative associations between annual, monthly, and daily catchment-scale precipitation totals in the Cuvelai-Etosha Basin with ephemeral surface flooding extents and frequencies at Etosha Pan over the 2000–2022 period.

Table 4.2. Pearson correlation coefficients between satellite-derived catchment precipitation totals in the Cuvelai-Etosha Basin and lake surface inundation extents and frequency of flooding at Etosha Pan across annual, monthly (+1 and +2 month lags), and daily timescales from 2000 to 2022.

Time Period	Inundation Extent (km^2)	Flood Frequency (Days)
Annually	0.67**	0.64**
Monthly	0.21	0.094
+1 month lag	0.37*	0.31**
+2 month lag	0.42**	0.44**
Daily	0.047	0.00

* Significant at the 0.05 level, ** Significant at the 0.01 level

Annual trends in pan surface flooding were found to be significantly correlated with catchment-scale rainfall drivers (Table 4.2). Significant positive associations were found between annual catchment-scale precipitation totals and pan surface flooding extents ($r = 0.67$, $p < 0.01$) and frequencies ($r = 0.64$, $p < 0.01$) for the 2000–2022 time-series (Table 4.2). This corresponds with the close agreement observed between inter-annual trends in catchment-scale precipitation and pan surface flooding; where periods of above average precipitation in the Cuvelai-Etosha Basin generally coincided with periods of frequent and (or) extensive flooding of Etosha Pan (e.g., 2008–2012) and particularly dry years (e.g., 2015, 2016, and 2019) were characterised by both below average catchment-scale precipitation and a consistent decrease in pan surface flooding frequencies and extents (Figures 4.3, 4.9, and 4.10).

Statistically insignificant associations were found between monthly catchment precipitation totals and pan surface flooding extents ($r = 0.21$, $p = 0.26$) and frequencies ($r = 0.094$, $p = 0.20$) (Table 4.2) for corresponding months. However, seasonal trends in pan surface flooding variables were found to be significantly correlated with catchment-scale rainfall drivers when monthly lags were introduced. Significant moderate positive associations were found between monthly catchment-scale precipitation totals with one-month lagged pan surface flooding extents ($r = 0.37$, $p < 0.05$) and frequencies ($r = 0.31$, $p < 0.01$), which increased with a two-month lag in pan surface flooding extents ($r = 0.42$, $p < 0.01$) and frequencies ($r = 0.44$, $p < 0.01$) (Table 4.2).

These observations are consistent with the spatiotemporal trends in catchment-scale precipitation and pan surface flooding dynamics. Shown in Figure 4.14, pan surface inundation demonstrated a lagged response to seasonal catchment rainfall variability for the 2000–2022 period. Average monthly inundation extents generally increased one to two months following periods of extensive rainfall during the austral summer wet season (November – April), peaking in the months of March and April following periods of extensive rainfall in January and February (Figure 4.14). It is likely that this reflects the delay in which precipitation is drained from across the catchment, culminating at Etosha Pan via fluvial input from surrounding ephemeral river channels (namely the

Ekuma and Oshigambo rivers) (Figure 4.13; Bryant, 2003; Miller *et al.,* 2010; Hipondoka *et al.,* 2018).

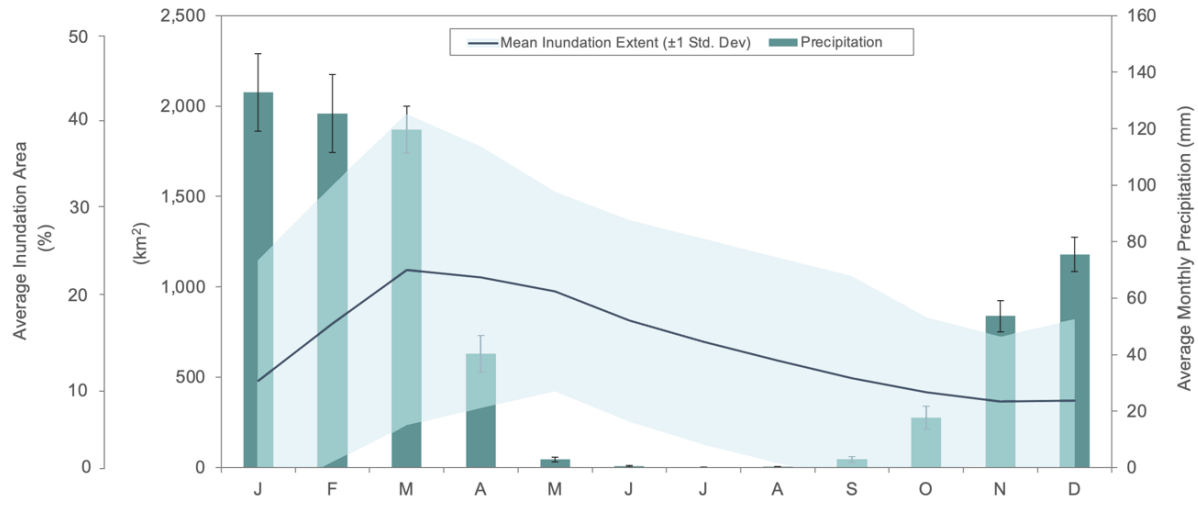


Figure 4.14. Mean monthly lake surface inundation extents (±1 standard deviation) at Etosha Pan and mean monthly precipitation totals in the Cuvelai-Etosha Basin (derived from satellite-retrieved [TRMM/GPM-IMERG] gridded precipitation data) from 2000 to 2022.

In contrast, no statistically significant correlations were found between catchment-scale precipitation and lake surface inundation extents and frequencies across daily timescales (Table 4.2), despite observations of precipitation falling directly onto Etosha Pan (Figures 4.7 and 4.8) that was found to contribute to pan surface inundation for 16% of flooding days in the 2000–2022 period (Figure 4.13).

4.3.5. The influence of global climate cycles on catchment precipitation and pan surface flooding dynamics

The statistically significant influence of catchment-scale precipitation on surface flooding at Etosha Pan across both seasonal and annual timescales highlights the

importance of exploring links between pan surface flooding and broader-scale hydrological drivers by examining potential relationships between catchment-scale rainfall variability and global climate cycles and sea surface temperature (SST) anomalies.

Shown in Table 4.3, significant correlations for the 2000–2022 time-series were observed between peak wet season (December – February [DJF]) rainfall anomalies in the Cuvelai-Etosha Basin and sea surface temperature anomalies for the Pacific (ENSO 3.4) regions ($r = –0.36$, $p < 0.05$) and the subtropical Indian Ocean Dipole (SIOD) ($r = 0.24$, $p < 0.01$) for the same period (Table 4.3). Significant weak correlations were also observed between wet season catchment rainfall anomalies and anomaly index values for the same three-month period of the previous year (DJF –1) for SIOD ($r = 0.16$, $p < 0.05$) and the East Indian Ocean (East IO) ($r = –0.12$, $p < 0.01$) (Table 4.3).

The significant negative correlation between wet season (DJF) rainfall and ENSO 3.4 SST anomalies corresponds to previous research observations of rainfall over southern Africa, suggesting that drier than normal conditions are related with positive SST anomalies during El Niño phases and wetter than normal conditions are associated with negative SST anomalies during La Niña events (Nicholson and Kim, 1997; Nicholson and Selato, 2000; Reason and Rouault, 2002; Bryant *et al.,* 2007; Lyon and Mason, 2007, 2009; Kane, 2009; Philippon *et al.,* 2012; Meque and Abiodun, 2015).

Table 4.3. Quarterly Pearson correlation coefficients between wet season (DJF) rainfall anomalies in the Cuvelai-Etosha Basin and tropical Pacific El Niño-Southern Oscillation SST (ENSO 3.4), subtropical Indian Ocean Dipole Index (SIOD), Indian Ocean (West IO and East IO), Tropical Southern Atlantic Index (TSA), Multivariate ENSO Index (MEI V2) and Dipole Mode Index (DMI) anomalies covering yearly positive leads (+1) and negative lags (-1) from 2000 to 2022.

Quarter		ENSO 3.4	SIOD	West IO	East IO	TSA	MEI V2	DMI
DJF	-1	-0.23	0.16*	0.22	-0.12**	-0.08	-0.27	0.11
MAM		-0.19	0.20	0.05	-0.25	0.33	-0.33	0.27
JJA		-0.15	0.37	0.02	-0.45	-0.02	-0.26	0.24
SON		-0.12	0.20	-0.15	-0.34	0.14	-0.25	-0.14
DJF	0	-0.36*	0.24**	-0.02	-0.38	-0.04	-0.40	-0.25
MAM		-0.34	-0.01	-0.16	-0.13	0.01	-0.36	-0.18
JJA		-0.08	0.15	0.18	0.00	-0.08	-0.12	0.02
SON		0.12	0.05	0.12	0.04	0.07	0.05	-0.07
DJF	+1	-0.34	0.45	0.13	-0.56	0.18	-0.41	-0.21

* Significant at the 0.05 level, ** Significant at the 0.01 level

Analyses of observational and reanalysis data have attributed such patterns to ENSO forcing an equivalent barotropic Rossby wave over southern Africa, which modifies regional mid-tropospheric vertical motions and precipitation anomalies (Ratnam *et al.,* 2014; Hoell *et al.,* 2015). El Niño (La Niña) is thus associated with high (low) pressure over southern Africa that produces anomalous decreases (increases) in precipitation relative to the average (Hoell *et al.,* 2017).

This is illustrated by comparisons of ENSO and SIOD cycles against observed (meteorological station) and satellite-retrieved monthly precipitation and pan surface inundation time-series for 2000–2022 displayed in Figure 4.15, which suggest that peaks

in monthly rainfall across the Cuvelai-Etosha Basin and subsequent flooding of Etosha Pan for the years 2006, 2008, 2009 and 2011 may be associated with the respective weak, moderate and moderate-strong La Niña events in the tropical Pacific. While relatively dry conditions recorded in 2003, 2010, 2013, 2016, 2019 and 2020 are shown to correspond with positive ENSO phases (Figure 4.15). For example, during a very strong El Niño event in 2015–2016 (Figure 4.15), average quarterly rainfall during the wet season (DJF) months of 2016 was the lowest recorded in the Cuvelai-Etosha Basin at 72 mm, compared to the mean DJF rainfall of 104 mm for the 2000–2022 time-series and subsequent pan surface inundation was almost negligible.

The significant positive correlations observed between wet season (DJF) rainfall anomalies and the SIOD index values for the DJF period of the corresponding and previous year (Table 4.3) also support a number of climate observation and modeling studies, which have shown that positive (negative) SIOD events tend to result in above (below) average rainfall over southern Africa during the austral summer wet season (Behera and Yagamata, 2001; Reason, 2001, 2002; Bryant *et al.,* 2007; Gaughan *et al.,* 2016; Hoell and Cheng, 2018). Correspondingly, monthly catchment precipitation values shown in Figure 4.15 are generally increased during positive SIOD phases and decline during negative phases.

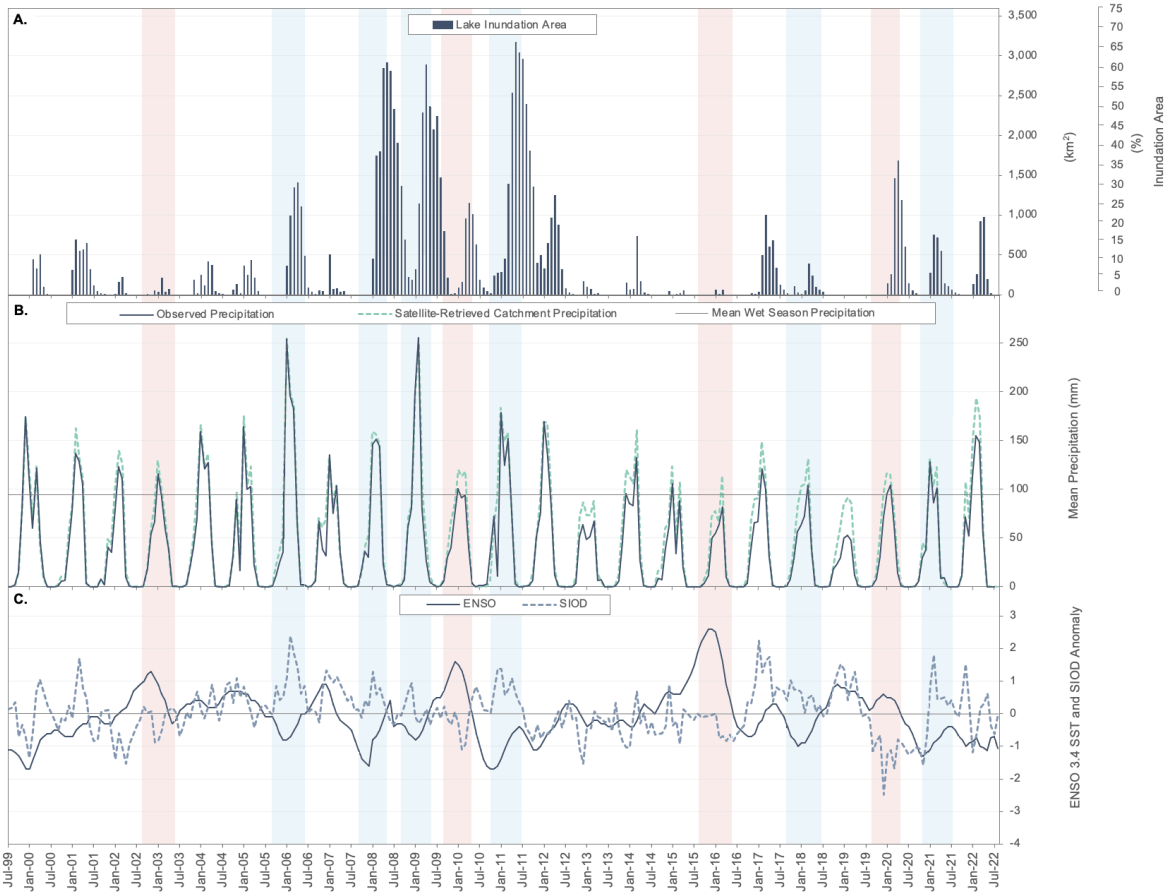


Figure 4.15. Monthly time-series of (a) lake surface inundation extents at Etosha Pan, (b) precipitation totals for the Cuvelai-Etosha Basin derived from ground-based observations and satellite-retrieved estimates (TRMM/GPM-IMERG), in addition to (c) El Niño-Southern Oscillation Sea Surface Temperature (ENSO 3.4 SST) and subtropical Indian Ocean Dipole Index (SIOD) anomalies for the period July 1999 – July 2022. Blue (red) shaded areas indicate where negative (positive) ENSO phases are aligned with positive (negative) phases of the SIOD and correspond to periods of increased (decreased) rainfall in the Cuvelai-Etosha Basin.

During the years of 2006, 2008, 2009, and 2011, where the highest DJF rainfall anomalies were recorded in the catchment and some of the highest monthly inundation extents were observed at Etosha Pan, the SIOD is in the opposite phase to ENSO (Figure 4.15). The climate indices are similarly opposed in 2003, 2010, 2016, and 2020 but their phases are reversed, corresponding to some of the lowest DJF rainfall

anomalies recorded in the catchment and relatively dry conditions at Etosha Pan (Figure 4.15).

Previous research has shown that when the SIOD and ENSO are in opposite phases, the SIOD enhances the ENSO-related atmospheric responses over southern Africa by strengthening the regional equivalent barotropic Rossby wave anomalous mid-tropospheric vertical motions and anomalous precipitation (Reason and Smart, 2015; Hoell *et al.,* 2017). It is, therefore, possible that the alignment of negative phases of ENSO and positive phases of SIOD might have contributed towards the increased DJF rainfall observed in 2006, 2009 and 2011, and the reduced DJF rainfall observed in 2003, 2010, 2016 and 2020 across the Cuvelai-Etosha Basin, posing significant implications for moisture conditions at Etosha Pan.

However, it can be seen in Figure 4.15 that in the years 2013 and 2019 some of the lowest DJF rainfall anomalies and negligible pan surface flooding extents were observed when the ENSO and SIOD were in the same phase and each in contradiction to their theoretical positive ENSO (El Niño) and negative SIOD configuration. Furthermore, the alignment of negative ENSO and positive SIOD phases did not result in above average catchment precipitation or extensive flooding of the pan surface in years 2018 and 2021 (Figure 4.15).

It is, therefore, noted that while significant correlations were observed, the influence of ENSO and SIOD cycles on rainfall variability in the Cuvelai-Etosha Basin and

subsequent inundation of Etosha Pan may also be modulated by the inherent variability in the strength and position of regional atmospheric features (e.g., the Angola Low) observed in previous investigations of precipitation dynamics in southern Africa (Reason, 2017; Munday and Washington, 2017; Howard and Washington, 2018; Crétat *et al.,* 2019; Howard *et al.,* 2019), which were not examined in this study.

4.4. Conclusion

This research has investigated the temporal and spatial dynamics of precipitation across the Cuvelai-Etosha Basin and subsequent surface flooding of Etosha Pan for the period from 2000 to 2022. Notably, it has established that a statistically significant relationship exists between these variables and with global scale climate cycles and sea surface temperature (SST) anomalies, thus providing a comprehensive regional hydrological context necessary for further research into the drivers of dust emissions from Etosha Pan. The key findings with respect to the objectives of research are as follows:

1) Both ground-based observations and satellite-retrieved data have shown consistent fluctuations in mean annual precipitation (572 mm $year^{-1}$) across the 2000–2022 time-series. Systematic differences in mean annual precipitation between ground-based and satellite-retrieved observations confirmed a spatial gradient of declining rainfall totals from northern regions to southern regions of the catchment. The seasonal cycle was characterised by an austral summer wet season that typically

lasts six months, from November to April, with the highest precipitation totals recorded in the months of January to March. Negligible precipitation occurred on average in June to August during the austral winter dry season.

2) Satellite-retrieved (MODIS and Landsat) surface water extents showed that ephemeral flooding of Etosha Pan occurred to some degree every year in the 2000–2022 time-series. However, mean surface inundation extents and frequency of flooding fluctuated considerably across the research period. Seasonal trends were characterised by widespread and frequent inundation of the pan surface during the latter end of the austral summer wet season, with the highest average inundation extents and frequencies recorded in the months of March to May, which gradually declined throughout the austral winter dry season. This timing of flooding events was consistent with previous research conducted at Etosha Pan in 1996–2000. However, measurements of ephemeral flooding in this research were considerably greater in magnitude and frequency than shorter-term trends observed in previous studies.

3) Analysis of lake surface inundation dynamics confirmed that floodwaters entering Etosha Pan were principally sourced from fluvial inputs by ephemeral river channels – namely the Ekuma and Oshigambo – draining the Cuvelai-Etosha Basin. However, for 21% of observed flood days, surface inundation was attributed exclusively to direct precipitation inputs and groundwater table fluctuations.

4) The timing, magnitude and spatial distribution of surface inundation at Etosha Pan were shown to be significantly influenced by annual and seasonal precipitation in the Cuvelai-Etosha Basin. Pan surface inundation demonstrated a lagged response to seasonal catchment rainfall, where average monthly inundation extents generally increased one to two months following periods of extensive rainfall during the austral summer wet season. It is likely that this reflects the delay in which precipitation is drained from across the catchment, culminating at Etosha Pan via fluvial input from surrounding ephemeral river channels.

5) It was found that inter-annual variabilities in catchment-scale precipitation were significantly associated with El Niño-Southern Oscillation (ENSO) cycles and changes in the subtropical Indian Ocean Dipole (SIOD). Data here concur with current understanding of the known drivers of regional rainfall variations in southern Africa, which suggest that generally wetter (dryer) than normal conditions are associated with negative (positive) ENSO and positive (negative) SIOD events. Findings therefore suggest that the spatiotemporal trends in surface flooding of Etosha Pan are indirectly determined by regional climatological drivers.

Fundamental dust emission studies within Etosha Pan and similar large regional sources have demonstrated that gross changes in the surface hydrology of an ephemeral lake can lead to significant changes in regional dust emissions (Reynolds *et al.,* 2007; Bryant *et al.,* 2007; Rashki *et al.,* 2012; Vickery *et al.,* 2013; Chappell *et al.,* 2023a).

Research investigations by Bryant (2003) and Mahowald *et al.* (2003) demonstrated that changes in the frequency and extent of natural inundation within the large ephemeral lake system lead to significant fluctuations in dust loadings on a seasonal and inter-annual basis. Yet, the limited observation period (< 10 years) precluded sufficient understanding of whether such patterns were solely a function of changes to sediment supply (via sediment delivery from surrounding river channels) or rather changes in sediment availability associated with fluctuations in surface moisture and erodibility conditions (both as a function of ephemeral inundation and/or direct precipitation on the pan surface). By extending the time-series of remote sensing data and analysis to the most recent twenty-year period, the first part of this thesis has presented a comprehensive hydrological context for Etosha Pan and the Cuvelai-Etosha Basin. Thus, facilitating further detailed analysis of the interactions between catchment precipitation, lake inundation events and sediment supply and availability dynamics to improve our understanding of the potential hydrological controls on aeolian dust emissions from Etosha Pan.

CHAPTER FIVE

Part 2

Determining the hydrological controls on dust emissions

Determining the hydrological controls on dust emissions

5.1. Introduction

The research presented in Part 1 of the thesis (see Chapter 4) offered insights into rainfall variability across the Cuvelai-Etosha Basin and the complex interactions between catchment-scale precipitation and runoff that lead to spatiotemporal variations in subsequent flooding of Etosha Pan, which must be considered when trying to understand the dust cycle from this source region (Bryant, 2003).

While remote sensing and field-based studies have explored the spatiotemporal dynamics of dust emissions from Etosha Pan (Vickery *et al.,* 2013), in relation to hydrological factors controlling sediment supply (Bryant, 2003; Mahowald *et al.,* 2003), and aeolian transport capacity (Clements and Washington, 2021, 2023; Wiggs *et al.*, 2022), the influence of hydrological controls on surface erodibility has yet to be examined. Research is needed to understand the implications of surface flooding events on sediment supply delivered from surrounding river channels and, perhaps more importantly, to understand the implications of surface inundation events and direct precipitation on to Etosha Pan on sediment availability dynamics (soil erodibility) that can determine the susceptibility of the surface to aeolian erosion. A comprehensive analysis of the interactions between catchment precipitation, lake inundation events and sediment supply and availability dynamics must therefore be conducted for a full

picture of the potential hydrological controls on aeolian dust emissions from Etosha Pan to be understood.

This chapter details the second part of the remote sensing-based research, which aims to identify the temporal and spatial dynamics of dust emissions from the pan surface and quantify the extent to which dust entrainment is associated with regional hydrology and ephemeral surface inundation dynamics for the period from 2000 to 2022.

The specific research objectives examined are to:

1) Determine the annual and seasonal trends in dust emission events detected using multi-sensor satellite platforms;

2) Identify the erosivity conditions associated with dust emission events from the pan;

3) Establish whether the frequency, timing and magnitude of dust emissions are associated with catchment-scale precipitation and ephemeral pan surface flooding.

5.2. Data Sources and Methods

5.2.1. Dust emission event detection

A multi-sensor satellite remote sensing approach was employed to examine the spatiotemporal dynamics of dust emissions at Etosha Pan and determine the potential relationships with regional hydrology, ephemeral surface inundation, and wind erosivity conditions for the period 2000–2022.

Satellite remote sensing is one of the most commonly used approaches to examine dust emissions owing to the unparalleled spatial and temporal coverage of satellite sensors (Akhlaq *et al.,* 2012; Ashpole and Washington, 2012; Shi *et al.,* 2020). Numerous techniques have been developed to detect and characterise dust source activity using satellite data. Examples include the use of polar orbiting satellite sensors, such as the Total Ozone Mapping Spectrometer (TOMS) (e.g., Prospero *et al.,* 2002; Washington *et al.,* 2003; Bryant *et al.,* 2007), the Ozone Mapping Instrument (OMI) (e.g., Ahn *et al.,* 2008, 2014), and the Moderate Resolution Imaging Spectroradiometer (MODIS) (e.g., Roskovensky and Liou, 2005; Qu *et al.,* 2006; Hao and Qu, 2007; Baddock *et al.,* 2009; Karimi *et al.,* 2012; Kandakji *et al.,* 2020). While others have utilised geostationary sensors, such as the Advanced Baseline Imager (ABI) onboard the Geostationary Operational Environmental Satellites (GOES) (e.g., Schmit *et al.,* 2008; Rivera Rivera *et al.,* 2010; Grasso *et al.,* 2021) and the Meteosat Second Generation Spinning Enhanced Visible and InfraRed Imager (MSG-SEVIRI) (e.g., Lensky and

Rosenfeld, 2008; Klüser and Schepanski, 2009; Ashpole and Washington, 2012; Romano *et al.,* 2013). A critical evaluation of the different capabilities of these satellite devices and associated data analysis techniques used to detect and characterise dust source activity in desert regions is given in Li, J. *et al.* (2021).

For the present research, the Spinning Enhanced Visible and InfraRed Imager aboard Meteosat's Second Generation satellites (MSG-SEVIRI; available from 2005 – present day) was used as the primary data source to detect dust emission events from Etosha Pan, owing to its high frequency of observations (available every 15 min) associated with a moderate but acceptable spatial resolution (3 km) for emission source identification (Schepanski *et al.,* 2007, 2009, 2012; Banks *et al.,* 2014).

A variety of approaches have been developed to identify and monitor desert dust emissions based on MSG-SEVIRI data. Many of these have exploited the unique spectral variability of absorption and reflection exhibited by mineral dust aerosols between 8 – 12 μm (Ackerman, 1997; Sokolik, 2002) through the use of Brightness Temperature Differences (BTDs) in the visible and infrared (VIR) and thermal infrared (TIR) channels to isolate the signature of airborne dust from cloud and surface features (Merchant *et al.,* 2006; Ashpole and Washington, 2012; Good *et al.,* 2012; Caton Harrison *et al.,* 2019).

The widely-used red-green-blue dust rendering scheme (Dust RGB) developed by Lensky and Rosenfeld (2008) utilises brightness temperature differences from selected

MSG-SEVIRI channels at 8.7, 10.8 and 12.0 μm in a false colour rendering scheme, in which dust appears a vivid magenta colour (Figure 5.1). The Dust RGB rendering scheme has provided the basis for numerous studies of Saharan dust sources (Schepanski *et al.,* 2007, 2009, 2012; Ashpole and Washington, 2013) and more recently in the identification of southern African dust sources (Vickery *et al.,* 2013; Eckardt *et al.,* 2020).

Nevertheless, the Dust RGB scheme is subject to several limitations (Brindley *et al.,* 2012; Banks and Brindley, 2013). For example, it can be difficult to detect thinner dust plumes or those in the early stages of activation near-source, as the thermal contrast between dust and land surface radiation is very small (Murray *et al.,* 2016; Miller *et al.,* 2017). In addition, the precise colouring of dust produced by the scheme can vary depending on the chemical composition and size of the dust particles, the height and thickness of the dust plume, atmospheric temperature and moisture content, and the underlying surface emissivity (Banks *et al.,* 2019; Grasso *et al.,* 2021). Consequently, the Dust RGB scheme is constrained by subjective interpretation and airborne dust detection can be challenging even for experts familiar with the Dust RGB product nuances (Berndt *et al.,* 2021).

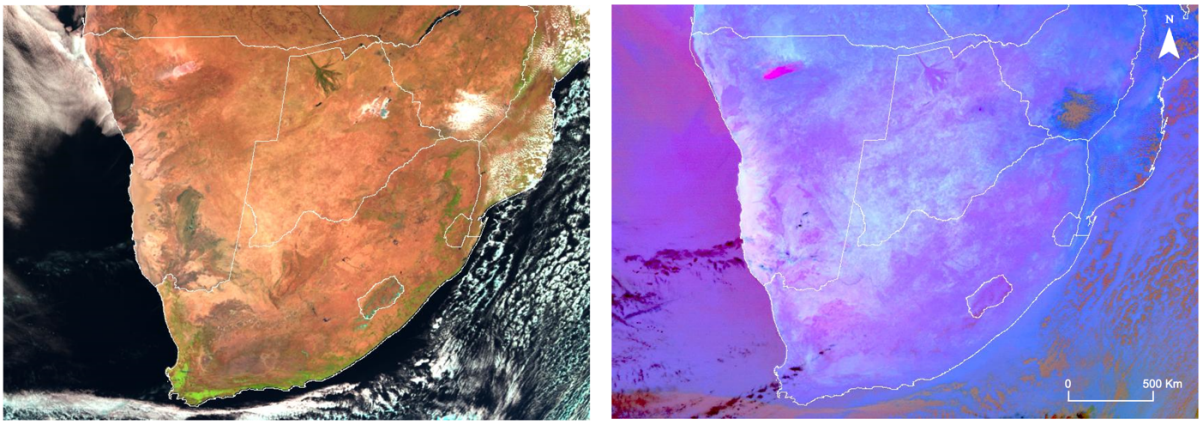


Figure 5.1. Rendered images highlighting a dust plume over Etosha Pan captured at 0800 UTC by MSG-SEVIRI on 7 September 2019. **Note:** the dust plume heading SW from Etosha Pan that is just visible in the true-colour composite in the left image is highlighted by a vivid magenta colour that contrasts with the pale blue land surface in the Dust RGB scheme (see Lensky and Rosenfeld, 2008) in the right image.

The current development of 'clear sky' background reduction algorithms (e.g., clear sky differencing, CSD) to enhance dust signals in MSG-SEVIRI false colour imagery forms the basis of ongoing research in this field (Li, J. *et al.,* 2021). These systems have overcome many of the limitations of the Dust RGB scheme through the subtraction of surface reflectance and thermal emission features associated with the underlying surface and atmospheric features to considerably improve dust event retrievals (Tramutoli *et al.,* 2010, 2019; Miller, 2014; Pavolonis *et al.,* 2015; Murray *et al.,* 2016; Marchese *et al.,* 2017; Miller *et al.,* 2017; Falcioneri *et al.,* 2020).

The clear sky differencing (CSD) multi-temporal analysis technique was employed in this study to detect and characterise desert dust plumes from MSG-SEVIRI data over Etosha Pan. A detailed description of the CSD technique is given in Murray *et al.* (2016). Developed to add considerable enhancement to the Dust RGB scheme by

Lensky and Rosenfeld (2008) for dust source detection from MSG-SEVIRI imagery, the CSD approach involves the derivation of a composite clear sky baseline signal for selected visible and infrared channels from MSG-SEVIRI scenes on an individual time-step and pixel basis. These are subtracted from each scene in the relevant channels and rendered in false-colour imagery to significantly enhance the signature of dust events for improved identification of dust source locations and dynamics (Murray *et al.,* 2016).

The CSD algorithm was selected over other desert dust detection algorithms and image rendering techniques owing to: its effective identification of airborne dust from Etosha Pan and other playa source regions in southern Africa (Murray *et al.,* 2016; Eckardt *et al.,* 2020); enhanced performance at discriminating desert dust from meteorological clouds and bright surfaces characteristic of arid and semi-arid environments (Shi *et al.,* 2020); improved ability to detect plume sources at the point of activation earlier in the diurnal cycle (Murray *et al.,* 2016; Miller *et al.,* 2017); and reduced sensitivity to observational conditions and dust plume properties (i.e., low levels of dust emission or dust emissions with high salt or low quartz content) (Banks *et al.,* 2019; Grasso *et al.,* 2021; Berndt *et al.,* 2021).

MSG-SEVIRI Data Pre-Processing

A time-series of MSG-SEVIRI Level 1.5 image data covering Etosha Pan for the period 2005–2022 was procured from the EUMETSAT Data Store (eumetsat.int/product/). The MSG-SEVIRI instrument is composed of 12 narrowband channels within the visible spectral and thermal infrared regions (Aminou, 2002). In order to estimate the clear sky background and render the false-colour difference imagery for dust source detection, the CSD scheme relies upon the derivation of solar reflectance values from the visible spectral and near-infrared channels (0.6, 0.8, and 1.6 μm) and brightness temperature from selected thermal channels (3.9, 8.7, 10.8, and 12.0 μm) of MSG-SEVIRI.

The process for converting raw data counts to solar reflectance for the visible channels and to brightness temperature for the thermal channels utilised in the CSD scheme is outlined by Murray *et al.* (2016). For clarity, the process that was applied to the MSG-SEVIRI image scenes in the 2005–2022 time-series for this research is summarised as follows.

The relationship between raw channel count and spectral radiance, B_λ (mW m^{-2} sr^{-1} $(cm^{-1})^{-1}$), is given by:

$$B_\lambda = \text{offset}_\lambda + \text{gain}_\lambda \cdot \text{count}_\lambda \tag{5.1}$$

where the offsets and gains are channel dependent and given in the raw data header.

The solar reflectance, R_λ, is given by:

$$R_\lambda = \frac{B_\lambda}{\mu_0 F_0(\lambda)} \tag{5.2}$$

where μ_0 is the cosine of the solar zenith angle and $F_0(\lambda)$ (mW m^{-2} sr^{-1} $(cm^{-1})^{-1}$) is the extra-terrestrial solar flux; expressed as a function of the extra-terrestrial solar flux at equinox, $\overline{F_0(\lambda)}$, and the Earth-Sun distance *ESD* (au):

$$F_0(\lambda) = \frac{\overline{F_0(\lambda)}}{ESD^2} \tag{5.3}$$

where $\overline{F_0(\lambda)} = 20.76$, 23.30 and 19.73 for the 0.6, 0.8, and 1.6 μm channels, respectively. *ESD* is a function of the Julian day:

$$\text{ESD(JD)} = 1 - 0.0167\ \cos\left(\frac{2\pi(\text{JD} - 3)}{365}\right) \tag{5.4}$$

For the thermal channels the variable used in the rendering scheme is brightness temperature, T_B, which is retrieved from radiance using the inverted Planck function (Tjemkes, 2005):

$$T_B = \left(\frac{c_2 v}{In\left\{\frac{c_1 v^3}{B_v} + 1\right\}} - b\right)/a \tag{5.5}$$

where v is the channel central wave number (cm^{-1}), $c_1 = 1.19104 \times 10^{-8}$ W m^{-2} $sr^{-1}$$(cm^{-1})^{-1}$ and $c_2 = 1.43877$ K$(cm^{-1})^{-1}$, and a and b are channel dependent constants (Murray *et al.,* 2016).

Clear Sky Estimation

A clear sky baseline was first determined for each individual image pixel from the MSG-SEVIRI time-series at an hourly resolution. The clear sky reflectance estimates are calculated for all seasons, hence several transient signals associated with cloud, changes in vegetation cover and surface moisture, and biomass smoke haze had to be accounted for (Murray *et al.,* 2016).

Climatic conditions in the Etosha region are predominantly influenced by two high pressure systems, the South Atlantic Anticyclone and the Botswana Anticyclone (Mendelsohn *et al.,* 2013). These high-pressure systems dominate over the austral winter dry season (May – September) causing predominantly clear sky conditions over the region (Williams, 2010) and move southward during the austral summer (October – April) allowing the inter-tropical convergence zone (ITCZ) with warm moist air to also move southwards, triggering cloud formation and subsequent precipitation (see section 4.3.1; Piketh *et al.,* 2000, 2002; Hamunyela *et al.,* 2022). In addition to the well-documented non-negligible effects of cloudiness conditions on spectral reflectance (Rossow and Garder, 1993; Ackerman *et al.,* 1998; Ipe *et al.,* 2003), precipitation in turn causes further spatiotemporal variations in surface reflectance associated with seasonal fluctuations in vegetation cover in the catchment (Mendelsohn *et al.,* 2013) and surface moisture on Etosha Pan itself (see sections 4.3.1 and 4.3.2; Bryant, 2003; Mahowald *et al.,* 2003; Bryant *et al.,* 2007).

There may also be day-to-day fluctuations in the baseline reflectance due to biomass-induced smoke haze. Biomass burning is a common pursuit associated with agricultural practices and land management in southern Africa (Alleaume *et al.,* 2005; Eck *et al.,* 2013; Vakkari *et al.,* 2018), and can result in the presence of smoke plumes and (or) a general haze that may lower reflectance values in the visible range depending on the amount of burning, wind direction, and distance from source (Myhre *et al.,* 2003; Vickery *et al.,* 2013; Chauvigné *et al.,* 2021).

The clear sky reflectance estimate for the MSG-SEVIRI channel centred on 0.6 μm was derived from a 21-day rolling mean for a given day and time in order to account for potential modulations in clear sky reflectance by cloud, biomass smoke haze, changes in surface moisture and vegetation cover. To mitigate for cloud-shadowing and smoke effects, the third lowest reflectance value was applied as a lower baseline (Murray *et al.,* 2016). Reflectance values within +12% of this value in the 21-day window were retained to remove major cloud effects but allowed for day-to-day variations in nominally clear sky conditions that may be a result of small changes in atmospheric and surface conditions (Murray *et al.,* 2016).

Equation 5.6 illustrates the procedure mathematically:

$$\text{For days where } \left(\rho_{0.6}^{d} < \rho_{0.6}^{k} < 1.12 \times \rho_{0.6}^{d}\right)$$

$$\left\{\rho_{0.6}^{csn} = \left(\sum_{k=n-10}^{k=n+10} \rho_{0.6}^{k}\right)/m\right\} \tag{5.6}$$

where, for each pixel at each time step, $\rho_{0.6}^{d}$ is the 0.6 μm lower baseline reflectance (i.e., the third lowest reflectance) over the 21-day rolling window, $\rho_{0.6}^{k}$ is the 0.6 μm reflectance on day k, m is the number of days used in the clear sky average, and $\rho_{0.6}^{csn}$ is the derived clear sky 0.6 μm reflectance on day n (Murray *et al.,* 2016).

The 0.6 μm clear sky composites generated by this process for each pixel and each time-step of the MSG-SEVIRI image series were subsequently used to subsample reflectance and brightness temperatures in the other channels of interest in order to derive a consistent set of clear sky composite images.

Image Enhancement

The clear sky composites were used to enhance the signal emanating from dust events from the MSG-SEVIRI image time-series. An RGB image rendering approach was applied using two different schemes: one which utilised MSG-SEVIRI shortwave (solar reflectance and near-infrared) bands and one which used thermal infrared bands. In the shortwave channels, the RGB bands were assigned values given by the scaled difference between the channels of interest on the given day and time, and the corresponding clear sky composite value (Equation 5.7) yielding clear sky difference (CSD) images. Corresponding thermal images were rendered from brightness temperature information using a double difference approach, subtracting the clear sky composite difference between selected channels from the corresponding instantaneous difference (Equation 5.8) (Murray *et al.,* 2016).

$$\left\{\begin{array}{l} \mathrm{Red}_{8\mathrm{bit}} = 15^{*}255^{*}\left(\rho_{1.6\mu m} - \rho_{1.6\mu m}^{csn}\right) \\ \mathrm{Green}_{8\mathrm{bit}} = 15^{*}255^{*}\left(\rho_{0.8\mu m} - \rho_{0.8\mu m}^{csn}\right) \\ \mathrm{Blue}_{8\mathrm{bit}} = 15^{*}255^{*}\left(\rho_{0.6\mu m} - \rho_{0.6\mu m}^{csn}\right) \end{array}\right\} \quad (5.7)$$

$$\left\{\begin{array}{l} \mathrm{Red}_{8\mathrm{bit}} = 0.5^{*}255^{*}\left\{\left(\mathrm{BT}_{12.0\mu m} - \mathrm{BT}_{10.8\mu m}\right) - \left(\mathrm{BT}_{12.0\mu m}^{csn} - \mathrm{BT}_{10.8\mu m}^{csn}\right)\right\} \\ \mathrm{Green}_{8\mathrm{bit}} = 0.25^{*}255^{*}\left\{\left(\mathrm{BT}_{3.9\mu m} - \mathrm{BT}_{10.8\mu m}\right) - \left(\mathrm{BT}_{3.9\mu m}^{csn} - \mathrm{BT}_{10.8\mu m}^{csn}\right)\right\} \\ \mathrm{Blue}_{8\mathrm{bit}} = 0.5^{*}255^{*}\left\{\left(\mathrm{BT}_{8.7\mu m} - \mathrm{BT}_{10.8\mu m}\right) - \left(\mathrm{BT}_{8.7\mu m}^{csn} - \mathrm{BT}_{10.8\mu m}^{csn}\right)\right\} \end{array}\right\} \quad (5.8)$$

Given that no single scheme is optimal for all events and all times (Murray *et al.,* 2016; Bin Abdulwahed *et al.,* 2019; Li J. *et al.,* 2021), both schemes were rendered simultaneously to aid interpretation of the resultant imagery and thus give greater confidence in the discrimination of source activity.

Figure 5.2 shows an example of the CSD outputs rendered alongside standard (non-CSD) true-colour composites generated using three MSG-SEVIRI visible spectral and near-infrared channels (0.6, 0.8, and 1.6 μm) and the Dust RGB scheme developed by Lensky and Rosenfeld (2008) from a combination of MSG-SEVIRI thermal channels (8.7, 10.8, and 12.0 μm) at two-hourly time-steps during a dust plume event on 2 August 2015. It can be seen that both the reflectance and thermal CSD composites offer considerable improvements in the delineation of the dust plume event from the background features within the MSG-SEVIRI imagery.

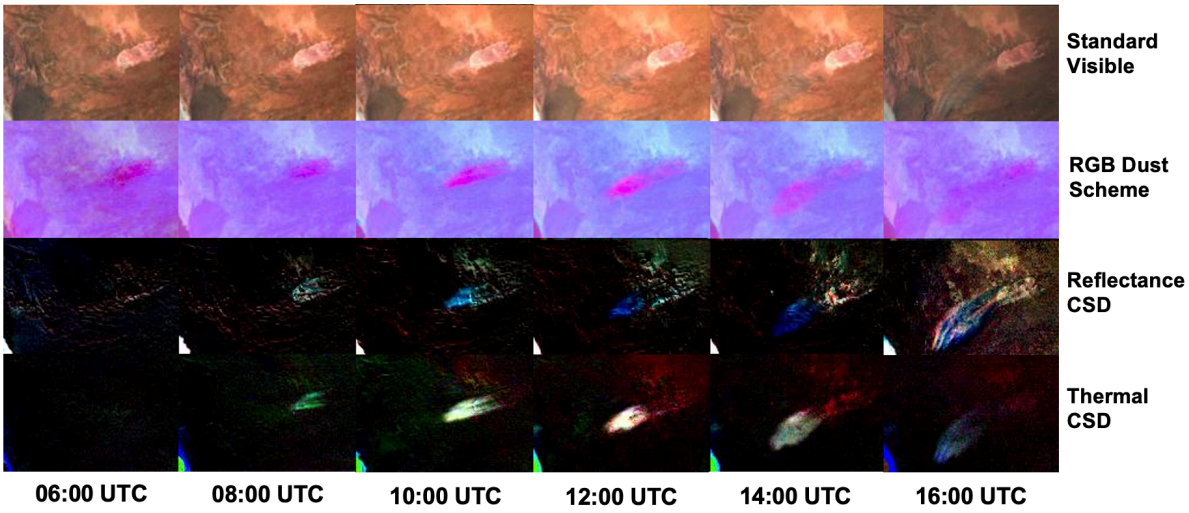


Figure 5.2. Rendered images highlighting a dust plume over Etosha Pan at two-hourly time-steps captured by MSG-SEVIRI on 2 August 2015. Top row: MSG-SEVIRI standard visible RGB; Second row: standard RGB dust scheme; Third row: reflectance CSD RGB; and bottom row: thermal CSD RGB.

Additional Data Sources for Dust Event Detection

The CSD algorithm was applied for MSG-SEVIRI time-series data available from 2005 to 2022. However, this approach leaves a gap of approximately 5 years (2000–2005) in data coverage for dust emission detection within the 2000–2022 research period. Indeed, it has been recognised that no single remote sensing product exists to provide a long-term record for the systematic detection and characterisation of dust plume sources at a continental or regional scale and that a synergistic approach to remote sensing data and algorithm use is often appropriate (Baddock *et al.,* 2009, 2021; Bryant, 2013; Pavolonis *et al.,* 2015).

With a moderately high revisit frequency (up to two views per day), the Moderate Resolution Imaging Spectroradiometer (MODIS) aboard NASA's Terra and Aqua

satellites provides a consistent long-term (2000 – present day) image time-series at moderate spatial resolutions of 500 m up to 1 km, which have been widely employed for detecting desert plumes in different geographic regions (e.g., Zhang *et al.,* 2008; Karimi *et al.,* 2012; Park *et al.,* 2014; Singh *et al.,* 2019; Nobakht *et al.,* 2021). Vickery *et al.* (2013) demonstrated the combined use of visually-interpreted MODIS and MSG-SEVIRI Dust RGB composite data from 2005 to 2008 to develop the most comprehensive inventory of dust plumes and sources for southern Africa to date. The authors highlight the relative advantages to be gained from the multisensor approach; where the 500 m spatial resolution of MODIS observations enabled fine-scale identification of plume source locations (Vickery *et al.,* 2013), which complement the high temporal resolution of MSG-SEVIRI observations that provide information on the evolution of dust events necessary to link dust entrainment processes to the prevailing atmospheric and surface conditions (Mishra *et al.,* 2015; She *et al.,* 2018; Hennen *et al.,* 2019).

Accordingly, MODIS Surface Reflectance (MOD02QKM/MYD02QKM) data available at 500 m spatial resolution for satellite overpass times ~1030 UTC (Terra) and ~1330 UTC (Aqua) were acquired from NASA's LAADS DAAC data portal (https://ladsweb.modaps.eosdis.nasa.gov/). Twice-daily MODIS true-colour (bands 1, 4 and 3) image time-series were used as a supplementary data source for the manual detection and characterisation of dust emission events from Etosha Pan for the period 2000–2005 and to further enhance the identification of dust plume sources and activity

for the period 2005–2022 from MSG-SEVIRI imagery, thus ensuring complete data coverage for the research period.

The manual interpretation of MSG-SEVIRI and MODIS composite data is effective, but it is also very time-intensive and subject to user and subjectivity constraints (Schepanski *et al.,* 2009; Ashpole and Washington, 2012; Bryant, 2013). Ongoing research efforts continue to improve methods and automate retrieval approaches to aid dust source detection and characterization using both MSG-SEVIRI and MODIS data (Shi *et al.,* 2020; Li, J. *et al.,* 2021). The Robust Satellite Technique (RST) and subsequent refinements for desert dust detection (RST_{DUST} and $eRST_{DUST}$) are examples of an automated multi-temporal analysis technique based upon a background subtraction approach similar to the Murray *et al.* (2016) CSD scheme, which offer an efficient, objective and reproducible means of detecting, tracking and characterising dust plumes from large satellite time-series data (Tramutoli, 2007, Tramutoli *et al.,* 2010; Marchese *et al.,* 2017).

Several research applications have demonstrated the adaptability of the RST technique to different remote sensing data sources, enabling analysis across extended study periods where data gaps may exist from individual satellite sensors (Sannazzaro *et al.,* 2014; Tramutoli *et al.,* 2019; Falconieri *et al.,* 2020). However, the approach remains limited to the detection of large, optically-thick plumes characteristic of established dust events some days after the initial uplift (Li, J. *et al.,* 2021) and further refinements

are needed to improve detection of dust signals that are weak and transient in nature, which are characteristic of dust events in southern Africa (Washington *et al.,* 2003; Ginoux *et al.,* 2012; Vickery *et al.,* 2013).

Quantifying Dust Emission Magnitude

Analyses of MSG-SEVIRI CSD and MODIS true-colour image time-series facilitated the detection, tracking and derivation of metadata (i.e., source, uplift timing, direction and duration) of dust plume events for the period 2000–2022. Such analyses provide a semi-quantitative description of dust plume events but do not provide a means of measuring their magnitude, which is necessary to understand the relative emissivity of sources in response to environmental drivers over space and time (Bryant, 2003).

The MODIS Level 2 operational aerosol products developed using the enhanced Deep Blue retrieval algorithm provide quantitative information concerning dust emission magnitude through measurements of Aerosol Optical Depth (AOD) at 0.55 μm (Hsu *et al.,* 2004, 2006, 2013). MODIS Deep Blue AOD has been routinely used by researchers for the high resolution satellite-based assessment of atmospheric dust loading in arid environments (e.g., Kaufman *et al.,* 2005; Baddock *et al.,* 2009; Ginoux *et al.,* 2010; Ridley *et al.,* 2012; Sayer *et al.,* 2014; Bilal *et al.,* 2017).

To estimate the magnitude of airborne dust events from Etosha Pan, MODIS Terra AOD Level 2 product (MOD04_L2) data at 10 km spatial resolution (Levy *et al.,*

2015) were acquired from NASA's LAADS DAAC data portal (https://ladsweb.modaps.eosdis.nasa.gov/). Near real-time AOD values produced at 5 minute temporal resolution were aggregated to produce a daily mean AOD time-series.

To prevent the potential misinterpretation of increased dust event magnitudes caused by non-dust aerosols (i.e., biomass-induced smoke aerosols) surrounding the Etosha study region, daily AOD estimates were separated a priori by simultaneous assessment of daily active fire locations at 1 km spatial resolution derived using the MODIS Collection 6 Active Fire product (MCD14DL) (Giglio *et al.,* 2003, 2006, 2016) procured from NASA's Fire Information for Resource Management System (FIRMS) data archive (https://earthdata.nasa.gov/firms). Anomalous daily AOD values that coincided with the occurrence of active fire events observed in nearby regions surrounding the study area were subsequently removed to generate a daily AOD time-series showing magnitudes of mineral dust loading exclusively from Etosha Pan.

Establishing a Dust Event Inventory

The combined use of MSG-SEVIRI image composites, MODIS imagery and AOD data products allowed for the approximate position (±3 km) of plume sources to be scrutinised and plume metrics, including source coordinates, timing, direction, duration and magnitude (AOD), to be captured and compiled in a GIS database of spatially referenced vector points (Table 5.1). These individual plume event records and subsequent daily aggregates of dust days and aerosol optical depth (AOD) values

(Table 5.1) were used to identify potential trends in dust emission events across the overall study period (2000–2022), in addition to their seasonal and inter-annual variability.

Table 5.1. Dust event metrics used at varying temporal scales of analysis derived from MSG-SEVIRI and MODIS satellite sensors over Etosha Pan from 2000 to 2022.

Dust Metric	Description	Unit
Plume Event		
Source Location	Point source coordinates of the dust plume origin on the pan surface	Longitude/latitude (X/Y)
Start Time	Time at the earliest observed onset of a dust plume event	HH:MM, DD/MM/YYYY
End Time	Time at which the dust plume is observed to detach from its source origin on the pan surface	HH:MM, DD/MM/YYYY
Duration	Difference between the start and end time of each plume event	Minutes
Direction	Orientation of transport of the dust plume event	Degrees, °
Detection Sensor	Satellite sensor from which a dust plume was identified	MSG-SEVIRI/MODIS TERRA/MODIS AQUA
Magnitude	Average MODIS-retrieved Aerosol Optical Depth (AOD; a measure of aerosol loading in the total atmospheric column) value for the 3 km pixels corresponding to the dust plume event	AOD value, 0.0 – 5.0
Daily		
Dust plume frequency	Number of dust plume events observed emitting from Etosha Pan on a given day	Count of dust plume events per day
Dust day/non-dust day	Binary classification depicting whether a dust plume event was observed emitting from Etosha Pan on a given day	0 (no dust)/1 (dust)
Magnitude	Average daily MODIS-retrieved Aerosol Optical Depth (AOD; a measure of aerosol loading in the total atmospheric column) value over Etosha Pan	AOD value, 0.0 – 5.0
Monthly – Annually		
Dust plume frequency	Number of dust plume events observed emitting from Etosha Pan for a given period	Count of dust plume events/month or year
Dust day frequency	Number of 'dust days' in which a dust plume was observed emitting from Etosha Pan for a given period	Count of dust days/month or year
Magnitude	Average daily MODIS-retrieved Aerosol Optical Depth (AOD; a measure of aerosol loading in the total atmospheric column) value over Etosha Pan	AOD value, 0.0 – 5.0

5.2.2. Meteorological context for dust emissions

To determine the erosivity conditions associated with dust emissions from Etosha Pan, the detected dust events were evaluated against near-surface wind regimes derived from ERA5-Land (10 m wind speed and wind gusts) reanalysis data for corresponding periods. The ERA5-Land reanalysis model provides up to 70 years of hourly wind predictions at a 9 km spatial resolution (Muñoz-Sabater *et al.,* 2021) that have been routinely employed to study atmospheric and land surface conditions in arid and semi-arid regions where the availability of measured data is very low (Forootan *et al.,* 2017; Jury*,* 2021; Hou *et al.,* 2022). The ERA5-Land climate reanalysis dataset has been established as a valid representation of local atmospheric conditions at Etosha Pan, specifically. In a comprehensive evaluation of surface wind regimes at Etosha Pan, Gadal *et al.* (2022) observed a close agreement between predictions of the ERA5-Land climate reanalysis and continuous in-situ measurements of local wind speed and direction for multiple seasonal cycles in 2015–2018.

Hourly estimates of wind conditions (10 m horizontal $[u]$ and vertical $[v]$ components and wind gusts) at Etosha Pan for the period 2000–2022 were derived from ERA5-Land reanalysis obtained from the Copernicus Climate Change Service Data Store (https://cds.climate.copernicus.eu/). Calculated u and v vector components were corrected with relevant off-set and scaling factors, from which wind speeds (m s^{-1}) and direction (°) were computed. Wind gusts (m s^{-1}) are defined as the maximum value,

within the hourly observation period, of the 3-second running average wind speed (ECMWF: IFS Documentation CY47R3, 2021).

Both hourly estimates and derived daily averages of wind conditions were compared with detected dust plume events, dust day frequencies, and aerosol optical depth (AOD) values to determine the meteorological contexts for detected dust emissions at Etosha Pan. Furthermore, the strength of associations between metrics of dust emissions from the pan surface (dust plume event/dust day frequencies and AOD) and local wind conditions (wind speeds and wind gusts) were tested using statistical analysis (Pearson Correlation).

5.2.3. Hydrological controls and dust emissions

Regional hydrology is known to have a significant influence upon sediment supply and availability dynamics in the context of dust emission potential, both from Etosha Pan specifically (Bryant, 2003; Mahowald *et al.,* 2003; Bryant *et al.,* 2007) and from ephemeral pan and playa environments globally (e.g., Prospero *et al.,* 2002; Reynolds *et al.,* 2007, 2009; Baddock *et al.,* 2009, 2011, 2015; Webb and Strong, 2011; Sweeney *et al.,* 2016; Marx *et al.,* 2022, among others).

In line with these observations, the potential associations between precipitation events in the Cuvelai-Etosha Basin, consequent ephemeral flooding of Etosha Pan, and the spatiotemporal dynamics of dust plume event frequencies and magnitudes (AOD) were tested using statistical analysis (Pearson Correlation). Daily, monthly, and annual

catchment precipitation totals and pan flooding frequencies and extents derived in Part 1 of the thesis (see sections 4.3.1. and 4.3.2.) were evaluated against corresponding dust event frequencies and magnitudes (AOD) over the 2000–2022 period.

5.3. Results and Discussion

5.3.1. Dust emission event detection

Dust event detection by MSG-SEVIRI and MODIS satellite sensors

A total of 785 dust plumes were detected from Etosha Pan over the course of 428 days in the 2000–2022 analysis period. The inter-annual variations in dust plume events and associated dust day frequencies (see Table 5.1) detected from MSG-SEVIRI CSD and MODIS true-colour composites are displayed in Figures 5.3 and 5.4, respectively. Results indicate that dust plumes were observed emanating from Etosha Pan every year, to varying degrees, throughout the study period (Figure 5.3).

Comparisons of Figures 5.3 and 5.4 show analogous temporal trends in detected dust plume event and dust day frequencies, where, for example, years in which the most plumes were detected (e.g., 2015, 2016 and 2019) correspond to years with the highest observed number of dust days. However, the total number of plumes detected each year were generally greater than the total number of observed dust days (Figures 5.3 and 5.4), indicating that several individual plume events were detected in a single dust day. For instance, in 2015 a total of 138 individual dust plumes were observed over the course of 74 dust days.

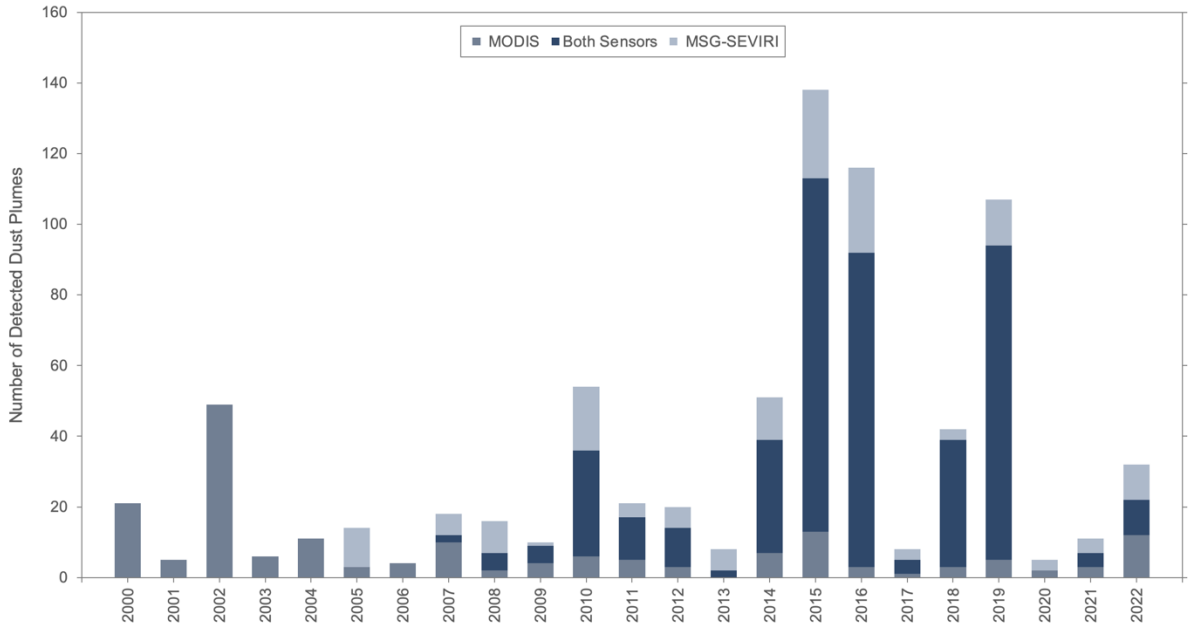


Figure 5.3. Annual frequency of dust plume events at Etosha Pan detected from MODIS true-colour imagery only (grey), MSG-SEVIRI CSD composites only (light blue) and events detected from both sensors (dark blue) from 2000 to 2022.

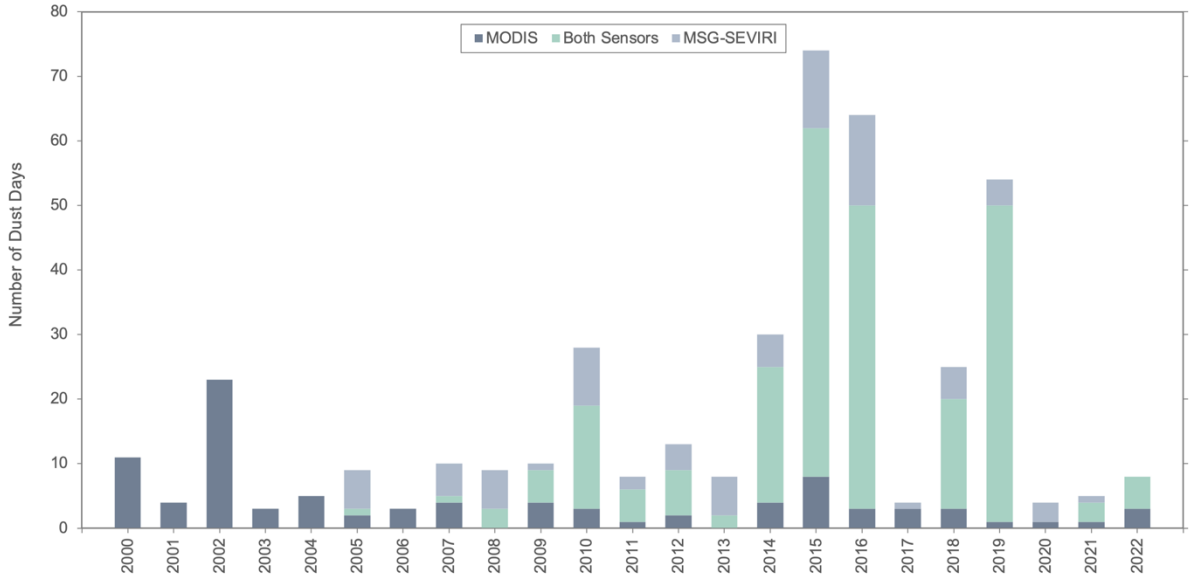


Figure 5.4. Annual frequency of dust days (i.e., days on which dust plumes were observed emitting from the study region) at Etosha Pan detected from MODIS true-colour imagery only (grey), MSG-SEVIRI CSD composites only (light blue) and events detected from both sensors (green) from 2000 to 2022.

Figures 5.3 and 5.4 illustrate a general agreement in plume event and dust day detection frequencies derived from MSG-SEVIRI and MODIS image time-series. Of the 785 individual plume events detected in the 2000–2022 period, a total of 443 plume events (56% of total detected plume events) were observed from both sensors. While 183 plumes (24% of total detected plume events) were identified from MODIS imagery but were missed in analyses of MSG-SEVIRI CSD data, and 159 plumes (20% of total detected plume events) were identified from MSG-SEVIRI CSD but were missed in analyses of MODIS imagery. Correspondingly, of the 428 observed dust days, a total of 241 dust days (57% of total detected dust days) were detected using both sensors. While 92 dust days (21% of total detected dust days) were identified only from MODIS imagery and 95 dust days (22% of total detected dust days) were identified only from MSG-SEVIRI CSD data.

As noted in similar studies (e.g., Baddock *et al.,* 2009; Schepanski *et al.,* 2009, Rivera Rivera *et al.,* 2010; Vickery *et al.,* 2013), such discrepancies were generally explained by four factors: the availability and coverage of satellite observations across the analysis period, the spatial resolution of image data, the temporal resolution of image data, and the user errors and (or) subjectivity associated with the manual interpretation technique for the detection of dust plume events from image time-series.

The MODIS image record of observations from Terra and Aqua satellites over Etosha Pan was available for the entire duration of the research period (2000–2022), whereas

the MSG-SEVIRI data record was not available until 2005. Accordingly, Figures 5.3 and 5.4 show that for the period 2000–2004, 92 dust plume events and 47 dust days were detected solely from MODIS true-colour imagery. For the remaining years (2005–2022) in which observation records were available from both sensors, instances where dust events were exclusively detected from MODIS true-colour imagery and not MSG-SEVIRI CSD composites were principally a consequence of differences in the spatial resolutions of the two datasets. The 500 m pixel resolution of MODIS data captured dust plumes that were too small to distinguish from the 3 km pixel resolution of MSG-SEVIRI data. As a result, several individual plume sources were identified from MODIS imagery that were either poorly characterised as a single plume event or not detected at all from the MSG-SEVIRI CSD data.

In contrast, instances where dust events were exclusively detected from MSG-SEVIRI CSD composites and not MODIS true-colour imagery were primarily a result of differences in the temporal resolutions of the two datasets. The high revisit frequency of MSG-SEVIRI enabled a time-series of CSD composite images to be generated at an hourly resolution for a 24 hr period. Consequently, this facilitated the identification of plume events that occurred outside of the narrow observation windows of MODIS at the satellite overpass times of ~1030 UTC (Terra) and ~1330 UTC (Aqua) each day (Figure 5.5).

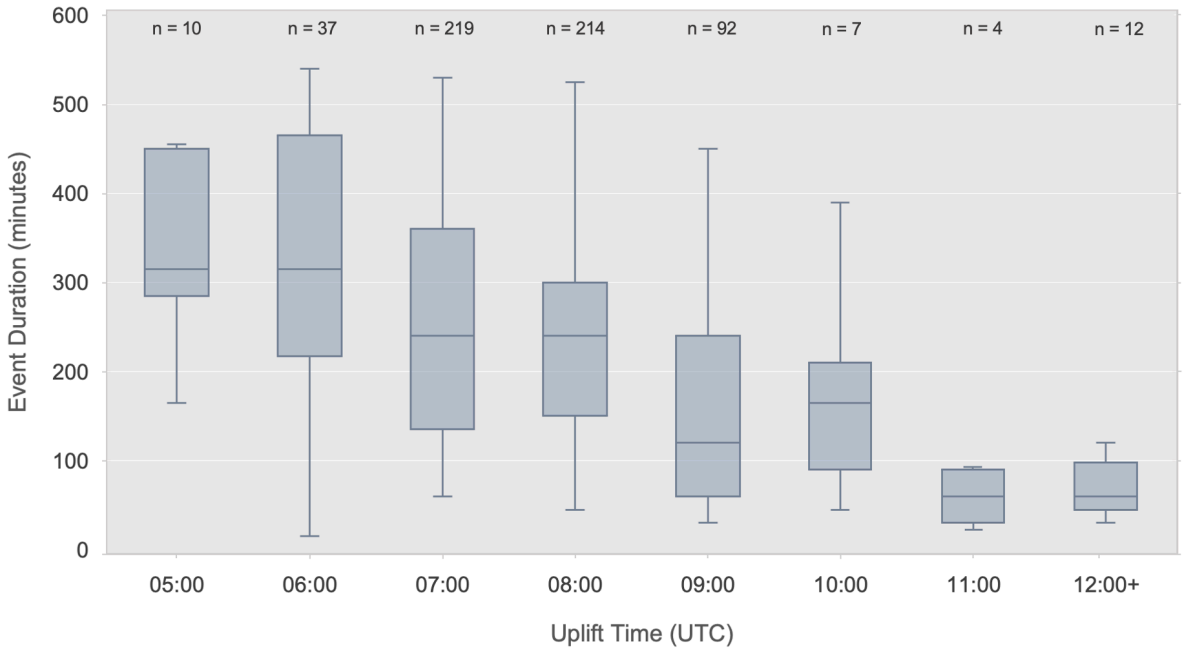


Figure 5.5. Box and whisker plots showing dust events detected from MSG-SEVIRI CSD time-series discriminated by measured time of uplift (UTC) and event duration (defined as the time in minutes between the measured time of uplift at-source and when the connection between the plume tail and source becomes detached).

From analysis of MODIS and MSG-SEVIRI imagery between 2005 and 2008, Vickery *et al.* (2013) found that dust emissions from Etosha Pan were typically short-lived, early morning events. Shown in Figure 5.5, analysis of plume events detected only from MSG-SEVIRI CSD time-series data from 2000 to 2022 revealed that the majority (96%) of dust events were observed in the early morning hours between 0500 – 0900 UTC (peak frequency at 0700 – 0800 UTC). However, a smaller proportion (4%) of dust events were observed in the mid-morning between 1000 – 1100 UTC and afternoon to late evening hours between 1200 – 2200 UTC.

The morning dust events were typically longer in duration (lasting anywhere between 30 and 550 minutes) compared to the relatively short-lived (restricted to durations of

30 to 120 minutes) afternoon/evening events (Figure 5.5). This is in line with field observations by Wiggs *et al.* (2022), in which the general distinction between earlier/longer dust emission events and later/shorter dust emission events was associated with two contrasting climatological mechanisms driving dust dynamics in different seasons; the breakdown of low-level jets (LLJ) in austral winter mornings, and cold pool outflows (CPO) associated with convective storms in austral summer evenings.

Despite implementing the same manual interpretation analysis of MODIS and MSG-SEVIRI imagery, research by Vickery *et al.* (2013) found that Etosha Pan generated 32 dust plumes over 22 days between 2005 to 2008, whereas the present research observed 52 plume events generated from Etosha Pan over 31 days for the corresponding period (Figures 5.3 and 5.4). It is possible this is a consequence of the improved detection of weaker transient dust event signals from MSG-SEVIRI imagery afforded by the clear sky differencing (CSD) approach (Murray *et al.,* 2016) in this research that may have been missed using the Dust RGB rendering scheme (Lensky and Rosenfeld, 2008) in Vickery *et al.* (2013). Nevertheless, detection using either method involves a degree of human error and (or) subjectivity constraints on the part of the observer (Schepanski *et al.,* 2009; Brindley *et al.,* 2012; Bryant, 2013).

Regardless of the specific sensor or analysis technique, satellite remote sensing-based dust detection does not necessarily capture inherent seasonal and diurnal dust emission

variations occurring from a source region, leading to some important biases (Kocha *et al.,* 2013). For example, many dust plumes associated with cold pool outflow events in the austral summer were unlikely to be detected in this study due to the obscuration of convective storm clouds in the remote sensing imagery (Hennen *et al.,* 2019; 2024; Nobakht *et al.,* 2021; Wiggs *et al.,* 2022; Clements and Washington, 2023). Efforts to conduct large-scale field campaigns at major source locations that enable a comprehensive assessment of dust event dynamics and controls over extended periods form the basis of ongoing research (e.g., Marticorena *et al.,* 2010, 2017; Allen *et al.,* 2015; Haustein *et al.,* 2015; Cui *et al.,* 2019a; Wiggs *et al.,* 2022). Nevertheless, satellite remote sensing facilitates multi-temporal observations of dust source activity across varied spatial scales (i.e., from pinpointing plume origin within a few km to quantifying global emissions) and temporal scales (i.e., from the dynamics of individual dust emission events up to the long-term activity of emissive source areas), which remain crucial in guiding ground-based observations (Bryant, 2013; von Holdt *et al.,* 2017) as well as informing the development of models representing dust emission into the atmosphere (Haustein *et al.,* 2015; Klose *et al.,* 2019; Zhao *et al.,* 2022).

Annual Trends

The inter-annual variations in dust aerosol optical depth (AOD) and number of dust plume events and dust days at Etosha Pan derived from MSG-SEVIRI and MODIS satellite data from 2000 to 2022 are displayed in Figure 5.6. Results indicate

that both mean AOD and number of dust plume events and dust days fluctuated annually throughout the research period, but the datasets show good correspondence.

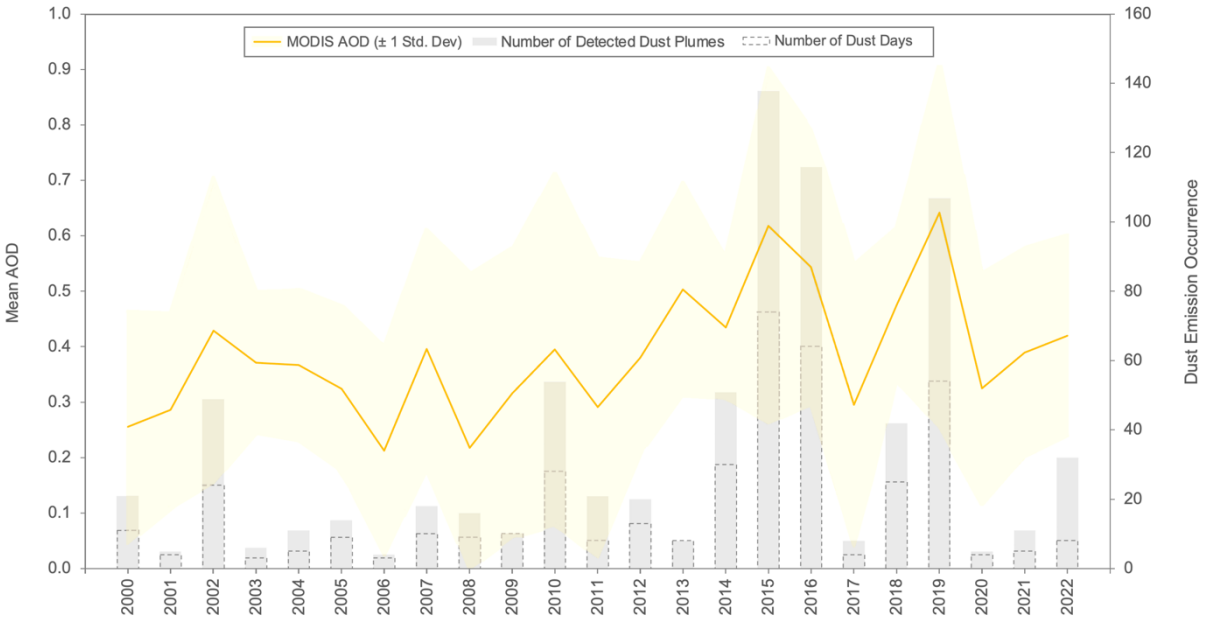


Figure 5.6. Annual values of mean daily AOD and total number of dust plume events and dust days at Etosha Pan from 2000 to 2022.

Elevations in AOD values and the highest number of dust plume events and dust day occurrences were recorded in 2015 (mean AOD: 0.62 ±0.35; 138 dust plumes within 74 dust days), 2016 (mean AOD: 0.54 ±0.25; 116 dust plumes within 64 dust days), and 2019 (mean AOD: 0.64 ±0.39; 107 dust plumes within 54 dust days) (Figure 5.6). It was during these particularly dry years that precipitation values were recorded below the catchment average (572 mm) across the Cuvelai-Etosha Basin for corresponding hydrological years (July – June) of 2015 (462 mm), 2016 (379 mm) and 2019 (411 mm) (see Figure 4.3, Chapter 4). Similarly, both the annual lake surface inundation extents and flooding frequencies were consistently lower than average values (574.9 km^2; 148

days flooded) at Etosha Pan in 2015 (40.7 km^2; 14 days flooded), 2016 (58.2 km^2; 27 days flooded), and 2019 (17.3 km^2; 9 days flooded), respectively (see Figure 4.9, Chapter 4).

However, elevations in mean annual AOD values were not always synonymous with the annual number of dust plume events and dust days. For example, elevations in aerosol optical depth values were observed in 2013 (mean AOD: 0.50 ±0.19) despite the relative infrequency of observed dust emissions (8 dust plumes within 8 dust days) (Figure 5.6). This was the result of advected mineral dust aerosols in the region caused by emissive events from smaller pans and ephemeral river channels (iishana) surrounding Etosha Pan under dry conditions, as previously noted by Bryant (2003). Further work to establish the contribution of these smaller fluvial dust sources is, therefore, needed to gain a comprehensive view of the dust load from the Etosha region.

Seasonal Cycle

Figure 5.7 shows the seasonality associated with average AOD and the number of dust plume events and dust days at Etosha Pan for the period 2000 to 2022. Dust emission activity occurred in the region throughout the annual cycle but frequent events and higher aerosol optical depths were observed in the dry austral winter, coinciding with periods of low rainfall across the Cuvelai-Etosha Basin (see Figures 4.7 – 4.10, Chapter 4) and a typically dry pan surface (see Figures 4.13 and 4.14, Chapter 4) with a supply of material more susceptible to entrainment by wind, as recognised

from previous remote sensing analyses and ground-based measurements (Bryant, 2003; Mahowald *et al.,* 2003; Bryant *et al.,* 2007; Vickery *et al.,* 2013; von Holdt *et al.,* 2017; Wiggs *et al.,* 2022).

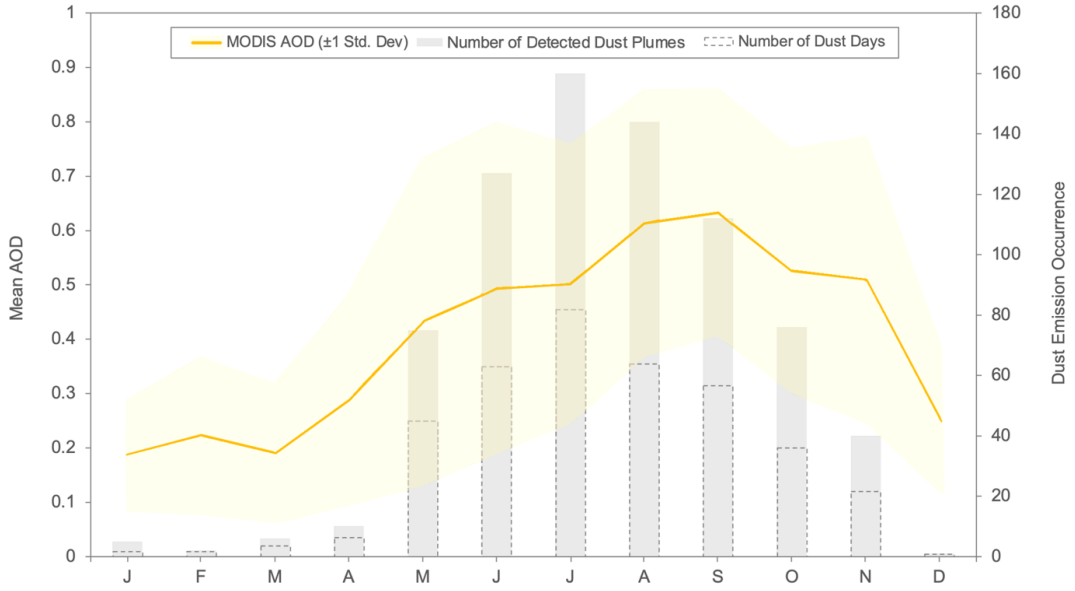


Figure 5.7. Monthly values of mean daily AOD and total number of dust plume events and dust days at Etosha Pan from 2000 to 2022.

High frequencies of dust plume activity and elevations in aerosol optical depth values over Etosha Pan were recorded between May – November, with a peak in activity in the period June – September (Figure 5.7). The highest frequencies of dust events were observed in July, with a total of 160 dust plumes recorded throughout 91 active dust days in the 2000–2022 analysis period (Figure 5.7). While mean aerosol optical depth values generally peaked in September (mean AOD: 0.6 ±0.22), following a two-month lag since peak dust plume activity (Figure 5.7).

5.3.2. Meteorological context for dust emissions

To determine the erosivity conditions associated with observed dust emissions from Etosha Pan, the detected dust events were evaluated against near-surface wind regimes derived from ERA5-Land (10 m wind speed and wind gusts) reanalysis data. Figure 5.8 shows the frequency of dust plume events observed in 2000–2022 compared to the 10 m wind speeds and directions according to ERA5-Land reanalysis data for the corresponding time and location of initial uplift. Results indicate a clear predominance in dust plume development from Etosha Pan driven by winds from a preferred direction, where 93% of dust plume events were initiated by winds originating from the E–NE ($n = 785$; Figure 5.8).

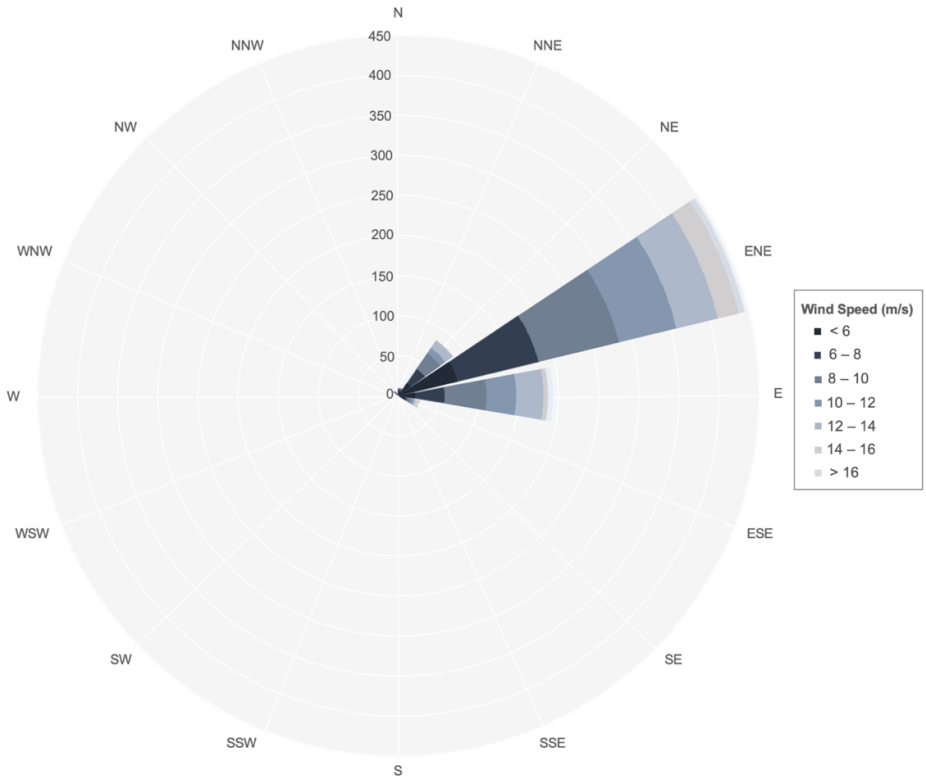


Figure 5.8. ERA5-Land 10 m wind speeds and directions associated with the activation of dust plume events at Etosha Pan from 2000 to 2022 ($n = 785$).

Previous work has demonstrated that dust emissions from Etosha Pan are associated with E-NE winds exceeding erosive threshold speeds of c. >6 m s^{-1} (Bryant *et al.,* 2007; Vickery *et al.,* 2013; Wiggs *et al.,* 2022). In line with these observations, it was found that strong winds exceeding 6 m s^{-1} originating from the E-NE (60°–80°) were responsible for the majority of dust emission events from the pan surface during the study period (Figure 5.8).

Figure 5.9 illustrates the inter-annual trends in erosion thresholds for detected dust plume events compared with 10 m wind speeds derived from ERA5-Land reanalysis data for the corresponding time and location of initial uplift.

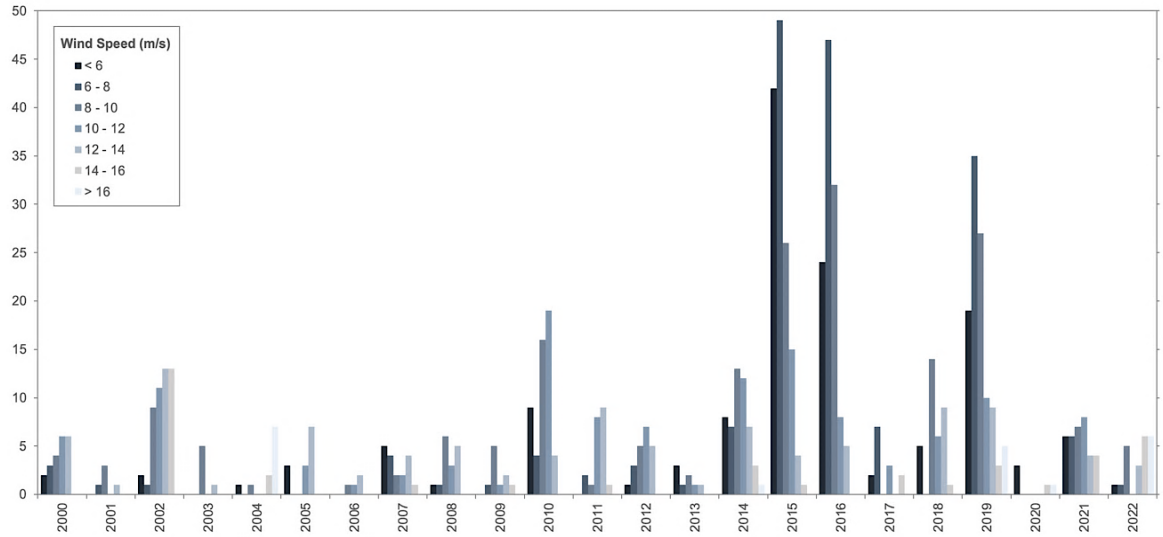


Figure 5.9. Annual frequency of 10 m wind speed thresholds for dust plume events observed at Etosha Pan from 2000 to 2022.

Overall, the lowest threshold wind speed recorded at time of uplift for a dust event was 1.24 m s^{-1} and the highest was 16.48 m s^{-1} for the 2000–2022 analysis period. While dust plume events were observed to occur across this range of measured wind speeds

each year, thresholds for erosion were notably lower (< 6 up to 8 m s^{-1}) for a greater proportion of dust plume events recorded during especially dry and highly emissive years of 2015, 2016 and 2019 (Figure 5.9).

Figure 5.10 shows the 2000–2022 ERA5-Land daily 10 m wind speeds (Figure 5.10a) and wind gusts (Figure 5.10b), binned and plotted as relative frequencies for the active dust season (i.e., the period from May to November where greater dust emission activity was observed [see Figure 5.7] and lake inundation extents were generally small [see Figures 4.13 and 4.14, Chapter 4]), for the Etosha region. Dust days (i.e., days that dust plumes were observed emitting from the pan surface) are binned according to the corresponding ERA5-Land average wind speeds and gusts for each dust day and plotted as a relative frequency in each graph, respectively.

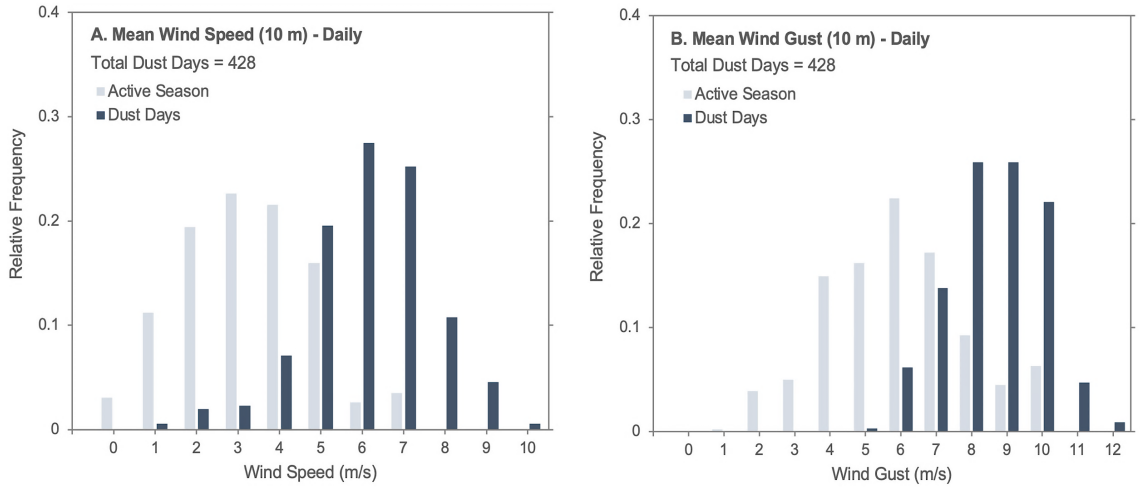


Figure 5.10. Frequency distributions of ERA5-Land (a) daily mean wind speeds and (b) daily mean wind gusts associated with the active dust emission season (grey) and for dust days only (dark blue) plotted as a function of relative wind speed frequency.

Shown in Figure 5.10a, the observed dust emission days were associated with higher wind speeds, and typically peaked at daily mean wind speeds of 6 m s^{-1} to 7 m s^{-1}. Correspondingly, mean daily AOD measured over the Etosha region was found to be significantly correlated with ERA5-Land daily mean wind speeds ($r = 0.48$, $p < 0.01$). The association was improved when mean wind speeds were cubed (W^3) ($r = 0.50$, $p < 0.01$), in line with previous observations in southern Africa (Bryant *et al.,* 2007) and dust modelling studies (Luo *et al.,* 2003, 2004).

Shown in Figure 5.10b, the observed dust emission days also correspond with periods of higher ERA5-Land daily mean wind gusts, which typically peaked at 8 m s^{-1} to 9 m s^{-1}. Further, mean daily AOD values were found to be significantly correlated with ERA5-Land wind gusts ($r = 0.49$, $p < 0.01$) over the Etosha region during the research period.

Research by Engelstaedter and Washington (2007a,b) similarly found improved agreement between ERA-40 wind gust data and dust emissions in North Africa, attributed to the importance of turbulence and near surface convergence on dust uplift related to the breakdown of nocturnal low-level jets (LLJs) for morning emission events during winter months (Fiedler *et al.,* 2013; Heinold *et al.,* 2013; Allen and Washington, 2014) and cold pool outflows from convective storms for afternoon emission events during summer (Marticorena *et al.*, 2010; Marsham *et al.*, 2013; Allen *et al.,* 2015). Indeed, recent field-based research has noted similar dust emission dynamics associated

with turbulent, gusty winds driven by LLJ activity in the austral winter and convective storm activity in the austral summer at Etosha Pan (Clements and Washington, 2021; Wiggs *et al.,* 2022).

5.3.3. Hydrological controls and dust emissions

It can be seen from the analyses conducted in this research that connections exist between measured dust emissions at Etosha Pan and surface wind speed dynamics across daily timescales. In addition, associations have been drawn between dust emissions, rainfall in the Cuvelai-Etosha Basin and surface flooding at Etosha Pan across both annual and seasonal scales. Mean daily time-series data displayed in Figure 5.11 further elucidates in detail how these variables relate within the broader hydrological system and the extent to which they influence dust source activity at Etosha Pan for the 2000–2022 analysis period.

Shown in Figure 5.11a, temporal trends in mean daily AOD generally correlate with ERA5-Land mean daily cubed wind speeds (W^3) measured over Etosha Pan, particularly for the years 2000–2005. However, trends in the two variables diverge in 2006, where negative AOD anomalies (−2 standard deviations) were observed despite positive cubed wind speed anomalies of the same order (+2 standard deviations) for the corresponding period. This may suggest that dust emissions were reduced despite the occurrence of above-average wind speeds over the Etosha region.

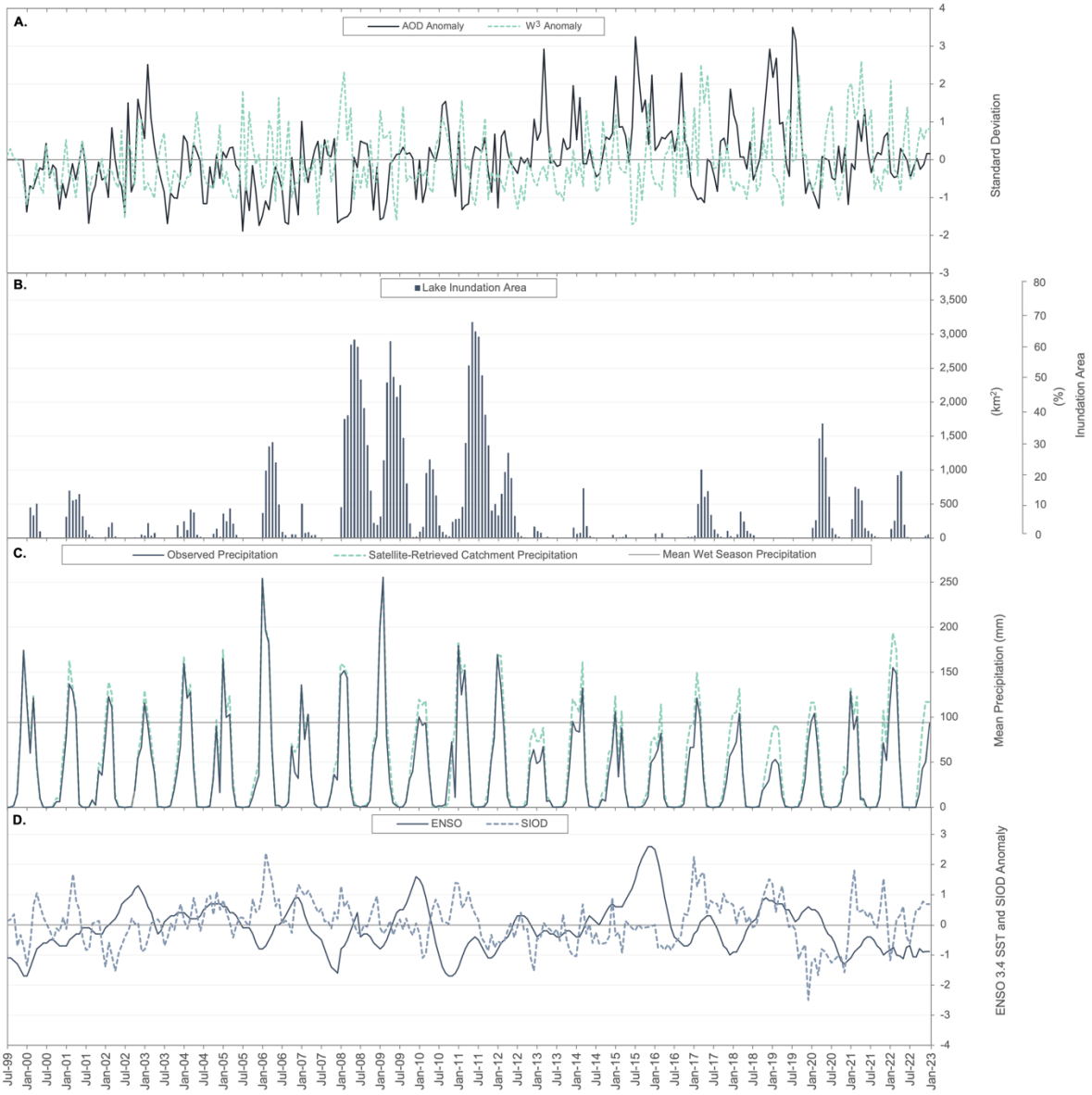


Figure 5.11. Monthly time-series of (a) MODIS aerosol optical depth (AOD) and cubed surface wind speed (W^3) anomalies, (b) lake surface inundation extents at Etosha Pan, (c) precipitation totals for the Cuvelai-Etosha Basin derived from ground-based observations and satellite-retrieved estimates (TRMM/GPM-IMERG), in addition to (d) El Niño-Southern Oscillation Sea Surface Temperature (ENSO 3.4 SST) and subtropical Indian Ocean Dipole Index (SIOD) anomalies for the period July 1999 – December 2022.

This divergence trend corresponds with key changes in surface hydrology of Etosha Pan (Figure 5.11b), where the pan surface transitioned from completely dry in November 2005 to a steady increase in flooding extent reaching up to 1,500 km^2 (30% pan area) in April 2006 (Figure 5.11b) following a significant increase in mean monthly catchment precipitation (~250 mm $month^{-1}$) (Figure 5.11c). It is possible that such trends were driven by the opposing negative ENSO phase (La Niña event) in the tropical Pacific and positive SIOD phase (Figure 5.11d) (see also section 4.3.5; Reason and Smart, 2015; Hoell *et al.,* 2017).

Similarly, negative AOD anomalies were observed despite positive cubed wind speed anomalies for the years 2008, 2009, 2011, 2017 and 2020 (Figure 5.11a). These periods correspond with prolonged episodes of frequent and extensive flooding of Etosha Pan (Figure 5.11b), following periods of above average precipitation (Figure 5.11c), which generally correlate with a negative ENSO phase (La Niña event) and (or) a positive SIOD phase (Figure 5.11d) (see also section 4.3.5).

In contrast, significant positive AOD anomalies (+3 standard deviations) were observed in 2013, 2015, 2016 and 2019 despite negative cubed wind speed anomalies measured in the corresponding periods (Figure 5.11a). This indicates a considerable increase in dust emissions above average conditions, despite a reduction in wind speeds in the region. Indeed, thresholds for erosion were markedly lower (< 6 m s^{-1}) for a greater proportion of dust plume events observed in these years (see Figure 5.9). This

corresponds with very dry periods where the observed extent of inundation across the pan was negligible (< 100 km^2 month^{-1}; Figure 5.11b), following periods of below average precipitation (< 100 mm month^{-1}; Figure 5.11c), potentially linked to the observed positive ENSO phase (El Niño event) and (or) negative SIOD phase for corresponding years (Figure 5.11d) (see also section 4.3.5).

The data from these time-series indicate a very close connection between the hydrological cycle of wet season precipitation, lake inundation and drying, and the emission of dust from Etosha Pan. The previous chapter revealed statistically significant associations between catchment precipitation and lake inundation extents and frequencies across both annual and seasonal scales (see section 4.3.4). Further, it was shown that these relationships were associated with global climate cycles and sea surface temperature anomalies (ENSO and SIOD) (see section 4.3.5).

Accordingly, statistical (Pearson Correlation) tests were performed to quantify the extent to which regional hydrology may influence dust emission activity from Etosha Pan. Table 5.2 shows Pearson correlation coefficients between data reflecting dust emission activity (AOD and plume event frequencies) and key hydrological variables (surface flooding extent [km^2] and flooding frequency [flood days]) and catchment-scale precipitation (mm) in the Cuvelai-Etosha Basin for the 2000–2022 analysis period.

Table 5.2. Pearson correlation coefficients between satellite-derived lake surface inundation extents and frequency of flooding at Etosha Pan, catchment precipitation in the Cuvelai-Etosha Basin and dust emission magnitudes (AOD) and plume event frequency at Etosha Pan across annual (+1, +2 and +3 year lags), monthly (+1, +2 and +3 month lags), and daily timescales from 2000 to 2022.

Time Period	Inundation Extent (km^2)		Flood Frequency (Days)		Catchment Precipitation (mm)	
	Aerosol Optical Depth (AOD)	Dust Event Frequency (Plume Count)	Aerosol Optical Depth (AOD)	Dust Event Frequency (Plume Count)	Aerosol Optical Depth (AOD)	Dust Event Frequency (Plume Count)
Annually	-0.52**	-0.48*	-0.39**	-0.55**	-0.56**	-0.46*
+1 year lag	-0.31	0.43	-0.19	-0.25	-0.35	-0.42
+2 year lag	-0.11	-0.14	0.053	-0.098	-0.16	-0.20
+3 year lag	-0.15	-0.28	-0.08	-0.26	-0.44	-0.59
Monthly	-0.22**	-0.26**	-0.20**	-0.31**	-0.57**	-0.40**
+1 month lag	-0.05	-0.22**	-0.03	-0.23**	-0.45**	-0.35**
+2 month lag	0.092	-0.17**	0.098	-0.13*	-0.35**	-0.24**
+3 month lag	0.16**	0.14*	0.18**	0.05	0.23*	-0.085
Daily	-0.19*	-0.042	-0.17	-0.09	-0.31*	-0.24**

* Significant at the 0.05 level, ** Significant at the 0.01 level

Across annual timescales, significant moderate negative associations were found between both pan surface inundation extents and flooding frequencies with AOD ($r =$ –0.52, $p < 0.01$ and $r =$ –0.39, $p < 0.01$, respectively) and plume event frequencies ($r =$ –0.48, $p < 0.05$ and $r =$ –0.55, $p < 0.01$, respectively) (Table 5.2). This suggests that, as might be expected, dust emission activity at Etosha Pan is significantly reduced during 'wet years' characterised by extensive and frequent inundation of the pan surface. This reflects the immediate influence of floodwater presence on the pan surface

inhibiting the availability of sediment from erosion despite the presence of high wind speeds over the region (Bryant, 2003; Mahowald *et al.,* 2003; Bryant *et al.,* 2007). Correspondingly, significant negative associations were also found across shorter timescales, between monthly pan surface flooding variables and dust emission activity variables for corresponding months (r = –0.20 to –0.31, $p < 0.01$) and between daily observed inundation extents and AOD (r = –0.19, $p < 0.05$) (Table 5.2).

Significant moderate negative associations were also found between catchment precipitation and dust emission variables (AOD and plume event frequencies) across all timescales of interest (Table 5.2). This further suggests that despite the presence of elevated wind speeds, dust emissions were inhibited during and immediately following periods of rainfall. Table 5.2 shows that the negative associations between catchment precipitation and dust emission variables (AOD and plume event frequencies) were stronger than associations between pan surface flooding and dust emission activity, particularly across shorter-term monthly and daily timescales. For example, the negative correlation coefficient was greater between monthly AOD and precipitation for corresponding months (r = –0.57, $p < 0.01$) than those observed with monthly mean inundation extents (r = –0.22, $p < 0.01$) and frequencies (r = –0.20, $p < 0.01$) (Table 5.2).

Previous research in similar playa sources has shown that changes in soil moisture and salinity in response to both direct precipitation and associated groundwater table fluctuations can alter surface crust stability and the inter-particle cohesive forces that

determine surface resistance to aeolian entrainment (Reynolds *et al.,* 2009; Buck *et al.,* 2011; Nachshon *et al.,* 2011). Hence, the significant influence of precipitation on inhibiting dust emissions observed in the data presented here likely reflects the effects of rainfall-induced changes in surface moisture and water table levels, which further compound the presence of water on the pan surface associated with flooding events, restricting the availability of surface sediment to aeolian erosion. Indeed, the gradual reduction in correlation coefficients as consecutive monthly lags were introduced (Table 5.2) may reflect the weakening effect of surface water presence and subsurface moisture dynamics on inhibiting sediment availability for erosion as the surface dries out (Mahowald *et al.,* 2003; Reynolds *et al.,* 2007, 2009).

Observations from the data presented here corroborate those of Bryant (2003) and Mahowald *et al.* (2003), which suggest that rainfall-driven surface flooding dynamics have a significant influence on the timing and magnitude of aeolian dust emissions at Etosha Pan. Bryant (2003) hypothesised that it was through influencing sediment supply dynamics, in which flood events deliver a supply of sediment from ephemeral channel inputs that becomes susceptible to wind erosion in the following dry seasons (with a lag of 1–2 years), that ultimately determines atmospheric dust loadings from the pan surface. The data in the 2000–2022 time-series displayed in Figure 5.11 similarly show a notable increase in dust emissions during the dry years of 2013, 2015, 2016 and 2019, which followed particularly wet years of 2006, 2008, 2009, 2011 and 2012 characterised by frequent and extensive surface inundation of the pan. However, correlations between dust emission variables and pan surface flooding and catchment-

scale rainfall drivers with annual lags of +1, +2 and +3 years were found not to be significant (Table 5.2). Nevertheless, Table 5.2 shows that when a shorter (+3 month) lag was introduced, positive associations were found between monthly pan surface flooding extents with mineral dust AOD ($r = 0.16$, $p < 0.01$) and dust plume event frequencies ($r = 0.14$, $p < 0.05$) as well as between monthly pan surface flooding frequencies and AOD ($r = 0.18$, $p < 0.01$). A significant positive association was also found between monthly catchment precipitation totals and AOD with a +3 month lag ($r = 0.23$, $p < 0.05$) (Table 5.2). This suggests that ephemeral inundation and (or) wetting of the pan surface by rainfall promoted dust emissions across much shorter seasonal timescales (~3 months) compared with the 1–2 year lags observed in previous studies (Bryant, 2003; Mahowald *et al.,* 2003).

It is possible that during the 2000–2022 analysis period sediment inputs were supplied from ephemeral channels draining into Etosha Pan given that the majority (79%) of lake surface inundation events were sourced from fluvial inputs (see section 4.3.3; Figure 4.13, Chapter 4). However, the spatiotemporal distributions of dust event sources in relation to flooding frequencies displayed in Figure 5.12 indicate that dust emission events were not necessarily confined to regions of previous inundation, which might be expected if sediment deposits from ephemeral flooding events formed the majority of material for dust emissions (Bryant, 2003). Nevertheless, most emission events were observed emanating from surfaces that had experienced some degree of flooding and (or) wetting in the corresponding year preceding the emission event (Figure 5.12).

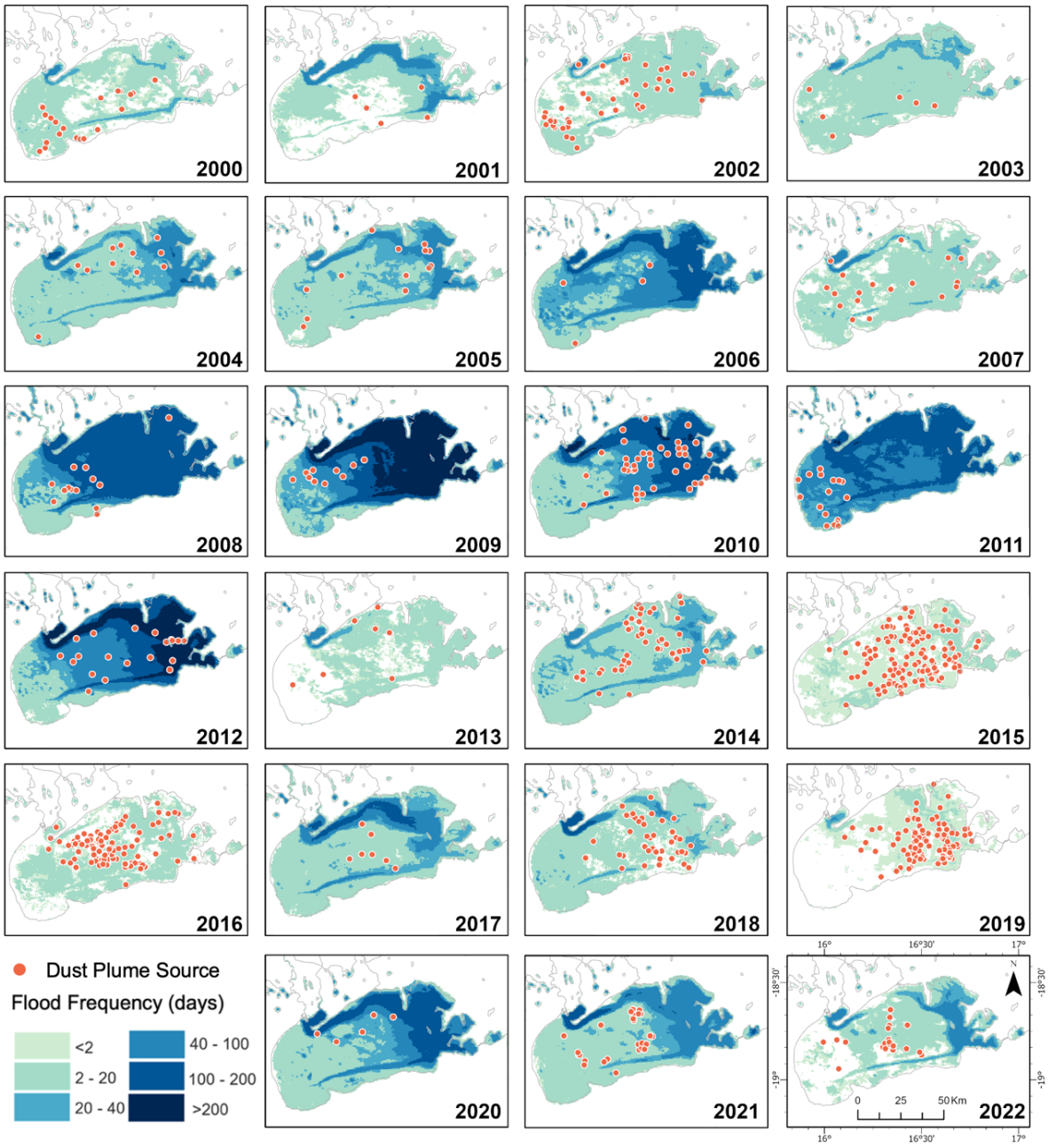


Figure 5.12. Spatiotemporal distributions of annual dust emission events (orange points) and lake surface inundation frequencies (where the value of each pixel indicates the frequency in days that it has experienced flooding for hydrological years [July – June]) at Etosha Pan from 2000 to 2022.

Therefore, the spatiotemporal dynamics of dust emissions may correspond to changes in surface erodibility driven by hydrological factors, rather than solely through sediment supply dynamics. Given the presence of evaporite minerals in surface sediment and groundwater at Etosha Pan (Herdtfelder, 1984; Buch and Rose, 1996; Bhattachan *et al.,* 2015, Li *et al.,* 2018), it is possible that basin-scale hydrological conditions could occasionally promote dust emissions at Etosha Pan shortly after heavy rainfall events through salt crust breakdown mechanisms, as has been observed in studies of similar playa dust sources with evaporite mineral crusts (e.g., Cahill *et al.,* 1996; Gillette *et al.,* 1997; Niemeyer *et al.,* 1999; Zender and Kwon, 2005; Reynolds *et al.,* 2007, 2009; Bullard *et al.,* 2008; Macpherson *et al.,* 2008; Baddock *et al.,* 2009, 2011, 2015; Strong *et al.,* 2011; Sweeney *et al.,* 2011; Nield *et al.,* 2015, 2016b).

Accordingly, satellite-derived surface crust moisture conditions (i.e., time since wetting and frequency of wetting) were examined for dust plume event sources at the corresponding time of emission. Results displayed in Figure 5.13 indicate a higher frequency of dust plume events from surfaces characterised by crust surfaces that have been subject to moist conditions in months prior to an emission event. In Figure 5.13a, peak dust event frequencies (~50% of all detected plume events) were sourced from surfaces that had been wetted between 100 and 200 days (3 – 6.5 months) prior to emission, corresponding to the positive associations found between precipitation, ephemeral flooding and three-month lagged dust emissions activity (Table 5.2).

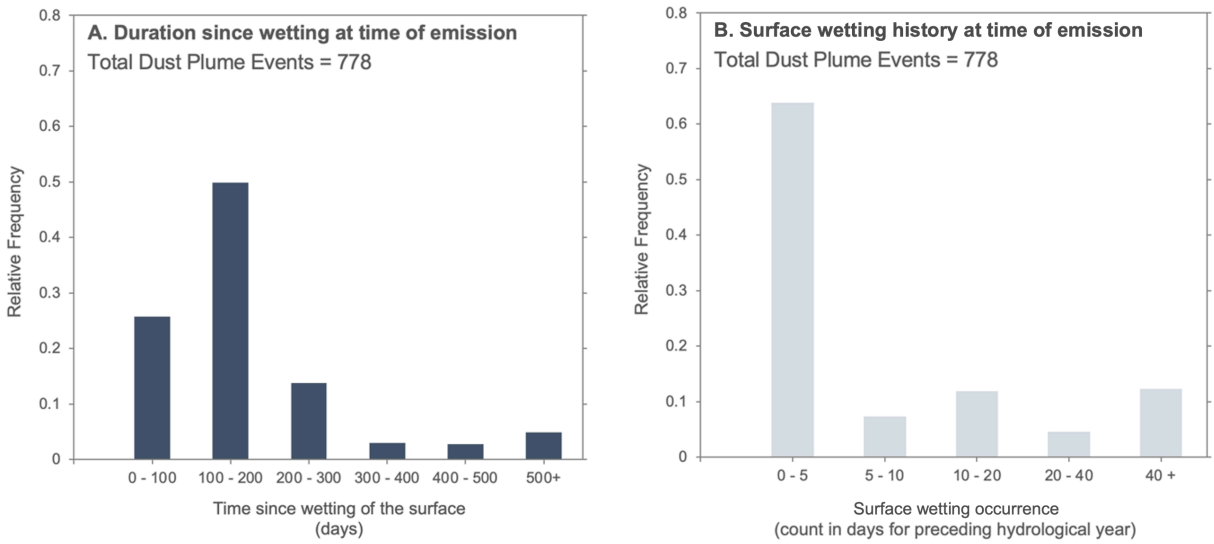


Figure 5.13. Frequency distributions of (a) the number of days since wetting and (b) wetting occurrences (count in days) for the preceding hydrological year (July – June) of dust source surfaces at the time of emission plotted as a function of corresponding dust plume events recorded at Etosha Pan from 2000 to 2022.

Surrounding this period, dust event frequencies were generally associated with surfaces recently disturbed by moist conditions from ephemeral rainfall and flooding events between 1 – 100 days (25% of all detected plume events) and between 200 – 300 days (15% of all detected plume events) (Figure 5.13a). Across these timescales, it is possible that pre-existing wind resistant evaporite mineral crusts were initially dissolved during rainfall and flooding events (Zender and Kwon, 2005; Bryant *et al.,* 2007; Klose *et al.,* 2019), with subsequent drying leading to the development of salt efflorescences, thin surface crusts and (or) the production of loose aggregated evaporite minerals at the surface that are highly susceptible to wind erosion (Reynolds *et al.,* 2007, 2009; Macpherson *et al.,* 2008; Sweeney *et al.,* 2011, 2016; Nield *et al.,* 2015, 2016a,b; De Deckker, 2019).

In contrast, $< 10\%$ of all detected plume events were sourced from relatively dry surfaces that had not been subject to moisture (either precipitation or flooding) for > 300 days (Figure 5.13a). This suggests that prolonged arid conditions may supress dust emissions at Etosha Pan, potentially due to the formation of hard evaporite mineral crusts that are resistant to wind erosion (Reynolds *et al.,* 2007, 2009; Milewski *et al.,* 2019).

Further, Figure 5.13b shows that peak dust event frequencies (~60% of all detected plume events) were sourced from surfaces that had been wetted no more than five daily instances in the hydrological year preceding emission. This suggests that rainfall and (or) ephemeral flooding may promote dust emissions in following months, provided that surface and near-surface sediment conditions do not exceed a threshold level of moisture from frequent wetting that may inhibit the availability of sediment to aeolian erosion and subsequently suppress dust emission.

5.4. Conclusion

This chapter has presented a comprehensive analysis of the temporal and spatial dynamics of aeolian dust emissions from Etosha Pan and quantified the extent to which dust emission is associated with hydrological and erosivity drivers for the period 2000–2022. Notably, analyses have established the significant, albeit complex, interactions evident between precipitation, ephemeral surface inundation events and sediment

availability dynamics. The key findings with respect to the objectives of the research are:

1) Multi-sensor satellite (MSG-SEVIRI and MODIS) observations have shown consistent fluctuations in mean annual mineral dust aerosol optical depth (AOD) and dust plume event and dust day frequencies across the 2000–2022 time-series. Measurements of dust magnitudes and emission event frequencies both peaked in the years of 2015, 2016 and 2019, characterised by anomalously dry conditions at Etosha Pan associated with below average precipitation totals in the Cuvelai-Etosha Basin. A distinct dust season was observed in the dry austral winter lasting from May to November, with a peak in dust emissions in the period June to September, where dust events were typically observed in the early morning hours between 0500–0900 UTC. Some dust emission events were also observed in the afternoon to late evening hours and in the austral summer, although such events may have been underestimated in the remote sensing data presented here owing to the presence of clouds obscuring satellite-based detection.

2) Analysis of detected dust events against near-surface wind regimes derived from ERA5-Land model reanalysis data revealed a clear directional predominance in dust emissions associated with prevailing E-NE winds in the region. Observed dust emissions showed a significant correlation with higher wind speeds and wind gust values, which typically peaked at wind speeds above 6 m s^{-1}.

3) The frequency, timing and magnitude of dust emissions at Etosha Pan were shown to be significantly influenced by annual and seasonal variations in catchment-scale precipitation and ephemeral flooding events. Findings from this research confirm the observations of previous studies at Etosha Pan, that periods of rainfall and subsequent extensive inundation of the pan surface initially suppressed dust emissions. However, it was found that ephemeral inundation and (or) wetting of the pan surface by rainfall promoted dust emissions across much shorter seasonal timescales (~3 months) compared with the 1–2 year lags observed in previous studies. Analyses of the spatiotemporal interactions between catchment precipitation, ephemeral surface inundation and dust emission events suggest that emissions correspond to changes in surface erodibility associated with recent moderate surface wetting. It is surmised that such minor wetting of the pan surface may impact on the stability of evaporite mineral surface crusts with a consequent impact on the susceptibility of the surface to wind erosion. This is in contrast to earlier studies, which inferred a function for sediment supply driven by ephemeral inundation. The study presented here found no evidence for this dynamic.

Overall, analyses of the 2000–2022 time-series of satellite observations presented in this chapter indicate that basin-scale hydrology has an important influence on the timing and magnitude of dust emissions from Etosha Pan. A discrete and sensitive set of associations were established between dust emission events and catchment-scale precipitation and pan surface flooding dynamics, which may be related to changes in

sediment availability (i.e., surface erodibility) associated with recent surface wetting affecting the stability of evaporite mineral crusts and surface moisture conditions. This presents an opportunity to investigate the potential relationships between hydrological conditions and pan surface crust properties, and to ascertain how these might influence surface susceptibility to wind erosion and dust emission from the ephemeral playa.

CHAPTER SIX

Part 3

Controls on sediment availability in the formation of dust emission 'hot-spots' on Etosha Pan

Controls on sediment availability in the formation of dust emission 'hot-spots' on Etosha Pan

6.1. Introduction

Analyses of the spatiotemporal interactions between catchment precipitation, ephemeral surface inundation and dust events presented in Part 2 of the thesis (see Chapter 5) indicate that patterns of dust emission from Etosha Pan are associated with changes in the availability of sediment to aeolian entrainment. The twenty-year time-series of dust activity corroborated the observations of previous studies at Etosha (Bryant, 2003; Mahowald *et al.,* 2003), that wet season precipitation and ephemeral flooding events intuitively lead to the suppression of dust emissions. However, a positive association was also found between wet season precipitation and enhanced dust emissions across seasonal (~3 months) timescales. These associations may reflect changes in surface erodibility which, in similar ephemeral playa environments, have been linked with the changing stability of surface crusts (Reheis, 2006; Bryant *et al.,* 2007; Reynolds *et al.,* 2007, 2009; Elmore *et al.,* 2008; Macpherson *et al.,* 2008; Nield *et al.,* 2016a,b; Sweeney *et al.,* 2016; De Deckker, 2019).

The combination of seasonal rainfall, ephemeral flooding and high evaporation rates within closed drainage basins favours the development of crusted surfaces by efflorescence of evaporite (salt) minerals, which can exert a profound influence on both the amount of fine material available for aeolian erosion and on the spatial and

temporal distribution of dust emissions (Cahill *et al.,* 1996; Gill, 1996; Goldstein *et al.,* 2017; Zhang, G. *et al.,* 2021). As precipitation ceases and, in years with pan inundation, the recession of surface flooding occurs during seasonal dry periods, the on-going evaporation of near-surface groundwater results in the precipitation of salt minerals at the surface, of which the specific mineralogy is controlled by the composition of the evaporating solutes (Buck *et al.,* 2011; Milewski *et al.,* 2019; Dai *et al.,* 2022). Field investigations of playa surfaces have shown that under certain climatic conditions, salt minerals may precipitate to form soft "puffy" crusts with loose unconsolidated individual crystals at and near the surface that can be directly entrained by wind (Gillette *et al.,* 1980; Reynolds *et al.,* 2007, 2009; Buck *et al.,* 2011; Nield *et al.,* 2016a; De Deckker, 2019), or they can form hard crusts composed of interlocking crystals (Langston and McKenna Neuman, 2005; Goldstein *et al.,* 2017).

Such differences in the morphology and mechanical properties of surface crusts have been found to vary depending on the different types of evaporite minerals that precipitate at the surface. For example, salt crusts composed of hydrous/anhydrous minerals (e.g., sulphate and carbonate salts) have been witnessed to generate loose crusts that are highly erodible (Bucher and Stein, 2016; Nield *et al.,* 2016a). By contrast, sodium chloride-rich evaporites have been found to reduce the potential for dust emission by forming hard, cemented layers composed of interlocking crystals that play a stabilising role in protecting the playa surface against wind erosion (Nickling and Ecclestone, 1981; Bullard *et al.,* 2011). In the context of dust emissions a

potentially more important factor than mineralogy is the interlocking nature of precipitated crystals (Gillette *et al.,* 2001; Nachshon *et al.,* 2011; Lee and Kurtis, 2017; Zhang, Z. *et al.,* 2018; Zhang *et al.,* 2021). In a study at the Salton Sea (USA), Buck *et al.* (2011) noted that the specific crystal habits (i.e., the size and shape of the crystals) and degree of interlocking crystals, rather than the chemical composition of the surface salt crust, played the greatest role in affecting dust emissions. Thus, the presence or absence of salt crusts as well as the mineralogical composition and interlocking nature of the precipitated crystals play a significant role in determining sediment erodibility by wind (Goudie, 2018). Given the high solubility of salt minerals, these crust variables are dynamic and heterogenous in both space and time (Buck *et al.,* 2006, 2011), influenced by changing surface moisture regimes and local climate conditions (Nield *et al.,* 2016a,b; Dai *et al.,* 2022).

While a few relevant studies have established the presence of evaporite minerals at Etosha Pan (e.g., Herdtfelder, 1984; Buch and Rose, 1996; Bhattachan *et al.,* 2015, Li *et al.,* 2018), the relationship between the mineralogical and physical crust composition, surface erodibility and dust emissions is not known. Since dynamic surface erodibility, potentially linked to surface crust mineralogy and morphology, is an important influence on the occurrence of dust emission, it is necessary to identify the specific minerals that make up the surface of Etosha Pan, monitor how the surface mineralogical and morphological properties may vary over space and time in response

to changing hydrological and climatic conditions, and establish the potential links to dust emissions.

Therefore, the focus of this chapter is to advance on the remote sensing analyses from Parts 1 and 2 of the thesis and carry out a higher resolution investigation of surface crust geochemistry, hydrological dynamics, and local climate conditions at Etosha Pan. In particular, it aims to utilise a combination of multispectral Landsat OLI time-series data with ground-truth spectroscopic and mineralogical data for the period 2018–2022 to determine the sub-basin level mineralogical, hydrological and climatological controls on sediment availability that make specific surfaces on Etosha Pan prone to enhanced dust emissions – so called 'hot-spots' of emission.

The specific research objectives are to:

1) Identify the specific locations and surface properties (i.e., the appearance, colour and texture) of dust emission 'hot-spots' compared with non-emissive surfaces on the pan;
2) Resolve the geochemical properties of emissive 'hot-spots' through spectral signature analysis for mineralogical interpretation of the pan surface and its development over multiple seasons;
3) Examine the surface moisture dynamics, crust and climatological conditions surrounding the development and activation of emissive 'hot-spots'.

6.2. Data Sources and Methods

6.2.1. Identification of 'hot-spot' emissive surfaces

For the initial identification of highly emissive dust 'hot-spots' at Etosha Pan, statistical point pattern analysis (nearest neighbour ratio; Kandakji *et al.,* 2020) was performed to identify significant clusters of dust emission events from spatially-referenced dust plume source frequencies derived from associated analyses of MSG-SEVIRI and MODIS data (see section 5.2.1). However, due to their moderate (500 m – 3 km) spatial resolutions, further detailed investigation of the specific properties of these dust 'hot-spot' surfaces is challenging using MSG-SEVIRI or MODIS data (Muhs *et al.,* 2014).

In contrast, NASA's Landsat-8 and 9 polar-orbiting satellite missions offer a consistent source of multispectral imagery at moderate-high spatial resolution (30 m) and temporal resolution (8 days) to inspect emissions source characteristics at an unprecedented level of detail (von Holdt *et al.,* 2017, 2019; Bakker *et al.,* 2019; Baddock *et al.,* 2021). Accordingly, satellite imagery collected from the Landsat 8–9 Operational Land Imager (OLI) sensors (available from 2013 and 2021 – present day, respectively) were used to examine the specific surface characteristics of highly emissive 'hot-spot' dust source locations compared with non-emissive surfaces and to determine if and how they might change in relation to dust emission dynamics.

Level-2 Landsat 8-9 OLI data were acquired through the USGS Earth Explorer data portal (www.earthexplorer.com). A total of 74 cloud-free Landsat 8-9 OLI images spanning the austral winter dry seasons (March – October) between 2018 and 2022 were used to produce true-colour (bands 4, 3, 2) and false-colour composite (bands 5, 4, 3) image time-series over the pan. Such band combinations have been shown to enhance detection of changes in the physical and chemical properties of surface sediments based on their spectral characteristics in the visible–near infrared (VNIR) wavelengths (Korsman *et al.,* 1999; Zander *et al.,* 2022). The image time-series were analysed by visual interpretation to identify changes in the appearance (i.e., in colour and texture) of the surface prior to, during, and following dust emission events from 'hot-spot' regions compared with non-emissive 'control' surfaces.

6.2.2. Geochemical analysis of 'hot-spot' emissive surfaces

In order to investigate the potential mineralogical changes in surface sediment distributions and crust dynamics associated with the development of dust emission 'hot-spots', geochemical analyses of the pan surface were performed by spectral signature analysis of the moderate spectral resolution Landsat 8-9 OLI satellite time-series data. Such analyses were validated with ground-truth spectroscopic and mineralogical data collected during the austral winter dry seasons from 2018 to 2022.

In contrast to traditional field and laboratory methods for the analysis of sediment mineralogy, reflectance spectroscopy offers a rapid, inexpensive and non-destructive

tool for investigating playa crust and near-surface sediment mineralogical properties (Kruse, 1988; Kodikara *et al.,* 2012; Hamzehpour and Marcolli, 2024). In the visible and shortwave infrared wavelength region (0.4 – 2.5 μm), various iron-, hydroxyl-, sulphate-, carbonate- and water-bearing minerals exhibit diagnostic spectral properties (Hunt and Salisbury, 1970, 1971; Hunt, 1977, 1979; Clark and Rencz, 1999; Kokaly *et al.,* 2017). The spectral features (i.e., position, shape, depth and width) can be explained by the characteristic absorption of electromagnetic energy that is controlled by the chemical structure of the material (Crowley, 1991; van der Meer, 2001; Xu *et al.,* 2022). These spectral properties are used to identify the type of mineral and estimate its abundance in the soil mixture by reflectance spectroscopy in the laboratory and remote sensing (imaging spectrometry) by airborne and spaceborne sensors (Drake, 1995; Ben-Dor *et al.,* 2009; Kodikara *et al.,* 2012; Milewski *et al.,* 2017, 2019).

Analysis based on remotely-sensed spectral reflectance observations offers the capability for fast and cost-effective mapping of surface mineral distributions and their study over time (Goetz *et al.,* 1985; Kruse and Perry, 2013; Peyghambari and Zhang, 2021). This approach has long proved useful for mapping the predominant mineralogies and depositional environments of desert playas and can offer insight into the geochemical and hydrological controls on playa mineral and surface crust development (Crowley, 1991; Bryant, 1996; Milewski *et al.,* 2020).

Previous studies have utilised both airborne and spaceborne hyperspectral optical sensors (e.g., AVIRIS and EO-1 Hyperion, respectively) for the analysis and mapping of playa crust mineralogy, which provide high spectral resolution imagery periodically for improved discrimination and quantification of complex mineral assemblages (Hubbard and Crowley, 2005; Kodikara *et al.,* 2012; Milewski *et al.,* 2017). However, the availability of multitemporal hyperspectral data over Etosha Pan is presently limited.

Recent advances have led to the development of a wide range of spaceborne imaging spectroscopy missions to provide extensive hyperspectral data to research and application communities (Rast and Painter, 2019). Examples include NASA's Earth Surface Mineral Dust Source Investigation (EMIT; launched on July 14, 2022), a hyperspectral sensor mounted to the exterior of the International Space Station (ISS) with the direct mission objective to determine the mineral composition of natural dust production sources around the world (Green *et al.,* 2019, 2023). In addition, the next generation of hyperspectral satellite programmes, such as the Precursore IperSpettrale della Missione Applicativa (PRISMA; launched on March 22, 2019) (Cogliati *et al.,* 2021) and the ESA's Copernicus Hyperspectral Imaging Mission (CHIME; launch scheduled for 2028) (Nieke and Rast, 2018; Nieke *et al.,* 2023), are designed to operationally acquire hyperspectral imagery over large areas on a frequent (sub-monthly) and consistent basis. The technical developments of these contemporary and

upcoming sensor platforms will offer new opportunities for improved characterisation and monitoring of complex playa mineralogies and their dynamics over time.

Presently, multispectral optical sensors, such as Landsat 8-9 OLI, commonly revisit the same location within weeks and offer moderate to high spatial resolution data on a global scale, which allow seasonal to sub-monthly updates of surface conditions for playa basins worldwide (Kruse and Perry, 2013). This is especially important for monitoring surface crust mineralogy dynamics in relation to dust emissions, and their potential links to climate drivers (Milewski *et al.,* 2020). However, the spectral resolution of data collected from these traditional optical multispectral satellite sensors are orders of magnitude lower than hyperspectral sensors (Milewski *et al.,* 2019; Radwin and Bowen, 2021; Vivone, 2023).

Nevertheless, a large body of research has employed multispectral satellite sensors (e.g., Landsat TM and OLI, Advanced Land Imager [ALI] and Advanced Spaceborne Thermal Emission and Reflectance Radiometer [ASTER]) to map evaporite basins throughout the world and have shown that there is enough spectral information captured within broadband multispectral data to effectively discriminate a number of useful mineralogical crust types on the playa surface (e.g., Chapman *et al.,* 1989; Millington *et al.,* 1987, 1989; Bryant, 1996; Hubbard and Crowley, 2005; White and Eckardt, 2006; Alanazi and Ghrefat, 2013; Li *et al.,* 2014; Bowen *et al.,* 2017; Flahaut *et al.,* 2017; Soltaninejad and Ranjbar, 2018; Gürbüz, 2019; Milewski *et al.,* 2020). In a comparison study, Ghrefat and Goodell (2011) showed that Landsat data are able

to identify general mineralogical land cover classes and produce similar mapping results to high spectral resolution spaceborne Hyperion data when validated with high spectral resolution ground data. Hence, this approach was similarly performed in this study.

Many multispectral methodologies have been developed to map playa surface mineralogy from Landsat data, such as spectral matching or sub-pixel classification (e.g., Chapman *et al.,* 1989; Drake *et al.,* 1994; Bryant, 1996; van der Meer, 2006; Katra and Lancaster, 2008; Kodikara *et al.,* 2012, 2023; Radwin and Bowen, 2021). In this study, a fully constrained linear spectral unmixing method was applied using Landsat 8-9 OLI satellite time-series data to differentiate and quantitatively map the spatial distributions of surface minerals on Etosha Pan over the austral winter dust seasons from 2018 to 2022.

Linear spectral unmixing offers a standard and easily reproducible technique for mapping playa surface mineral distributions from both single date and multi-date imagery that is also capable of determining the proportion (abundance) of different surficial minerals contained within mixed surface sediment assemblages at the sub-pixel level (*c.* < 30 m) (Crowley, 1991, 1993; Settle and Drake, 1993; Drake *et al.,* 1994; Crowley and Hook, 1996; Bryant, 1996; Ferrier *et al.,* 2002; Jin *et al.,* 2019). The use of a "fully constrained" mixture model requires that pure examples of each material component in the mixture must be known in order to fit the pure endmember spectra to the imagery and estimate their proportions in each pixel (Settle and Drake, 1993; Bryant, 1996; Hubbard and Crowley, 2005). After identifying these endmembers

from the image or a spectral library, the linear mixture model is applied by least squares fitting of the endmember spectra to all pixels in the image (Jin *et al.,* 2019). The reflectance of each image pixel is assumed to be a linear combination of the reflectance of each material component (or endmember) present within the pixel according to their respective abundance coefficients (Kodikara *et al.,* 2023).

The identification of spectral endmembers and mapping of evaporite minerals and associated sediments at Etosha Pan by linear spectral unmixing involved the collection of surface sediment samples in the field, their analyses using reflectance spectroscopy and X-ray diffraction, and the processing and interpretation of moderate spectral resolution Landsat 8-9 OLI satellite imagery.

Field Sampling

Surface sediment samples were acquired from associated research on Etosha Pan in July and September 2018 and from a fieldwork campaign conducted in September 2022 (see Figure 6.4 for ground sample locations). A total of 20 sediment samples comprised of surface crust (upper 2 cm), subsurface (2 – 5 cm depth) and surface ripple features were collected from a single emissive 'hot-spot' sample site located in the pan centre both during (July) and towards the end (September) of the austral winter dust season in 2018 and from five sample sites situated along a transect in the southern portion at the end of the winter dust season in September 2022. The five sample sites from the 2022 field campaign were strategically selected based upon remote sensing analyses conducted in earlier chapters of this research to ensure that they

demonstrated the potential range of hydrological contexts (i.e., frequently wetted and/or flooded to dry and hard salt crust surfaces), surface emissivities (i.e., non-emissive to highly emissive 'hot-spot' regions), and climatological environments. This ensured that field samples represented much of the variability of surface conditions and presumed sediment mixtures on the pan but was also achievable given the accessibility constraints for investigation across an extensive and physically challenging field environment.

Spectral Reflectance Analysis

Reflectance spectra of field samples were acquired using the Analytical Spectral Devices (ASD) FieldSpec Pro FR spectroradiometer (Malvern Panalytical Ltd., Malvern, UK) under controlled laboratory conditions. The ASD FieldSpec Pro is a portable field/laboratory instrument, which registers reflected radiation in the visible-near infrared (VNIR) to shortwave infrared (SWIR) spectral range between 350 nm and 2500 nm (Malvern Panalytical, 2022).

In the laboratory, the collection of sediment sample spectra was performed using the ASD High-Intensity Contact Probe (CP; direct contact with the soil) to mitigate potential errors associated with changing illumination and atmospheric variables. The ASD CP setup houses a 100 W reflectorised halogen lamp aligned at 12° to the probe body and an aperture for a fibre-optic measurement cable aligned at 35° to the probe body. The sensed spot has a diameter d_{probe} = 1.1 cm with a field-of-view (FOV) = 1.33 cm^2 (Malvern Panalytical, 2022).

Powdered samples (particle size < 2 mm) of surface crust and near-surface sediments pertaining to individual sample sites were each placed in a glass petri dish and the ASD CP was put in direct contact with the sediment, followed by registration of the spectrum. Each measurement was repeated five times for each sediment sample and then averaged to produce a representative spectrum per sample, thus ensuring a higher signal-to-noise ratio. Between each sediment sample, the spectroradiometer was calibrated using a Spectralon® diffuse reflectance plate. The position, shape, depth and width of absorption features in each sample spectra were used to identify mineral phases in the field samples based on close correspondence with laboratory spectra of 'pure' mineral types contained with the US Geological Survey (USGS) Spectral Library (Kokaly *et al.,* 2017).

X-Ray Diffraction Analysis

The mineralogical interpretation of the reflectance spectra from the field samples was verified using X-ray diffraction (XRD) analysis. XRD analyses were carried out by J. Azain and J. Leidelmeijer at the US Geological Survey (USGS) Geology, Geophysics, and Geochemistry Science Center. The sediment samples were air-dried and passed through a 2 mm sieve and the XRD analyses were performed by step scanning using a X'Pert PRO diffraction system (PANalytical BV, Almelo, the Netherlands). The diffraction patterns of the samples were interpreted using the High Score software (PANalytical BV), which allowed the qualitative phase composition and the quantitative mineralogical composition of each sample (in weight %) to be determined.

Spectral Endmember Definition

The mineralogical content and associated target spectra (endmembers) from XRD analysis and ground-based spectral reflectance analysis of surface sediment samples obtained in July and September 2018 provided the necessary training data set to calibrate the linear spectral unmixing model for mapping surface sediment distributions at Etosha Pan. A total of nine mineral types were identified from the spectral and chemical analyses. Detailed mineral characterisations of individual field samples collected in 2018 are given in Table 6.1.

Table 6.1. X-ray diffraction (XRD) results for Etosha sediment samples obtained in July and September 2018. For the location of ground sample points, see Figure 6.4.

Mineral	Sample ID					
	July 2018			September 2018		
	CS	SS	RS	CS	SS	RS
	% (v/v)					
*Analcime ($NaAlSi_2O_6{\cdot}H_2O$)	28.4	45.6	46.5	24.0	45.0	11.0
Calcite ($CaCO_3$)	17.8	30.8	34.9	2.0	6.0	13.0
Gypsum ($CaSO_4{\cdot}2H_2O$)	1.0	2.2	–	1.0	–	–
Halite ($NaCl$)	43.9	8.7	6.1	36.0	0.0	3.0
Montmorillonite $[(Na,Ca)_{0.33}(Al,Mg)_2Si_4O_{10}{\cdot}n(H_2O)]$	–	6.0	7.0	Trace	15.0	10.0
Muscovite $[(Kal_2(AlSi_3O_{10})(F,OH)_2]$	1.1	1.6	1.8	37.0	25.0	45.0
Saponite $[(\frac{1}{2}Ca,Na)_{0.33}(Mg,Fe^{+2})_3(Si,Al)_4O_{10}(OH)_2{\cdot}4H_2O)]$	7.8	5.0	3.7	Trace	6.0	18.0
Thenardite (Na_2SO_4)	Trace	Trace	Trace	–	3.0	–
Trona ($Na_3(CO_3)(HCO_3){\cdot}2H_2O$)	Trace	Trace	Trace	–	–	–

CS = Crusted surface (0 – 2 cm depth); SS = Soft subsurface (2 – 5 cm depth); RS = Rippled surface features.
*Minerals undetected by reflectance spectroscopy.

XRD analyses of sediment samples found an upper surface that comprised an efflorescent salt crust composed of evaporite mineral deposits, which included halite ($NaCl$), calcite ($CaCO_3$), gypsum ($CaSO_4 \cdot 2H_2O$), thenardite (Na_2SO_4) and trona ($Na_3(CO_3)(HCO_3) \cdot 2H_2O$), and the hydrated phyllosilicate muscovite (mica group) [$(Kal_2(AlSi_3O_{10})(F,OH)_2$]. Surface crusts were underlain by fine grain subsurface sediments low in organic matter and composed of varying mixtures of analcime (zeolite) ($NaAlSi_2O_6 \cdot H_2O$), clay silicate minerals saponite [$(\frac{1}{2}Ca,Na)_{0.33}(Mg,Fe^{+2})_3(Si,Al)_4O_{10}(OH)_2 \cdot 4H_2O$)] and montmorillonite [$(Na,Ca)_{0.33}(Al,Mg)_2Si_4O_{10} \cdot n(H_2O)$], muscovite [$(Kal_2(AlSi_3O_{10})(F,OH)_2$], and calcite ($CaCO_3$) crystals. Surface ripple features formed from abraded surface crusts were composed of varying mixtures of the evaporite, clay and rock-forming silicate mineral deposits.

Figure 6.1 displays the spectral properties of eight mineral phases identified from the 2018 field samples that were incorporated as endmembers in the linear spectral unmixing model. Also presented are the water absorption features and the relative positions and resolutions of relevant Landsat 8–9 OLI bands in the VNIR–SWIR wavelengths. Since negligible traces of the evaporite mineral trona were found in the field samples, it was not incorporated as a mineral endmember in the linear spectral unmixing model.

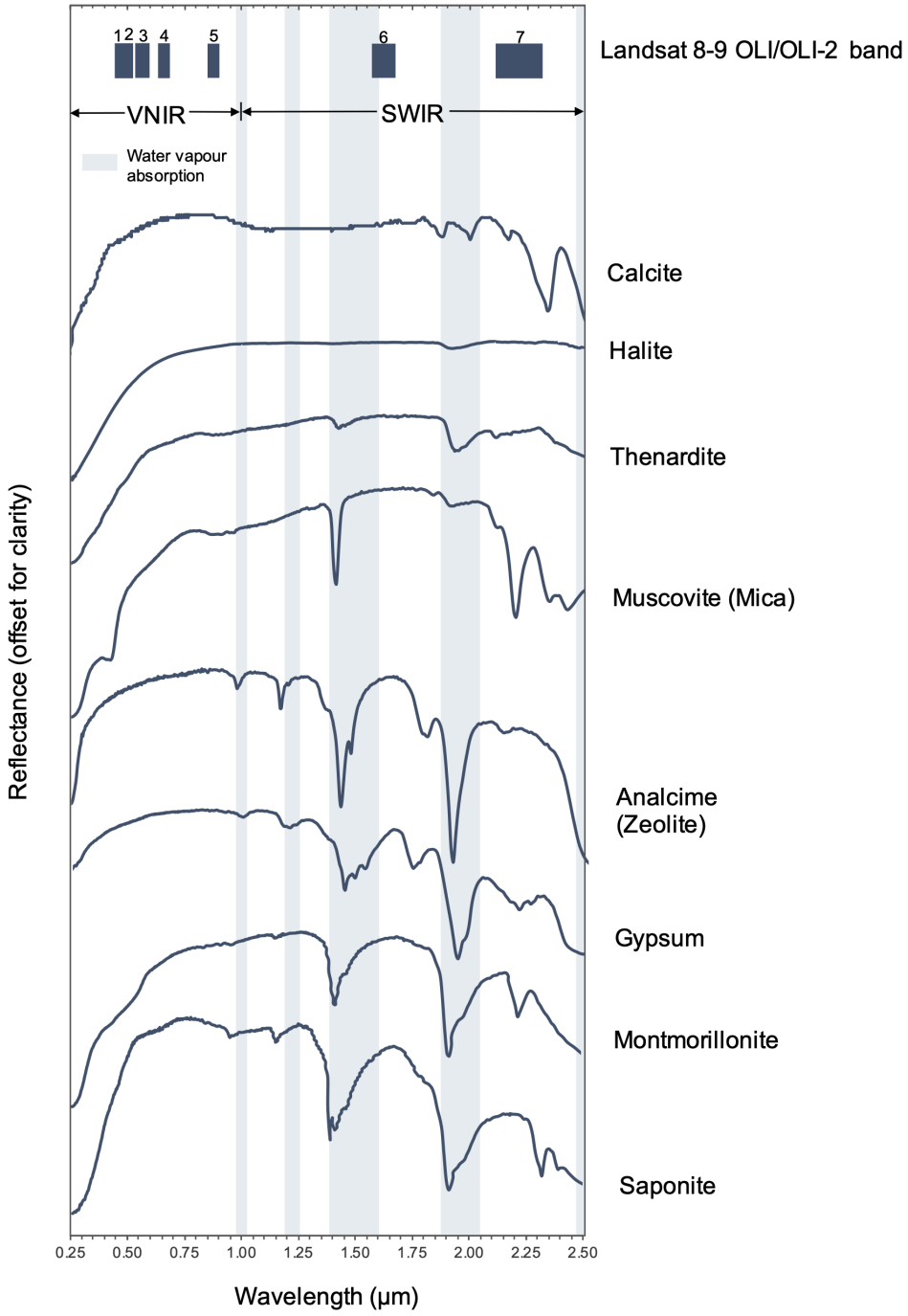


Figure 6.1. VNIR – SWIR reflectance spectra for the eight mineral phase spectral endmembers identified from field samples at Etosha Pan correlated with the spectral resolution and wavelengths of the Landsat 8-9 OLI sensors. Spectra are offset vertically for viewing purposes. Grey bars indicate locations of atmospheric absorption bands. Reference mineral spectra sourced from the USGS Spectral Library (Kokaly *et al.*, 2017).

Although reference spectra for the selected mineral endmembers identified in Figure 6.1 are found in the USGS Spectral Library, they do not account for any moisture found in field samples or spectral mixing of endmembers (Kokaly *et al.,* 2017; Radwin and Bowen, 2021). Nevertheless, assessment of endmember spectral characteristics helped to inform, produce, and interpret the linear spectral unmixing model to quantitatively map the range of mineral phases on the surface of the playa from Landsat 8–9 OLI image time-series.

Mineral Mapping with Landsat 8-9 OLI Satellite Sensor Imagery

Linear spectral unmixing was used to map the presence and relative abundances of the eight mineralogical endmembers (Figure 6.1) from pixel spectra of the Landsat 8-9 OLI image time-series of the pan surface across austral winter dry seasons from 2018–2022. Figure 6.2 displays a schematic diagram illustrating the image processing workflow implemented in this study.

Prior to the unmixing procedure, the Normalized Difference Vegetation Index (NDVI) (Rouse *et al.,* 1973) and Modified Normalized Difference Water Index (MNDWI) (Xu, 2006) were first used to isolate and mask vegetation and surface water (Figure 6.2). A standard NDVI threshold of 0.2 was selected to detect shrub and other vegetation surrounding the pan (Gandhi *et al.,* 2015). Thresholds for MNDWI were chosen by referencing previous research conducted on Etosha Pan and other smaller pans in the Cuvelai-Etosha Basin (Hamunyela *et al.,* 2022).

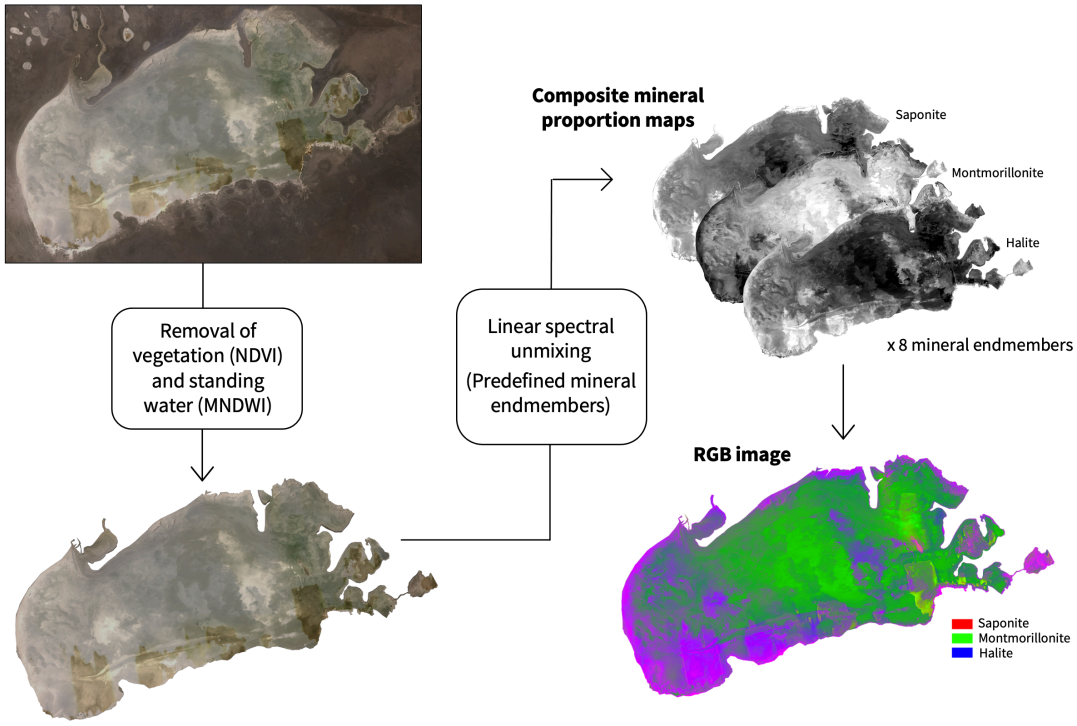


Figure 6.2. Workflow diagram illustrating the processing pathway for the production of mineral proportion maps and RGB images using a fully constrained linear spectral unmixing method on Landsat 8–9 OLI satellite time-series data.

The mixture model was then constrained by least squares fitting of the spectral characteristics of each unmasked image pixel with the 'pure' library spectra (endmembers) of the eight mineral phases from the USGS Spectral Library for the 7 spectral bands in the VNIR–SWIR range of Landsat 8–9 OLI sensors (Figure 6.1). In doing this, proportion estimates for each of the eight mineral endmembers in each pixel were forced to sum to 100 per cent (Bryant, 1996). This enabled the generation of surface compositional map time-series displaying the relative proportions of selected minerals found in the Landsat 8–9 OLI image time-series, where the reflectance values (brightness) of each of the eight mixture model band outputs represented the scaled relative abundance (0 – 100) of each mineral (Figure 6.2).

These output images were used to generate RGB composite image maps, where relative proportions of selected minerals of interest were rendered through the red (R), green (G), and blue (B) channels of the image composite using a linear contrast stretch (Figure 6.2). The RGB composite maps allowed areas of mineralogical mixing to be mapped over space and time.

Mixture Model Validation

Validation of the linear spectral unmixing technique was performed through comparisons of mixture model map outputs with ground reference data. Surface sediment samples collected from five different sites on the pan in September 2022 were used for this purpose. Mineral abundances derived from X-ray diffraction (XRD) analysis of field samples were compared statistically (Linear Regression) with mineral proportion estimates for corresponding image pixel locations derived from the linear mixture model output for one specific Landsat OLI scene of the pan surface captured promptly after field sample collection.

Regression plots showing the correlation between linear spectral mixture model proportion estimates and the observed abundances for each of the eight mineral phases are presented in Figure 6.3. Upon comparison it is observed that the proportion estimates of mineral endmembers on the mixture model map output show good correspondence to the mineral abundances estimated from XRD analysis of field samples, with the coefficient of determination (R^2) greater than 0.7, which is significant at the 0.001 confidence level (Figure 6.3a).

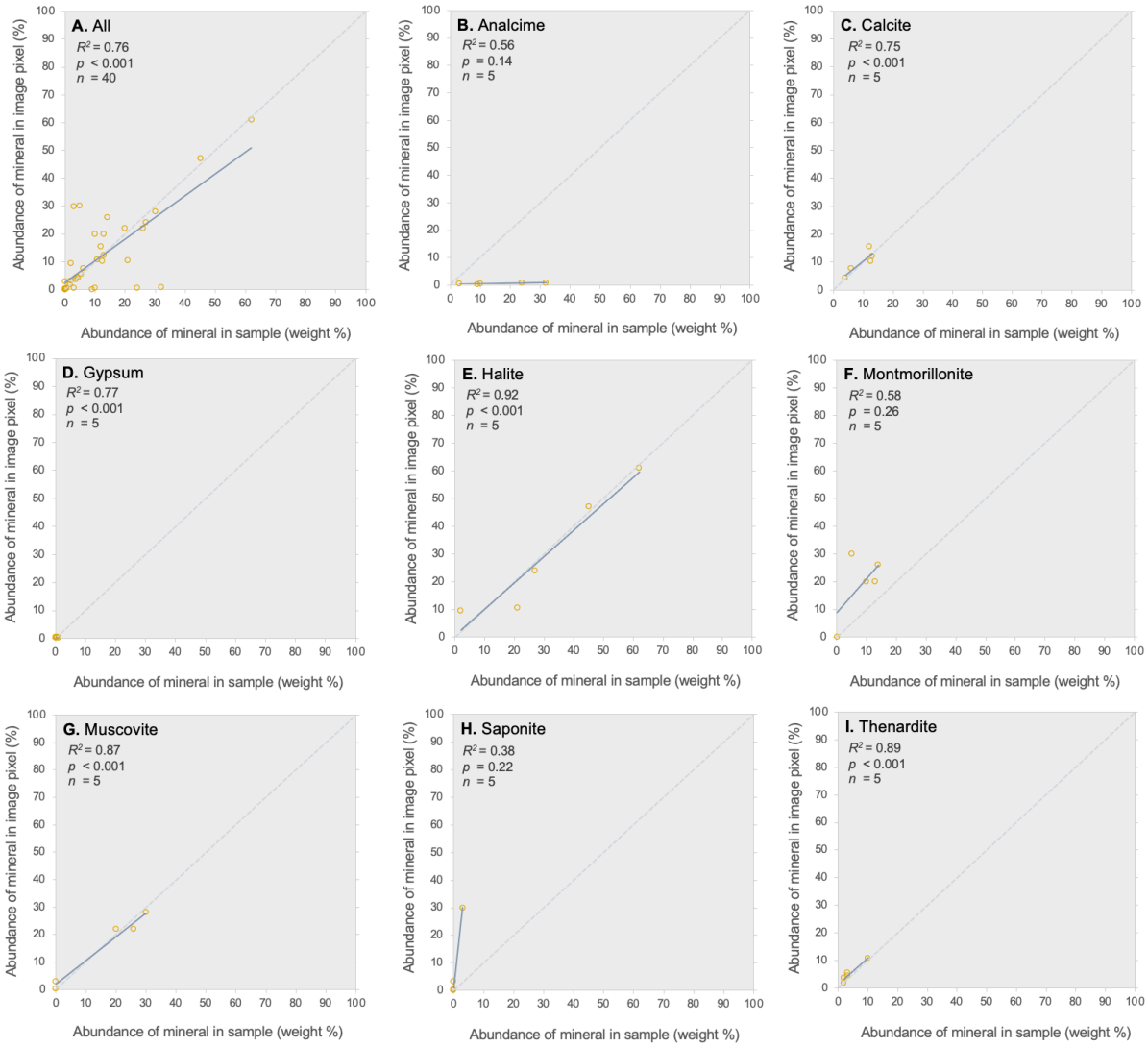


Figure 6.3. Scatterplots of predicted mineral abundances based on pixel values from linear spectral unmixing of image data and the measured (XRD) mineral content (weight %) of ground samples collected in September 2022 for (a) all mineral endmembers, (b) analcime, (c) calcite, (d) gypsum, (e) halite, (f) montmorillonite, (g) muscovite, (h) saponite, and (i) thenardite mineral endmembers. The dashed line represents 1:1 of predicted vs. measured results and the solid line represents the outcome of linear regression. For the location of ground sample points, see Figure 6.4. For detailed mineralogical (XRD) results for surface crust and near-surface sediment samples acquired in September 2022, see Table 7.3 (Chapter 7).

The performance of the linear spectral unmixing technique presented in this research for mapping pan surface minerals is comparable to previous studies (Bryant, 1996; White and Eckardt, 2006; Jin *et al.,* 2019; Milewski *et al.,* 2019). Using a linear spectral unmixing analysis technique at the Chott el Djerid salt playa in Tunisia, Bryant (1996) found correlations between proportions extracted from multispectral Landsat TM imagery and XRD mineralogy of surface samples for gypsum ($R^2 = 0.835$, $p < 0.001$) and halite ($R^2 = 0.935$, $p < 0.001$) endmembers.

The results from this research suggest that the linear spectral unmixing technique can be successfully used to estimate mineral abundances on Etosha Pan from multispectral Landsat OLI imagery. However, the performance of the linear mixture model varies depending on the mineral of interest (Figure 6.3b-i). The results show that the parameters provide the strongest estimates for halite ($R^2 = 0.92$, $p < 0.001$) and thenardite ($R^2 = 0.89$, $p < 0.001$) and the weakest performance for analcime (zeolite) ($R^2 = 0.56$, $p = 0.14$), montmorillonite ($R^2 = 0.58$, $p = 0.26$), and saponite ($R^2 = 0.38$, $p = 0.22$).

The regression plots in Figure 6.3 indicate that predictions based on linear spectral unmixing of image data consistently underestimate abundances of analcime (zeolite) and consistently overestimate abundances of montmorillonite and saponite compared with measured (XRD) results. This may in part reflect an inherent assumption of the semi-quantitative analysis technique. Based on reflectance spectroscopy, the linear

spectral unmixing method determines the mineralogical properties of sediment based exclusively from the spectral characteristics of the readily-observed external surface of sediment particles (Settle and Drake, 1993; Bryant, 1996; Ferrier *et al.,* 2002). From X-ray diffraction (XRD) analysis conducted in this study and preliminary energy-dispersive X-ray analysis with a Scanning Electron Microscope (SEM-EDX) performed by G. Breit at the USGS, it was found that montmorillonite and saponite produced a coating around the analcime (zeolite) particles that formed the bulk mineralogy of surface ripple and subsurface field sediment samples (Table 6.1) (Breit, 2022; personal communication). This montmorillonite and saponite coating may have obscured the analcime (zeolite) absorption features in both the field sample and image pixel reflectance spectra. Hence, it is possible that the linear spectral unmixing technique misclassified the concealed analcime (zeolite) mineral contents of sediment particles as montmorillonite and saponite, which were more readily-detected by spectral analysis.

Nevertheless, these errors were deemed acceptable for the purpose of this study, which seeks to examine the general surface sediment distribution across Etosha Pan over time rather than provide a specific quantification of mineral abundances for sediment particles. Provided the knowledge that montmorillonite and (or) saponite mineral estimates may also consist of analcime (zeolite) minerals is recognised in the interpretation of composite mineral proportion maps generated by spectral unmixing.

Overall, the validation results suggest the linear spectral unmixing technique is able to successfully map the predominant mineralogies present at Etosha Pan. However, the performance of the linear spectral unmixing technique remains limited by the spatial and spectral resolutions of the imagery and may be compromised by changes to surface mineralogy, moisture variability, atmospheric absorption, illumination conditions, sensor viewing geometry, and the presence of minerals other than the chosen endmembers (Ferrier *et al.,* 2002; Kruse and Perry, 2013; Radwin and Bowen, 2021). Hence, the presented composite mineral proportion maps generated by spectral unmixing, although useful for monitoring the general geochemistry through time and determining its potential influence on dust emissions, should be used with discretion (Kodikara *et al.,* 2012; Milewski *et al.,* 2019).

6.2.3. Determining the hydrological and climatological conditions on emissive and non-emissive surfaces

To determine the hydrological and climatological influences on pan surface properties, the satellite image and RGB composite mineral map time-series were compared with corresponding satellite-retrieved surface wetness data and climate variables for the 2018–2022 research period. Daily surface inundation extent and frequency time-series derived from satellite data (see sections 4.2.3 – 4.2.4) were used to discern hydrological contexts (i.e., surface wetting frequencies and time since wetted from ephemeral inundation events, direct precipitation and water table fluctuations) of emissive 'hot-spot' surfaces compared with non-emissive 'control' surfaces.

ERA5-Land reanalysis data from the European Centre for Medium-Range Weather Forecasts (ECMWF) was used to identify the atmospheric processes contributing to the formation of emissive 'hot-spot' surfaces compared with non-emissive 'control' surfaces. Parameters extracted for the analysis of Etosha Pan from 2018 to 2022 included surface air temperature (2 m), dew point temperature (2 m) and horizontal (u) and vertical (v) components of wind (10 m). Relative humidity (RH) was derived from the 2 m surface air temperature (t) and dew point temperature (t_d) based on the Magnus (1844) formula:

$$RH = 100 \times \left(\frac{e^{\frac{\beta \times t_d}{\lambda + t_d}}}{e^{\frac{\beta \times t}{\lambda + t}}} \right) \quad (6.1)$$

where RH, in percent, is a function of t and t_d in degrees Celsius, and the revised Magnus coefficients $\beta = 17.625$ and $\lambda = 243.04°$ C (Alduchov and Eskridge, 1996; Lawrence, 2005; Mateus *et al.,* 2021). Wind speed (ws), in m s^{-1}, was calculated as the square root of the sum of the squared u and v components at each model grid point ($ws = \sqrt{u^2 + v^2}$). Hourly estimates for each climate parameter were then aggregated to generate daily mean time-series of climate conditions.

Daily time-series of surface hydrology and climate factors were compared with satellite image and spectral unmixing map time-series to determine potential links with changes in the pan surface (e.g., in colour, texture and geochemistry) prior to, during and following the initiation of dust emission events.

6.3. Results and Discussion

6.3.1. Identification of 'hot-spot' emissive surfaces

Statistical point pattern analysis of spatially-referenced dust plume source frequencies for the 2018 to 2022 observation period enabled the identification of significant clusters of dust events at the sub-basin scale. It was found that individual dust plume events typically occurred from a multitude of point sources that consistently originated from specific areas toward the central region of Etosha Pan (Figure 6.4; see also Figure 5.12, Chapter 5).

These intense localized dust production areas, which have commonly been termed 'hot-spots' for dust emission (Gillette, 1999), emerged as visually-distinctive features on the pan surface when displayed using Landsat 8–9 OLI false-colour satellite image composites. Selected image comparisons displayed in Figure 6.4a show the occurrence and distribution of dust plumes sourced from these 'hot-spots' (outlined) during the emissive dry seasons in 2018, 2019 and 2022, which appear to differ in colour and texture from the surrounding pan surface in the false-colour satellite imagery. These 'hot-spot' regions were markedly absent during non-emissive (control) dry seasons in 2020 and 2021 (Figure 6.4b).

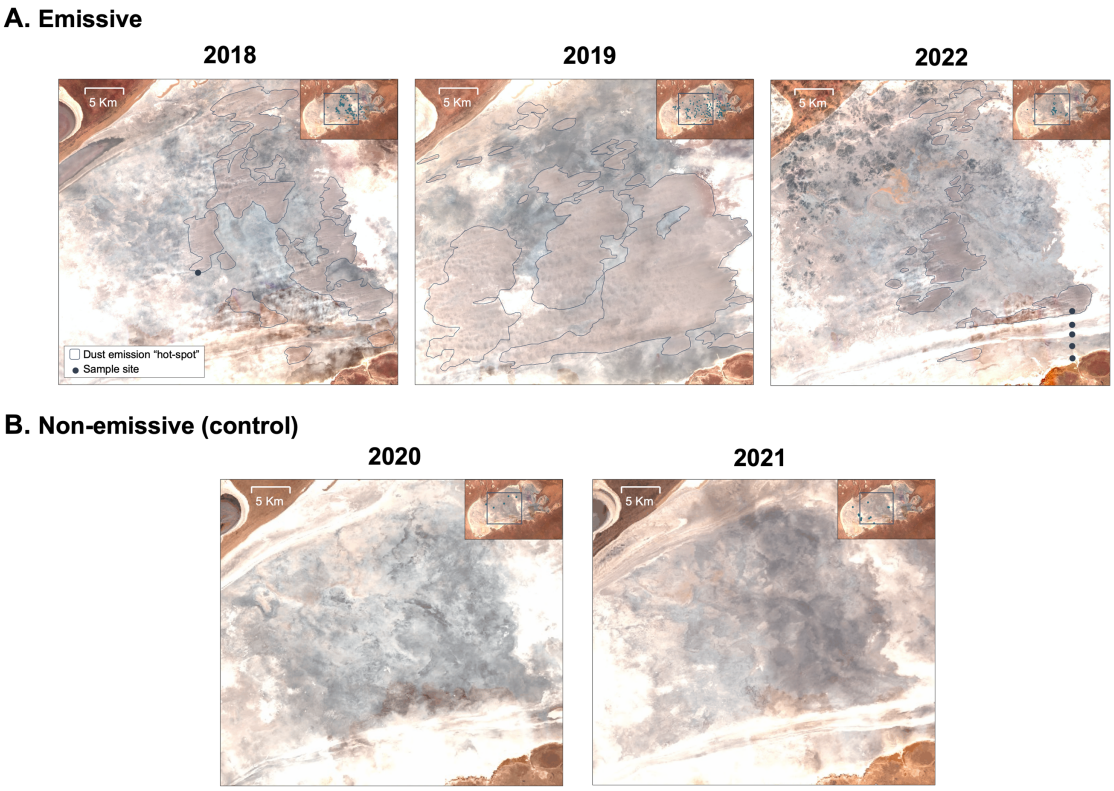


Figure 6.4. Landsat 8-9 OLI false-colour (bands 5, 4, 3) image composites of Etosha Pan showing (a) the occurrence and distribution of dust plumes sourced from emission 'hot-spots' (outlined in navy) during emissive dry seasons in 2018, 2019 and 2022 compared with (b) non-emissive (control) dry seasons in 2020 and 2021. **Note:** Map insets show dust plume events identified at the pan-scale using MODIS and MSG-SEVIRI datasets for respective years (see Chapter 5).

Comparisons of false-colour image time-series of the pan surface at the end of the austral summer wet season and across the austral winter dry season (March to October) from 2018 to 2022 in Figure 6.5 provide an opportunity to observe the occurrence and evolution of these 'hot-spot' surfaces prior to, during, and following dust emission events.

During the emissive years of 2018, 2019 and 2022, moisture on the pan surface began to dry at the end of the wet season in March and the pan surface appears light grey-blue in colour in the earlier time-slices of the false-colour imagery (Figures 6.5a,b,e,

respectively). Further into the austral winter dry season in the months of April to June, much of the surface appears to have dried, emphasised by the reduction in surface water extents within floodwater channels situated in the northern and southern regions of the pan. This period was also characterised by the concurrent emergence of brown patches on the pan surface that were visually distinctive from the local surroundings in the false-colour imagery during emissive years (Figure 6.5a,b,e).

Satellite observations captured throughout the dry season confirm that it was these brown coloured surfaces that represented the 'hot-spot' regions generating dust emissions from Etosha Pan. A total of 91 observed dust emission days were recorded during the 2018–2022 analysis period, the majority (83 dust days) associated with dust plumes sourced from isolated dust emission 'hot-spot' regions on the pan surface. Landsat 8-9 OLI images captured on emissive days, such as 5 July 2018 (Figure 6.5a), 25 August 2019 (Figure 6.5b) and 30 June 2022 (Figure 6.5e), show dust plumes originating exclusively from these visually-distinctive emissive surfaces.

The size and distribution of these 'hot-spot' regions on the playa surface were not consistent between emissive years (Figure 6.4a; Figure 6.5a,b,e). For instance, emissive 'hot-spot' surfaces for the 2019 dust season extended up to 30 km in diameter, which were greater in extent compared with those observed during the 2018 and 2022 dust seasons that on average ranged between 1 and 10 km in diameter.



Figure 6.5. Landsat 8-9 OLI false-colour (bands 5, 4, 3) image composite time-series of surface change at Etosha Pan following the end of the austral summer wet seasons and across the austral winter dry seasons (March to October) of (a) 2018, (b) 2019, (c) 2020, (d) 2021 and (e) 2022. **Note:** The formation of brown patches of emissive sediment surfaces visible in 2018, 2019 and 2022 that are not present in 2020 and 2021.

However, a consistent trend observed across all emissive years was that the areal extents of 'hot-spot' surfaces typically increased following each major dust emission event (Figure 6.5a,b,e). This is highlighted in Figure 6.6, where selected image time-slices illustrate the incremental growth in 'hot-spot' surfaces following two major emission events that occurred during the 2018 dust season.

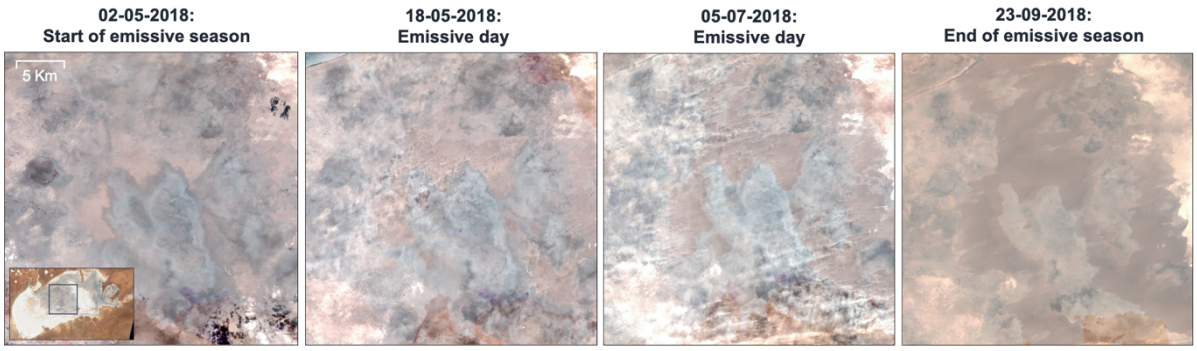


Figure 6.6. Landsat 8-9 OLI false-colour (bands 5, 4, 3) image composites of Etosha Pan showing the increased extents of brown coloured 'hot-spot' surfaces following major dust emission events during the 2018 dry season.

The varying spatial extents of emissive 'hot-spot' surfaces revealed an interdependent relationship with dust emission frequencies, whereby the expansion of 'hot-spot' surfaces following major dust emission events appeared to promote the activation of further dust plumes from these source regions (Figure 6.5a,b,e). The larger total extent of emissive 'hot-spot' features were, in turn, associated with greater dust emissions from the pan. The highest number of dust emission events recorded in 2019 (107 plume events during 54 active dust days) occurred where dust emission 'hot-spots' on the pan surface were most widespread (maximum total surface area: 1,261 km^2), compared with other emissive years where 'hot-spots' were smaller and more closely clustered in

2018 (maximum total surface area: 491 km^2; 42 dust plume events within 25 dust days) and 2022 (maximum total surface area: 95 km^2; 22 dust plume events within 10 dust days).

The Landsat 8–9 OLI false-colour image time-series in Figure 6.5 reveal that by the end of the dust season in September, the brown coloured emission hot-spot regions appeared to have grown in size for all emissive years (2018, 2019 and 2022; Figure 6.5a,b,e). While the later time-slices indicate that by the start of the following wet season commencing in October, the emissive 'hot-spots' were no longer present and the pan surface appears restored to the former light grey-blue colour in the false-colour imagery (Figure 6.5a,b,e).

In contrast, there is no evidence for the presence of emissive hot-spot surfaces developing in non-emissive (control) years 2020 (Figure 6.5c) and 2021 (Figure 6.5d). Rather, during the 2020 and 2021 dry seasons the pan surface maintained a consistent grey-blue appearance in the false colour imagery that underwent relatively minimal change (Figure 6.5c,d). With the exception of the gradual drying of surface moisture and recession of floodwaters at a comparatively slower rate than that observed for emissive years (Figure 6.5a,b,e).

Field observations corroborate the visible differences in the appearance of dust emission 'hot-spots' on the pan surface interpreted from the false-colour satellite imagery. A field photo displayed in Figure 6.7 shows the surface at the sediment sample site

situated on the border of a dust emission 'hot-spot' at the end of the 2018 dust season (see Figure 6.4a for the 2018 sample site location). A clear delineation in the colour and texture of the pan surface was observed between the emissive 'hot-spot' region and the non-emissive surroundings (Figure 6.7).

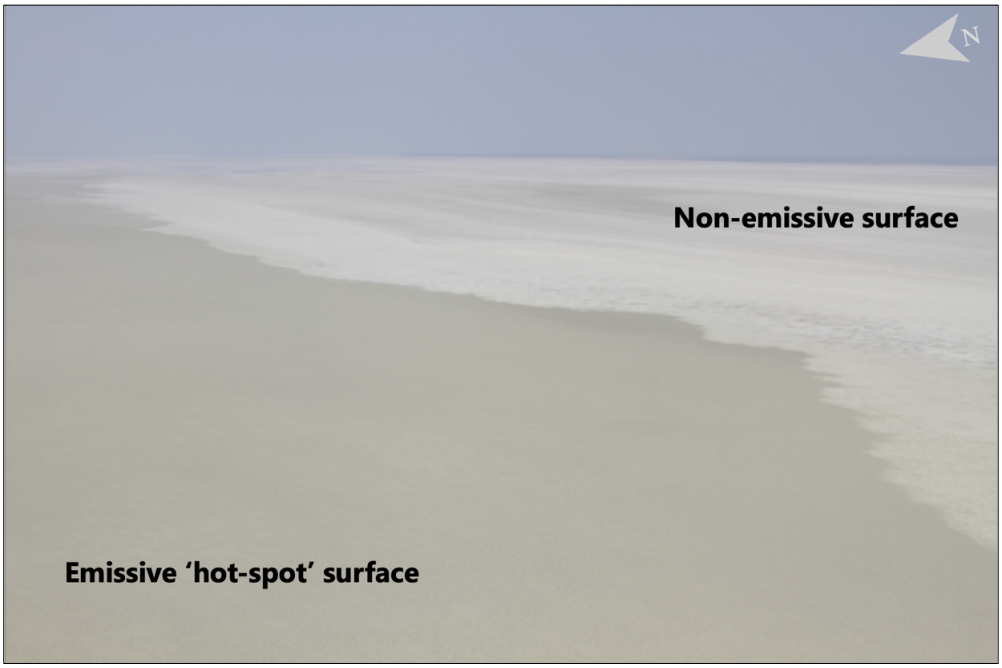


Figure 6.7. Field photo taken from the border of an emissive 'hot-spot' sample site located in the centre of Etosha Pan at the end of the dust season in September 2018 (Photo credit: G. Wiggs, 2018).

Such differences in the appearance of the surface of dust emission 'hot-spot' regions noted from both ground-based and satellite image observations may be clarified through field and satellite-derived mineralogical interpretations of pan surface sediments over time.

6.3.2. Geochemistry of 'hot-spot' emissive surfaces

Comparative examples of RGB composite map time-series showing differences in the distributions of predominant mineral phases: saponite (R), montmorillonite (G) and halite (B), on the pan surface during the emissive 2018 dry season and during the non-emissive 2021 dry season are displayed in Figures 6.8 and 6.9, respectively. For reference, supplementary RGB composite map time-series generated for all years in the 2018–2022 observation period are given in Appendix 2.

Figure 6.8 shows the spatial development of dust emission 'hot-spots' and associated mineralogical changes in time slices throughout the dust season together with the corresponding false-colour images of the pan area. Time slices were selected to allow a good representation of the changing surface properties. The RGB composite maps for the 2018 dust season can be interpreted such that bright shades of blue indicate a halite (evaporite) crust had developed across much of the pan surface at the end of the 2018 wet season (Figure 6.8a). Emerging shades of green in Figures 6.8b–d indicate proportions of montmorillonite (clay) minerals were greater across emissive 'hot-spot' surfaces, particularly following dust emission events, whereas proportions of halite minerals were dominant in surrounding non-emissive regions but were reduced following peaks in dust emissions from 'hot-spot' regions. Such trends were consistent across dry seasons for all emissive years (2018, 2019 and 2022) during the observation period (Figure 6.8; see also Figures A2.1 and A2.3, Appendix 2).

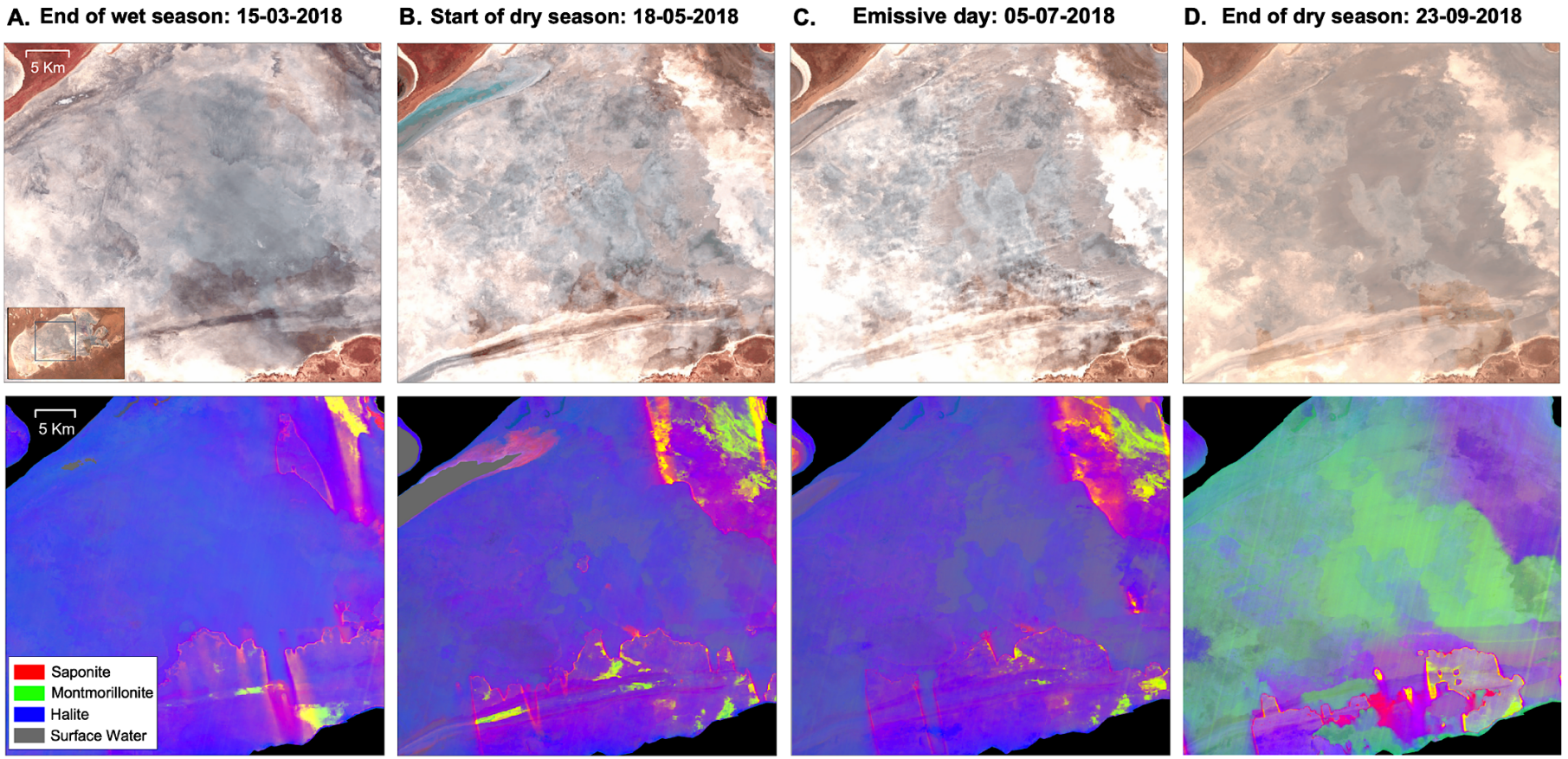


Figure 6.8. Temporal comparisons of Landsat 8-9 OLI false-colour composite (bands 5, 4, 3) images of surface change at Etosha Pan across the 2018 winter dry season showing the development of emissive 'hot-spot' surfaces and linear spectral unmixing model output RGB image composite maps for corresponding image dates, where RGB channels delineate estimates of relative mineral abundances (%) for (R) saponite, (G) montmorillonite and (B) halite minerals, respectively.

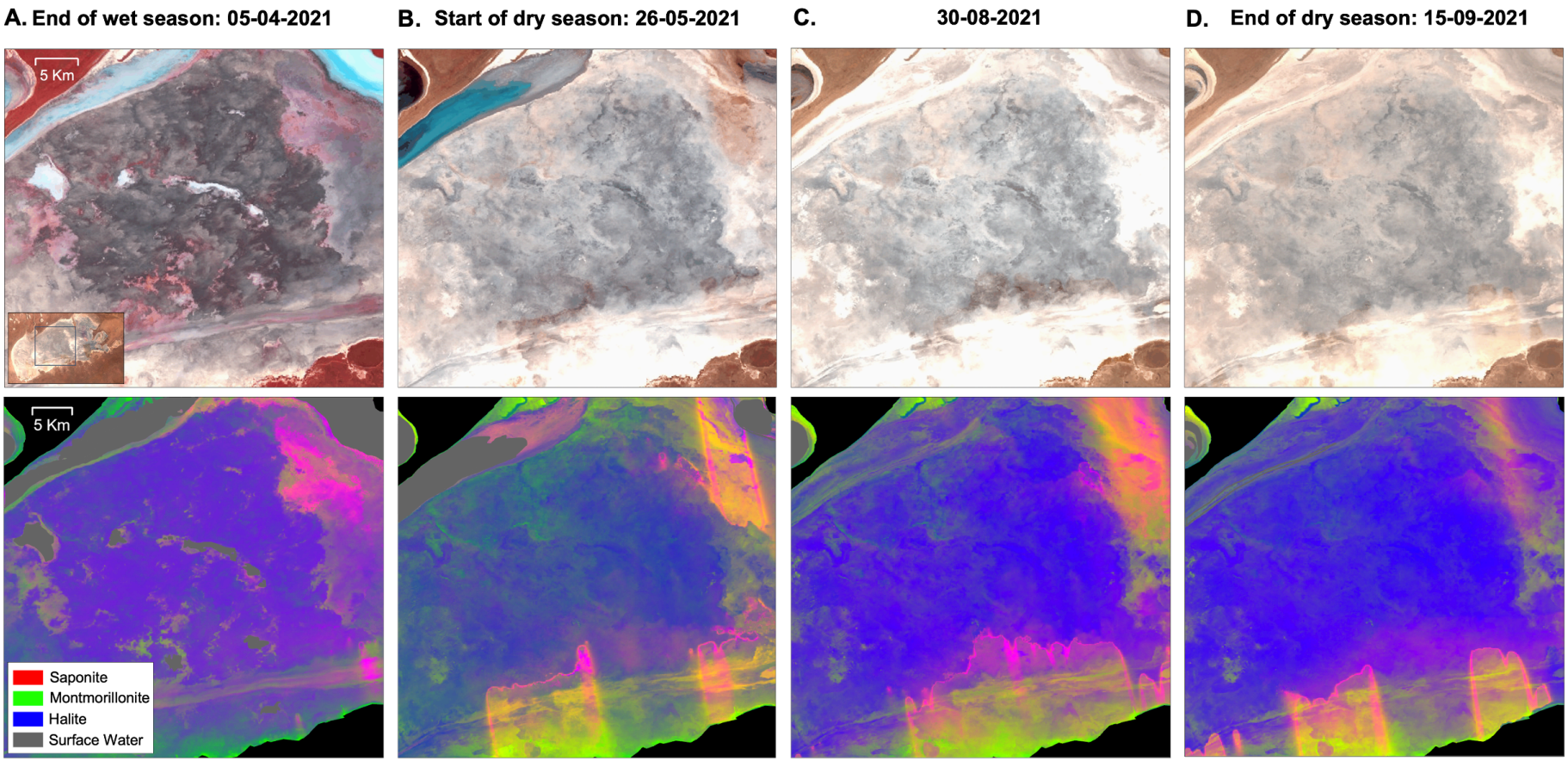


Figure 6.9. Temporal comparisons of Landsat 8-9 OLI false-colour composite (bands 5, 4, 3) images of surface change at Etosha Pan across the 2021 winter dry season and linear spectral unmixing model output RGB image composite maps for corresponding image dates, where RGB channels delineate estimates of relative mineral abundances (%) for (R) saponite, (G) montmorillonite and (B) halite minerals, respectively.

This suggests that what distinguishes emissive 'hot-spot' regions in both appearance and texture from satellite and ground-based observations (Figures 6.4a, 6.5a,b,e, 6.6 and 6.7) was the absence of an evaporite (halite) surface crust, which formed much of the non-emissive surface in the surrounding area. In contrast, the higher proportions of montmorillonite across emissive 'hot-spots' may likely correspond to soft subsurface sediments rich in montmorillonite, saponite, analcime (zeolite) and muscovite minerals (Table 6.1) being exposed to the surface.

The RGB composite map time-series in Figure 6.9 show a divergent mineralogy and pan surface evolution for corresponding time-slices during the non-emissive 2021 dry season. In Figure 6.9a, moisture can be seen on the pan surface with surface water present in isolated regions (grey shaded areas) toward the end of the wet season in April. Dull purple shades indicate a mixed pan surface composition of halite (blue) and saponite (red) minerals in similar proportions. This might suggest a mixed evaporite crust develops, with clay silicate subsurface materials being evident at the surface during the early stages of drying. Figures 6.9b–d show the gradual development of the evaporite crust several months later in the dry season than during emissive years, where bright shades of blue indicate greater proportions of halite across the pan surface that persist throughout August and September (Figure 6.9). This delayed development of a pan-wide halite crust across the surface was similarly observed in the non-emissive 2020 dry season (see Figure A2.2, Appendix 2).

The RGB composite maps indicate that halite ($NaCl$) represented the predominant evaporite mineral phase observed on the crusted surface of Etosha Pan to varying degrees during both emissive and non-emissive years (Figures 6.8 and 6.9). X-ray diffraction (XRD) analysis confirmed halite abundances between 2.0 – 62.0% for crust surface sediment samples acquired in 2018 and 2022 (Table 6.1; Figure 6.3e). Indeed, there have been a small number of studies at Etosha Pan which have similarly pointed to the presence of halite ($NaCl$) and other evaporite minerals in surface sediments and groundwater. Buch and Rose (1996) identified and analysed thin surface crusts along the edge of the pan with an emphasis on investigating deeper Quaternary sediments. By extracting the soluble component from surface crust samples and re-crystalising the brine they obtained stable evaporite phases; principally halite ($NaCl$), thenardite (Na_2SO_4), trona ($Na_3(CO_3)(HCO_3)\cdot 2H_2O$) and hanksite ($Na_{22}K(SO_4)_9(CO_3)_2Cl$) (Buch and Rose, 1996). Herdtfelder (1984) also found halite and thenardite in the region whilst Rahm and Buch (1997) noted strong chemical signatures indicating the presence of sodium (Na), potassium (K), chloride (Cl^-), sulphate (SO_4) and bicarbonate (HCO_3) in Etosha sediments. More recent research by Bhattachan *et al.* (2015) investigated one salt sample from the surface of Etosha Pan and found a clear Cl/SO_4 component, which they suggest derived from sodium chloride (halite) and sodium sulphate (thenardite), and (or) double salts (e.g., sulphohalite). Li *et al.* (2018) investigated deeper groundwaters and obtained samples from both east and west of the pan. Their research focused on characterising the groundwater types in the region but noted the

likelihood of halite and other *Na* phases underlying the pan. It is noted, however, that the mineralogical interpretations presented in these studies were commonly derived from borehole investigations and analyses of surface crusts along the playa margin. By contrast, this study is the first to present the mineralogical compositions of surface crust and near-surface sediments from specific sources of known dust emission located in the centre of Etosha Pan.

With respect to the relationship between salt types and the potential for dust emission, efflorescent crusts composed predominantly of halite (*NaCl*) minerals have received considerable attention (Nickling and Ecclestone, 1981; Langston and McKenna Neuman, 2005; Buck *et al.,* 2011, Nield *et al.,* 2016a,b). They have been found to be widely distributed in many playa dust sources, such as the Omongwa pan in the southern Kalahari (Mees, 1999; Mees and Van Ranst, 2011; Milewski *et al.,* 2017, 2019, 2020), the Bonneville Salt Flats, the Salton Sea, Yellow Lake playa and Owens Lake in North America (Levy *et al.,* 1999; Reynolds *et al.,* 2007, 2009; Buck *et al.,* 2011; Sweeney *et al.,* 2016; Bowen *et al.,* 2017), Kati Thanda-Lake Eyre in Australia (Bowler, 1986; Tweed *et al.,* 2011), the Aral Sea in Central Asia (Mees and Singer, 2006) and Lop Nur Salt Lake in China (Li, R. *et al.,* 2020).

In contrast to sulphate and carbonate salt minerals (e.g., thenardite and trona) that commonly produce "hairy" or "puffy" crusts on the playa surface, which are very soft and porous in texture and have been witnessed to be directly deflated by the wind

(Eswaran, 1984; Teller and Last, 1990; Goodall *et al.,* 2000; Buck *et al.,* 2011), soluble salts (e.g., halite) increase the threshold friction velocity via cementing of sediment particles (Nickling and Ecclestone, 1981; Crowley, 1991; Langston and McKenna Neuman, 2005; Sweeney *et al.,* 2011; Goudie, 2018). However, it has also been observed that halite crusts which are formed directly following a rainfall and (or) flooding event tend to be friable and can produce cracks as they dry; generating aggregates small enough to be transported by the wind and which may act as saltators further disrupting the surface/subsurface sediments, thus facilitating wind erosion (Gillette *et al.,* 2001; Reynolds *et al.,* 2007, 2009; Sweeney *et al.,* 2011).

It is, therefore, possible that the evaporite (halite) surface crust formed at the very start of the dry season (i.e., March to April) directly following ephemeral wetting of the pan surface in the emissive years of 2018, 2019 and 2022 (Figure 6.8a; see also Figures A2.1a and A2.3a, Appendix 2) may potentially be weaker and subsequently more vulnerable to disturbance and deflation by surface winds. This, in turn, might present a potential mechanism by which the breakdown of the surface crust leads to the exposure of isolated regions composed of subsurface sediments rich in silicate minerals at the surface to form the highly emissive 'hot-spot' dust sources observed from both satellite- and ground-based mineralogical investigations (Figure 6.8b,c,e; Table 6.1; see also Figures A2.1 and A2.3, Appendix 2). Whereas the development of the evaporite (halite) surface crust later in the dry season (i.e., June to September) in non-emissive years 2020 and 2021 (Figure 6.9, see also Figure A2.2, Appendix 2) with

a potentially higher halite content (indicated by the brighter blue shades in Figures 6.9c,d, for example) may reflect a more resistant surface to aeolian erosion and thus reduce the emissivity potential.

Satellite and ground-based investigations of the pan surface morphology and geochemistry indicate that dust emission 'hot-spots' are associated with changing surface mineralogy characteristics, potentially linked to the breakdown of an evaporite (halite) surface crust. Indeed, the desiccative formation and subsequent disturbance of evaporite surface crusts has long been observed as a key mechanism governing the potential for dust emission from numerous desert ephemeral playa dust sources worldwide (e.g., Cahill *et al.,* 1996; Gillette *et al.,* 1997; Niemeyer *et al.,* 1999; Reynolds *et al.,* 2007, 2009; Bullard *et al.,* 2008; Macpherson *et al.,* 2008; Baddock *et al.,* 2009, 2011, 2015; Sweeney *et al.,* 2011, 2016; Nield *et al.,* 2015, 2016b; Klose *et al.,* 2019). Hence, further investigation into what controls the formation and breakdown of the surface crust is necessary since it is that which ultimately controls the spatial and temporal development of 'hot-spots' of dust emission.

6.3.3. Determining the hydrological and climatological conditions on emissive and non-emissive surfaces

Figure 6.10 illustrates the inter-annual variations and local climate conditions of dust emission 'hot-spots' on the surface of Etosha Pan, which were observed from the satellite image data (see section 6.3.1.) during emissive dry seasons in 2018, 2019 and 2022 but were markedly absent during non-emissive dry seasons in 2020 and 2021.

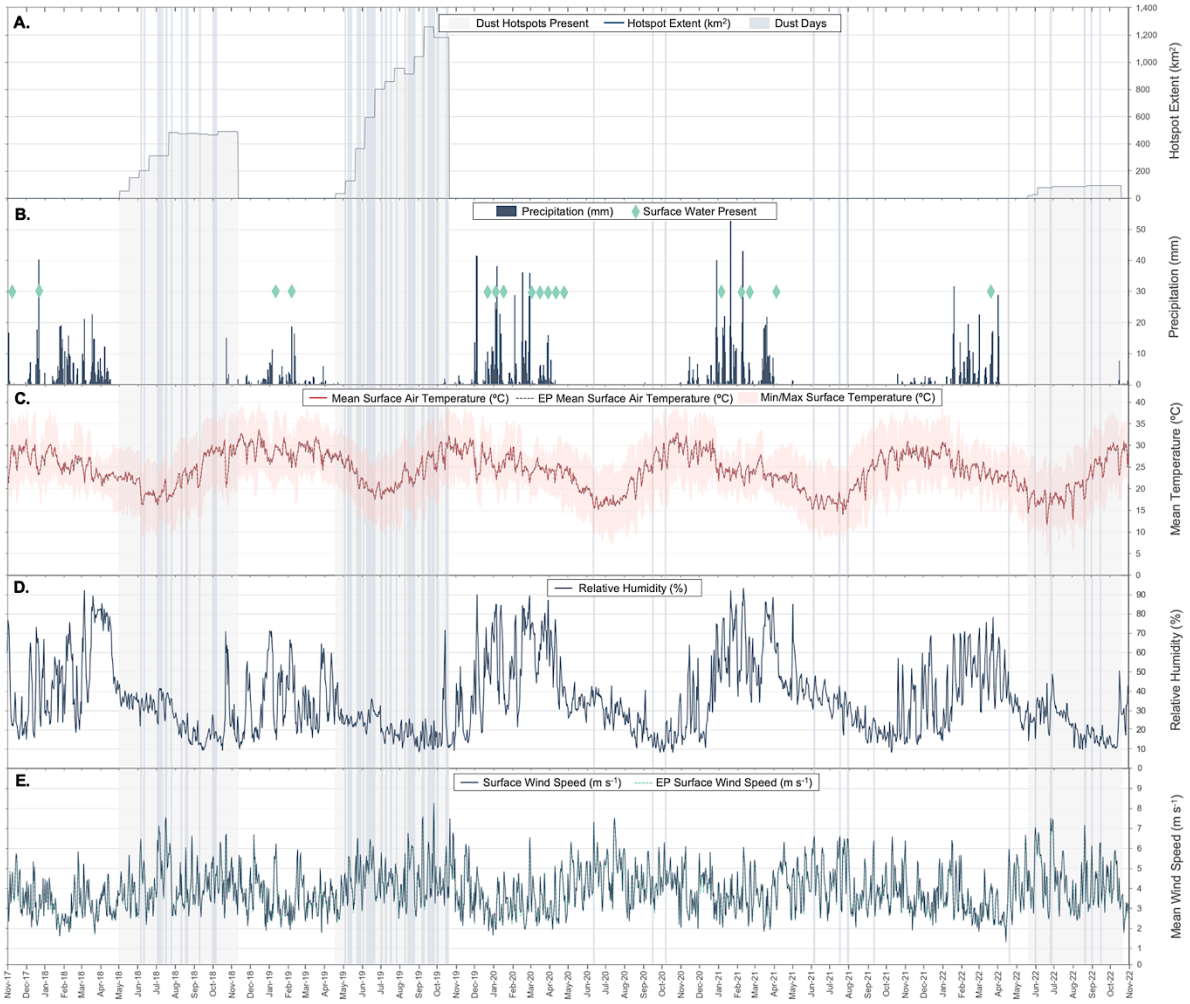


Figure 6.10. Daily time-series of (a) dust emission 'hot-spot' extents with dust day occurrences derived from satellite observations (Landsat 8-9, MODIS and MSG-SEVIRI), (b) flooding event occurrences and precipitation totals derived from satellite estimates (MODIS and GPM-IMERG), in addition to climatological parameters (c) surface temperature, (d) relative humidity, and (e) wind speeds extracted from the ERA5–Land climate reanalysis dataset for the region of interest compared with average conditions for Etosha Pan for corresponding periods in November 2017 – 2022.

While the extent and spatial distribution of these dust emission 'hot-spot' regions varied between emissive years (Figure 6.4a and 6.5a,b,e), their observed timing and duration was similar (Figure 6.10a) regulated by seasonal precipitation and surface moisture dynamics (Figure 6.10b). Dust emission 'hot-spots' typically emerged at the start of the austral winter dry season between the months of May and June and

remained on the surface until the months of October and November, coinciding with the start of the austral summer wet season (Figure 6.10a,b, see also Figure 6.5a,b,e). Shown in Figure 6.10b, mean daily precipitation totals recorded across the central region of the pan surface during the austral summer wet season for emissive years 2018, 2019, and 2022 (1.83 mm ±4.13 mm on average) were lower than average daily precipitation totals observed in non-emissive years 2020 (3.24 mm ±7.43 mm) and 2021 (2.96 mm ±7.04 mm). A greater frequency of flooding events on the pan surface was also recorded in the wet season of non-emissive years 2020 (7 events) and 2021 (4 events) than emissive years 2018, 2019 and 2022 (1–2 events) (Figure 6.10b). Flooding events in the wet season of emissive years 2018, 2019 and 2022 were also smaller in extent (see Figures 4.9 and 5.11b, Chapters 4 and 5), but nonetheless reached the central surface in some isolated regions (see Figure 4.10, Chapter 4).

In Figure 6.10a, dust emission 'hot-spots' consistently emerged during emissive years 2018, 2019 and 2022 following a period of dry conditions (1–3 months) since a precipitation event (Figure 6.10b) and a greater period (2–5 months) following a pan surface flooding event in the preceding wet season (Figure 6.10b). In contrast, the marked absence of dust emission 'hot-spot' surfaces in the dry seasons of 2020 and 2021 (Figure 6.10a) followed a prolonged period of elevated precipitation, which lasted from the start of the preceding wet season in October and into the dry season in May (Figure 6.10b). In both 2020 and 2021, surface water remained present in isolated regions on the pan in the dry season months of April to May (Figure 6.5c,d). Correspondingly, a considerable reduction in dust emissions was observed throughout

the dry seasons of 2020 (3 dust days) and 2021 (6 dust days), which were not associated with the development of the visually- and mineralogically-distinctive 'hot-spot' surfaces observed during emissive years (Figure 6.10a). These findings indicate that variations in the development of dust emission 'hot-spots' on Etosha Pan are directly influenced by the timing and extent of precipitation governing direct moisture on the pan surface and ephemeral flooding events.

Despite differences in the timing, frequency and extent of precipitation and ephemeral flooding events on the pan surface between emissive years (2018, 2019 and 2022) and non-emissive years (2020 and 2021), the formation of an extensive halite crust was consistently observed from RGB composite map time-series for all dry seasons during the 2018–2022 analysis period (Figures 6.8 and 6.9; see also Appendix 2). This suggest that the development of the evaporite-rich surface following the austral summer wet season does not entirely depend on the redistribution of salt minerals from an extensive flooding event, as has been observed in similar ephemeral playa environments (e.g., Mees, 1999; Artieda *et al.,* 2015; Bowen *et al.,* 2017). Rather, there is likely a key role for evaporation from shallow groundwater in the capillary fringe in developing an evaporite crust by efflorescence of subsurface brines (Goodall *et al.,* 2000; Reynolds *et al.,* 2007; Buck *et al.,* 2011; Milewski *et al.,* 2020).

During the austral winter months (May–October) of the 2018–2022 analysis period, atmospheric conditions were very dry with no precipitation recorded between May to September (Figure 6.10b). In this desiccation period, the pan surface shifted to much

higher concentrations of halite, indicated by the bright shades of blue in the RGB composite maps (Figures 6.8 and 6.9; see also Appendix 2). This development of a very bright, halite-rich surface is observed for each year. However, its formation occurred in earlier months between the austral summer wet season and winter dry season (March–April) for emissive years 2018, 2019 and 2022 (Figure 6.8a; see also Appendix 2), and in later dry season months (August–September) for non-emissive years 2020 and 2021 (Figure 6.9c,d; see also Appendix 2). Figure 6.10c shows that these two discrete periods were characterised by mean daytime temperatures ranging between ~20–25° C, separated by a period in which the lowest average temperatures (~15° C) were recorded in June–July. A continuous decline in relative humidity was also observed in this period for all years (Figure 6.10d), with values ranging from >60% following the summer rains in March and April and falling to 10–20% later in the dry season months of August to September.

During emissive years (2018, 2019 and 2022) the evaporite crust that formed at the start of the austral winter dry season in the months of March to April was influenced by very low precipitation totals (Figure 6.10b), declining mean surface temperatures (Figure 6.10c) and high relative humidity conditions (>60%) (Figure 6.10d). In turn, regions of the surface crust formed under these conditions were found to be associated with the emergence and development of dust emission 'hot-spots' during periods of increased aeolian activity in the austral winter dry season (May to October) of emissive years (Figure 6.10e). Dust emission events observed from 'hot-spot' regions correlate

with mean daily wind velocities exceeding critical thresholds of approximately 6 m s^{-1} (Figure 6.10e), that have similarly been observed in previous research (see section 5.3.2; Bryant *et al.,* 2007; Vickery *et al.,* 2013; Murray *et al.,* 2016) and connected to low level jet activity in the austral winter dry season (Clements and Washington, 2021; Wiggs *et al.,* 2022). In turn, the observed changes in the areal extent of these 'hot-spot' surfaces following emissive events (Figure 6.10a; see also Figure 6.5a,b,e) appears to be driven by increased erosivity conditions, potentially associated with the deflation of the evaporite crust to further expose soft subsurface sediments which constitute the surface mineralogy in these highly emissive regions (Figure 6.8d; Table 6.1).

It is possible that during the non-emissive years of 2020 and 2021 elevations in surface and subsurface moisture, as a consequence of antecedent precipitation and surface flooding conditions, imposed on the desiccation of the pan surface and subsequently delayed the evaporative development of the salt (predominantly halite) crust surface until later in the dry season. Consequently, the evaporite crust that formed in the later austral winter months of August to September was influenced by prolonged arid conditions characterised by a lack of precipitation (Figure 6.10b), rising mean surface temperatures (from ~15° C in June–July reaching up to 30° C by September; Figure 6.10c) and a continuous decline in relative humidity (falling to ~10–20% in August–September; Figure 6.10d). Elevations in mean daily wind velocities around 6–8 m s^{-1} were registered in the 2020 and 2021 austral winter dry seasons, as similarly observed in the dry seasons of emissive years (2018, 2019 and 2022), and the few recorded dust

days observed in these years were associated with erosive wind speed values >6 m s^{-1} (Figure 6.10d). Nonetheless, individual dust emission events were significantly smaller in both frequency and magnitude in 2020 and 2021 (see Figure 5.6, Chapter 5) and their isolated occurrence did not constitute discernible 'hot-spot' source regions on the playa surface (Figure 6.4b; Figure 6.10a).

The delayed formation of the surface salt crust may have therefore contributed to the lack of emissive 'hot-spots' on the playa by altering the erodibility conditions of the surface. From a microstructural perspective, the crystal habit (i.e., the size and shape of the crystals) of salt minerals presents a key factor for influencing the potential of dust emission when the abrasion of salt crusts occurs by aeolian erosion (Joeckel and Clement, 1999; Dai *et al.,* 2022). Crystal habits can vary considerably and are controlled by the environmental conditions (i.e., soil moisture, surface air temperature, and relative humidity) occurring at the time of mineral formation (Jafarzadeh and Burnham, 1992; Amit and Yaalon, 1996; Buck *et al.,* 2006; Warren, 2010, 2016; Nield *et al.,* 2015). Even for the same salt mineral, changing environmental conditions can alter the crystal habit through rehydration and dehydration, inducing the modification of the morphology and mechanical properties of salt crusts on surface soils (Gillette *et al.,* 2001; Buck and Van Hoesen, 2002; Lee and Kurtis, 2017; Zhang, Z. *et al.,* 2018; Zhang *et al.,* 2021).

Previous field and laboratory experiment studies have shown that when exposed to prolonged arid conditions and low relative humidity at the time of formation, efflorescent playa systems dominated by halite have the potential to develop into continuous interlocking crusted surfaces sufficiently thick to shut down all dust emission (Gill, 1996; Pelletier and Cook, 2005; Reynolds *et al.,* 2007; McLaurin *et al.,* 2011; Quick and Chadwick, 2011). It is possible that similar changes in the structural properties of the surface salt crusts at Etosha Pan in 2020 and 2021 may have occurred given their development under similar environmental conditions later in the dry season, which potentially inhibited the development of dust emission 'hot-spots' despite a seasonal increase in aeolian activity.

A comprehensive understanding of the mineralogical and morphological characteristics of the surface, as affected by antecedent environmental conditions, requires detailed investigation that could not be achieved from the remote sensing analyses conducted in this study. Further in-situ monitoring of the ephemeral playa surface is therefore needed to resolve the complex relationships between hydrological parameters (i.e., precipitation and flooding dynamics) and local climate conditions (i.e., temperature and humidity), and their influence on the efflorescent salt crust and subsurface properties (e.g., crust thickness, soil profile, and mineralogical composition) in order to identify what specific conditions determine the susceptibility of the pan surface crust to wind erosion.

Nevertheless, the observed differences in the formation rate of the evaporite (halite) surface on Etosha Pan between emissive and non-emissive years in this study suggest that the timing of the salt efflorescence process, driven by precipitation, temperature and moisture dynamics, represents an important control in determining the availability of sediment on the pan surface for dust emission.

6.4. Conclusion

This chapter has investigated the surface geochemistry, hydrological contexts, and climatic environments that control dust emission dynamics at Etosha Pan for the period 2018–2022. It has established that dust emissions from the pan are characterised by 'hot-spots' – clusters of individual plumes frequently emanating from isolated regions on the surface that are visually and mineralogically distinctive from non-emissive surfaces. Analyses of multitemporal satellite remote sensing and model reanalysis data showed that dust emission 'hot-spots' emerge from the deflation of efflorescent evaporite surface crusts, which occur as a function of preceding hydrological conditions (ephemeral flooding and precipitation) and surface wind dynamics. The key findings with respect to the objectives of the research are:

1) Statistical point pattern analysis of dust plume source locations derived from satellite data enabled the identification of clusters of dust sources ('hot-spots') in the central region of the pan surface. The development of visually distinctive dust emission 'hot-spot' surfaces ranging between 1–30 km in diameter were observed

from Landsat 8-9 OLI false-colour time-series data during the emissive austral winter dry seasons (March to November) of 2018, 2019 and 2022, that were markedly absent from the pan surface during the non-emissive austral winter dry seasons of 2020 and 2021. Inter-annual and seasonal variations in the occurrence and spatial extents of emissive 'hot-spot' surfaces indicated an interdependent relationship with dust emission frequencies, whereby the expansion of 'hot-spot' surfaces following the occurrence of major dust emission events in turn promoted further dust emissions from these source regions.

2) Laboratory-based reflectance spectroscopy and X-ray diffraction analysis of field samples found that surface sediments at Etosha Pan were primarily composed of halite, calcite, montmorillonite, saponite, analcime (zeolite) and muscovite mineral phases. Using validated linear spectral unmixing analysis it was possible to quantitatively map the distributions of selected mineral phases on the surface of the playa from Landsat 8-9 OLI image time-series. Mineralogical investigations revealed that an efflorescent salt crust composed of evaporite mineral deposits (i.e., halite), which formed much of the non-emissive surface on the pan, was absent from emissive 'hot-spot' regions to expose subsurface sediments composed of varying mixtures of clay and rock-forming silicate minerals (i.e., montmorillonite, saponite, zeolite and muscovite) underneath.

3) Seasonal transitions in the surface crust were identified and related to the environmental processes of the pan's flooding and desiccation cycles. Results

showed that the development of emissive 'hot-spot' dust sources were associated with the formation of a mixed evaporite (predominantly halite) mineral crust through the process of salt efflorescence initiated by wet season precipitation and ephemeral flooding events. High winds in the dry season break down this mineral crust, exposing large quantities of subsurface sediments that are extremely susceptible to aeolian entrainment. However, notably, the development rate of the evaporite crust, influenced by the timing of seasonal precipitation and recession of surface flooding, was identified as an important control on the development of 'hot-spots' of dust emission. Evaporite crusts that formed at the start of the dry season (i.e., March–April), that were influenced by very low precipitation totals, declining mean surface temperatures and high relative humidity conditions, were found to be associated with the development of dust emission 'hot-spots' during periods of increased aeolian activity in May to October of emissive years. While for non-emissive years, it was found that an increase in moisture on the pan surface for corresponding months (i.e., March–April) caused a delay in the drying process and the subsequent development of evaporite crusts to later in the dry season (i.e., June–September) that were, in turn, influenced by the absence of precipitation, rising mean surface temperatures and a decline in relative humidity. This inhibited the emergence of dust emission 'hot-spots' on the pan surface despite periods of increased aeolian activity. It is proposed that these differences in environmental conditions (i.e., surface moisture, surface air temperature, and relative humidity)

at the time of the formation of the evaporite surface crust and their potential effects on its geochemistry and associated physical properties play a key role in determining the susceptibility of the surface to aeolian erosion and dust emission.

Henceforth, the research conducted in Parts 1 to 3 of the thesis has identified the broader-scale sediment availability drivers and dynamics of dust emissions from Etosha Pan. However, the collective interpretations drawn from these analyses remain limited to primarily remote investigations of atmospheric conditions, surface crust and sediment properties, which do not easily facilitate examination of the specific surface erodibility conditions that influence the nature and magnitude of windblown dust emissions at-source. Further field-based investigations remain necessary to identify the specific surface crust and sediment properties (e.g., crust thickness, soil profile, and mineralogical composition) and local environmental conditions that govern the availability of sediment for aeolian erosion and thus the potential for dust emission at the surface. This would provide vital in-situ measurement data needed to verify remote sensing observations collected in Parts 1 to 3 and would help towards resolving the complex interconnections between basin-scale hydrological and climatological conditions, sub-basin scale efflorescent salt crust and subsurface properties, and the local-scale erodibility conditions and sediment properties that govern the spatial and temporal dynamics of dust emissions from this significant source region.

CHAPTER SEVEN

Part 4

Surface controls on sediment availability for dust emissions

Surface controls on sediment availability for dust emissions

7.1. Introduction

It was established from the research presented in Part 3 of the thesis (see Chapter 6) that dust emissions from Etosha Pan are characterised by clusters of individual plumes frequently emanating from isolated source regions on the playa surface. The emergence of these 'hot-spots' of dust emission were connected to dynamic changes in sediment availability, potentially driven by the breakdown and deflation of efflorescent evaporite surface crusts, as a function of the pan surface geochemistry, hydrological regimes (i.e., seasonal precipitation and ephemeral flooding) and local climate factors.

Dust modelling efforts have recognised that inherent complexities in dynamic sediment availability generate high spatial and temporal heterogeneity in dust emissions from playa landforms (Haustein *et al.,* 2015), which are poorly depicted in model parameterisations owing to uncertainties associated with interpretation of coarse-scale remotely sensed data and a general lack of detailed field verification data (Bryant, 2013; Csavina *et al.,* 2014; Klose *et al.,* 2019; Mei *et al.,* 2020; Wiggs *et al.,* 2022). Indeed, the collective interpretations drawn from subsequent analyses conducted in Parts 1 to 3 of this thesis are based upon estimates of atmospheric conditions, surface crust and sediment properties established from remote sensing data at moderate spatial

and temporal resolutions. While these data sources have enabled the broader-scale sediment availability drivers and dynamics of dust emissions from Etosha Pan to be determined, they do not allow for concise conclusions to be drawn concerning the specific surface erodibility conditions that govern the availability of sediment for dust emission at-source.

High quality field data at the local scale are vital in characterising the erodibility of playa landforms and in constraining or validating dust models to more accurately determine the contribution and natural variability of dust loading from these significant dust source regions (Cui *et al.,* 2019a,b). Recent developments in field-based dust research include the widespread adoption of established methods and equipment for monitoring dust emission (e.g., passive sediment traps and laboratory wind tunnel experiments) alongside the application of new technologies for understanding the emission potential of surfaces within source regions (Greeley, 2020; von Holdt *et al.,* 2021; McKenna Neuman, 2024).

Dust flux measurements made by a new generation of field-portable wind tunnels can provide information related to the range and magnitude of dust produced from landforms and highlight the inherent spatial and temporal variability in dust emission potential from specific source regions at the local scale (Etyemezian *et al.,* 2007; Sweeney *et al.,* 2008, 2016; Vos *et al.,* 2020, 2021). Several field studies on salt pan emissivity have gathered empirical data on shear velocity thresholds (u_{*t}) necessary for particle movement, which have provided novel insights into the physical processes

of dust emission and its dependency on sediment erodibility characteristics (Roney and White, 2004; King *et al.,* 2011; Sweeney *et al.,* 2011, 2022; Dickey *et al.,* 2023).

Etosha Pan is one of the few playa environments that is relatively accessible for field-based investigation. However, much of the previous research in this region has focused on examining the geochemical properties of surface sediment and groundwater samples obtained from the playa margin and surrounding region (Herdtfelder, 1984; Buch and Rose, 1996; Rahm and Buch, 1997; Li *et al.,* 2018). While only a few studies have explored the geochemistry of erodible material on the pan surface, focusing exclusively on total phosphorous, total nitrogen and soluble iron to determine terrestrial and marine fertilization potential (Bhattachan *et al.,* 2015; Dansie *et al.,* 2017b).

Recent field-based studies at Etosha Pan have involved direct observation of the emission process, and specific identification of the climatological context of emissions from source areas (Clements and Washington, 2021, 2023). Using a combination of remote sensing and field-based measurements of dust emissions and associated meteorological conditions, Wiggs *et al.* (2022) offered an insight into the likely major controls of local air temperature, relative humidity, and precipitation on surface erodibility in governing dust event dynamics on Etosha Pan. However, the researchers note that high resolution surface erodibility data specific to the precise emitting surfaces would offer a far more robust comprehension (Wiggs *et al.,* 2022). Yet, no

other sediment or surface erodibility measurements relevant to aeolian dust emission from Etosha Pan are available in the literature to date.

An opportunity therefore exists to collect in-situ measurements of dust emissions and surface properties on the ephemeral playa to identify the specific processes and conditions that determine the availability of sediment for aeolian erosion and to understand how surface erodibility affects the nature and magnitude of dust emissions. These data collected at the experimental surface "plot" scale, allied with the remote sensing measurements obtained at the basin/landform scale from research presented in Parts 1 to 3 of the thesis, can help towards resolving the interconnections between basin scale hydrological and climatological conditions, sub-basin scale efflorescent salt crust and subsurface properties (e.g., crust thickness, soil profile, and mineralogical composition), and determine how these controls influence the spatiotemporal variations in dust emissions across the playa surface. This will, in turn, provide a useful evidence base for elucidating the complex controls on sediment availability for aeolian erosion from ephemeral lake beds in order to improve model representations of dust emission from these highly dynamic landforms.

Accordingly, the purpose of this chapter is to determine the local-scale erodibility conditions and sediment properties of specific surfaces that form 'hot-spots' of frequent dust emission as identified in Part 3 of the thesis (see Chapter 6) compared with surfaces on the playa that are non-emissive. To achieve this, a field study was conducted in the southern portion of Etosha Pan in September 2022. In-situ estimates

of fugitive PM_{10} (i.e., particulate matter with an aerodynamic diameter smaller than 10 µm) emissions were obtained for a series of representative surfaces using a small portable field wind tunnel (PI-SWERL). These were compared with measurements of surface and near-surface physical characteristics and sediment properties in order to identify the specific surface erodibility controls on dust emissions from the ephemeral playa.

The specific research objectives are to:

1) Measure the erosivity threshold for dust emission and potential dust flux at increasing shear velocity from dust emission 'hot-spot' surfaces and other surface types across the pan;
2) Determine the physical and mineralogical properties of the pan surface and near-surface, especially where surface crusts are present, for sites of varying emissivity on the pan surface;
3) Identify the key surface properties and erodibility characteristics that influence the susceptibility of the pan surface to aeolian entrainment and dust emission.

The in-situ collection of measurements from precise emissive (and non-emissive) source regions on the pan surface will thus determine the specific surface characteristics and controls on 'hot-spot' sources of dust emissions identified in the previous chapter. Notably, these measurements also represent the first quantification of sediment erodibility characteristics on the surface of Etosha Pan.

7.2. Data Sources and Methods

7.2.1. Field site selection

Field studies were performed between 22 and 24 September 2022 across five strategically positioned sample sites along a 6.6 km transect in the south of Etosha Pan (Figure 7.1). Coinciding with the end of the dry season, this study period falls within one of the most active months in terms of dust activity at Etosha (see Figure 5.7, Chapter 5; Vickery *et al.,* 2013; Clements and Washington, 2021, 2023; Wiggs *et al.,* 2022).

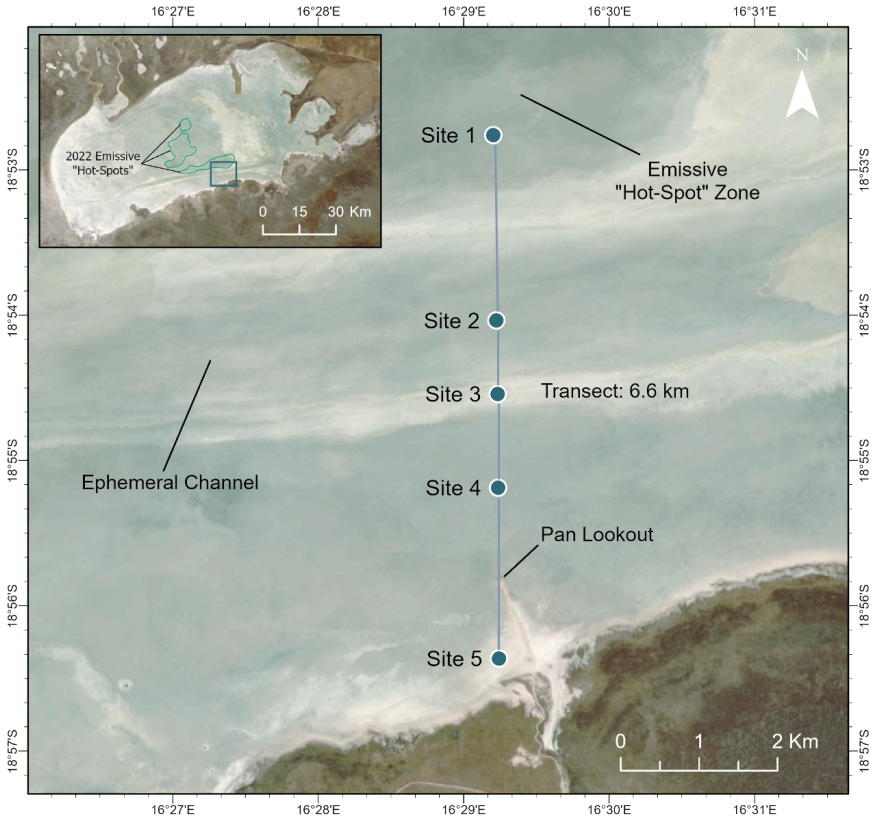


Figure 7.1. Field site locations in the south of Etosha Pan as part of the research campaign conducted in September 2022. Field studies were conducted at each of the five sites positioned along a 6.6 km transect that encompassed a range of surface features of varying emissivity potential. Sentinel-2 L2A true colour (bands 4,3,2) composite image captured on 21 September 2022.

Sample sites were selected to represent the range of surface conditions, hydrological contexts and presumed surface crust characteristics on the pan with varying emissivity potential (e.g., from non-emissive established salt crusts to highly emissive 'hot-spot' regions). Suitable sites were identified from satellite remote sensing observations of catchment-scale hydrology and ephemeral surface inundation, dust emission sources, and pan surface mineralogy and characteristics for the 2021/2022 hydrological year following the methods outlined in Parts 1 to 3 of the thesis (see Chapter 3 and Chapters 4, 5 and 6, respectively). This approach enabled field investigation of the potential range of emissivity conditions on the pan surface from sample locations that were relatively accessible for field-based investigation.

The locations and descriptions of surface characteristics for each of the field sites are given in Table 7.1. Figure 7.2 shows the variability in surface conditions evident at each site along the transect.

Table 7.1. Field site locations and descriptions, as informed by satellite remote sensing observations of dust emissions and pan surface characteristics and wetting regimes. **Note:** Days since surface wetting refers to the number of days since moisture was observed on the surface and wetted frequency refers to the count in days that moisture was observed for the corresponding hydrological year (July – June) preceding an emission event or field observation at a given site.

Site Name	Description	Location	Elevation (m asl)	Distance from shoreline (km)	Days since surface wetting	Wetted Frequency (days)
Site 1	Situated on an emissive 'hot-spot' area following a large-scale seasonal dust event, where dust emissions were observed prior to the field campaign in August and September 2022.	-18.879325, 16.48673	1,081.80	7.21	174	1
Site 2	Situated on a recently flooded ephemeral channel.	-18.90061, 16.48707	1,082.20	4.90	79	33
Site 3	Situated on a salt crust beside a recently flooded ephemeral channel.	-18.90904, 16.48724	1,082.80	3.90	152	19
Site 4	Situated on an emissive 'hot-spot' area preceding a large-scale seasonal dust event, where dust emissions were observed after the field campaign in October 2022.	-18.91979, 16.48728	1,082.80	2.70	172	2
Site 5	Situated on an established salt crust at the playa margin.	-18.93939, 16.48738	1,084.30	0.58	578	0

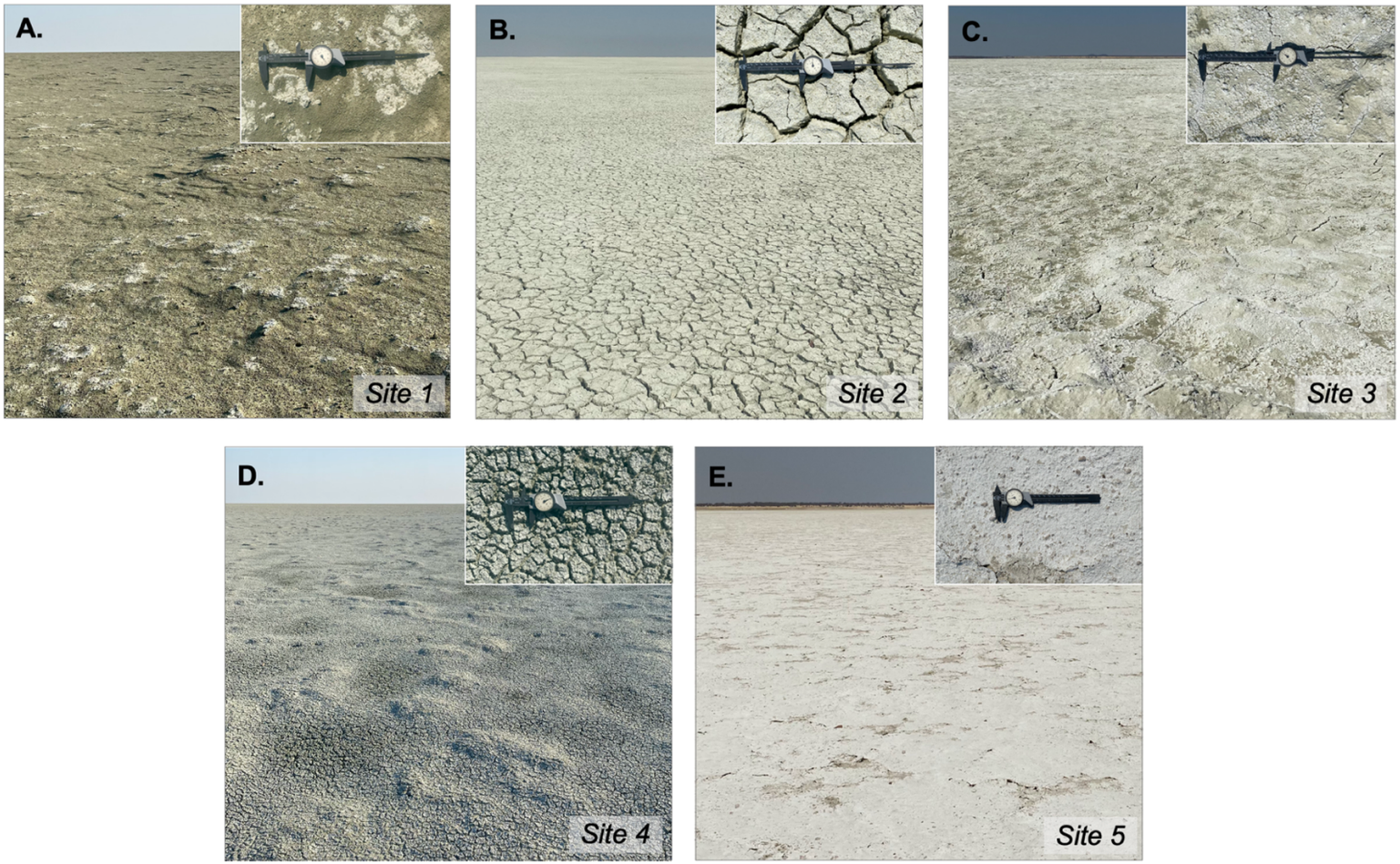


Figure 7.2. Field sites and key surface features examined in September 2022. Inset photos show a close-up of the pan surface at each site. Field photos show considerable spatial heterogeneity in surface characteristics between sites: (a) Site 1 - Emissive 'hot-spot' surface (following dust events) with deflated crust exposing fine clay subsurface sediments; (b) Site 2 - Recently flooded ($<$100 days) ephemeral channel; (c) Site 3 - Salt-crusted surface at the edge of the ephemeral channel; (d) Site 4 - Emissive 'hot-spot' surface (preceding dust events) that features intermittent mounds of mixed clay sediments and salt crystals underlying the surface crust; and (e) Site 5 - Established salt-crusted surface at the playa margin.

7.2.2. On-site measurements

At each site, a 10 m transect was established perpendicular to the predominant E-NE wind. At each location the following was carried out: (1) erosivity thresholds for emission and potential dust flux were measured using the PI-SWERL (see below) at 2 m intervals along the transect; (2) measurements of surface crust depth, strength and soil moisture content were collected at 10 cm intervals along the transect; (3) a shallow (~0.3 m) soil pit was excavated to observe physical characteristics of the near-surface profile; and (4) surface crust and sediment samples were collected for particle size and geochemical analysis.

Okaukuejo meteorological station (see Figure 4.1, Chapter 4 for location) recorded mean minimum and maximum temperatures of 16.5 and 33.8 °C respectively during the field sampling, with no precipitation recorded during the entire month.

Measurement of Potential Dust Emissions

A Portable In-Situ Wind Erosion Laboratory (PI-SWERL; Desert Research Institute, Las Vegas, NV, USA) was used to measure wind erosion thresholds and dust emission flux at each sample site (Figure 7.3). A detailed description of the PI-SWERL system is provided by Etyemezian *et al.* (2007, 2014) and Sweeney *et al.* (2008).

Briefly, the PI-SWERL instrument (Figure 7.3) consists of a computer-controlled 24-volt DC motor attached to the top of an open-bottomed cylindrical chamber with a diameter of 0.57 m and a height of 0.25 m. Within the chamber there is a flat annular

ring, which is positioned 0.05 m above the ground surface. As the annular ring revolves about its centre axis, a velocity gradient forms between the flat bottom of the ring and the underlying ground, creating a shear stress (N/m^2) on the surface (Sweeney *et al.*, 2008).

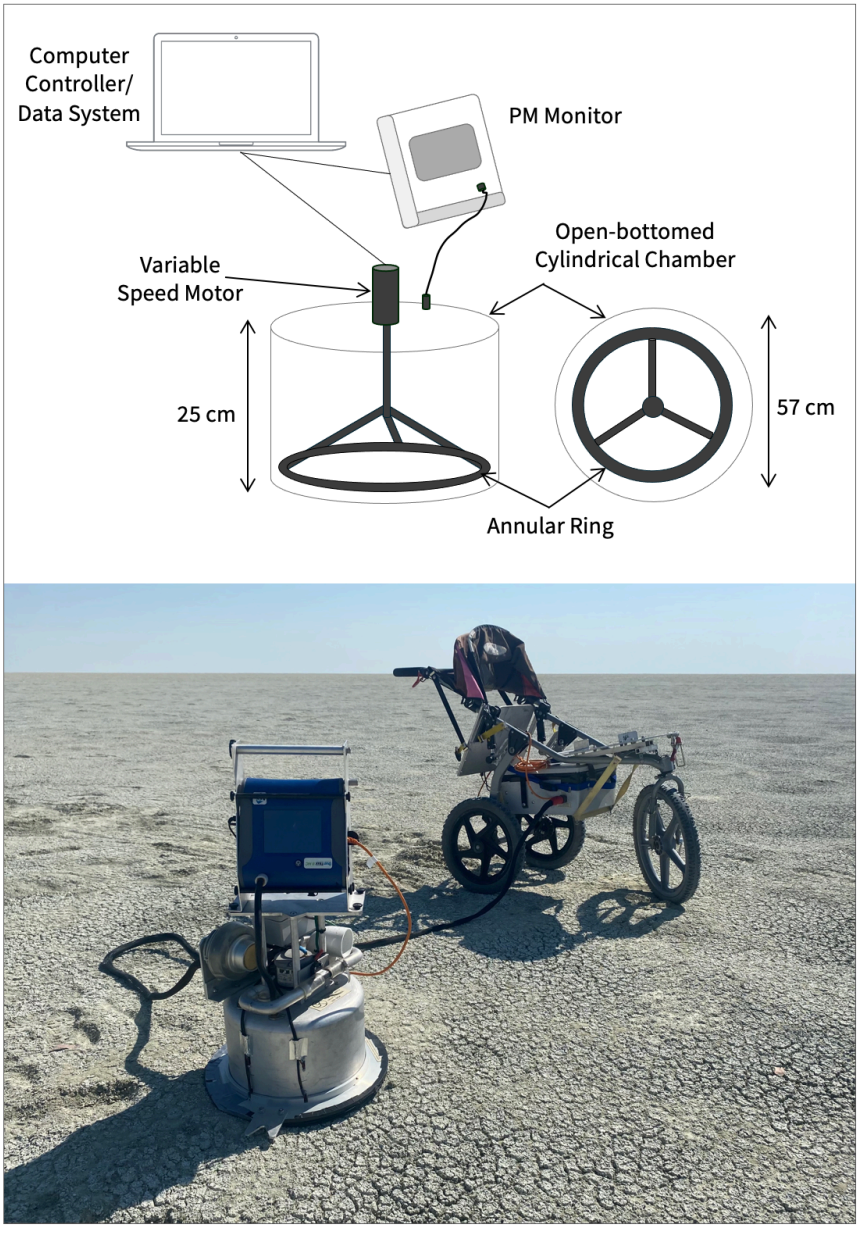


Figure 7.3. The Portable In-Situ Wind Erosion Laboratory (PI-SWERL) device and its portable buggy.

The magnitude of the shear stress depends on the rate of rotation, expressed as revolutions per minute (RPM). The rotation speed of the annular ring can be varied from 500 to 4000 RPM resulting in respective friction velocity (u_*) values from 0.16 to 0.69 m s^{-1} (Etyemezian *et al.*, 2007). Increasing the RPM therefore increases the surface friction velocity and once the surface friction velocity exceeds the threshold for erosion, sediment particles become entrained and dust emission occurs (Sweeney *et al.,* 2008; Kavouras *et al.,* 2009; van Leeuwen *et al.,* 2021). The PM_{10} (aerodynamic particulate diameter < 10 µm) concentration (mg m^{-3}) inside the PI-SWERL chamber is monitored by a DustTrak II nephelometer (Model 8530, TSI Inc., Shoreview MN, USA) using a light scattering technique (Etyemezian *et al.,* 2007; Sweeney *et al.,* 2008).

In tests on a variety of desert surfaces, measured emissions have compared favourably with those from large straight line portable wind tunnels, making the PI-SWERL a valid tool for measuring the potential for dust generation (Sweeney *et al.,* 2008). Due to its compact size, portability and ease of use, the PI-SWERL allows for relatively fast, repeatable measurements to be made in places that traditional large field wind tunnels cannot access (Munkhtsetseg *et al.,* 2016). It has successfully been used to facilitate field measurements on the dust emission potential of playa surfaces in many different regions in the world (e.g., Baddock *et al.,* 2011a,b; Buck *et al.,* 2011; King *et al.,* 2011; Sweeney *et al.,* 2011, 2016; Cui *et al.,* 2019a,b; von Holdt *et al.,* 2019; Dickey *et al.,* 2023).

Illustrated in Figure 7.4, two different PI-SWERL experimental tests were conducted in this study: a ramp test to detect the threshold friction velocity (u_{*t}) for PM_{10} emission (Figure 7.4a) and a step test to measure the amount of emitted PM_{10} at specific values of u_* above u_{*t} (Figure 7.4b). A total of 10 replicate measurements (5 ramp tests and 5 step tests) were completed systematically along the 10 m transect at each site to gain a reasonable assessment of dust emission potential for the range of local surface conditions.

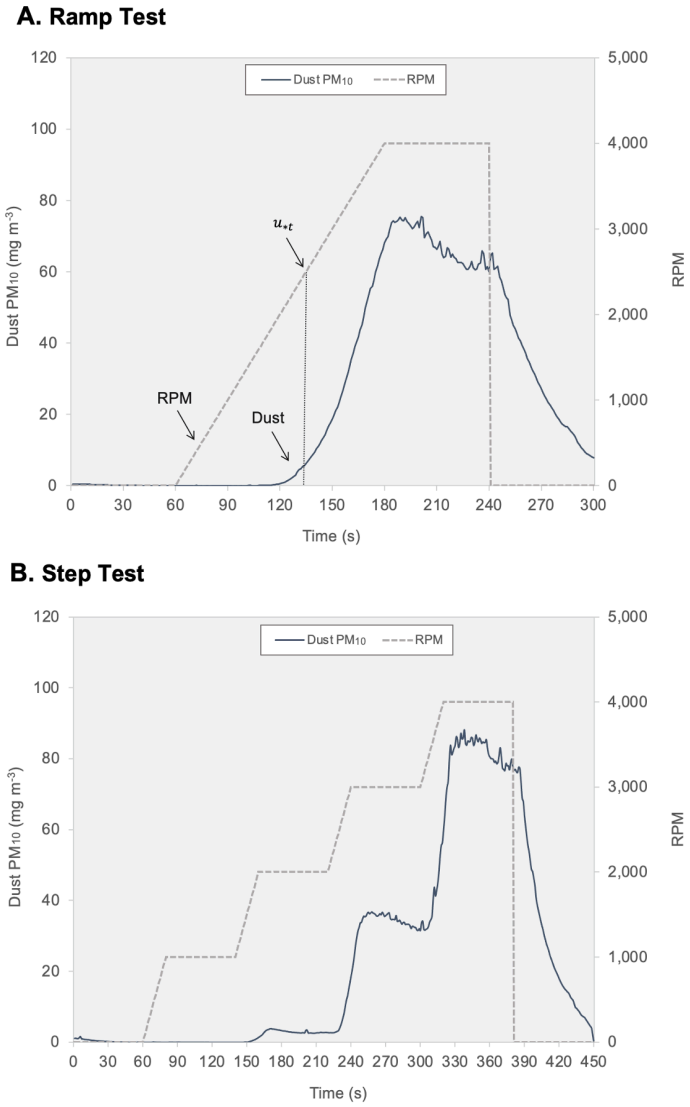


Figure 7.4. PI-SWERL test sequence configurations and examples of dust emissions response observed for the (a) ramp test and (b) step test.

To prevent cross-contamination between experiments, the inside of the PI-SWERL chamber was cleaned with a brush after each test run. In addition, a cleaning cycle was initially performed at each test site and following each consecutive series of ramp/step test runs. The cleaning cycle was a ramp test on a clean test surface (i.e., a control tray) at 4000 RPM for 180 s. This procedure ensured that any dust particles that remained in the instrument after simple cleaning with a brush were removed from the PI-SWERL chamber.

A ramp test, where the revolutions per minute (RPM) are increased linearly to simulate the effects of increasing wind, was first conducted to detect the threshold friction velocity (u_{*t}) for PM_{10} emission (Figure 7.4a). The friction velocity exerted by the PI-SWERL to the effective area (u_{*eff}) is determined by the rotation speed (RPM) of the annular ring that creates the air stream in the measurement chamber, determined empirically as:

$$u_{*eff} = C_1 \times \alpha^4 \times RPM^{\frac{C_2}{\alpha}} \quad (7.1)$$

where u_{*eff} is the friction velocity (m s^{-1}), C_1 refers to a constant of 0.000683, C_2 is a constant of 0.832 and α is a calibration parameter that depends on the surface roughness (Etyemezian *et al.,* 2007). An α value of 0.90, corresponding to the salt crust and (or) polygonal crust dominated playa roughness category, was applied for all field sites in this study (Etyemezian *et al.,* 2014; Sweeney *et al.,* 2016; Hartshorn *et al.,* 2023).

During each ramp test, the PI-SWERL cylindrical chamber was initially cleaned by fresh air vented from a blower at a constant flow rate (100 L min^{-1}) for 60 s. Afterwards, the RPM was steadily increased from zero to a target value of 4000 RPM within a time span of 120 s and maintained for 240 s; after which the RPM was reduced to zero within 30 s. The target value of 4000 RPM was selected based on previous research that has shown that the corresponding friction velocity of 0.69 m s^{-1} (Equation 7.1) is sufficient to generate dust emission for most dry sediment surfaces, including salt crusted playas (Etyemezian *et al.,* 2007). The threshold friction velocity (u_{*t}) for emission was determined as the point at which the PM_{10} concentration (mg m^{-3}) began to increase rapidly and continually above a fluctuating background value for a minimum of 10 s (Figure 7.4a) (van Leeuwen *et al.,* 2021).

Additionally, a step test, where a target RPM was sustained for a given period before being increased to a new value, was performed to measure the amount of emitted PM_{10} at specific values of u_* (Figure 7.4b). As shown in Equation 7.2, the concentration of PM_{10} (mg m^{-3}) for each step was converted to an emission flux (E_i) (mg m^{-2} s^{-1}):

$$E_i = \frac{\sum_{begin,i}^{end,i} (C \times F \times t_0)}{(t_{end,i} - t_{begin,i}) \times A_{eff}} \tag{7.2}$$

where C is the PM_{10} concentration (mg m^{-3}), F is the blower flow rate for fresh air entering the PI-SWERL chamber (m^3 s^{-1}), A_{eff} is the effective area underneath the

annular ring (0.057 m^2), t is the test time (s) at the beginning ($t_{begin,i}$) and ending ($t_{end,i}$) of each step level i, and t_0 is the nephelometer sampling time (Etyemezian *et al.,* 2007; Sweeney *et al.,* 2008, 2011).

During each step test, the PI-SWERL chamber was initially cleaned by fresh air vented from a blower for 60 s. After which 20 s ramps were used to attain successively higher RPMs, or friction velocities, in a series of steps with target values of 1000, 2000, 3000 and 4000 RPM that were each maintained for 60 s. Then, the RPM was reduced to zero within 10 s.

The PM_{10} dust flux for each step increase in PI-SWERL speed and equivalent shear velocity (u_*) were compared between field sites in order to ascertain the potential range of emissions for different surfaces on the pan. Additionally, mean PM_{10} dust flux values were compared specifically at a u_* of 0.56 m s^{-1} to provide a relative measure for emissions on the differing surfaces. This is a friction velocity that is commonly used for comparing relative values of dust emission flux from PI-SWERL measurements in various experimental studies (e.g., Sweeney *et al.,* 2008, 2011; Sweeney and Mason, 2013; von Holdt *et al.,* 2019; Cui *et al.,* 2019a; Vos *et al.,* 2020, 2021). A u_* of 0.56 m s^{-1} represents a wind speed of approximately 13 m s^{-1} at 10 m height, a common velocity during wind events at Etosha that has been linked with observed dust events (see section 5.3.2; Clements and Washington, 2021; Wiggs *et al.,* 2022).

Measurement of Surface and Sediment Properties

To determine the surface erodibility characteristics that control the relative emissivity of surfaces at each field site, measurements of various surface (crust type, thickness and strength) and sediment properties (moisture content, texture and mineralogy) were assessed against measurements of the PM_{10} dust emissions as determined by the PI-SWERL.

Measurements of surface crust thickness, strength and soil moisture content were collected simultaneously alongside the PI-SWERL tests (Figure 7.5). Crust strength was measured with two instruments commonly used in wind erosion studies (e.g., Goossens, 2004; Goossens and Buck, 2009; Li *et al.,* 2010; Ellis *et al.,* 2012; Feng *et al.,* 2013; Sweeney and Mason, 2013; Sharratt and Vadella, 2014; von Holdt *et al.,* 2019) to describe the resistance of the surface to aeolian erosion. A portable field spring penetrometer (Model H-4195, Humboldt Mfg. Co., Schiller Park, IL, USA) was used to measure the surface compressive strength (i.e., the amount of force required to break the surface crust) in kg/cm^2. In addition, a torvane pocket shear vane (Model 26-2261, ELE International, Milton Keynes, UK) was used to measure the surface shear strength (Figure 7.5a). A torvane determines the torsional shear stress before failure in kPa, which can be used as an indicator for resistance to shearing forces applied by wind and abraders to a surface (Vos *et al.,* 2020, 2021). The torvane used in this study was custom-designed as a handheld instrument for field use and consisted of a large (sensitive) vane (47.6 mm diameter) with eight blades and a penetration depth of 3 mm.

Subsurface volumetric soil moisture content was recorded at 6 cm depth using a handheld soil moisture sensor (ML3 Thetaprobe, Delta-T Devices Ltd., Cambridge, UK) (Figure 7.5b). All surface and sediment properties were measured at 10 cm intervals along the 10 m transect beside the PI-SWERL test surfaces and averaged.

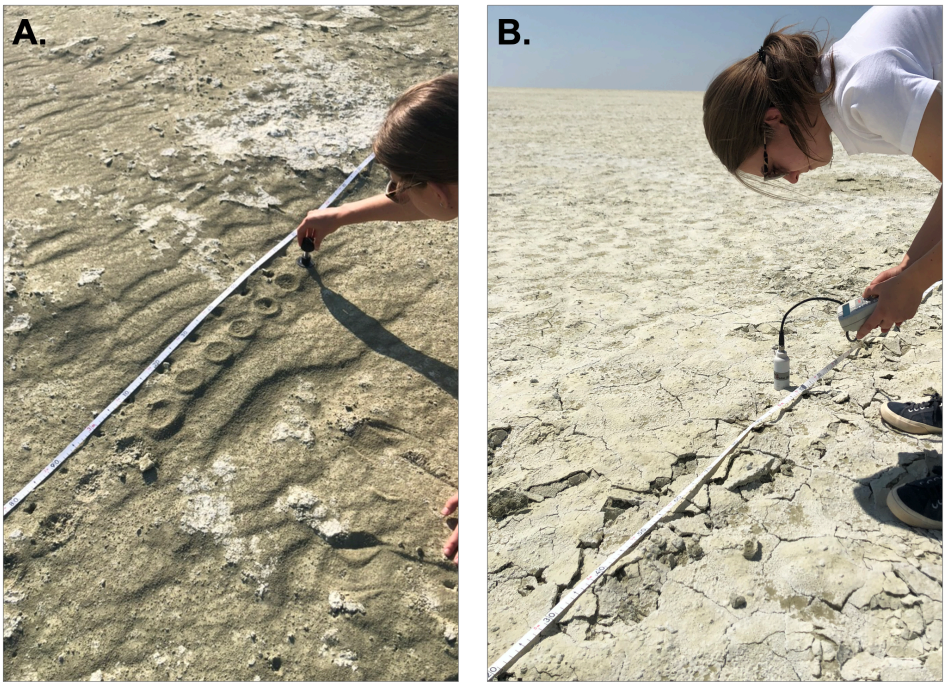


Figure 7.5. Measurements of surface and sediment properties recorded at 10 cm intervals along the 10 m transect at each field site. (a) Crust strength was measured using a portable field penetrometer (compressive strength) and a torvane pocket shear vane (shear strength; pictured) and (b) soil moisture content was measured at 6 cm depth using a ML3 Thetaprobe handheld sensor.

At each of the 5 sites, a shallow pit (~0.3 m) was excavated to describe the surface and near-surface properties (e.g., crust depth, upper soil profile and approximate distance to water table). The water table depth was estimated by measurement of the distance from the surface to the point at which underlying subsurface sediments were

water-saturated. Surface crust and near-surface (top 5 cm) sediment samples were collected for grain size and mineralogical analyses in the laboratory.

7.2.3. Laboratory Analyses

To determine the particle size distributions of sediment at each field site, wet grain size analyses were performed by laser diffraction in the laboratory at the University of Oxford. The field samples were first air-dried and passed through a 2 mm sieve to retain sediment particles and (or) aggregates definable as 'sand' and smaller. Representative subsamples were run through a Malvern Mastersizer Hydro 2000MU (Malvern Panalytical Ltd., Malvern, UK) particle size analyser (with a resolution of 0.02 to 2000 µm) at 1 bar pressure, using the predefined Scirocco Standard Operating Procedure (SOP). If the obscuration rate did not fall between 10% and 20%, the test was repeated with an appropriate increase or decrease of sediment mass. The sediment textural properties were then determined using the classification system of the United States Department of Agriculture (USDA), based on the percentage contents of clay (<2 µm), silt (2–50 µm), and sand (50–2000 µm).

The mineralogical compositions of sediment samples were examined by X-ray diffraction (XRD) analyses carried out by J. Azain and J. Leidelmeijer at the US Geological Survey (USGS) Geology, Geophysics, and Geochemistry Science Center. The XRD analyses were performed by step scanning using a X'Pert PRO diffraction system (PANalytical BV, Almelo, the Netherlands). The diffraction patterns of the

samples were interpreted using the High Score software (PANalytical BV) to determine the mineralogical composition (in weight %) of each sample.

7.3. Results and Discussion

7.3.1. PM_{10} emissions

Measurements of threshold shear velocities for PM_{10} emission (m s^{-1}) and potential PM_{10} emissions flux (mg m^2 s^{-1}) at a specific shear velocity from PI-SWERL experimental tests are summarised in Table 7.2. Mean PI-SWERL measurement values (±1 standard deviation) show that there was considerable variability between different sites and in measurements acquired within the same sites in terms of both the critical friction velocity thresholds for PM_{10} dust generation and the relative amount of PM_{10} emitted at a friction velocity (u_*) of 0.56 m s^{-1} (Table 7.2).

The data in Table 7.2 show the range of mean threshold shear velocities for PM_{10} emission for the different crusted surfaces at each sample site. For Sites 2 and 3, no threshold value is given since no significant emissions flux above background levels ($>$ 0.01 mg m s^{-1}) was recorded from these surfaces within the range of shear velocity values (0.16 to 0.69 m s^{-1}) measured using the PI-SWERL instrument. For sites where significant PM_{10} dust emissions were detected above background levels within the bounds of the PI-SWERL instrument, threshold friction velocities for emission ranged between 0.38 and 0.61 m s^{-1} (Table 7.2).

Table 7.2. Mean and standard deviation of measured threshold friction velocities for PM_{10} emission (m s^{-1}) and potential PM_{10} emissions (mg m^2 s^{-1}) measured at a shear velocity of 0.56 m s^{-1} from replicate tests given for each site. **Note:** *Data correspond to the geometric mean and geometric standard deviation of potential PM_{10} emissions flux.

Site Name	**Threshold Friction Velocity (m s^{-1})**		**Potential Emission Flux (mg m s^{-1}) at 0.56 m s^{-1}**	
	Mean	σ	Mean*	σ*
Site 1	0.38	0.046	1.19	1.16
Site 2	–	–	0.00057	1.30
Site 3	–	–	0.0017	5.96
Site 4	0.52	0.11	0.151	2.15
Site 5	0.61	0.044	0.073	1.14

* Geometric mean and standard deviation.

Assuming an aerodynamic roughness length calculated for the playa surface (z_0 = 0.0004 m), comparable to those of playa surfaces reported in similar studies (e.g., Wolfe and Nickling, 1996; King *et al.,* 2011; Nield *et al.,* 2014), the threshold friction velocities in Table 7.2 correspond to wind speeds of 6.5 – 15.5 m s^{-1} at 10 m height, which have been correlated with observed dust plume events from Etosha Pan in remote sensing investigations described in Chapter 5 of this research thesis (see section 5.3.2) and in previous studies (Bryant *et al.,* 2007; Vickery *et al.,* 2013; Clements and Washington, 2021). Results are also consistent with previous field-based research at Etosha Pan by Wiggs *et al.* (2022) that established a critical shear velocity of ~0.34 m s^{-1} (wind speeds c. 7.25 m s^{-1} at 3.18 m height) for dust emission events identified from ground-based observations between July 2015 – June 2016.

In addition, Table 7.2 shows average PM_{10} dust emission flux measurements for all sites at a friction velocity (u_*) of 0.56 m s^{-1}. The data correspond to the geometric mean (average of the logarithmic values, raised to the exponent of 10) of potential PM_{10} emissions from all replicate tests at the specified friction velocity. Accordingly, the results show that the potential PM_{10} emissions at some sites are several orders of magnitude higher than other sites. Additionally, the large variability in PM_{10} emissions across replicate measurements within the same site is demonstrated by the geometric standard deviation, which expresses an order of magnitude variation between emission rates with every integer increase. Table 7.2 shows that on average, the highest PM_{10} emissions at $u_* = 0.56$ m s^{-1} were observed from the emissive 'hot-spot' surface at Site 1 (1.19 mg m s^{-1}). Sites 4 and 5 also exhibit significantly higher emissions compared to surfaces on the ephemeral channel at Sites 2 and 3, where lesser amounts (< 0.01 mg m s^{-1}) of emitted PM_{10} were measured by the PI-SWERL (Table 7.2).

Previous field investigations by Wiggs *et al.* (2022) have quantified the relative magnitude of dust events at Etosha Pan using measures of horizontal dust flux and event flux, which are distinct from vertical dust flux resolved from the PI-SWERL measurements in the present study. Nevertheless, the mean PM_{10} dust flux values are consistent with previously reported vertical dust fluxes at $u_* = 0.56$ m s^{-1} from both PI-SWERL and traditional field wind tunnel studies on a variety of salt crusted playas, which range from 0–0.002 mg m s^{-1} up to ~3.0 mg m s^{-1} (Houser and Nickling, 2001a,b;

Macpherson *et al.,* 2008; Buck *et al.,* 2011; King *et al.,* 2011; Sweeney *et al.,* 2008, 2011, 2016; Cui *et al.,* 2015, 2019a; Van Pelt *et al.,* 2020; Vos *et al.,* 2021).

The values of potential PM_{10} emissions for the range of shear velocities tested using the PI-SWERL instrument are displayed in Figure 7.6 on a logarithmic scale. As might be expected, as u_* was increased, so was the emission flux for all sites (Figure 7.6).

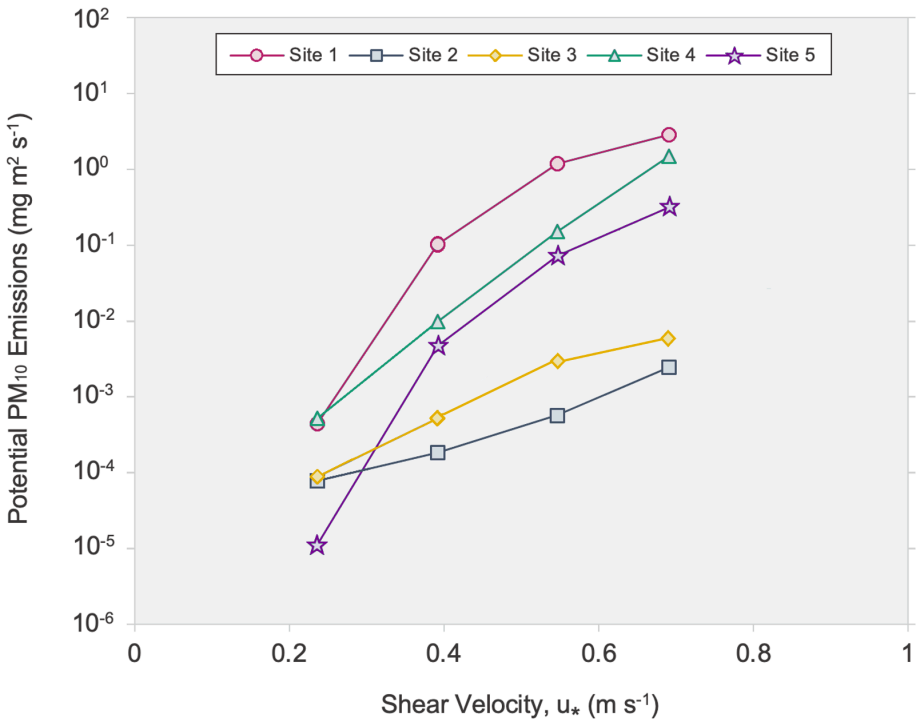


Figure 7.6. Average wind shear velocity (u_*) and the log-transform of potential PM_{10} dust emissions measured by the PI-SWERL at each site.

The highest PM_{10} emissions flux for all values of shear velocity were observed at Sites 1 and 4 (Figure 7.6). Site 1 consistently generated the highest average emissions rate for each set friction velocity. This was due to the character of PM_{10} dust emissions from the surface, which demonstrated a rapid increase in dust concentration at the beginning of each RPM step that were sustained at a relatively high level for the

duration of the PI-SWERL test run (Figure 7.7). Whereas at Site 4, PM_{10} emissions initially peaked as a high magnitude pulse of dust was emitted at the beginning of each RPM step, followed by a decline in emissions to background levels (Figure 7.7), which resulted in lower average emissions rates than Site 1 for equivalent shear velocities exceeding critical threshold values (Figure 7.6) and specifically at 0.56 m s^{-1} (Table 7.2).

In Figure 7.6, potential PM_{10} emissions observed at Sites 2, 3 and 5 were several orders of magnitude lower than Sites 1 and 4 for all equivalent shear velocities. While the surface at the playa margin (Site 5) had the greatest step increase in emissions flux across the range of friction velocity values tested by the PI-SWERL instrument (Figure 7.6).

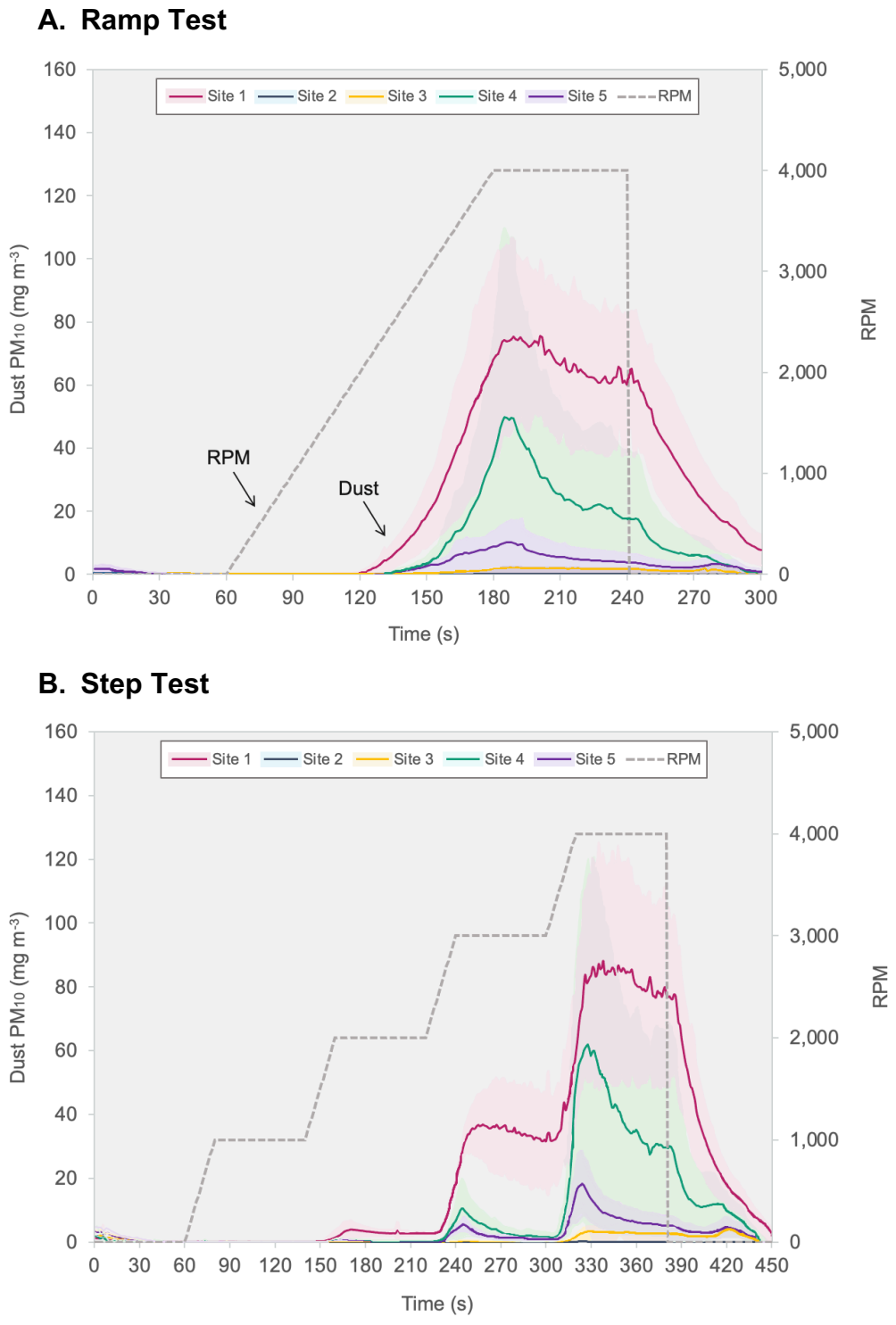


Figure 7.7. Average dust emissions response from surfaces at each field site for PI-SWERL test sequences for the (a) ramp test and (b) step test. **Note:** Different emissions responses were found from emissive 'hot-spot' surfaces during both the ramp and step tests, where sustained emissions were observed from Site 1 and peaked emissions were observed from Site 4.

7.3.2. Surface characterisation

Quantitative measurements of several surface (crust type, thickness and strength) and sediment properties (moisture content, texture and mineralogy) at each PI-SWERL test site underlined the considerable local-scale spatial heterogeneity in surface and near-surface conditions both within and between test sites across the 6.6 km transect, as indicated in Figure 7.2.

Sediment Geochemistry

Detailed mineral characterisations of surface crust and sediment samples are given in Table 7.3. XRD analyses of sediment samples indicated that surface crusts and subsurface sediments across all sites in the southern portion of Etosha Pan were composed of varying mixtures of evaporite and silicate minerals, but almost all commonly contained halite ($NaCl$), calcite ($CaCO_3$), analcime (zeolite) ($NaAlSi_2O_6 \bullet H2O$) and montmorillonite [$(Na,Ca)_{0.33}(Al,Mg)_2Si_4O_{10}(OH)_2 \bullet n(H_2O)$] mineral deposits (Table 7.3).

Results from the XRD analyses are consistent with analyses of sediment samples acquired from dust emission 'hot-spot' surfaces situated in the centre of Etosha Pan in 2018, which found an efflorescent salt crust composed of evaporite mineral deposits: halite, calcite, gypsum, thenardite and trona, and the hydrated phyllosilicate muscovite (mica group), underlain by fine grain subsurface sediments composed of analcime (zeolite) with a thin coating of clay silicate minerals montmorillonite and saponite (see section 6.2.2).

Table 7.3. X-ray diffractometry (XRD) results for surface crust and sediment samples acquired from each of the five sample sites at Etosha Pan in September 2022.

Mineral	Site 1			Site 2		Site 3		Site 4		Site 5	
	CS	SS	RS	CS	SS	CS	SS	CS	SS	CS	SS
	% (v/v)										
Analcime (zeolite) *($NaAlSi_2O_6 \cdot H_2O$)*	32.0	7.0	35.0	3.0	26.0	9.0	15.0	19.5	20.0	10.0	19.0
Anorthite *($CaAl_2Si_2O_8$)*	–	–	–	–	–	–	–	–	–	–	23.0
Biotite *[$K(Mg,Fe)_3(AlSi_3O_{10})(F,OH)_2$]*	–	4.0	–	–	–	–	–	–	–	3.0	2.0
Calcite *($CaCO_3$)*	13.0	9.0	14.0	6.0	7.0	4.0	9.0	12.5	13.0	13.0	14.0
Dolomite *[$CaMg(CO_3)_2$]*	–	–	–	–	–	–	–	–	–	15.0	18.0
Glauconite *[$(K,Na)(Fe,Al,Mg)_2(Si,Al)_4O_{10}(OH)_2$]*	–	–	–	–	–	–	–	–	3.5	–	–
Goethite *[α-$FeO(OH)$]*	–	–	–	–	–	2.0	–	–	1.0	–	–
Halite *($NaCl$)*	27.0	26.0	10.0	45.0	6.0	65.0	19.0	2.0	15.5	29.0	4.0
Montmorillonite *[$(Na,Ca)_{0.33}(Al,Mg)_2(Si_4O_{10})(OH)_2 \cdot nH_2O$]*	5.0	4.0	5.0	2.0	2.0	–	3.0	2.0	5.0	–	1.0
Muscovite *[$Kal_2(AlSi_3O_{10})(F,OH)_2$]*	–	29.0	32.0	30.0	27.0	20.0	30.0	23.0	27.0	–	–
Nontronite *[$(CaO_{0.5},Na)_{0.3}Fe^{3+}{}_2(Si,Al)_4O_{10}(OH)_2 \cdot nH_2O$]*	–	–	–	–	–	–	4.0	–	–	–	–
Orthoclase *($KAlSi_3O_8$)*	–	–	–	–	19.0	–	12.0	9.0	6.0	–	–
Palygorskite *[$(Mg,Al)_2Si_4O_{10}(OH) \cdot 4(H_2O)$]*	–	1.0	–	–	–	–	–	–	–	–	–
Phlogopite *($KMg_3(AlSi_3O_{10})(F,OH)_2$*	23.0	6.0	–	–	13.0	–	–	9.5	2.0	–	–
Pollucite *[$Cs(Si_2Al)O_6 \cdot nH_2O$]*	–	–	–	–	–	–	1.0	–	–	–	–
Quartz *(SiO_2)*	–	–	–	14.0	–	Trace	7.0	19.5	3.0	13.0	–
Sanidine *[$K(AlSi_3O_8)$]*	–	8.0	–	–	–	–	–	3.0	–	7.0	15.0
Saponite *[$Ca_{0.25}(Mg,Fe)_3((Si,Al)_4O_{10})(OH)_2 \cdot n(H_2O)$]*	–	6.0	4.0	–	–	–	–	–	4.0	–	–
Thenardite *(Na_2SO_4)*	–	–	–	–	–	–	–	–	–	10.0	4.0

CS = Crusted surface (0 – 2 cm depth); SS = Soft subsurface (2 – 5 cm depth); RS = Rippled surface features.

From mineral investigations of the field samples collected in 2022, muscovite [$(KaAl_2(AlSi_3O_{10})(F,OH)_2$] was commonly identified in surface and subsurface sediments for all sites, with the exception of Site 5 on the playa margin (Table 7.3). Site 5 was also the only site where the evaporite (salt) minerals thenardite (Na_2SO_4) and dolomite [$CaMg(CO_3)_2$] were found in surface crust and subsurface sediment samples. Other minerals present in some locations but not others included: feldspar minerals anorthite ($CaAl_2Si_2O_8$), orthoclase ($KAlSi_3O_8$), and sanidine [$K(AlSi_3O_8)$]; phyllosilicates phlogopite [$(KMg_3(AlSi_3O_{10})(F,OH)_2$] and palygorskite [$(Mg,Al)_2Si_4O_{10}(OH)\cdot 4(H_2O)$]; smectite clays glauconite [$(K,Na)(Fe,Al,Mg)_2(Si,Al)_4O_{10}(OH)_2$], nontronite [$(CaO_{0.5},Na)_{0.3}Fe^{3+}{}_2(Si,Al)_4O_{10}(OH)_2\cdot nH_2O$] and saponite [$(\frac{1}{2}Ca,Na)_{0.33}(Mg,Fe^{+2})_3(Si,Al)_4O_{10}(OH)_2\cdot 4(H_2O)$]; as well as goethite [$\alpha$-$FeO(OH)$], pollucite [$Cs(Si_2Al)O_6\cdot nH_2O$], and quartz ($SiO_2$) (Table 7.3).

Of the five surfaces tested, only Site 1 had ripple features at the surface (Figure 7.8), demonstrating that active saltation of the surface sediment had taken place. Shown in Table 7.3, the accumulations of sediment were composed of a mixture of evaporite (halite and calcite), rock-forming micas (analcime and muscovite) and smectite clay (montmorillonite and saponite) mineral deposits, potentially derived from a combination of abraded salt crust and fine subsurface sediment aggregates.

Quantitative measurements of physical crust and subsurface sediment properties for each field site are displayed in Table 7.4.

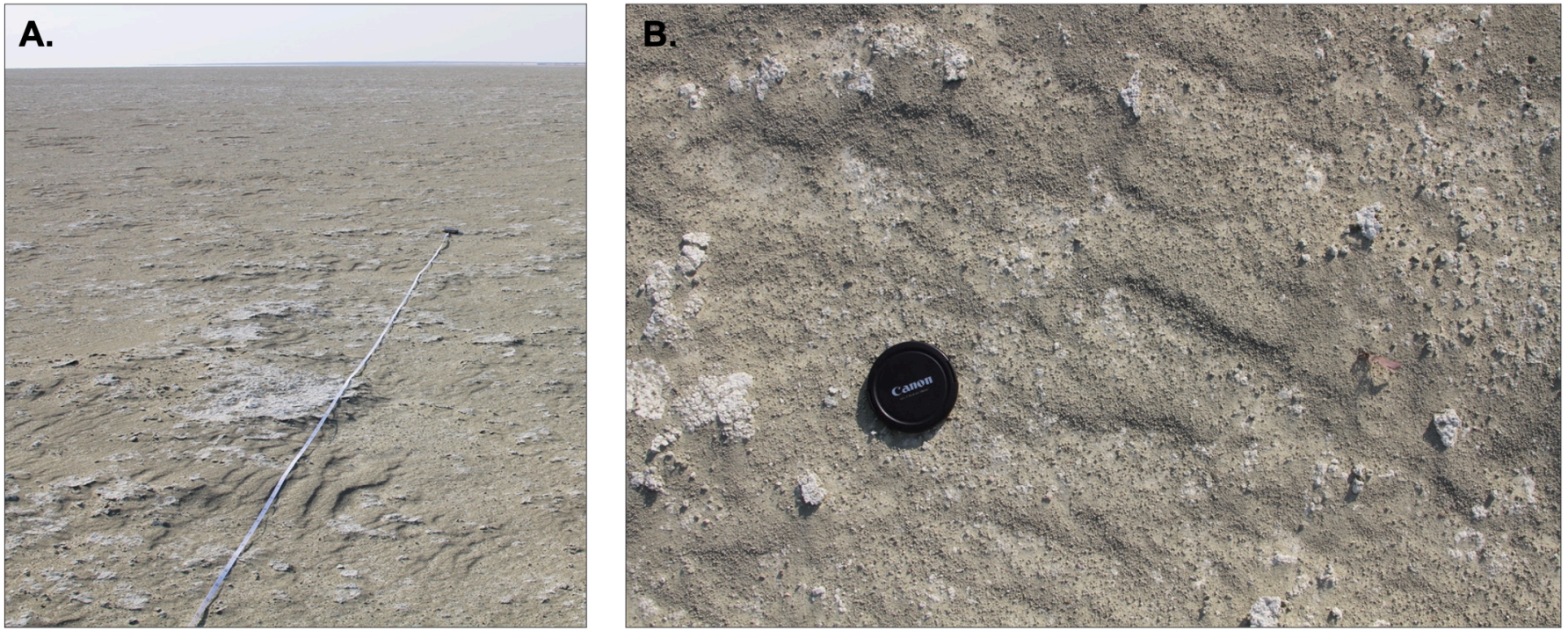


Figure 7.8. Field photos taken from Site 1 showing broken crust fragments (white) and ripple features (a) across the 10 m measurement transect and (b) close-up at the surface.

Table 7.4. Physical characteristics of the five sample sites at Etosha Pan in September 2022, including mean (±1 standard deviation) physical crust depth, compressive and shear strength, surface (0–60 mm) soil moisture, approximate depth to capillary fringe or water table, and surface (0–1 cm) soil texture. **Note:** Surface soil texture data were determined by laser particle size analysis as reported in section 7.2.3.

	Crust Properties (n = 500)								**Sediment Properties**				
Site Name	**Crust Depth (cm)**		**Compressive Strength (kg/cm^{-2})**		**Shear Strength (kPa)**		**0–60 mm Soil Moisture (%)**		**Approx. depth to capillary fringe or water table (cm)**	**Soil Texture Fraction (%)**			**Soil Texture Classification**
	Mean	σ	Mean	σ	Mean	σ	Mean	σ		Clay (< 2 µm)	Silt ($2 - 50$ µm)	Sand ($50 - 2000$ µm)	
Site 1	0.20	0.17	0.59	0.41	4.84	1.41	7.16	2.92	15.0	63.3	30.39	6.31	Clay
Site 2	0.082	0.024	2.48	0.97	36.82	2.80	3.44	2.85	10.0	37.43	46.07	16.5	Silty Clay Loam
Site 3	0.047	0.031	0.73	0.34	26.74	3.57	3.99	2.56	25.0	39.18	43.45	17.37	Silty Clay Loam
Site 4	0.42	0.27	0.77	0.56	9.42	2.07	3.75	2.83	20.0	36.71	55.58	7.71	Silty Clay Loam
Site 5	0.31	0.17	0.97	0.55	10.59	4.17	8.27	2.80	> 30.0	14.53	35.92	49.55	Loam

Surface Crusting

Surface crusts were present to varying degrees at all sites (Figure 7.2 and Figure 7.9). Average crust depths were greater at Sites 1, 4 and 5, ranging between 0.20 – 0.42 cm (Table 7.4). However, significant variability surrounding mean crust depth values was also observed across multiple measurements at Site 1 (0.20 ±0.17 cm) and Site 4 (0.42 ±0.27 cm).

At Site 1, such variability was due to the partial abrasion and removal of the surface crust by the wind during major emission events that occurred from the emissive 'hot-spot' during the dry season preceding field investigations. This resulted in an irregular surface consisting of a partial salt crust interspersed with large areas consisting of exposed clay-rich and rock-forming silicate mineral subsurface sediments (Figures 7.2a and 7.8a; Table 7.3). In contrast, at Site 4 such variability corresponded to the considerable range in the thickness of the irregular crust across the surface. At this site, crust depth was smaller (~0.10 cm) for surfaces overlying intermittent mounds of very fine silicate mineral sediments and efflorescent salt crystals, and were larger (~0.40 – 2 cm) for flat surfaces between the soft mounded features (Figure 7.9d). In contrast, very thin crusts (0.047 – 0.082 cm) were observed on surfaces located at the ephemeral channel (Sites 2 and 3) (Table 7.4; Figure 7.9b,c), which were closely bonded to the underlying subsurface sediments in many instances (Figure 7.9b).



Figure 7.9. Field photos showing heterogeneity in crust thickness between sites: (a) Site 1 - Emissive 'hot-spot' surface with a crust of moderate thickness that was mostly abraded following dust events; (b) Site 2 - recently flooded ephemeral channel with a very thin crust that was closely bonded to subsurface sediments; (c) Site 3 – Very thin salt crust at the edge of the ephemeral channel; (d) Site 4 - Emissive 'hot-spot' surface with a highly variable friable crust ranging between thin crusts overlying soft intermittent mounds of fine efflorescent salt crystals and silicate mineral sediments, and large crust depths for flat surfaces between the mounded features (pictured overlying near-surface materials); and (e) Site 5 – Established salt crust at the playa margin.

Measurements of the compressive and torsional shear strengths listed in Table 7.4 show that while the largest mean crust depths were observed at Sites 1 and 4, such crusts were also the weakest and most friable. Whereas the relatively thin surface crusts at Sites 2 and 3 exhibited the greatest compressive and shear strengths, respectively (Table 7.4). The continuous mixed evaporite crust at the playa margin (Site 5) was characterised by moderate compressive and torsional shear strengths compared with other field sites (Table 7.4).

Soil Moisture and Water Table Depth

Soil moisture measurements confirmed the dry conditions observed across all sites indicated by the time since wetting (i.e., the number of days since moisture was observed on the surface) and wetted frequencies (i.e., the count in days that moisture was observed on the surface) examined from remote sensing imagery (Table 7.1). Surface (0–60 mm) soil moisture contents were < 10 % for all sites (Table 7.4). The maximum soil moisture content was consistent for neighbouring Sites 2, 3 and 4 (3.44 – 3.99 %), despite varying depths to the underlying capillary fringe and (or) water table (Table 7.4).

Situated on an ephemeral channel, Site 2 had the shallowest depth to the water table (10 cm) and was most recently and frequently inundated in the preceding hydrological year (Table 7.1). However, measurements of volumetric soil moisture content suggest that Site 2 was the driest of all the field sites examined (Table 7.4).

In contrast, Site 5, located on the playa margin, had the greatest depth to the water table (>30 cm) and no moisture had been observed on the surface in the preceding hydrological year (Table 7.1). Yet, it had the greatest surface soil moisture content of all the sites examined (Table 7.4). It is noted, however, that inherent uncertainties are likely present in measurements of soil moisture content owing to the complexities associated with accurately separating available soil moisture content from water contained in hydrated salt minerals that comprise many of the crusted surfaces examined in this study (Table 7.3) (King *et al.,* 2011).

Relative elevations in surface soil moisture content were similarly recorded at Site 1 (Table 7.4), where the physical salt crust had largely been removed to expose fine sediments at the surface.

Sediment Texture

Analysis of surface (0–1 cm) soil texture showed that of all sites examined, the surface at Site 1 had a high content of clay-size sediment (< 2 µm fraction = 63%; Table 7.4), with a greater moisture retention capacity than coarser-textured sediments (silt and/or sand) (Bowler, 1973; Zhang and Shao, 2013). Shown in Figure 7.10, sediment samples obtained from the surface ($0-2$ cm), near-surface ($2-5$ cm) and ripple features on the emissive 'hot-spot' at Site 1 were characterised by very fine clay-size sediment textures.

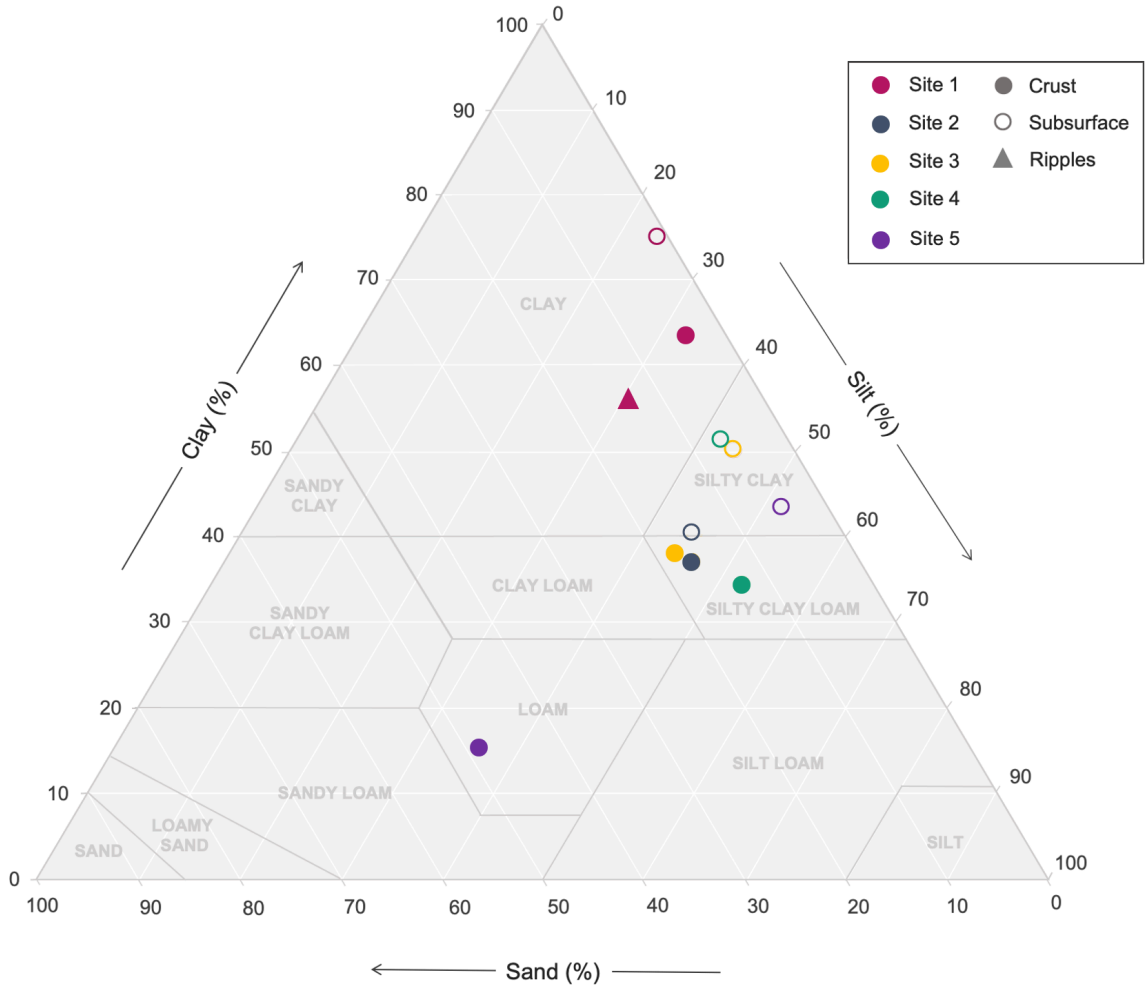


Figure 7.10. Ternary plot depicting textures (percent sand, silt and clay) of surface crust and near-surface sediments (top 5 cm) of field sample sites.

In contrast, coarser grain sizes formed a larger proportion of the surface composition for the four other crusted surfaces examined (>2 µm fraction = 64 – 86% for Sites 2 – 5; Table 7.4). Figure 7.10 shows the majority of surface crust and near-surface sediment samples obtained from Sites 2 to 5 were classified as silty-clay and silty-clay-loam. The largest grain sizes were found from the salt crusted surface at Site 5 on the playa margin (Sand fraction [50 – 2000 µm] = 49.55%; Table 7.4 and Figure 7.10).

7.3.3. Discussion – Surface erodibility controls on PM_{10} emissions

In-situ field observations have shown considerable local-scale heterogeneity in surface erodibility conditions, sediment properties and consequent dust emissions at Etosha Pan. Results indicate that across a relatively small area, the pan surface displays large variability in threshold friction velocities required to mobilise sediment and a range of emission rates spanning one to three orders of magnitude (Table 7.2 and Figure 7.6).

Heterogeneity of emissions has been widely documented in wind tunnel investigations of playa environments, which have recognised sediment availability – as a function of surface crusting, sediment geochemistry, moisture content and texture factors – as the primary control of emission potential (e.g., Nickling and Gillies, 1989, 1993; Macpherson *et al.,* 2008; Baddock *et al.,* 2011b; Ono *et al.,* 2011; Sweeney *et al.,* 2011; Dickey *et al.,* 2023). Similarly, such factors had a varying influence on the availability of sediment and thus the potential for dust emission across the surface of Etosha Pan.

Surface Crusting

The properties of the surface crust on a playa directly affect the supply of fine-grained material available for deflation (Baddock *et al.,* 2011b; Haustein *et al.,* 2015). Illustrated in Figure 7.2 and Table 7.4, considerable variation in the type and strength of crusting was found over a relatively small area of Etosha Pan. Investigations conducted in Part 1 of the thesis have shown that the playa experiences ephemeral

flooding of its surface (see Chapter 4), which investigations conducted in Part 3 of the thesis suggest that may result in the development of an uneven evaporite (salt) crust of varying morphology and various states of formation and degradation (see Chapter 6). Consequently, the crust presents a surface which is highly variable and dynamic in both roughness and erodibility, with subsequent effects on the distribution of sites of aeolian dust emission.

In the absence of moisture and vegetation, crusts play a stabilizing role in protecting the playa surface against wind erosion and can thus determine the intensity and frequency of dust emission (Cahill *et al.,* 1996; Moayeri *et al.,* 2023). The results from the PI-SWERL tests and crust strength measurements showed that areas with crusts that were hard and continuous (Sites 2, 3 and 5) effectively protected the playa surface against wind erosion, evidenced by the higher threshold velocity (u_*) values required to initiate particle movement and narrow range of dust emissions measured from multiple PI-SWERL tests (Table 7.2).

In contrast, the most emissive surfaces, Sites 1 and 4, did not contain a continuous consolidated crust. Situated on a dust emission 'hot-spot', the surface at Site 1 was highly uneven and disturbance of the salt crust following wind erosion events earlier in the dry (dust) season had exposed a large supply of loose erodible material at the surface (Figure 7.2a). This is consistent with the lower u_* required to initiate emissions observed at Site 1 (Table 7.2). Moreover, the vast supply of fine sediment (< 2 µm

fraction = 63%; Table 7.4) available for erosion meant that high-magnitude emissions were generated at Site 1 that were several orders of magnitude greater than other test sites for equivalent shear velocities (Table 7.2 and Figure 7.6).

The enhanced emission rates observed at Site 1 may have been compounded by saltation activity from the high proportion of loose sediment aggregates that formed ripple features on the surface (Figures 7.2a and 7.8), which were absent from any other test surfaces (Figure 7.2b-e). It is assumed these aggregates are composed of broken down crust and subsurface sediments, given the high fraction of both evaporite (salt) and silicate minerals in their composition (Table 7.3). Similar research has shown that surfaces with available sediment for saltation begin emitting dust at lower u_* (Gillette *et al.,* 1980, 1982; Nickling and Gillies, 1989, 1993; Shao *et al.,* 2003; Sweeney *et al.,* 2011, 2023; Nield *et al.,* 2016b; Vos *et al.,* 2020, 2021), which is consistent with the lower threshold velocity ($u_{*t} = 0.38$ m s^{-1}) for entrainment observed at Site 1 (Table 7.2).

Furthermore, results from the PI-SWERL test sequences showed the surface at Site 1 demonstrated sustained emissions for each step increase in shear velocity (Figure 7.7), potentially due to bombardment of saltating material facilitating the continued release of fine material from the surface (Gillette *et al.,* 2001; Houser and Nickling, 2001a,b; Macpherson *et al.,* 2008; Baddock *et al.,* 2011b), thus generating the highest average PM_{10} dust emissions flux of all test sites for equivalent shear velocities (Figure 7.6).

Conversely, the surface at Site 4 was characterised by a highly irregular polygonal crust that had remained relatively undisturbed at the time of measurement (Figure 7.2d). Yet, the surface demonstrated a similar high emissivity, albeit to a lesser extent, to the dust emission 'hot-spot' at Site 1 (Table 7.2 and Figure 7.6).

While the crust surface at Site 4 was largely intact, it was also extremely friable, and measurements of the compressive and torsional shear strength were comparable to that of the disturbed crust and loosened sediment surface at Site 1 (Table 7.4). Consequently, the surface crust at Site 4 was susceptible to disturbance from the shearing forces of winds even at moderate velocities (Table 7.2). This was further evidenced from PI-SWERL test sequences (Figure 7.7), which showed that the surface was characterised by peaked emissions immediately following step increases in shear velocity caused by a high magnitude pulse of dust that was released as stores of underlying fine sediments were exposed to aerodynamic entrainment by surface winds.

Given the significance of differences in the development and properties of surface crusts on the emissivity characteristics observed between field sites, it is necessary to consider the potential influence of sediment geochemistry, moisture content, and texture controls on crust variability between emissive surfaces (Sites 1 and 4) and non-emissive surfaces (Sites 2, 3, and 5) on the playa.

Sediment Geochemistry

Mineralogical interpretations by XRD analysis have shown that the geochemical composition of surface crusts and subsurface materials varied among sites, with potential consequences for the emissivity of sediments.

Notably, halite occurred to varying degrees across all test surfaces but was found to dominate surface crust compositions at Sites 2 and 3 (45–65%; Table 7.3), which PI-SWERL tests found to be the least emissive. Whereas relative abundances of halite were considerably reduced (2–27%) in crust compositions for the most emissive surfaces, Sites 1 and 4 (Table 7.3). These crusts were readily disturbed and subsequently removed by surface winds at moderate friction velocities as measured using the portable wind tunnel. This resulted in the exposure of highly erodible fine-grained subsurface sediments composed of varying mixtures of evaporite (i.e., halite and calcite) mineral crystals and silicate minerals (i.e., analcime [zeolite], montmorillonite, saponite and muscovite) at the surface (Table 7.3), which corroborate field and satellite remote sensing estimates of the surface geochemical characteristics of dust emission 'hot-spots' described in Part 3 of the thesis (see section 6.3.2).

Indeed, high abundances of sodium chloride-rich evaporites (e.g., halite) have been found to significantly increase the threshold friction velocity of playa surfaces by forming crusts with hard, cemented layers composed of interlocking crystals (Nickling and Ecclestone, 1981; Langston and McKenna Neuman, 2005; Buck *et al.,* 2011;

Bullard *et al.,* 2011; Goldstein *et al.,* 2017). By contrast, surfaces composed of hydrous/anhydrous evaporite minerals with acicular or prismatic crystal habits (e.g., sulphate salts), which dissolve and re-precipitate repeatedly (i.e., diurnally or seasonally) under certain climatic conditions, produce loose, "puffy" crusts comprised of unconsolidated mineral crystal aggregates that have been observed to be directly entrained by the wind (Gillette *et al.,* 1980, 2001; Reynolds *et al.,* 2007; Elmore *et al.,* 2008; Bucher and Stein, 2016; De Deckker, 2019).

However, moderate halite abundances (29%) were observed in the surface crust situated along the playa margin at Site 5, that were similar to the emissive 'hot-spot' surface at Site 1 (27%). Site 5 was also the only test surface where hydrous/anhydrous evaporite minerals (e.g., thenardite) were found in both crust and subsurface sediments (Table 7.3). Yet, PI-SWERL tests showed that the threshold friction velocity for erosion was considerably higher and the potential PM_{10} emissions observed were several orders of magnitude lower at Site 5 than for emissive 'hot-spot' surfaces at Sites 1 and 4 (Table 7.2).

Soil Moisture and Approximate Water Table Depth

It is possible that groundwater dynamics may have modulated the emissive potential of surfaces at Etosha Pan, given its influence on the presence and crystal habits of evaporite minerals in surface salt crusts (Buck *et al.,* 2011; Goldstein *et al.,* 2017). Both emissive 'hot-spot' surfaces at Sites 1 and 4 shared moderately high water

tables (15–20 cm) estimated from the depth at which subsurface sediments were saturated with water, whereas the estimated water table position at Site 5 was measured much further from the surface (>30 cm) (Table 7.4). Field and laboratory investigations from various salt-dominated (i.e., wet playa) basins have shown that the retention of undersaturated water associated with a shallow depth to groundwater can dissolve pre-existing surface crusts that previously resisted wind erosion (Reynolds *et al.,* 2009; Nield *et al.,* 2015, 2016b; Klose *et al.,* 2019) and grant a continuous replenishing supply of salts to the playa surface via capillary action (Buck *et al.,* 2011), generating salt efflorescences and fresh surface crusts (Reynolds *et al.,* 2007, 2009; Milewski *et al.,* 2019). In contrast, the potential lack of interactions between salt minerals and moisture dynamics as a result of prolonged dry conditions at the surface and in subsurface sediments at Site 5 (Table 7.1) may have contributed to the development of the wind-resistant salt crust surface (Figure 7.2e), which effectively hindered the erosion of sediment from the surface despite its theoretical potential for emissions based on its mineralogical composition alone.

Despite the intrinsic links that have been established between hydrological dynamics and dust emissions at Etosha Pan in Parts 2 and 3 of the thesis (see Chapters 5 and 6), as well as the noted influence of surface moisture conditions on surface erodibility in ephemeral playa environments (e.g., Reheis and Urban, 2011; Dai *et al.,* 2020; Cheng *et al.,* 2022), no clear correlation was evident between PM_{10} emission and field measurements of soil moisture content in this study. This may in part be due to the

consistent dry soil moisture conditions observed for all surfaces across the limited spatial area (topsoil moisture content $< 10\%$) (Table 7.4). In addition to the inherent uncertainties in surface moisture measurements associated with complexities in separating available soil moisture content from water contained in hydrated salt minerals present in the playa surface crust (King *et al.,* 2011). Furthermore, some surfaces (i.e., Sites 2, 3 and 5) with low enough soil moisture values to allow for dust emission were inhibited by the presence of a hard and (or) continuous salt crust (Figure 7.2b,c,e; Table 7.4).

Nevertheless, the results presented here highlight the importance of surface moisture in determining the potential emissivity of the playa surface over a seasonal scale through its influence on the development and properties of the surface salt crust. As other studies have established, the growth of the surface crust is strongly tied to moisture availability in the environment (Amézketa, 1999; Oztas and Fayetorbay, 2003; Nield *et al.,* 2016a,b).

In this study, the most emissive surfaces (Sites 1 and 4) shared similar moisture regimes, characterised by some moderate wetting of the surface ($1-2$ times) from seasonal precipitation and (or) ephemeral flooding of the playa surface ($\sim 5-6$ months prior to emission) in the preceding hydrological year as estimated from remote sensing observations (Table 7.1) and a relatively shallow water table (15–20 cm) approximated by field measurements (Table 7.4). Under these conditions, new salt minerals may

have continuously been drawn to the surface through capillary water movement and evaporation, which likely disrupted pre-existing surface crusts and (or) provided an additional source of fine materials for dust emissions (Buck *et al.,* 2011). These sites underwent a similar desiccation period in the dry season (Table 7.1), during which the development of surfaces characterised by weak, irregular mixed evaporite surface crusts with moderate abundances of halite and calcite occurred (Tables 7.3 and 7.4). In turn, these crusts were readily disturbed and subsequently removed by surface winds at moderate friction velocities as measured using the portable wind tunnel.

In contrast, sites with the lowest emissions were either situated on an ephemeral channel (Sites 2 and 3) that had been recently and frequently inundated in the preceding hydrological year (Table 7.1) and correspondingly characterised by a shallow estimated water table depth (up to 10 cm) (Table 7.4) or situated on the playa margin (Site 5) that had not been inundated for a considerable period (Table 7.1) and with a much a larger estimated depth to the water table (>30 cm) (Table 7.4). It is possible that these opposing moisture conditions impeded the availability of sediment for emission through different mechanisms. In the former case (i.e., Sites 2 and 3), repeated saturation of the soil profile by frequent inundation combined with a water table close to the surface potentially increased cohesion between the surface crust and underlying subsurface sediments (McKenna Neuman and Nickling, 1989; Pelletier, 2006; Dai *et al.,* 2020). While prolonged dry conditions (i.e., Site 5) inhibited any dissolution of the surface salt crust, resulting in a wind-resistant surface crust which constrains the

amount of fine material available for aeolian erosion (Reynolds *et al.,* 2007, 2009; Bucher and Stein, 2016; Dai *et al.,* 2022).

However, a specific understanding of surface moisture and moisture-related effects on salt crust and sediment properties, and how these vary spatially and temporally on the ephemeral playa, could not be achieved from the limited observations in this study. Further work is needed to elucidate the complex relationships between hydrological parameters (i.e., precipitation and flooding dynamics), local variations in surface moisture conditions, and their influence on salt crust properties and dynamics in order to better understand how the consequent characteristics of the salt crusts affect sediment supply availability for dust emissions from the playa surface. Nonetheless, the observations from this study have identified the key surface moisture regimes and moisture-related effects on the physical and geochemical characteristics of surface salt crusts that influence the development of highly emissive 'hot-spot' surfaces on Etosha Pan.

Sediment Texture

Lastly, there was no significant change in the potential emissivity of the pan surface in relation to soil texture. The surface with the highest emissions flux (Site 1) also contained the highest content of clay-size particles of all test sites (Table 7.4 and Figure 7.10). This was primarily related to the absence of crust and predominance of fine subsurface material exposed at the surface (Figure 7.2a and Figure 7.8). While

some of the lowest emissions came from sites with a similar spread in texture (i.e., silty clay loam) as surfaces with moderate to high emissions (Sites 2 and 3, and Site 4, respectively). The key parameter for this mismatch was surface crusting, which restricted the availability of erosive material from surfaces despite a relatively uniform grain size. This further suggests that surface crusts exert a major influence on potential dust production from Etosha Pan, perhaps more important than soil texture in many cases.

7.4. Conclusion

A field investigation was conducted to determine the local-scale surface erodibility conditions and sediment properties that govern the potential for dust emission from Etosha Pan. Novel field-based measurements of critical wind velocity thresholds and dust flux estimates using a portable field wind tunnel (PI-SWERL) and of various surface crust and near-surface sediment properties were recorded from a series of representative surfaces in the southern portion of the playa. Results have shown considerable local-scale heterogeneity in surface erodibility conditions and consequent dust emissions. Notably, it was found that the formation and degradation of surface crusts, influenced by surface moisture dynamics and geochemical characteristics, are key controls that directly affect the supply of fine-textured material available for deflation and thus the potential for dust emission from the pan. Specifically, the key findings with respect to the research objectives are as follows:

1) PI-SWERL estimates of threshold shear velocities for PM_{10} emission and potential PM_{10} emissions flux at increasing shear velocities showed considerable variability both within and between test surfaces over a limited spatial area on the pan. Mean threshold friction velocities for PM_{10} entrainment ranged from $0.38\ m\ s^{-1}$ for highly emissive 'hot-spot' areas (pre- and post- large-scale seasonal dust emission events) to greater than $0.69\ m\ s^{-1}$ for recently flooded and salt-crusted areas of the playa. Similarly, PM_{10} vertical flux rates were several magnitudes higher for 'hot-spot' surfaces compared to recently flooded and salt-crusted surfaces.

2) Quantitative measurements of surface and soil profiles highlight considerable local-scale heterogeneity in surface salt crust (type, thickness and strength) and surface sediment properties (moisture content, texture and mineralogy) at Etosha Pan. It was found that highly emissive surfaces had the largest mean crust depths but had the weakest compressive and torsional shear strengths. These surfaces also shared comparable moisture regimes, as indicated by similar time periods since wetting of the surface ($\sim 5-6$ months prior to emission), wetting frequencies ($1-2$ times) and a relatively shallow approximate water table depth ($15-20$ cm). While the least emissive surfaces shared similarly thin, resistant surface crusts, formed under opposing moisture conditions (i.e., frequent inundation and a very shallow depth to the water table vs. prolonged dry conditions and a large depth to the water table) that restricted the availability of fine material for dust emission. Mineralogical investigations of sediment samples indicated that surface crusts and

subsurface sediments were composed of varying mixtures of evaporite and silicate mineral deposits, with the predominance of halite mineral abundances in surface crust compositions representing a potential key limiting factor to surface emissivity.

3) Variations in erodibility conditions associated with the development and degradation of the highly dynamic salt crust, as a function of seasonal surface moisture regimes, ultimately determines the susceptibility of surfaces to aeolian entrainment and the consequent spatiotemporal distributions of aeolian dust emissions at Etosha Pan. The results from the field investigation have shown that the most emissive surfaces shared similar moisture regimes characterised by some moderate wetting of the surface from seasonal precipitation and (or) ephemeral flooding of the playa surface in the preceding hydrological year. These sites underwent a similar desiccation period in the dry season, leading to the development of surfaces characterised by weak, irregular surface crusts with moderate abundances of halite and calcite (evaporite) minerals. These crusts were vulnerable to disturbance and were subsequently removed by surface winds at moderate friction velocities as measured using the portable wind tunnel. This resulted in the exposure of a large supply of highly erodible, fine textured subsurface sediments composed of varying mixtures of evaporite crystals and silicate minerals. In some instances, this also generated sediment aggregates capable of lowering wind erosion thresholds and facilitating the continued release of fine materials from the surface by saltation bombardment. In contrast, the least emissive surfaces were

characterised by opposing extremes in seasonal moisture conditions (recent and frequent wetting/flooding vs. prolonged dry conditions). Nevertheless, these opposing surface moisture regimes were both associated with the development of surfaces that were similarly characterised by salt crusts that were hard, continuous and (or) consolidated with underlying subsurface sediments, which effectively protected the playa surface against wind erosion at these sites. These observations highlight the importance of seasonal surface moisture and moisture-related effects on the development and properties of surface salt crusts in determining the spatiotemporal variability in dust emission potential of surfaces across the ephemeral playa. In turn, they also offer a critical body of evidence as to how basin-scale hydrological drivers relate to local-scale surface moisture regimes and crust conditions to ultimately determine the variability in dust emission potential.

CHAPTER EIGHT

Conclusions

Conclusions

The overall aim of this thesis was to investigate the complex environmental controls on aeolian erosion and dust emissions in a major ephemeral lake basin. To achieve this, analyses of remote sensing data and in-situ field experiments were conducted in a detailed examination of the local and regional controls on the emission of mineral dust from one key ephemeral lake dust source in southern Africa, Etosha Pan in Namibia.

The investigation was divided into four parts, each pertaining to four individual research objectives (see section 1.2), which together worked towards resolving the multi-scale influence and interconnections between the hydrological contexts, physical and geochemical characteristics of the surface, and climatic environments controlling sediment availability for aeolian dust emissions from the ephemeral playa. The four key research objectives are addressed individually below, and a discussion of the main findings is presented.

<u>Part 1</u> – *To quantify the temporal and spatial dynamics of precipitation events across the Cuvelai-Etosha Basin and subsequent flooding of Etosha Pan and place them in context with global scale climate cycles for the period from 2000 to 2022.*

The outcomes of Part 1 of this research have enabled a comprehensive regional hydrological context of the Cuvelai-Etosha Basin from 2000–2022 to be established for the first time. This facilitated subsequent research to determine the potential hydrological controls on sediment supply and availability for aeolian dust emissions at Etosha Pan.

Mean annual precipitation measured across the Cuvelai-Etosha Basin was 572 mm $year^{-1}$ for the 2000–2022 analysis period. However, precipitation totals fluctuated considerably between years with extensive rainfall (~725 – 800 mm $year^{-1}$ in 2006, 2009, and 2011) and relatively dry conditions (~380 – 460 mm $year^{-1}$ in 2013, 2015, 2016, and 2019). The seasonal cycle was characterised by an austral summer wet season from November to April, with the highest precipitation totals recorded in the months of January to March. Analyses of satellite and meteorological station data established a spatial gradient in precipitation across the catchment, in which the total amount of precipitation was higher in the north-east regions (~700 – 820 mm $year^{-1}$) that declined towards the south-west regions (~240 – 300 mm $year^{-1}$) of the basin.

Annual and seasonal trends in ephemeral flooding of Etosha Pan were shown to correspond with precipitation dynamics in the Cuvelai-Etosha Basin. Satellite-retrieved (MODIS and Landsat) surface water extents revealed widespread and frequent inundation of the pan surface surrounding years with extensive rainfall (2008–2012) and drought conditions observed during dry years (2015, 2016, and 2019). Across

seasonal timescales, ephemeral flooding of the pan surface typically occurred during the latter end of the austral summer wet season (i.e., March to May) as precipitation was drained from the upper reaches of the basin via ephemeral river channels, which culminate at Etosha Pan.

Accordingly, analyses of lake surface inundation dynamics revealed that floodwaters entering Etosha Pan were principally sourced from fluvial inputs, namely the Ekuma and Oshigambo rivers draining the Cuvelai-Etosha Basin from the north. Notably, however, this study was the first to attribute a sizeable proportion (21%) of observed flood days exclusively to direct precipitation inputs and groundwater table fluctuations, rather than solely fluvial sources as noted in previous studies of basin hydrology in the region (e.g., Bryant, 2003; Mahowald *et al.,* 2003; Hamunyela *et al.,* 2022).

The research established that the timing, extent and frequency of ephemeral inundation of Etosha Pan were significantly influenced by annual and seasonal precipitation in the Cuvelai-Etosha Basin. It was revealed that pan surface inundation exhibited a lagged response to seasonal catchment rainfall, where the average monthly inundation extent of the pan increased one to two months following periods of extensive rainfall during the austral summer wet season. Correspondingly, statistically significant positive associations were found between monthly catchment precipitation totals with one- to two-month lagged pan surface flooding extents and frequencies.

In addition, a significant proportion of the observed variability in precipitation was attributed to El Niño–Southern Oscillation (ENSO) and changes in the subtropical Indian Ocean Dipole (SIOD), which are known to have an important role in modulating regional rainfall variability in southern Africa (Bryant *et al.,* 2007; Gaughan *et al.,* 2016; Gore *et al.,* 2020). It was found that extensive (negligible) surface flooding of Etosha Pan as a result of above (below) average precipitation anomalies in the austral summer wet season were associated with negative (positive) ENSO and positive (negative) SIOD events. Such divergent shifts in pan surface moisture conditions were further amplified when the ENSO and SIOD were in opposite phases. These findings suggest that global scale climate cycles and associated regional climatological drivers play a significant part in the hydrological cycle of Etosha Pan.

<u>Part 2</u> – To identify the temporal and spatial variability in dust emissions from the pan surface and quantify the extent to which dust entrainment is controlled by regional hydrology and ephemeral surface inundation dynamics for the period from 2000 to 2022.

The research conducted in Part 2 of this thesis significantly furthered our understanding of the inter-annual and seasonal fluctuations in aeolian dust emissions from Etosha Pan and quantified the extent to which dust entrainment is controlled by regional hydrology, through sediment availability dynamics, as well as erosivity drivers.

Measurements of mineral dust aerosol optical depth (AOD) and dust event frequencies detected using multi-sensor (MSG-SEVIRI and MODIS) satellite data products showed dust emissions emanating from Etosha Pan every year, to varying degrees, during the 2000–2022 analysis period. A distinct dust season was identified in the dry austral winter (May to November), where dust events were typically observed in the early morning hours, which have recently been related to the breakdown of nocturnal low-level jets (LLJs) (Clements and Washington, 2021; Wiggs *et al.,* 2022). Some dust source activity was also observed in the afternoon hours and in the austral summer. However, the magnitude and frequency of such events may have been underestimated in this study owing to the presence of convective storm clouds driving emissions that obscure satellite-based detection (Hennen *et al.,* 2019; 2024; Nobakht *et al.,* 2021; Wiggs *et al.,* 2022; Clements and Washington, 2023).

Analysis of detected dust events against surface wind regimes derived from ERA5–Land model reanalysis data confirmed a clear directional predominance in dust plume development initiated by prevailing E-NE winds that have been observed in previous remote sensing and field-based investigations in the region (Vickery *et al.,* 2013; Murray *et al.,* 2016; Clements and Washington, 2021, 2023; Wiggs *et al.,* 2022). Measured dust emission metrics (i.e., number of dust plumes/days and AOD) showed a significant correlation with higher wind speeds and wind gust values, where a peak in dust emissions was observed for wind speeds above 6 m s^{-1} at 10 m height.

This research also confirmed the significant influence of basin-scale hydrological factors on the emission of dust from Etosha Pan, as noted in previous studies in the region (Bryant, 2003; Mahowald *et al.,* 2003; Bryant, 2007). Comparisons of satellite-retrieved rainfall, lake inundation, mineral aerosols, and climate data for the 2000–2022 period have shown that the frequency, timing and magnitude of aeolian dust emissions are statistically significantly associated with catchment-scale precipitation and associated ephemeral pan surface flooding dynamics, in addition to surface wind speed variability. Together with the statistically significant associations established between catchment precipitation, pan surface flooding, and the El Niño-Southern Oscillation (ENSO) and subtropical Indian Ocean Dipole (SIOD) sea surface temperature anomalies in Part 1 of the thesis, the findings of this research therefore suggest that a significant proportion of the observed variability in both the dust and hydrological cycle of this source could be attributed to large-scale ENSO and SIOD climate cycles. Seasonal increases (reductions) in dust emissions were therefore associated with positive (negative) ENSO and negative (positive) SIOD events.

Statistically significant negative associations were found between catchment precipitation and measures of dust emission activity (AOD and plume event frequencies) across daily to annual timescales. These were stronger than the significant negative associations found between variables describing pan surface flooding (inundation extents and flooding frequencies) and dust emission activity. Therefore, an increase in catchment precipitation had a greater influence than pan surface flooding

on reducing dust emissions from Etosha Pan. It is likely that this reflects the compounding influence of surface wetting directly from rainfall over the pan as well as precipitation-induced flooding events via ephemeral river channels draining the Cuvelai-Etosha Basin on increasing pan surface moisture and water table levels, which can inhibit the availability of surface sediments to aeolian erosion.

The spatiotemporal dynamics of dust emissions observed in this investigation corroborate the general observations of Bryant (2003) and Mahowald *et al.* (2003), that periods of heavy rainfall and subsequent extensive inundation of the surface initially suppress dust emissions from Etosha Pan. However, it was found that ephemeral inundation and wetting of the pan surface by direct precipitation promoted dust emission upon drying of the surface across seasonal timescales (~3 months). This observed increase in dust emissions upon drying of surface moisture occurred across a shorter timescale compared with the 1-2 year lags observed in prior studies (Bryant, 2003; Mahowald *et al.,* 2003).

The findings of this research suggest that dust emissions from Etosha Pan correspond to changes in surface erodibility, in close association with preceding hydrological conditions, which determine the availability of sediment for aeolian erosion. This is in contrast to prior studies in the region, which inferred a function for sediment supply driven by ephemeral inundation (Bryant, 2003). Comparisons of the spatiotemporal distributions of dust event sources in relation to flooding frequencies indicated that

dust emission events were not necessarily confined to regions of previous inundation, which might be expected if sediment deposits from ephemeral flooding events formed the principal supply of material for dust emissions. Nevertheless, the majority of emission events were observed emanating from surfaces that had experienced some degree of flooding and (or) precipitation in the preceding hydrological year. Such associations have likewise been found in similar ephemeral playa environments globally, and have consistently been attributed to local-scale changes in the stability of evaporite (salt) mineral crusts and surface moisture conditions (e.g., Reheis, 2006; Bryant *et al.,* 2007; Reynolds *et al.,* 2007, 2009; Elmore *et al.,* 2008; Macpherson *et al.,* 2008; Nield *et al.,* 2015, 2016a,b; Sweeney *et al.,* 2016; De Deckker, 2019).

From the data presented in this study, it was inferred that seasonal rainfall and (or) ephemeral flooding can promote dust emissions in subsequent months, provided that surface conditions do not exceed a threshold level of moisture from frequent inundation and (or) wetting that may inhibit the availability of sediment to aeolian erosion and subsequently suppress dust emission. It was found that the majority (60%) of detected dust plume events were sourced from surfaces that had been wetted no more than five times in 3 – 6.5 months preceding emission. Prolonged arid conditions were associated with reduced dust emissions; potentially due to the formation of hard evaporite mineral crusts that are resistant to wind erosion. Whereas direct precipitation and (or) ephemeral flooding of the pan surface may have dissolved pre-existing wind resistant evaporite mineral crusts; with subsequent drying possibly leading to the development

of salt efflorescences, thin surface crusts, or the production of loose sediment aggregates that are susceptible to wind erosion.

Part 3 – To determine the sub-basin level controls on sediment availability (erodibility) that make specific surfaces on Etosha Pan prone to enhanced dust emissions.

In Part 3 of the thesis, statistical point pattern analysis of dust plume source locations established that dust emissions from Etosha Pan were characterised by clusters of individual plumes frequently emanating from isolated source regions on the playa surface – commonly referred to as 'hot-spots' of dust emission in the literature (Gillette, 1999; Reynolds *et al.,* 2007; Goudie, 2008; Walker *et al.,* 2009). Analyses of Landsat 8-9 OLI image time-series data for the period 2018–2022 revealed the inter-annual and seasonal variations in the occurrence, spatial distribution and development of these highly emissive dust 'hot-spot' surfaces, which ranged between 1–30 km in diameter and were found to be visually distinctive from non-emissive surfaces.

Validated linear spectral unmixing analyses of multispectral Landsat 8-9 OLI image time-series together with ground-truth spectroscopic and mineralogical data revealed an efflorescent salt crust composed of mixed evaporite mineral deposits (predominantly halite) on the pan surface in the austral winter dry season. For isolated emissive 'hot-spots', this evaporite crust was absent from the surface. Rather, the surface mineralogy observed in these 'hot-spot' regions corresponded with exposed subsurface sediments composed of varying mixtures of clay and rock-forming silicate minerals (i.e.,

montmorillonite, saponite, analcime [zeolite] and muscovite). While these minerals have been identified in previous field and laboratory studies at Etosha Pan (e.g., Hertfelder, 1984; Buch and Rose, 1996; Bhattachan *et al.,* 2015; Li *et al.,* 2018), this research investigation was the first to determine the surface mineralogical composition of specific sources of aeolian dust emissions from the pan.

Analyses of multitemporal satellite remote sensing and ERA5-Land climate reanalysis data for the 2018–2022 period showed that these visually and mineralogically distinctive emissive 'hot-spot' dust sources likely emerge due to the desiccative formation and subsequent degradation of the mixed evaporite surface crusts by surface winds, which lead to the exposure of finely textured and highly-erodible subsurface sediments. This mechanism for dust emission has similarly been observed in other ephemeral (saline) playa dust sources worldwide (e.g., Bryant *et al.,* 2007; Reynolds *et al.,* 2007, 2009; Macpherson *et al.,* 2008; Baddock *et al.,* 2009, 2011, 2015; Goudie, 2018; De Deckker, 2019; Klose *et al.,* 2019).

The investigation presented here further identified the timing of the evaporite crust formation as an important control on the development of 'hot-spots' of dust emission. Evaporite crusts that formed on the pan surface at the start of the austral winter (i.e., March to April) were associated with the emergence of dust emission 'hot-spots' during periods of increased aeolian activity throughout the dry season (May to October). Whereas an observed increase in moisture on the pan surface following a prolonged

period of increased seasonal rainfall and ephemeral flooding caused a delay in the desiccative formation of evaporite crusts to later in the dry season (i.e., June to September). This corresponded with a reduction in dust emissions, despite a seasonal increase in wind strength. Hence, dust emissions were predominantly sourced from areas that were characterised by neither persistent moisture nor prolonged dry conditions.

Results suggest that the spatiotemporal variations in surface emissivity may be driven by changes in local environmental conditions (i.e., surface moisture, surface air temperature, and relative humidity) at the time of crust formation. These factors can modify the structural properties (e.g., the size, shape and interlocking nature of the precipitated crystals) of surface salt crusts and, in turn, alter the susceptibility of the surface to aeolian erosion and dust emission (Langston and McKenna Neuman, 2005; Buck *et al.,* 2011; Sweeney *et al.,* 2011; Goldstein *et al.,* 2017; Goudie, 2018; Zhang, Z. *et al.,* 2018, 2021).

Further in-situ investigations of surface water–groundwater interactions and their influence on the geochemical and physical characteristics of the surface at Etosha Pan across seasonal timescales together with more detailed examination of the specific salt mineral assemblages and crystal habits of resultant surface crusts (e.g., SEM-EDX analyses) remain necessary to elucidate precisely how dynamic variations in the mineralogical and morphological characteristics of the evaporite crust over time (as affected by varying surface moisture regimes and local climate conditions) ultimately

determine the susceptibility of the pan surface to wind erosion. Whilst such detailed analyses could not be achieved within the scope of the field and laboratory investigations presented in this thesis, such an approach offers a significant opportunity for future research.

Part 4 – To quantify the local-scale surface erodibility conditions and sediment properties that govern the potential for dust emission from Etosha Pan.

The outcomes from a field investigation presented in Part 4 of the thesis revealed considerable local-scale heterogeneity in surface erodibility conditions and consequent dust emissions at Etosha Pan, which were closely related to the physical characteristics of surface evaporite crusts.

Quantitative measurements of critical wind velocity thresholds for PM_{10} emission and dust flux rates using a small portable field wind tunnel (PI-SWERL) found mean threshold friction velocities (u_*) for PM_{10} emission ranged from 0.38 $m\,s^{-1}$ for highly emissive dust 'hot-spot' surfaces (pre- and post- large-scale seasonal dust emission events) to greater than 0.69 $m\,s^{-1}$ for recently flooded and salt-crusted areas of the playa. PM_{10} vertical flux rates measured with the portable wind tunnel were one to three orders of magnitude higher for emissive 'hot-spot' surfaces compared to recently flooded and salt-crusted surfaces.

Notably, assessments of dust emission potential against corresponding surface crust and near-surface sediment properties corroborated theoretical assumptions drawn from

remote sensing analyses conducted in previous chapters, which suggest that surface moisture dynamics across seasonal timescales represent an important control on the potential emissivity of the playa surface through its influence on the development and properties of the surface evaporite crust.

Highly emissive dust 'hot-spot' surfaces shared similar moisture regimes, characterised by some moderate wetting of the surface ($1-2$ times) as a result of seasonal precipitation and (or) ephemeral flooding ($\sim 5-6$ months prior to emission) in the preceding hydrological year, and a subsequently relatively shallow water table ($15-20$ cm) measured from the surface at-source. These sites underwent a similar desiccation period in the dry season, which ultimately led to the development of surfaces characterised by weak, highly irregular mixed evaporite (halite and calcite) surface crusts. These crusts were readily disturbed by surface winds at moderate friction velocities both prior to and during PI-SWERL tests. This resulted in the exposure of loose, fine textured and highly erodible subsurface sediments rich in clay and rock-forming silicate minerals (montmorillonite, saponite, analcime [zeolite] and muscovite) to the surface and in some instances the generation of sediment aggregates capable of lowering wind erosion thresholds and facilitating the continued release of fine erodible materials by saltation bombardment. The large supply of fine sediment available for erosion meant that high-magnitude emissions were generated from these surfaces, which were several orders of magnitude greater than other test sites for equivalent shear velocities as applied with the portable wind tunnel.

In contrast, surfaces with negligible dust emissions were either situated on an ephemeral channel characterised by moisture presence in near-surface sediments associated with both recent and frequent inundation in the preceding hydrological year or were situated on the pan margin where the surface had not been inundated for a considerable period. It was inferred that these opposing moisture conditions impeded the availability of sediment for emission through different mechanisms. In cases where the surface had been frequently wetted and (or) inundated, repeated saturation of the soil profile increased cohesion between the surface crust and underlying subsurface sediments (McKenna Neuman and Nickling, 1989; Pelletier, 2006; Dai *et al.,* 2020). In contrast, in cases where the surface had not been wetted and (or) inundated during the preceding hydrological year or longer, the persistent dry conditions inhibited any dissolution of the surface salt crust, resulting in a wind-resistant surface that restricted the availability of fine material for dust emission (Reynolds *et al.,* 2007, 2009; Bucher and Stein, 2016; Dai *et al.,* 2022). In turn, these sites were characterised by thin, resistant evaporite crusts that were hard, continuous, and (or) consolidated with underlying subsurface sediments, which effectively protected the pan surface against wind erosion. This was evidenced by the higher threshold velocity (u_*) values required to initiate particle movement and narrow range of dust emissions measured from multiple PI-SWERL tests.

Overall Conclusions and Future Research

The outcomes from this research have shown that dynamic shifts in erodibility conditions associated with the formation and degradation of an evaporite (salt) crust, as a function of seasonal surface moisture regimes, play a significant part in determining the spatial and temporal dynamics of dust emissions from this source region. It was found that seasonal precipitation across the Cuvelai-Etosha Basin and subsequent flooding of Etosha Pan represent critical controls on sediment availability for aeolian dust emissions from the ephemeral playa, which were associated with broader-scale global climate cycles and sea surface temperature anomalies (ENSO and SIOD). The research established that dust emissions were characterised by localized 'hot-spots' of dust production from discrete source regions, rather than uniform emissions from across the playa surface as a whole. These dust 'hot-spot' regions were associated with changing surface mineral crust dynamics, as controlled by the timing and extent of wetting by precipitation and flooding.

Accordingly, the research presented in this thesis underlines the importance of surface moisture dynamics and its impacts on surface mineral crust properties in controlling local-scale variations in sediment availability for dust emission at Etosha Pan. These findings support a growing body of evidence gathered from a number of remote sensing investigations (Bryant *et al.,* 2007; Vickery *et al.,* 2013; Cheng *et al.,* 2022), in-situ field measurements (Reynolds *et al.,* 2007, 2009; King *et al.,* 2011; Strong *et al.,* 2011; Haustein *et al.,* 2015; Cui *et al.,* 2019a; Klose *et al.*, 2019; von Holdt *et al.,* 2019;

Sweeney *et al.,* 2022; Dickey *et al.,* 2023) and laboratory experiments (Buck *et al.,* 2011; Nield *et al.,* 2015, 2016a,b) that demonstrate similar dynamics occurring in various other saline and ephemeral lake bed environments worldwide. Therefore, it is proposed that attempts to better represent the controls and seasonal variations in surface moisture dynamics and subsequent moisture-related effects on surface salt crust properties and sediment availability would be a key and worthwhile endeavour towards improving large-scale model simulations of dust emissions from ephemeral lake bed sources.

It is recognised that refinements to surface parameters within coarse-scale dust model estimates remain inherently challenging due to scaling issues and difficulties with obtaining in-situ measurement data (Shao *et al.,* 2011; Bryant, 2013; Kandakji *et al.,* 2020; Kok *et al.,* 2021a; Baddock *et al.,* 2021). The research presented in this thesis demonstrates a comprehensive analysis approach. It draws necessary connections between field-based observations of local-scale processes and erodibility conditions controlling dust production at the surface with the space and time scales of satellite remote sensing observations of dust plume frequencies and dynamics, surface properties (e.g., mineralogy), and broader-scale hydrological and climatic drivers used in the parameterisation, calibration and validation of regional and global dust models. This analysis approach could be applied to study similar ephemeral playa dust sources elsewhere, providing a critical evidence base to support model estimates of dust production from these globally significant source regions.

REFERENCE LIST

Abell, J.T., Rahimi, S.R., Pullen, A., Lebo, Z.J., Zhang, D., Kapp, P., Gloege, L., Ridge, S., Nie, J. and Winckler, G. (2020) A Quantitative Model-Based Assessment of Stony Desert Landscape Evolution in the Hami Basin, China: Implications for Plio-Pleistocene Dust Production in Eastern Asia. *Geophysical Research Letters*, *47*(20), e2020GL090064.

Acharya, T.D., Lee, D.H., Yang, I.T. and Lee, J.K. (2016) Identification of water bodies in a Landsat 8 OLI image using a J48 decision tree. *Sensors*, *16*(7), 1075.

Ackerman, S.A. (1997) Remote sensing aerosols using satellite infrared observations. *Journal of Geophysical Research: Atmospheres*, *102*(D14), 17069–17079.

Ackerman, S.A., Strabala, K.I., Menzel, W.P., Frey, R.A., Moeller, C.C. and Gumley, L.E. (1998) Discriminating clear sky from clouds with MODIS. *Journal of Geophysical Research: Atmospheres*, *103*(D24), 32141–32157.

Adebiyi, A.A., Kok, J.F., Wang, Y., Ito, A., Ridley, D.A., Nabat, P. and Zhao, C. (2020) Dust Constraints from joint Observational-Modelling-experiMental analysis (DustCOMM): comparison with measurements and model simulations. *Atmospheric Chemistry and Physics*, *20*(2), 829–863.

Adebiyi, A.A., Kok, J.F., Murray, B.J., Ryder, C.L., Stuut, J.B.W., Kahn, R.A., Knippertz, P., Formenti, P., Mahowald, N.M., García-Pando, C.P. and Klose, M. (2023) A review of coarse mineral dust in the Earth system. *Aeolian Research*, *60*, 100849.

Ahmadi-Molaverdi, M., Jabbari, I. and Fathnia, A. (2022) Geomorphological and spatial analysis of dust sources in Ilam Province, Iran. *Sedimentary Geology*, *436*, 106168.

Ahn, C., Torres, O. and Bhartia, P.K. (2008) Comparison of ozone monitoring instrument UV aerosol products with Aqua/Moderate Resolution Imaging Spectroradiometer and Multiangle Imaging Spectroradiometer observations in 2006. *Journal of Geophysical Research: Atmospheres*, *113*(D16).

Ahn, C., Torres, O. and Jethva, H. (2014) Assessment of OMI near-UV aerosol optical depth over land. *Journal of Geophysical Research: Atmospheres*, *119*(5), 2457–2473.

Akhlaq, M., Sheltami, T.R. and Mouftah, H.T. (2012) A review of techniques and technologies for sand and dust storm detection. *Reviews in Environmental Science and Bio/Technology*, *11*(3), 305–322.

Alanazi, H.A. and Ghrefat, H.A. (2013) Spectral analysis of multispectral Landsat 7 ETM+ and ASTER data for mapping land cover at Qurayah Sabkha, Northern Saudi Arabia. *Journal of the Indian Society of Remote Sensing*, *41*, 833–844.

Albani, S., Mahowald, N.M., Perry, A.T., Scanza, R.A., Zender, C.S., Heavens, N.G., Maggi, V., Kok, J.F. and Otto-Bliesner, B.L. (2014) Improved dust representation in the Community Atmosphere Model. *Journal of Advances in Modeling Earth Systems*, *6*(3), 541–570.

Alduchov, O.A. and Eskridge, R.E. (1996) Improved Magnus form approximation of saturation vapor pressure. *Journal of Applied Meteorology and Climatology*, *35*(4), 601–609.

Alleaume, S., Hely, C., Le Roux, J., Korontzi, S., Swap, R.J., Shugart, H.H. and Justice, C.O. (2005) Using MODIS to evaluate heterogeneity of biomass burning in southern African savannahs: a case study in Etosha. *International Journal of Remote Sensing*, *26*(19), 4219–4237.

Allen, C.J., Washington, R. and Engelstaedter, S. (2013) Dust emission and transport mechanisms in the central Sahara: Fennec ground-based observations from Bordj Badji Mokhtar, June 2011. *Journal of Geophysical Research: Atmospheres*, *118*(12), 6212–6232.

Allen, C.J. and Washington, R. (2014) The low-level jet dust emission mechanism in the central Sahara: Observations from Bordj-Badji Mokhtar during the June 2011 Fennec Intensive Observation Period. *Journal of Geophysical Research: Atmospheres*, *119*(6), 2990–3015.

Allen, C.J., Washington, R. and Saci, A. (2015) Dust detection from ground-based observations in the summer global dust maximum: Results from Fennec 2011 and 2012 and implications for modeling and field observations. *Journal of Geophysical Research: Atmospheres*, *120*(3), 897–916.

Alsumaiti, T.S., Hussein, K., Ghebreyesus, D.T. and Sharif, H.O. (2020) Performance of the CMORPH and GPM IMERG Products over the United Arab Emirates. *Remote Sensing*, *12*(9), 1426.

Amézketa, E. (1999) Soil aggregate stability: a review. *Journal of sustainable agriculture*, *14*(2-3), 83–151.

Aminou, D.M.A. (2002) MSG's SEVIRI instrument. *ESA Bulletin (0376-4265)*, 111, 15–17.

Amit, R. and Yaalon, D.H. (1996) The micromorphology of gypsum and halite in Reg soils—The Negev Desert, Israel. *Earth Surface Processes and Landforms*, *21*(12), 1127–1143.

Anisimov, A., Tao, W., Stenchikov, G., Kalenderski, S., Prakash, P.J., Yang, Z.L. and Shi, M. (2017) Quantifying local-scale dust emission from the Arabian Red Sea coastal plain. *Atmospheric Chemistry and Physics*, *17*(2), 993–1015.

Ansmann, A., Rittmeister, F., Engelmann, R., Basart, S., Jorba, O., Spyrou, C., Remy, S., Skupin, A., Baars, H., Seifert, P. and Senf, F. (2017) Profiling of Saharan dust from the Caribbean to western Africa–Part 2: Shipborne lidar measurements versus forecasts. *Atmospheric Chemistry and Physics*, *17*(24), 14987–15006.

Artieda, O., Davila, A., Wierzchos, J., Buhler, P., Rodríguez-Ochoa, R., Pueyo, J. and Ascaso, C. (2015) Surface evolution of salt-encrusted playas under extreme and continued dryness. *Earth Surface Processes and Landforms*, *40*(14), 1939-1950.

Ashpole, I. and Washington, R. (2012) An automated dust detection using SEVIRI: A multiyear climatology of summertime dustiness in the central and western Sahara. *Journal of Geophysical Research: Atmospheres*, *117*(D8).

Ashpole, I. and Washington, R. (2013) A new high-resolution central and western Saharan summertime dust source map from automated satellite dust plume tracking. *Journal of Geophysical Research: Atmospheres*, *118*(13), 6981–6995.

Baddock, M.C., Bullard, J.E. and Bryant, R.G. (2009) Dust source identification using MODIS: a comparison of techniques applied to the Lake Eyre Basin, Australia. *Remote Sensing of Environment*, *113*(7), 1511–1528.

Baddock, M.C., Gill, T.E., Bullard, J.E., Acosta, M.D. and Rivera Rivera, N.I. (2011a) Geomorphology of the Chihuahuan Desert based on potential dust emissions. *Journal of Maps*, *7*(1), 249–259.

Baddock, M.C., Zobeck, T.M., Van Pelt, R.S. and Fredrickson, E.L. (2011b) Dust emissions from undisturbed and disturbed, crusted playa surfaces: cattle trampling effects. *Aeolian Research*, *3*(1), 31–41.

Baddock, M.C., Parsons, K., Strong, C., Leys, J. and McTainsh, G. (2015) Drivers of Australian dust: a case study of frontal winds and dust dynamics in the lower Lake Eyre basin. *Earth Surface Processes and Landforms*, *40*(14), 1982–1988.

Baddock, M.C., Ginoux, P., Bullard, J.E. and Gill, T.E. (2016) Do MODIS-defined dust sources have a geomorphological signature? *Geophysical Research Letters*, *43*(6), 2606–2613.

Baddock, M.C., Bryant, R.G., Acosta, M.D. and Gill, T.E. (2021) Understanding dust sources through remote sensing: Making a case for CubeSats. *Journal of Arid Environments*, *184*, 104335.

Bakker, N.L., Drake, N.A. and Bristow, C.S. (2019) Evaluating the relative importance of northern African mineral dust sources using remote sensing. *Atmospheric Chemistry and Physics*, *19*(16), 10525–10535.

Banks, J.R. and Brindley, H.E. (2013) Evaluation of MSG-SEVIRI mineral dust retrieval products over North Africa and the Middle East. *Remote Sensing of Environment*, *128*, 58–73.

Banks, J.R., Brindley, H.E., Hobby, M. and Marsham, J.H. (2014) The daytime cycle in dust aerosol direct radiative effects observed in the central Sahara during the Fennec campaign in June 2011. *Journal of Geophysical Research: Atmospheres*, *119*(24), 13861–13876.

Banks, J.R., Hünerbein, A., Heinold, B., Brindley, H.E., Deneke, H. and Schepanski, K. (2019) The sensitivity of the colour of dust in MSG-SEVIRI Desert Dust

infrared composite imagery to surface and atmospheric conditions. *Atmospheric Chemistry and Physics*, *19*(10), 6893–6911.

Banks, J.R., Heinold, B. and Schepanski, K., 2022. Impacts of the desiccation of the Aral Sea on the Central Asian dust life-cycle. *Journal of Geophysical Research: Atmospheres*, *127*(21), e2022JD036618.

Bauer, S.E., Mishchenko, M.I., Lacis, A.A., Zhang, S., Perlwitz, J. and Metzger, S.M. (2007) Do sulfate and nitrate coatings on mineral dust have important effects on radiative properties and climate modeling? *Journal of Geophysical Research: Atmospheres*, *112*(D6).

Behera, S.K. and Yamagata, T. (2001) Subtropical SST dipole events in the southern Indian Ocean. *Geophysical Research Letters, 28*(2), 327–330.

Belnap, J., Munson, S.M. and Field, J.P. (2011) Aeolian and fluvial processes in dryland regions: the need for integrated studies. *Ecohydrology*, *4*(5), 615–622.

Ben-Dor, E., Chabrillat, S., Demattê, J.A.M., Taylor, G.R., Hill, J., Whiting, M.L. and Sommer, S. (2009) Using imaging spectroscopy to study soil properties. *Remote Sensing of Environment*, *113*, S38-S55.

Bergametti, G., Marticorena, B., Rajot, J. L., Foret, G., Alfaro, S. C. and Laurent, B. (2018) Size-resolved dry deposition velocities of dust particles: In situ measurements and parameterizations testing. *Journal of Geophysical Research: Atmospheres, 123*(19), 11080–11099.

Bergametti, G., Rajot, J. L., Marticorena, B., Féron, A., Gaimoz, C., Chatenet, B., Coulibaly, M., Koné, I., Maman, A. and Zakou, A. (2022) Rain, wind, and dust concentrations in the Sahel. *Journal of Geophysical Research: Atmospheres, 127*(3), e2021JD035802.

Berndt, E.B., Elmer, N.J., Junod, R.A., Fuell, K.K., Harkema, S.S., Burke, A.R. and Feemster, C.M. (2021) A machine learning approach to objective identification of dust in satellite imagery. *Earth and Space Science*, *8*(6), e2021EA001788.

Bhattachan, A., D'Odorico, P., Baddock, M.C., Zobeck, T.M., Okin, G.S. and Cassar, N. (2012) The Southern Kalahari: a potential new dust source in the Southern Hemisphere? *Environmental Research Letters*, *7*(2), 024001.

Bhattachan, A., D'Odorico, P. and Okin, G.S. (2015) Biogeochemistry of dust sources in Southern Africa. *Journal of Arid Environments*, *117*, 18–27.

Bilal, M., Nichol, J.E. and Wang, L. (2017) New customized methods for improvement of the MODIS C6 Dark Target and Deep Blue merged aerosol product. *Remote Sensing of Environment*, *197*, 115–124.

Bin Abdulwahed, A., Dash, J. and Roberts, G. (2019) An evaluation of satellite dust-detection algorithms in the Middle East region. *International Journal of Remote Sensing*, *40*(4), 1331–1356.

Bowen, B.B., Kipnis, E.L. and Raming, L.W. (2017) Temporal dynamics of flooding, evaporation, and desiccation cycles and observations of salt crust area change at the Bonneville Salt Flats, Utah. *Geomorphology*, *299*, 1–11.

Bowler, J.M. (1973) Clay dunes: their occurrence, formation and environmental significance. *Earth-Science Reviews*, *9*(4), 315–338.

Bowler, J.M. (1986) Spatial variability and hydrologic evolution of Australian lake basins: analogue for Pleistocene hydrologic change and evaporite formation. *Palaeogeography, Palaeoclimatology, Palaeoecology*, *54*(1–4), 21–41.

Breit, G.N. (2022) Email to Natasha S. Wallum, 11 September.

Brindley, H., Knippertz, P., Ryder, C. and Ashpole, I. (2012) A critical evaluation of the ability of the Spinning Enhanced Visible and Infrared Imager (SEVIRI) thermal infrared red-green- blue rendering to identify dust events: Theoretical analysis. *Journal of Geophysical Research: Atmospheres*, *117*(D7).

Brungard, C.W., Boettinger, J.L. and Hipps, L.E. (2015) Wind erosion potential of lacustrine and alluvial soils before and after disturbance in the eastern Great Basin, USA: Estimating threshold friction velocity using easier-to-measure soil properties. *Aeolian Research*, *18*, 185–203.

Bryant, R.G. (1996) Validated linear mixture modelling of Landsat TM data for mapping evaporite minerals on a playa surface: methods and applications. *International Journal of Remote Sensing*, *17*(2), 315–330.

Bryant, R.G. (2003) Monitoring hydrological controls on dust emissions: preliminary observations from Etosha Pan, Namibia. *Geographical Journal*, *169*(2), 131–141.

Bryant, R.G. (2013) Recent advances in our understanding of dust source emission processes. *Progress in Physical Geography*, *37*(3), 397–421.

Bryant, R.G. and Rainey, M.P. (2002) Investigation of flood inundation on playas within the Zone of Chotts, using a time-series of AVHRR, *Remote Sensing of Environment*, 82(2–3), 360–375.

Bryant, R.G., Bigg, G.R., Mahowald, N.M., Eckardt, F.D. and Ross, S.G. (2007) Dust emission response to climate in southern Africa. *Journal of Geophysical Research: Atmospheres*, *112*(D9).

Bryant, R.G., Eckardt, F.D., Vickery, K., Wiggs, G.F.S., Hipondoka, M., Murray, J.E., Brindley, H., King, J., Nield, J., Thomas, D.S.G. and Washington, R. (2015)

Remote sensing of dust source characteristics and emission controls on a large playa, *Geophysical Research Abstracts EGU General Assembly*.

Bryant, R. G. and Baddock, M. C. (2021) Remote sensing of aeolian processes. Reference Module in Earth Systems and Environmental Sciences, 84–119.

Buch, M.W. and Rose, D. (1996) Mineralogy and geochemistry of the sediments of the Etosha Pan Region in northern Namibia: a reconstruction of the depositional environment. *Journal of African Earth Sciences*, *22*(3), 355–378.

Bucher, E.H. and Stein, A.F. (2016) Large salt dust storms follow a 30-year rainfall cycle in the Mar Chiquita Lake (Córdoba, Argentina). *PloS one*, *11*(6), e0156672.

Buck, B.J. and Van Hoesen, J.G. (2002) Snowball morphology and SEM analysis of pedogenic gypsum, southern New Mexico, USA. *Journal of Arid Environments*, *51*(4), 469–487.

Buck, B.J., Wolff, K., Merkler, D.J. and McMillan, N.J. (2006) Salt mineralogy of Las Vegas Wash, Nevada: morphology and subsurface evaporation. *Soil Science Society of America Journal*, *70*(5), 1639–1651.

Buck, B.J., King, J. and Etyemezian, V. (2011) Effects of salt mineralogy on dust emissions, Salton Sea, California. *Soil Science Society of America Journal*, *75*(5), 1971–1985.

Bullard, J. (2010) Bridging the gap between field data and global models: current strategies in aeolian research. *Earth Surface Processes and Landforms*, *35*(4), 496–499.

Bullard, J., Baddock, M.C., McTainsh, G. and Leys, J. (2008) Sub-basin scale dust source geomorphology detected using MODIS. *Geophysical Research Letters*, *35*(15).

Bullard, J.E., Harrison, S.P., Baddock, M.C., Drake, N., Gill, T.E., McTainsh, G. and Sun, Y. (2011) Preferential dust sources: A geomorphological classification designed for use in global dust-cycle models. *Journal of Geophysical Research: Earth Surface*, *116*(F4).

Cahill, T.A., Gill, T.E., Reid, J.S., Gearhart, E.A. and Gillette, D.A. (1996) Saltating particles, playa crusts and dust aerosols at Owens (dry) Lake, California. *Earth Surface Processes and Landforms*, *21*(7), 621–639.

Cakmur, R.V., Miller, R.L., Perlwitz, J., Geogdzhayev, I.V., Ginoux, P., Koch, D., Kohfeld, K.E., Tegen, I. and Zender, C.S. (2006) Constraining the magnitude of the global dust cycle by minimizing the difference between a model and observations. *Journal of Geophysical Research: Atmospheres*, *111*(D6).

Caton Harrison, T., Washington, R. and Engelstaedter, S. (2019) A 14 year climatology of Saharan dust emissions mechanisms inferred from automatically tracked dust plumes. *Journal of Geophysical Research: Atmospheres, 124,* 9665–9690.

Caton Harrison, T., Washington, R. and Engelstaedter, S. (2021) Satellite-derived characteristics of Saharan cold pool outflows during boreal summer. *Journal of Geophysical Research: Atmospheres*, *126*(3), e2020JD033387.

Chapman, J.E., Rothery, D. A., Francis, P. W. and Pontual, A. (1989) Remote sensing of evaporite mineral zonation in salt flats (salars). *International Journal of Remote Sensing, 10*(1), 245–255.

Chappell, A., Mctainsh, G., Leys, J. and Strong, C. (2003) Using geostatistics to elucidate temporal change in the spatial variation of aeolian sediment transport. *Earth Surface Processes and Landforms: The Journal of the British Geomorphological Research Group*, *28*(6), 567–585.

Chappell, A., Van Pelt, S., Zobeck, T. and Dong, Z. (2010) Estimating aerodynamic resistance of rough surfaces using angular reflectance. *Remote Sensing of Environment*, *114*(7), 1462–1470.

Chappell, A., Webb, N.P., Hennen, M., Schepanski, K., Ciais, P., Balkanski, Y., Zender, C.S., Tegen, I., Zeng, Z., Tong, D. and Baker, B. (2023a) Satellites reveal Earth's seasonally shifting dust emission sources. *Science of the Total Environment*, *883*, 163452.

Chappell, A., Webb, N.P., Hennen, M., Zender, C.S., Ciais, P., Schepanski, K., Edwards, B.L., Ziegler, N.P., Balkanski, Y., Tong, D. and Leys, J.F. (2023b) Elucidating hidden and enduring weaknesses in dust emission modeling. *Journal of Geophysical Research: Atmospheres*, *128*(17), e2023JD038584.

Chauvigné, A., Waquet, F., Auriol, F., Blarel, L., Delegove, C., Dubovik, O., Flamant, C., Gaetani, M., Goloub, P., Loisil, R. and Mallet, M. (2021) Aerosol above-cloud direct radiative effect and properties in the Namibian region during the AErosol, RadiatiOn, and CLOuds in southern Africa (AEROCLO-sA) field campaign–Multi-Viewing, Multi-Channel, Multi-Polarization (3MI) airborne simulator and sun photometer measurements. *Atmospheric Chemistry and Physics*, *21*(10), 8233–8253.

Che, X., Feng, M., Jiang, H., Song, J. and Jia, B. (2015) Downscaling MODIS Surface Reflectance to Improve Water Body Extraction. *Advances in Meteorology, 2015,* 1–13.

Che, X., Feng, M., Sexton, J., Channan, S., Sun, Q., Ying, Q., Liu, J. and Wang, Y. (2019) Landsat- based estimation of seasonal water cover and change in arid and semi-arid Central Asia (2000–2015). *Remote Sensing*, *11*(11), 1323.

Chen, J., Zhu, X., Vogelmann, J.E., Gao, F. and Jin, S. (2011) A simple and effective method for filling gaps in Landsat ETM+ SLC-off images. *Remote sensing of environment*, *115*(4), 1053–1064.

Chen, S., Huang, J., Zhao, C., Qian, Y., Leung, L.R. and Yang, B. (2013) Modeling the transport and radiative forcing of Taklimakan dust over the Tibetan Plateau: A case study in the summer of 2006. *Journal of Geophysical Research: Atmospheres*, *118*(2), 797–812.

Chen, S., Jiang, N., Huang, J., Xu, X., Zhang, H., Zang, Z., Huang, K., Xu, X., Wei, Y., Guan, X. and Zhang, X. (2018) Quantifying contributions of natural and anthropogenic dust emission from different climatic regions. *Atmospheric Environment*, *191*, 94–104.

Chen, W., Meng, H., Song, H. and Zheng, H. (2022) Progress in dust modelling, global dust budgets, and soil organic carbon dynamics. *Land*, *11*(2), 176.

Cheng, Y.B., Dickey, H., Yimam, Y.T., Schmid, B., Paxton, B., Schreuder, M. and Tran, R. (2022) Land surface parameterization at exposed playa and desert region to support dust emissions estimates in southern California, United States. *Remote Sensing*, *14*(3), 616.

Claquin, T., Schulz, M. and Balkanski, Y.J. (1999) Modeling the mineralogy of atmospheric dust sources. *Journal of Geophysical Research: Atmospheres*, *104*(D18), 22243–22256.

Clark, R.N. and Rencz, A.N. (1999) Spectroscopy of rocks and minerals, and principles of spectroscopy. *Manual of Remote Sensing*, *3*(11), 3–58.

Clements, M. and Washington, R. (2021) Atmospheric Controls on Mineral Dust Emission From the Etosha Pan, Namibia: Observations From the CLARIFY-

2016 Field Campaign. *Journal of Geophysical Research: Atmospheres*, *126*(14), e2021JD034746.

Clements, M. and Washington, R. (2023) Summer Dust Emissions From the Etosha Pan, Namibia: The Role of the Namib Anabatic-Sea Breeze System. *Journal of Geophysical Research: Atmospheres*, *128*(6), e2022JD036815.

Cogliati, S., Sarti, F., Chiarantini, L., Cosi, M., Lorusso, R., Lopinto, E., Miglietta, F., Genesio, L., Guanter, L., Damm, A. and Pérez-López, S. (2021) The PRISMA imaging spectroscopy mission: Overview and first performance analysis. *Remote Sensing of Environment*, *262*, 112499.

Congalton, R.G. and Green, K. (Eds.) (2019) *Assessing the Accuracy of Remotely Sensed Data: Principles and Practices* (3rd ed.) Boca Raton, FL: CRC Press.

Connelly, D.S., Thompson, D.R., Mahowald, N.M., Li, L., Carmon, N., Okin, G.S., Green, R.O. (2021) The EMIT mission information yield for mineral dust radiative forcing. *Remote Sensing of Environment, 258*, 113380.

Cooley, S.W., Smith, L.C., Ryan, J.C., Pitcher, L.H. and Pavelsky, T.M. (2019) Arctic-Boreal lake dynamics revealed using CubeSat imagery. *Geophysical Research Letters*, *46*(4), 2111–2120.

Crétat, J., Pohl, B., Dieppois, B., Berthou, S. and Pergaud, J. (2019) The Angola Low: relationship with southern African rainfall and ENSO. *Climate Dynamics*, *52*(3), 1783–1803.

Crouvi, O., Schepanski, K., Amit, R., Gillespie, A.R. and Enzel, Y. (2012) Multiple dust sources in the Sahara Desert: The importance of sand dunes. *Geophysical Research Letters*, *39*(13).

Crouvi, O., Dayan, U., Amit, R. and Enzel, Y. (2017) An Israeli haboob: Sea breeze activating local anthropogenic dust sources in the Negev loess. *Aeolian Research*, *24*, 39–52.

Crowley, J.K. (1991) Visible and near-infrared (0.4–2.5 μm) reflectance spectra of playa evaporite minerals. *Journal of Geophysical Research, 96*(B10), 16231–16231.

Crowley, J.K. (1993) Mapping playa evaporite minerals with AVIRIS data: A first report from Death Valley, California. *Remote Sensing of Environment*, *44*(2-3), 337–356.

Crowley, J.K. and Hook, S.J. (1996) Mapping playa evaporite minerals and associated sediments in Death Valley, California, with multispectral thermal infrared images. *Journal of Geophysical Research: Solid Earth*, *101*(B1), 643–660.

Crusius, J., Schroth, A.W., Gasso, S., Moy, C.M., Levy, R.C. and Gatica, M. (2011) Glacial flour dust storms in the Gulf of Alaska: Hydrologic and meteorological controls and their importance as a source of bioavailable iron. *Geophysical Research Letters*, *38*(6).

Csavina, J., Field, J., Félix, O., Corral-Avitia, A.Y., Sáez, A.E. and Betterton, E.A. (2014) Effect of wind speed and relative humidity on atmospheric dust concentrations in semi-arid climates. *Science of the Total Environment*, *487*, 82–90.

Cui, M., Lu, H., Sweeney, M.R., Mason, J.A., Feng, H. and Xu, Z. (2015) PM_{10} emission flux in the Tengger Desert and Mu Us Sand Field, northern China, measured by PI-SWERL. *Science Bulletin, 60*(17), 1621–1630.

Cui, M., Lu, H., Wiggs, G.F.S., Etyemezian, V., Sweeney, M.R. and Xu, Z. (2019a) Quantifying the effect of geomorphology on aeolian dust emission potential in northern China. *Earth Surface Processes and Landforms*, *44*(14), 2872–2884.

Cui, M., Lu, H., Etyemezian, V. and Su, Q. (2019b) Quantifying the emission potentials of fugitive dust sources in Nanjing, East China. *Atmospheric Environment*, *207*, 129–135.

Cuthbert, M.O., Taylor, R.G., Favreau, G., Todd, M.C., Shamsudduha, M., Villholth, K.G., MacDonald, A.M., Scanlon, B.R., Kotchoni, D.V., Vouillamoz, J.M. and Lawson, F.M. (2019) Observed controls on resilience of groundwater to climate variability in sub-Saharan Africa. *Nature*, *572*(7768), 230–234.

d'Andrimont, R. and Defourny, P. (2018) Monitoring African water bodies from twice-daily MODIS observation. *GIScience & Remote Sensing*, *55*(1), 130–153.

Dai, Y., Zhang, C., Cen, S., Wang, X., Liu, X. and Zhang, H. (2020) Abrasion of soil clods with different textures and moisture contents in sand flow environment. *Aeolian Research*, *46*, 100614.

Dai, J., Zhang, G., Liu, L., Shi, P., Zhang, H., Han, X., Xue, K., Hu, X., Zhang, J., Xiang, M. and Xiao, Y. (2022) Effects of efflorescence and subflorescence by different salts on soil physical properties and aeolian erosion. *Catena*, *215*, 106323.

Dansie, A.P., Wiggs, G.F.S. and Thomas, D.S.G. (2017a) Iron and nutrient content of wind-erodible sediment in the ephemeral river valleys of Namibia. *Geomorphology*, *290*, 335–346.

Dansie, A.P., Wiggs, G.F.S., Thomas, D.S.G. and Washington, R. (2017b) Measurements of windblown dust characteristics and ocean fertilization potential: The ephemeral river valleys of Namibia. *Aeolian research*, *29*, 30–41.

Dansie, A.P., Thomas, D.S.G., Wiggs, G.F.S. and Munkittrick, K.R. (2018) Spatial variability of ocean fertilizing nutrients in the dust-emitting ephemeral river catchments of Namibia. *Earth Surface Processes and Landforms*, *43*(3), 563–578.

Dansie, A.P., Thomas, D.S., Wiggs, G.F.S., Baddock, M.C. and Ashpole, I. (2022) Plumes and blooms–Locally-sourced Fe-rich aeolian mineral dust drives phytoplankton growth off southwest Africa. *Science of the Total Environment*, *829*, 154562.

Darmenova, K., Sokolik, I.N., Shao, Y., Marticorena, B. and Bergametti, G. (2009) Development of a physically based dust emission module within the Weather Research and Forecasting (WRF) model: Assessment of dust emission parameterizations and input parameters for source regions in Central and East Asia. *Journal of Geophysical Research: Atmospheres*, *114*(D14).

Dash, J. and Ogutu, B.O. (2016) Recent advances in space-borne optical remote sensing systems for monitoring global terrestrial ecosystems. *Progress in Physical Geography*, *40*(2), 322–351.

De Deckker, P. (2019) An evaluation of Australia as a major source of dust. *Earth-Science Reviews*, *194*, 536–567.

De Deckker, P., Munday, C.I., Brocks, J., O'Loingsigh, T., Allison, G.E., Hope, J., Norman, M., Stuut, J.B.W., Tapper, N.J. and van der Kaars, S. (2014) Characterisation of the major dust storm that traversed over eastern Australia in September 2009; a multidisciplinary approach. *Aeolian Research*, *15*, 133–149.

Deus, D. and Gloaguen, R. (2013) Remote sensing analysis of lake dynamics in semi-arid regions: implication for water resource management. Lake Manyara, East African Rift, Northern Tanzania. *Water*, *5*(2), 698–727.

Dickey, H., Schreuder, M., Schmid, B. and Yimam, Y.T. (2023) Quantifying dust emission potential of playa and desert surfaces in the Salton Sea Air Basin, California, United States. *Aeolian Research, 60*(100850).

Domingo, R.A., Southard, R.J. and Lee, K. (2010) Laboratory system for dust generation from soils. *Journal of Environmental Quality*, *39*(4), 1254–1261.

Drake, N.A. (1995) Reflectance spectra of evaporite minerals (400-2500 nm): applications for remote sensing. *International Journal of Remote Sensing*, *16*(14), 2555–2571.

Drake, N.A., Bryant, R.G., Millington, A.C. and Townshend, J.R. (1994) Playa sedimentology and geomorphology: Mixture modelling applied to Landsat Thematic Mapper data of Chott el Djerid, Tunisia. *Sedimentology and Geochemistry of Modern and Ancient Saline Lakes, SEPM Special Publication 50,* 125–131.

Duan, W., Maskey, S., Chaffe, P.L., Luo, P., He, B., Wu, Y. and Hou, J. (2021) Recent advancement in remote sensing technology for hydrology analysis and water resources management. *Remote Sensing*, *13*(1097).

Eck, T.F., Holben, B.N., Reid, J.S., Mukelabai, M.M., Piketh, S.J., Torres, O., Jethva, H.T., Hyer, E.J., Ward, D.E., Dubovik, O. and Sinyuk, A. (2013) A seasonal trend of single scattering albedo in southern African biomass-burning particles: Implications for satellite products and estimates of emissions for the world's largest biomass-burning source. *Journal of Geophysical Research: Atmospheres*, *118*(12), 6414–6432.

Eckardt, F.D., Washington, R. and Wilkinson, M.J. (2001) The origin of dust on the west coast of southern Africa. *Palaeoecology of Africa*, *27*, 207–219.

Eckardt, F.D., Bekiswa, S., von Holdt, J.R.C., Jack, C., Kuhn, N.J., Mogane, F., Murray, J.E., Ndara, N. and Palmer, A.R. (2020) South Africa's agricultural dust sources and events from MSG SEVIRI. *Aeolian Research*, *47*, 100637.

ECMWF (2021) IFS Documentation CY47R3: Part IV Physical Processes. Available: https://www.ecmwf.int/en/elibrary/81271-ifs-documentation-cy47r3-part-iv-physical-processes.

Ellis, J.T., Sherman, D.J., Farrell, E.J. and Li, B. (2012) Temporal and spatial variability of aeolian sand transport: Implications for field measurements. *Aeolian Research*, *3*(4), 379–387.

Elmore, A.J., Kaste, J.M., Okin, G.S. and Fantle, M.S. (2008) Groundwater influences on atmospheric dust generation in deserts. *Journal of Arid Environments*, *72*(10), 1753–1765.

Enfield, D.B., Mestas, A.M., Mayer, D.A. and Cid-Serrano, L. (1999) How ubiquitous is the dipole relationship in tropical Atlantic sea surface temperatures? *Journal of Geophysical Research: Oceans, 104,* 7841–7848.

Engelstaedter, S., Tegen, I. and Washington, R. (2006) North African dust emissions and transport. *Earth-Science Reviews*, *79*(1-2), 73–100.

Engelstaedter, S. and Washington, R. (2007a) Atmospheric controls on the annual cycle of North African dust. *Journal of Geophysical Research: Atmospheres*, *112*(D3).

Engelstaedter, S. and Washington, R. (2007b) Temporal controls on global dust emissions: The role of surface gustiness. *Geophysical Research Letters*, *34*(15).

Engert, S. (1997) Spatial variability and temporal periodicity of rainfall in the Etosha National Park and surrounding areas in northern Namibia. *Madoqua*, *1997*(1), 115–120.

Eswaran, H. (1984) 'Scanning electron microscopy of salt.' In: Murray, L. (Ed.) *McGraw-Hill yearbook of science and technology.* New York, NY, USA: McGraw-Hill Book Co., 403–405.

Etyemezian, V., Nikolich, G., Ahonen, S., Pitchford, M., Sweeney, M., Purcell, R., Gillies, J. and Kuhns, H. (2007) The Portable In Situ Wind Erosion Laboratory (PI-SWERL): A new method to measure PM10 windblown dust properties and potential for emissions. *Atmospheric Environment*, *41*(18), 3789–3796.

Etyemezian, V., Gillies, J.A., Shinoda, M., Nikolich, G., King, J. and Bardis, A.R. (2014) Accounting for surface roughness on measurements conducted with PI-SWERL: Evaluation of a subjective visual approach and a photogrammetric technique. *Aeolian Research*, *13*, 35–50.

Eugster, H.P. and Hardie, L.A. (1978) 'Saline lakes.' In: Lerman, A. (Ed.) *Lakes: chemistry, geology, physics*. New York, NY, USA: Springer, 237–293.

Evan, A.T., Flamant, C., Fiedler, S. and Doherty, O. (2014) An analysis of aeolian dust in climate models. *Geophysical Research Letters*, *41*(16), 5996–6001.

Evan, A.T., Fiedler, S., Zhao, C., Menut, L., Schepanski, K., Flamant, C. and Doherty, O. (2015) Derivation of an observation-based map of North African dust emission. *Aeolian Research*, *16*, 153–162.

Falconieri, A., Papagiannopoulos, N., Marchese, F., Filizzola, C., Trippetta, S., Pergola, N., Pappalardo, G., Tramutoli, V. and Mona, L. (2020) Validation of

Ash/Dust Detections from SEVIRI Data Using ACTRIS/EARLINET Ground-Based LIDAR Measurements. *Remote Sensing*, *12*(7), 1172.

Fang, J., Yang, W., Luan, Y., Du, J., Lin, A. and Zhao, L. (2019) Evaluation of the TRMM 3B42 and GPM IMERG products for extreme precipitation analysis over China. *Atmospheric research*, *223*, 24–38.

Farr, T.G., Rosen, P.A., Caro, E., Crippen, R., Duren, R., Hensley, S., Kobrick, M., Paller, M., Rodriguez, E., Roth, L. and Seal, D. (2007) The shuttle radar topography mission. *Reviews of geophysics*, *45*(2), RG2004.

Feng, G., Sharratt, B. and Vaddella, V. (2013) Windblown soil crust formation under light rainfall in a semiarid region. *Soil and tillage research*, *128*, 91–96.

Ferrier, G., White, K., Griffiths, G., Bryant, R.G. and Stefouli, M. (2002) The mapping of hydrothermal alteration zones on the island of Lesvos, Greece using an integrated remote sensing dataset. *International Journal of Remote Sensing*, *23*(2), 341–356.

Feyisa, G.L., Meilby, H., Fensholt, R. and Proud, S.R. (2014) Automated Water Extraction Index: A new technique for surface water mapping using Landsat imagery. *Remote Sensing of Environment*, *140*, 23–35.

Fiedler, S., Schepanski, K., Heinold, B., Knippertz, P. and Tegen, I. (2013) Climatology of nocturnal low-level jets over North Africa and implications for modeling mineral dust emission. *Journal of Geophysical Research: Atmospheres*, *118*(12), 6100–6121.

Fisher, A., Flood, N. and Danaher, T. (2016) Comapring Landsat water index methods for automated water classification in eastern Australia. *Remote Sensing of Environment, 175,* 167–182.

Flahaut, J., Martinot, M., Bishop, J.L., Davies, G.R. and Potts, N.J. (2017) Remote sensing and in situ mineralogic survey of the Chilean salars: An analog to Mars evaporate deposits? *Icarus*, *282*, 152–173.

Fookes, P.G. and Lee, E.M. (2018) The engineering geology of playas, salt playas and salinas. *Quarterly Journal of Engineering Geology and Hydrogeology*, *51*(2), 287–298.

Formenti, P. (2023) Mineral dust in Namibia: new research on emissions, transport and properties, *EGU General Assembly 2023.* Vienna, Austria, 24–28 April 2023, EGU23-3887.

Formenti, P., D'Anna, B., Flamant, C., Mallet, M., Piketh, S.J., Schepanski, K., Waquet, F., Auriol, F., Brogniez, G., Burnet, F. and Chaboureau, J.P. (2019) The aerosols, radiation and clouds in southern Africa field campaign in Namibia: Overview, illustrative observations, and way forward. *Bulletin of the American Meteorological Society*, *100*(7), 1277–1298.

Forootan, E., Safari, A., Mostafaie, A., Schumacher, M., Delavar, M. and Awange, J.L. (2017) Large-scale total water storage and water flux changes over the arid and semiarid parts of the Middle East from GRACE and reanalysis products. *Surveys in Geophysics*, *38*(3), 591–615.

Francis, D., Nelli, N., Fonseca, R., Weston, M., Flamant, C. and Cherif, C. (2022) The dust load and radiative impact associated with the June 2020 historical Saharan dust storm. *Atmospheric Environment*, *268*, 118808.

Frazier, P.S. and Page, K.J. (2000) Water body detection and delineation with Landsat TM data. *Photogrammetric engineering and remote sensing*, *66*(12), 1461–1468.

Gadal, C., Delorme, P., Narteau, C., Wiggs, G.F., Baddock, M., Nield, J.M. and Claudin, P. (2022) Local wind regime induced by giant linear dunes: comparison of ERA5-Land reanalysis with surface measurements. *Boundary-Layer Meteorology*, *185*(3), 309–332.

Gaiero, D.M., Simonella, L., Gassó, S., Gili, S., Stein, A.F., Sosa, P., Becchio, R., Arce, J. and Marelli, H. (2013) Ground/satellite observations and atmospheric modeling of dust storms originating in the high Puna-Altiplano deserts (South America): Implications for the interpretation of paleo-climatic archives. *Journal of Geophysical Research: Atmospheres*, *118*(9), 3817–3831.

Gandhi, G.M., Parthiban, B.S., Thummalu, N. and Christy, A. (2015) NDVI: Vegetation change detection using remote sensing and GIS–A case study of Vellore District. *Procedia computer science*, *57*, 1199–1210.

Gao, B.C. (1996) NDWI—A normalized difference water index for remote sensing of vegetation liquid water from space. *Remote Sensing of Environment*, *58*(3), 257–266.

Gaughan, A.E., Staub, C.G., Hoell, A., Weaver, A. and Waylen, P.R. (2016) Inter- and Intra-annual precipitation variability and associated relationships to ENSO and the IOD in southern Africa. *International Journal of Climatology*, *36*(4), 1643–1656.

Gherboudj, I., Beegum, S.N., Marticorena, B. and Ghedira, H. (2015) Dust emission parameterization scheme over the MENA region: Sensitivity analysis to soil moisture and soil texture. *Journal of Geophysical Research: Atmospheres*, *120*(20), 10-915–10,938.

Gholampour, A., Nabizadeh, R., Hassanvand, M.S., Taghipour, H., Nazmara, S. and Mahvi, A.H. (2015) Characterization of saline dust emission resulted from Urmia

Lake drying. *Journal of Environmental Health Science and Engineering*, *13*, 1–11.

Ghrefat, H.A. and Goodell, P.C. (2011) Land cover mapping at Alkali Flat and Lake Lucero, White Sands, New Mexico, USA using multi-temporal and multi-spectral remote sensing data. *International Journal of Applied Earth Observation and Geoinformation*, *13*(4), 616–625.

Giglio, L., Descloitres, J., Justice, C.O. and Kaufman, Y. (2003) An enhanced contextual fire detection algorithm for MODIS. *Remote Sensing of Environment*, *87,* 273–282.

Giglio, L., Csiszar, I. and Justice, C.O. (2006) Global distribution and seasonality of active fires as observed with the Terra and Aqua MODIS sensors. *Journal of Geophysical Research Biogeosciences*, *111*, G02016.

Giglio, L., Schroeder, W. and Justice, C. O. (2016) The Collection 6 MODIS active fire detection algorithm and fire products. *Remote Sensing of Environment*, *178*, 31–41.

Gill, T.E. (1996) Eolian sediments generated by anthropogenic disturbance of playas: human impacts on the geomorphic system and geomorphic impacts on the human system. *Geomorphology*, *17*(1-3), 207–228.

Gill, T.E., Zobeck, T.M. and Stout, J.E. (2006) Technologies for laboratory generation of dust from geological materials. *Journal of hazardous materials*, *132*(1), 1–13.

Gillette, D.A. (1999) A qualitative geophysical explanation for "hot spot" dust emitting source regions. *Contributions to atmospheric physics*, *72*(1), 67–77.

Gillette, D.A., Blifford Jr, I.H. and Fryrear, D.W. (1974) The influence of wind velocity on the size distributions of aerosols generated by the wind erosion of soils. *Journal of Geophysical Research*, *79*(27), 4068–4075.

Gillette, D.A., Adams, J., Endo, A., Smith, D. and Kihl, R. (1980) Threshold velocities for input of soil particles into the air by desert soils. *Journal of Geophysical Research: Oceans*, *85*(C10), 5621–5630.

Gillette, D.A., Adams, J., Muhs, D. and Kihl, R. (1982) Threshold friction velocities and rupture moduli for crusted desert soils for the input of soil particles into the air. *Journal of Geophysical Research: Oceans*, *87*(C11), 9003–9015.

Gillette, D.A., Fryrear, D.W., Gill, T.E., Ley, T., Cahill, T.A. and Gearhart, E.A. (1997) Relation of vertical flux of particles smaller than 10 μm to total aeolian horizontal mass flux at Owens Lake. *Journal of Geophysical Research: Atmospheres*, *102*(D22), 26009–26015.

Gillette, D.A., Niemeyer, T.C. and Helm, P.J. (2001) Supply-limited horizontal sand drift at an ephemerally crusted, unvegetated saline playa. *Journal of Geophysical Research: Atmospheres*, *106*(D16), 18085–18098.

Ginoux, P., Chin, M., Tegen, I., Prospero, J.M., Holben, B., Dubovik, O. and Lin, S.J. (2001) Sources and distributions of dust aerosols simulated with the GOCART model. *Journal of Geophysical Research: Atmospheres*, *106*(D17), 20255–20273.

Ginoux, P., Garbuzov, D. and Hsu, N.C. (2010) Identification of anthropogenic and natural dust sources using Moderate Resolution Imaging Spectroradiometer (MODIS) Deep Blue level 2 data. *Journal of Geophysical Research: Atmospheres*, *115*(D5).

Ginoux, P., Prospero, J.M., Gill, T.E., Hsu, N.C. and Zhao, M. (2012) Global-scale attribution of anthropogenic and natural dust sources and their emission rates based on MODIS Deep Blue aerosol products. *Reviews of Geophysics*, *50*(3).

Gliß, J., Mortier, A., Schulz, M., Andrews, E., Balkanski, Y., Bauer, S.E., Benedictow, A.M., Bian, H., Checa-Garcia, R., Chin, M. and Ginoux, P. (2021) AeroCom phase III multi-model evaluation of the aerosol life cycle and optical properties using ground-and space-based remote sensing as well as surface in situ observations. *Atmospheric Chemistry and Physics*, *21*(1), 87–128.

Goetz, A.F., Vane, G., Solomon, J.E. and Rock, B.N. (1985) Imaging spectrometry for earth remote sensing. *Science*, *228*(4704), 1147–1153.

Goldstein, H.L., Breit, G.N. and Reynolds, R.L. (2017) Controls on the chemical composition of saline surface crusts and emitted dust from a wet playa in the Mojave Desert (USA). *Journal of Arid Environments*, *140*, 50–66.

Gonçalves Ageitos, M., Obiso, V., Miller, R.L., Jorba, O., Klose, M., Dawson, M., Balkanski, Y., Perlwitz, J., Basart, S., Di Tomaso, E. and Escribano, J. (2023) Modeling dust mineralogical composition: sensitivity to soil mineralogy atlases and their expected climate impacts. *Atmospheric Chemistry and Physics*, *23*(15), 8623–8657.

Good, E.J., Kong, X., Embury, O., Merchant, C.J. and Remedios, J.J. (2012) An infrared desert dust index for the Along-Track Scanning Radiometers. *Remote Sensing of Environment*, *116*, 159–176.

Goodall, T.M., North, C.P. and Glennie, K.W. (2000) Surface and subsurface sedimentary structures produced by salt crusts. *Sedimentology*, *47*(1), 99–118.

Goossens, D. (2004) Effect of soil crusting on the emission and transport of wind-eroded sediment: field measurements on loamy sandy soil. *Geomorphology*, *58*(1-4), 145–160.

Goossens, D. and Buck, B. (2009) Dust dynamics in off-road vehicle trails: Measurements on 16 arid soil types, Nevada, USA. *Journal of Environmental Management*, *90*(11), 3458–3469.

Gore, M., Abiodun, B.J. and Kucharski, F. (2020) Understanding the influence of ENSO patterns on drought over southern Africa using SPEEDY. *Climate Dynamics*, *54*(1), 307–327.

Goudie, A.S. (2008) The History and Nature of Wind Erosion in Deserts. *Annual Review of Earth and Planetary Sciences, 36,* 97–119.

Goudie, A.S. (2014) Desert dust and human health disorders. *Environment international*, *63*, 101–113.

Goudie, A.S. (2018) Dust storms and ephemeral lakes. *Desert*, *23*(1), 153–164.

Grasso, L., Bikos, D., Torres, J., Dostalek, J.F., Wu, T.C., Forsythe, J., Cronk, H.Q., Seaman, C.J., Miller, S.D., Berndt, E. and Weinman, H.G. (2021) Satellite imagery and products of the 16 – 17 February 2020 Saharan Air Layer dust event over the eastern Atlantic: impacts of water vapor on dust detection and morphology. *Atmospheric Measurement Techniques*, *14*(2), 1615–1634.

Greeley, R. (2020) Aeolian landforms: laboratory simulations and field studies. In: Nickling, W.G. (Ed.) *Aeolian Geomorphology,* Routledge: London, UK, 195–211.

Green, R.O., Mahowald, N.M., Thompson, D.R., Clark, R., Ehlmann, B., Ginoux, P., Kalashnikova, O., Miller, R., Okin, G.S., Painter, T. and Perez, C. (2019) The

Earth Surface Mineral Dust Source Investigation Planned for the International Space Station. *Geophysical Research Abstracts*, *21*, 1.

Green, R.O., Mahowald, N.M., Thompson, D.R., Ung, C., Brodrick, P., Pollock, R., Bennett, M., Lundeen, S., Joyce, M., Olson-Duvall, W. and Oaida, B. (2023) Performance and Early Results from the Earth Surface Mineral Dust Source Investigation (EMIT) Imaging Spectroscopy Mission. *2023 IEEE Aerospace Conference*, Big Sky, MT, USA, 1–10.

Grini, A., Myhre, G., Zender, C.S. and Isaksen, I.S. (2005) Model simulations of dust sources and transport in the global atmosphere: Effects of soil erodibility and wind speed variability. *Journal of Geophysical Research: Atmospheres*, *110*(D2).

Groll, M., Opp, C., and Aslanov, I. (2013) Spatial and temporal distribution of the dust deposition in Central Asia—Results from a long term monitoring program. *Aeolian Research, 9,* 49–62.

Grousset, F.E. and Biscaye, P.E. (2005) Tracing dust sources and transport patterns using Sr, Nd and Pb isotopes. *Chemical Geology*, *222*(3-4), 149–167.

Guo, H., Chen, S., Bao, A., Behrangi, A., Hong, Y., Ndayisaba, F., Hu, J. and Stepanian, P.M. (2016) Early assessment of integrated multi-satellite retrievals for global precipitation measurement over China. *Atmospheric Research*, *176*, 121–133.

Gürbüz, E. (2019) Multispectral mapping of evaporite minerals using ASTER data: A methodological comparison from central Turkey. *Remote Sensing Applications: Society and Environment*, *15*, 100240.

Haas, E.M., Bartholomé, E. and Combal, B. (2009) Time series analysis of optical remote sensing data for the mapping of temporary surface water bodies in sub-Saharan western Africa. *Journal of Hydrology, 370,* 52–63.

Haas, E.M., Bartholomé, E., Lambin, E.F. and Vanacker, V. (2011) Remotely sensed surface water extent as an indicator of short-term changes in ecohydrological processes in sub-Saharan Western Africa. *Remote Sensing of Environment, 115*, 3436–3445.

Hahnenberger, M. and Nicoll, K. (2014) Geomorphic and land cover identification of dust sources in the eastern Great Basin of Utah, USA. *Geomorphology*, *204*, 657–672.

Hamilton, D.S., Perron, M.M., Bond, T.C., Bowie, A.R., Buchholz, R.R., Guieu, C., Ito, A., Maenhaut, W., Myriokefalitakis, S., Olgun, N. and Rathod, S.D. (2022) Earth, wind, fire, and pollution: Aerosol nutrient sources and impacts on ocean biogeochemistry. *Annual Review of Marine Science*, *14*, 303–330.

Hamunyela, E., Hipondoka, M., Persendt, F., Nghiyalwa, H.S., Thomas, C. and Matengu, K. (2022) Spatio-temporal characterization of surface water dynamics with Landsat in endorheic Cuvelai-Etosha Basin (1990–2021). *ISPRS Journal of Photogrammetry and Remote Sensing*, *191*, 68–84.

Hamzehpour, N. and Marcolli, C. (2024) Soil crust development on playa surfaces of Lake Urmia and its controlling factors: New insights to combat dust sources. *Catena*, *237*, 107799.

Hao, X. and Qu, J.J. (2007) Saharan dust storm detection using moderate resolution imaging spectroradiometer thermal infrared bands. *Journal of Applied Remote Sensing*, *1*(1), 013510.

Harris, A. R. and Mason, I. M. (1989) Lake area measurement using the AVHRR. *International Journal of Remote Sensing, 10*, 885–895.

Hartshorn, E., Sion, B., Sweeney, M.R., and McDonald, E. (2023) Visual Surface Roughness Look-up Table for PI-SWERL Measurements. Available: https://www.dri.edu/itap/PI-SWERL-Roughness.

Haustein, K., Washington, R., King, J., Wiggs, G.F.S., Thomas, D.S.G., Eckardt, F.D., Bryant, R.G. and Menut, L. (2015) Testing the performance of state-of-the-art dust emission schemes using DO4Models field data. *Geoscientific Model Development*, *8*(2), 341–362.

Heinold, B., Knippertz, P., Marsham, J.H., Fiedler, S., Dixon, N.S., Schepanski, K., Laurent, B. and Tegen, I. (2013) The role of deep convection and nocturnal low-level jets for dust emission in summertime West Africa: Estimates from convection-permitting simulations. *Journal of Geophysical Research: Atmospheres*, *118*(10), 4385–4400.

Hennen, M., White, K. and Shahgedanova, M. (2019) An assessment of SEVIRI imagery at various temporal resolutions and the effect on accurate dust emission mapping. *Remote Sensing*, *11*(918), 1–14.

Hennen, M., Chappell, A., Webb, N., Schepanski, K., Baddock, M.C., Eckardt, F.D., Kandakji, T., Lee, J., Nobakht, M. and von Holdt, J.R.C. (2022) Evaluating dust emission model performance using dichotomous satellite observations of dust emission. *Geoscientific Model Development Discussions*, *423,* 1–28.

Hennen, M., Chappell, A., Webb, N.P., Schepanski, K., Baddock, M.C., Eckardt, F.D., Kandakji, T., Lee, J.A., Nobakht, M. and von Holdt, J. (2024) A new framework for evaluating dust emission model development using dichotomous satellite observations of dust emission. *Science of the Total Environment*, *912*, 169237.

Herdtfelder, R. (1984) *Der Etoscha-Nationalpnrk. Iikologie und Verhalten. Wissenschaftliche Forschung Siidwestafrika* 17, 187. Windhoek, SWA Wissenschafliche Gesellschaft.

Herndon, K., Muench, R., Cherrington, E. and Griffin, R. (2020) An Assessment of Surface Water Detection Methods for Water Resource Management in the Nigerien Sahel. *Sensors*, *20*(2), 431.

Hipondoka, M.H.T. and Versfeld, W.D. (2006) Root system of Terminalia sericea shrubs across rainfall gradient in a semi-arid environment of Etosha National Park, Namibia. *Ecological Indicators*, *6*(3), 516–524.

Hipondoka, M.H.T., Mauz, B., Kempf, J., Packman, S., Chiverrell, R.C. and Bloemendal, J. (2014) Chronology of sand ridges and the Late Quaternary evolution of the Etosha Pan, Namibia. *Geomorphology*, *204*, 553–563.

Hipondoka, M.H.T., van der Waal, B.C.W., Ndeutapo, M.H. and Hango, L. (2018) Sources of fish in the ephemeral western iishana region of the Cuvelai–Etosha Basin in Angola and Namibia. *African Journal of Aquatic Science*, *43*(3), 199–214.

Hoell, A., Funk, C., Magadzire, T., Zinke, J. and Husak, G. (2015) El Niño–Southern Oscillation diversity and southern Africa teleconnections during austral summer. *Climate Dynamics*, *45*(5), 1583–1599.

Hoell, A., Funk, C., Zinke, J. and Harrison, L. (2017) Modulation of the southern Africa precipitation response to the El Niño-Southern Oscillation by the subtropical Indian Ocean dipole. *Climate Dynamics*, *48*(7), 2529–2540.

Hoell, A. and Cheng, L. (2018) Austral summer Southern Africa precipitation extremes forced by the El Niño-Southern oscillation and the subtropical Indian Ocean dipole. *Climate Dynamics*, *50*(9), 3219–3236.

Hou, C., Huang, D., Xu, H. and Xu, Z. (2022) Evaluation of ERA5 reanalysis over the deserts in northern China. *Theoretical and Applied Climatology*, 1–16.

Houser, C.A. and Nickling, W.G. (2001a) The emission and vertical flux of particulate matter $<$ 10 μm from a disturbed clay-crusted surface. *Sedimentology*, *48*(2), 255–267.

Houser, C.A. and Nickling, W.G. (2001b) The factors influencing the abrasion efficiency of saltating grains on a clay-crusted playa. *Earth Surface Processes and Landforms: The Journal of the British Geomorphological Research Group*, *26*(5), 491–505.

Howard, E. and Washington, R. (2018) Characterizing the synoptic expression of the Angola low. *Journal of Climate, 31*(17), 7147–7165.

Howard, E., Washington, R. and Hodges, K.I. (2019) Tropical lows in southern Africa: Tracks, rainfall contributions, and the role of ENSO. *Journal of Geophysical Research: Atmospheres*, *124*(21), 11009–11032.

Hsu, N.C., Tsay, S.C., King, M.D. and Herman, J.R. (2004) Aerosol properties over bright- reflecting source regions. *IEEE Transactions on Geoscience and Remote Sensing*, *42*(3), 557–569.

Hsu, N.C., Tsay, S.C., King, M.D. and Herman, J.R. (2006) Deep Blue Retrievals of Asian Aerosol Properties During ACE-Asia. *IEEE Transactions on Geoscience and Remote Sensing*, *44,* 3180–3195.

Hsu, N.C., Jeong, M.-J., Bettenhausen, C., Sayer, A.M., Hansell, R., Seftor, C.S., Huang, J. and Tsay, S.C. (2013) Enhanced Deep Blue aerosol retrieval algorithm: The second generation. *Journal of Geophysical Research: Atmospheres*, *118,* 9296–9315.

Huang, J.P., Liu, J.J., Chen, B. and Nasiri, S.L. (2015) Detection of anthropogenic dust using CALIPSO lidar measurements. *Atmospheric Chemistry and Physics*, *15*(20), 11653–11665.

Huang, C., Chen, Y., Zhang, S. and Wu, J. (2018) Detecting, extracting, and monitoring surface water from space using optical sensors: A review. *Reviews of Geophysics*, *56*(2), 333–360.

Hubbard, B.E. and Crowley, J.K. (2005) Mineral mapping on the Chilean–Bolivian Altiplano using co-orbital ALI, ASTER and Hyperion imagery: Data dimensionality issues and solutions. *Remote Sensing of Environment*, *99*(1-2), 173–186.

Huneeus, N., Schulz, M., Balkanski, Y., Griesfeller, J., Prospero, J., Kinne, S., Bauer, S., Boucher, O., Chin, M., Dentener, F. and Diehl, T. (2011) Global dust model intercomparison in AeroCom phase I. *Atmospheric Chemistry and Physics*, *11*(15), 7781–7816.

Hunt, G. R. (1977) Spectral signatures of particulate minerals in the visible and near infrared. *Geophysics, 42*(3), 501–513.

Hunt, G. R. (1979) Near-infrared (1.3-2.4 tam) spectra of alteration minerals – Potential for use in remote sensing, *Geophysics*, *44,* 1974–1986.

Hunt, G. R. and Salisbury, J. W. (1970) Visible and near-infrared spectra of minerals and rocks, 1, Silicate minerals, *Modern Geology, 1,* 283–300.

Hunt, G. R., and Salisbury, J. W. (1971) Visible and near-infrared spectra of minerals and rocks, II, Carbonates, *Modern Geology, 2,* 23–30.

Iizuka, S., Matsuura, T. and Yamagata, T. (2000) The Indian Ocean SST dipole simulated in a coupled general circulation model. *Geophysical Research Letters, 27,* 3369–3372.

Indoitu, R., Kozhoridze, G., Batyrbaeva, M., Vitkovskaya, I., Orlovsky, N., Blumberg, D. and Orlovsky, L. (2015) Dust emission and environmental changes in the dried bottom of the Aral Sea. *Aeolian Research*, *17*, 101–115.

Ipe, A., Clerbaux, N., Bertrand, C., Dewitte, S. and Gonzalez, L. (2003) Pixel-scale composite top- of-the-atmosphere clear-sky reflectances for Meteosat-7 visible data. *Journal of Geophysical Research: Atmospheres*, *108*(D19).

Jafarzadeh, A.A. and Burnham, C.P. (1992) Gypsum crystals in soils. *Journal of soil science*, *43*(3), 409–420.

Jickells, T.D., An, Z.S., Andersen, K.K., Baker, A.R., Bergametti, G., Brooks, N., Cao, J.J., Boyd, P.W., Duce, R.A., Hunter, K.A. and Kawahata, H. (2005) Global iron connections between desert dust, ocean biogeochemistry, and climate. *science*, *308*(5718), 67–71.

Jin, Q., Ma, Y., Pan, E., Fan, F., Huang, J., Li, H., Sui, C. and Mei, X. (2019) Hyperspectral unmixing with Gaussian mixture model and spatial group sparsity. *Remote Sensing*, *11*(20), 2434.

Jing, Y., Zhang, F. and Wang, X. (2018) Monitoring dynamics and driving forces of lake changes in different seasons in Xinjiang using multi-source remote sensing. *European Journal of Remote Sensing*, *51*(1), 150–165.

Joeckel, R.M. and Clement, B.A. (1999) Surface features of the Salt Basin of Lancaster County, Nebraska. *Catena*, *34*(3-4), 243–275.

Journet, E., Balkanski, Y. and Harrison, S.P. (2014) A new data set of soil mineralogy for dust-cycle modeling. *Atmospheric Chemistry and Physics*, *14*(8), 3801–3816.

Jury, M.R. (2021) Spreading of the semi-arid climate across South Africa. *Journal of Water and Climate Change*, *12*(8), 3734–3749.

Kaly, F., Marticorena, B., Chatenet, B., Rajot, J.L., Janicot, S., Niang, A., Yahi, H., Thiria, S., Maman, A., Zakou, A. and Coulibaly, B.S. (2015) Variability of mineral dust concentrations over West Africa monitored by the Sahelian Dust Transect. *Atmospheric Research*, *164*, 226–241.

Kandakji, T., Gill, T.E. and Lee, J.A. (2020) Identifying and characterizing dust point sources in the southwestern United States using remote sensing and GIS. *Geomorphology*, *353*, 107019.

Kane, R.P. (2009) Periodicities, ENSO effects and trends of some South African rainfall series: an update. *South African Journal of Science*, *105*(5), 199–207.

Karami, S., Hamzeh, N.H., Kaskaoutis, D.G., Rashki, A., Alam, K. and Ranjbar, A. (2021) Numerical simulations of dust storms originated from dried lakes in central and southwest Asia: The case of Aral Sea and Sistan Basin. *Aeolian Research*, *50*, 100679.

Karimi, N., Moridnejad, A., Golian, S., Vali Samani, J.M., Karimi, D. and Javadi, S. (2012) Comparison of dust source identification techniques over land in the Middle East region using MODIS data. *Canadian Journal of Remote Sensing*, *38*(5), 586–599.

Karydis, V.A., Tsimpidi, A.P., Bacer, S., Pozzer, A., Nenes, A. and Lelieveld, J. (2017) Global impact of mineral dust on cloud droplet number concentration. *Atmospheric Chemistry and Physics*, *17*(9), 5601–5621.

Katra, I. and Lancaster, N. (2008) Surface-sediment dynamics in a dust source from spaceborne multispectral thermal infrared data. *Remote sensing of Environment*, *112*(7), 3212–3221.

Kaufman, Y.J., Koren, I., Remer, L.A., Tanré, D., Ginoux, P. and Fan, S. (2005) Dust transport and deposition observed from the Terra-Moderate Resolution Imaging Spectroradiometer (MODIS) spacecraft over the Atlantic Ocean. *Journal of Geophysical Research: Atmospheres*, *110*(D10).

Kavouras, I.G., Etyemezian, V., Nikolich, G., Gillies, J., Sweeney, M., Young, M. and Shafer, D. (2009) A new technique for characterizing the efficacy of fugitive dust suppressants. *Journal of the Air & Waste Management Association*, *59*(5), 603–612.

Kawo, N.S., Hordofa, A.T. and Karuppannan, S. (2021) Performance evaluation of GPM-IMERG early and late rainfall estimates over Lake Hawassa catchment, Rift Valley Basin, Ethiopia. *Arabian Journal of Geosciences*, *14*(4), 1–14.

Kazamias, A.P., Sapountzis, M. and Lagouvardos, K. (2022) Evaluation of GPM-IMERG rainfall estimates at multiple temporal and spatial scales over Greece. *Atmospheric Research, 269*(106014).

Kim, D., Chin, M., Kemp, E.M., Tao, Z., Peters-Lidard, C.D. and Ginoux, P. (2017) Development of high-resolution dynamic dust source function-A case study with a strong dust storm in a regional model. *Atmospheric environment*, *159*, 11–25.

King, J., Etyemezian, V., Sweeney, M., Buck, B.J. and Nikolich, G. (2011) Dust emission variability at the Salton Sea, California, USA. *Aeolian Research*, *3*(1), 67–79.

Klein, I., Dietz, A.J., Gessner, U., Galayeva, A., Myrzakhmetov, A. and Kuenzer, C. (2014) Evaluation of seasonal water body extents in Central Asia over the past 27 years derived from medium-resolution remote sensing data. *International Journal of Applied Earth Observation and Geoinformation*, *26*, 335–349.

Klingmüller, K., Lelieveld, J., Karydis, V.A. and Stenchikov, G.L. (2019) Direct radiative effect of dust–pollution interactions. *Atmospheric chemistry and physics*, *19*(11), 7397–7408.

Klingmüller, K., Karydis, V.A., Bacer, S., Stenchikov, G.L. and Lelieveld, J. (2020) Weaker cooling by aerosols due to dust–pollution interactions. *Atmospheric Chemistry and Physics*, *20*(23), 15285–15295.

Klose, M., Shao, Y., Li, X., Zhang, H., Ishizuka, M., Mikami, M. and Leys, J.F. (2014) Further development of a parameterization for convective turbulent dust emission and evaluation based on field observations. *Journal of Geophysical Research: Atmospheres*, *119*(17), 10441–10457.

Klose, M., Gill, T.E., Etyemezian, V., Nikolich, G., Zadeh, Z.G., Webb, N.P. and Van Pelt, R.S. (2019) Dust emission from crusted surfaces: Insights from field measurements and modelling. *Aeolian research*, *40*, 1–14.

Klose, M., Jorba, O., Gonçalves Ageitos, M., Escribano, J., Dawson, M.L., Obiso, V., Di Tomaso, E., Basart, S., Montané Pinto, G., Macchia, F. and Ginoux, P. (2021) Mineral dust cycle in the Multiscale Online Nonhydrostatic AtmospheRe CHemistry model (MONARCH) version 2.0. *Geoscientific Model Development*, *14*(10), 6403–6444.

Klüser, L. and Schepanski, K. (2009) Remote sensing of mineral dust over land with MSG infrared channels: A new Bitemporal Mineral Dust Index. *Remote Sensing of Environment*, *113*(9), 1853–1867.

Knippertz, P. (2008) Dust emissions in the West African heat trough-the role of the diurnal cycle and of extratropical disturbances. *Meteorologische Zeitschrift*, *17*(5), 553–563.

Knippertz, P. (2014) 'Meteorological Aspects of Dust Storms.' In: Knippertz, P. and Stuut, J.W. (Eds.) *Mineral Dust: A Key Player in the Earth System*. Dordrecht, Netherlands: Springer, 121–179.

Knippertz, P. (2017) Mineral dust generation across northern Africa and its impacts. In *Oxford research encyclopaedia of climate science*. Available: https://doi.org/10.1093/acrefore/9780190228620.013.516

Knippertz, P. and Todd, M.C. (2012) Mineral dust aerosols over the Sahara: Meteorological controls on emission and transport and implications for modeling. *Reviews of Geophysics*, *50*(1).

Kobayashi, S. Ota, Y., Harada, Y., Ebita, A., Moriya, M., Onoda, H., Onogi, K., Kamahori, H., Kobayashi, C., Endo, H., Miyaoka, K., Takahashi, K. (2015) The JRA-55 Reanalysis: general specifications and basic characteristics. *Journal of the Meteorological Society of Japan, 93,* 5–48.

Kocha, C., Tulet, P., Lafore, J.P. and Flamant, C. (2013) The importance of the diurnal cycle of Aerosol Optical Depth in West Africa. *Geophysical Research Letters*, *40*(4), 785–790.

Kocurek, G. and Lancaster, N. (1999) Aeolian system sediment state: theory and Mojave Desert Kelso dune field example. *Sedimentology*, *46*(3), 505–515.

Kodikara, G.R., Woldai, T., van Ruitenbeek, F.J., Kuria, Z., van der Meer, F., Shepherd, K.D. and Van Hummel, G.J. (2012) Hyperspectral remote sensing of evaporate minerals and associated sediments in Lake Magadi area, Kenya. *International Journal of Applied Earth Observation and Geoinformation*, *14*(1), 22–32.

Kodikara, G.R., McHenry, L.J. and van der Meer, F.D. (2023) Spectral mapping of zeolite bearing paleolake deposits at Lake Tecopa, California and its implications for mapping zeolites on Mars. *Geosystems and Geoenvironment*, *2*(1), 100119.

Kok, J.F. (2011) Does the size distribution of mineral dust aerosols depend on the wind speed at emission? *Atmospheric Chemistry and Physics*, *11*(19), 10149–10156.

Kok, J.F. and Renno, N.O. (2009) A comprehensive numerical model of steady state saltation (COMSALT). *Journal of Geophysical Research: Atmospheres*, *114*(D17).

Kok, J.F., Parteli, E.J., Michaels, T.I. and Karam, D.B. (2012) The physics of wind-blown sand and dust. *Reports on progress in Physics*, *75*(10), 106901.

Kok, J.F., Albani, S., Mahowald, N.M. and Ward, D.S. (2014) An improved dust emission model–Part 2: Evaluation in the Community Earth System Model, with implications for the use of dust source functions. *Atmospheric Chemistry and Physics*, *14*(23), 13043–13061.

Kok, J.F., Ridley, D.A., Zhou, Q., Miller, R.L., Zhao, C., Heald, C.L., Ward, D.S., Albani, S. and Haustein, K. (2017) Smaller desert dust cooling effect estimated from analysis of dust size and abundance. *Nature Geoscience*, *10*(4), 274–278.

Kok, J.F., Ward, D.S., Mahowald, N.M. and Evan, A.T. (2018) Global and regional importance of the direct dust-climate feedback. *Nature Communications*, *9*(1), 1–11.

Kok, J.F., Adebiyi, A.A., Albani, S., Balkanski, Y., Checa-Garcia, R., Chin, M., Colarco, P.R., Hamilton, D.S., Huang, Y., Ito, A. and Klose, M. (2021a) Improved representation of the global dust cycle using observational constraints on dust properties and abundance. *Atmospheric Chemistry and Physics*, *21*(10), 8127–8167.

Kok, J.F., Adebiyi, A.A., Albani, S., Balkanski, Y., Checa-Garcia, R., Chin, M., Colarco, P.R., Hamilton, D.S., Huang, Y., Ito, A. and Klose, M. (2021b) Contribution of the world's main dust source regions to the global cycle of desert dust. *Atmospheric Chemistry and Physics*, *21*(10), 8169–8193.

Kok, J.F., Storelvmo, T., Karydis, V.A., Adebiyi, A.A., Mahowald, N.M., Evan, A.T., He, C. and Leung, D.M. (2023) Mineral dust aerosol impacts on global climate and climate change. *Nature Reviews Earth & Environment*, *4*(2), 71–86.

Kokaly, R.F., Clark, R.N., Swayze, G.A., Livo, K.E., Hoefen, T.M., Pearson, N.C., Wise, R.A., Benzel, W.M., Lowers, H.A., Driscoll. R.L. and Klein, A.J. (2017) USGS Spectral Library Version 7: USGS Geological Survey Data Series 1035, 61.

Korsman, T., Nilsson, M.B., Landgren, K. and Renberg, I. (1999) Spatial variability in surface sediment composition characterised by near-infrared (NIR) reflectance spectroscopy. *Journal of Paleolimnology*, *21*, 61–71.

Koven, C.D. and Fung, I. (2008) Identifying global dust source areas using high-resolution land surface form. *Journal of Geophysical Research: Atmospheres*, *113*(D22).

Kruse, F.A. (1988) Use of airborne imaging spectrometer data to map minerals associated with hydrothermally altered rocks in the northern grapevine mountains, Nevada, and California. *Remote Sensing of Environment*, *24*(1), 31–51.

Kruse, F.A. and Perry, S.L. (2013) Mineral mapping using simulated Worldview-3 short-wave-infrared imagery. *Remote Sensing*, *5*(6), 2688–2703.

Kumar, A., Shukla, G. and Singh, A. (2022) Long-range global transport and characterization of dust. In: Singh, R.P. (Ed.) *Asian Atmospheric Pollution*. Amsterdam, Netherlands: Elsevier, 483–504.

Lacaux, J.P., Tourre, Y.M., Vignolles, C., Ndione, J.A. and Lafaye, M. (2007) Classification of ponds from high-spatial resolution remote sensing: Application to Rift Valley Fever epidemics in Senegal. *Remote Sensing of Environment*, *106*(1), 66–74.

Landman, W.A. and Mason, S.J. (1999) Change in the association between Indian Ocean sea- surface temperatures and summer rainfall over South Africa and Namibia. *International Journal of Climatology: A Journal of the Royal Meteorological Society*, *19*(13), 1477–1492.

Langston, G. and McKenna Neuman, C. (2005) An experimental study on the susceptibility of crusted surfaces to wind erosion: a comparison of the strength properties of biotic and salt crusts. *Geomorphology*, *72*(1-4), 40–53.

Lawrence, M.G. (2005) The relationship between relative humidity and the dewpoint temperature in moist air: A simple conversion and applications. *Bulletin of the American Meteorological Society*, *86*(2), 225–234.

Lee, B.Y. and Kurtis, K.E. (2017) Effect of pore structure on salt crystallization damage of cement-based materials: Consideration of w/b and nanoparticle use. *Cement and Concrete Research*, *98*, 61–70.

Lee, J.A., Gill, T.E., Mulligan, K.R., Acosta, M.D. and Perez, A.E. (2009) Land use/land cover and point sources of the 15 December 2003 dust storm in southwestern North America. *Geomorphology*, *105*(1-2), 18–27.

Lee, J.A., Baddock, M.C., Mbuh, M.J. and Gill, T.E. (2012) Geomorphic and land cover characteristics of aeolian dust sources in West Texas and eastern New Mexico, USA. *Aeolian Research*, *3*(4), 459–466.

Lehner, B., Verdin, K. and Jarvis, A. (2008) New global hydrography derived from spaceborne elevation data. *Eos, Transactions, 89*(10), 93–94. Data available at: https://www.hydrosheds.org.

Lensky, I.M. and Rosenfeld, D. (2008) Clouds-aerosols-precipitation satellite analysis tool (CAPSAT). *Atmospheric Chemistry and Physics*, *8*(22), 6739–6753.

Levy, D.B., Schramke, J.A., Esposito, K.J., Erickson, T.A. and Moore, J.C. (1999) The shallow ground water chemistry of arsenic, fluorine, and major elements: Eastern Owens Lake, California. *Applied Geochemistry*, *14*(1), 53–65.

Levy, R., Hsu, C., *et al.* (2015) MODIS Atmosphere L2 Aerosol Product. NASA MODIS Adaptive Processing System, Goddard Space Flight Center, USA: http://dx.doi.org/10.5067/MODIS/MOD04_L2.061

Li, J., Okin, G.S., Herrick, J.E., Belnap, J., Munson, S.M. and Miller, M.E. (2010) A simple method to estimate threshold friction velocity of wind erosion in the field. *Geophysical Research Letters*, *37*(10).

Li, J., Menenti, M., Mousivand, A. and Luthi, S.M. (2014) Non-vegetated playa morphodynamics using multi-temporal landsat imagery in a semi-arid endorheic basin: Salar de Uyuni, Bolivia. *Remote Sensing*, *6*(10), 10131–10151.

Li, J., Wong, M.S., Lee, K.H., Nichol, J. and Chan, P.W. (2021) Review of dust storm detection algorithms for multispectral satellite sensors. *Atmospheric Research*, 105398.

Li, Q., Lu, L., Wang, C., Li, Y., Sui, Y. and Gong, H. (2015) MODIS-Derived Spatiotemporal changes of Major Lake Surface Areas in Arid Xinjiang, China, 2000-2014. *Water,* 7, 5731–5751.

Li, R., Liu, C., Xu, H., Jiao, P., Hu, Y., Fan, L. and Sun, X. (2020) Genesis of glauberite sedimentation in Lop Nur salt lake – constraints from thermodynamic simulation of the shallow groundwater in the Tarim River Basin, China. *Chemical Geology*, *537*, 119461.

Li, W., El-Askary, H., Thomas, R., Tiwari, S.P., Manikandan, K.P., Piechota, T. and Struppa, D. (2020) An assessment of the hydrological trends using synergistic approaches of remote sensing and model evaluations over global arid and semi-arid regions. *Remote Sensing*, *12*(3973).

Li, X., Sungmin, O., Wang, N. and Huang, Y. (2021) Evaluation of the GPM IMERG V06 products for light rain over Mainland China. *Atmospheric Research*, *253*, 105510.

Li, Z., Wang, G., Wang, X., Wan, L., Shi, Z., Wanke, H., Uugulu, S. and Uahengo, C.I. (2018) Groundwater quality and associated hydrogeochemical processes in Northwest Namibia. *Journal of Geochemical Exploration*, *186*, 202–214.

Liu, B., Wan, W., Xie, H., Li, H., Zhu, S., Zhang, G., Wen, L. and Hong, Y. (2019) A long-term dataset of lake surface water temperature over the Tibetan Plateau derived from AVHRR 1981–2015. *Scientific data*, *6*(1), 1–11.

Liu, X. and Zhou, J. (2021) Assessment of the Continuous Extreme Drought Events in Namibia during the Last Decade. *Water, 13*(2942), 1–18.

Lowenstein, T.K. and Hardie, L.A. (1985) Criteria for the recognition of salt-pan evaporites. *Sedimentology*, *32*(5), 627–644.

Lu, H. and Shao, Y. (2001) Toward quantitative prediction of dust storms: an integrated wind erosion modelling system and its applications. *Environmental Modelling & Software*, *16*(3), 233–249.

Lu, X., Wei, M., Tang, G. and Zhang, Y. (2018) Evaluation and correction of the TRMM 3B43V7 and GPM 3IMERGM satellite precipitation products by use of ground-based data over Xinjiang, China. *Environmental earth sciences*, *77*(5), 1–18.

Luo, C., Mahowald, N.M. and Del Corral, J. (2003) Sensitivity study of meteorological parameters on mineral aerosol mobilization, transport, and distribution. *Journal of Geophysical Research: Atmospheres*, *108*(D15).

Luo, C., Mahowald, N.M. and Jones, C. (2004) Temporal variability of dust mobilization and concentration in source regions. *Journal of Geophysical Research: Atmospheres*, *109*(D20).

Lyon, B. and Mason, S.J. (2007) The 1997–98 summer rainfall season in southern Africa. Part I: Observations. *Journal of Climate*, *20*(20), 5134–5148.

Lyon, B. and Mason, S.J. (2009) The 1997/98 summer rainfall season in southern Africa. Part II: Model simulations and coupled model forecasts. *Journal of Climate*, *22*(13), 3802–3818.

Lyons, M.B., Keith, D.A., Phinn, S.R., Mason, T.J. and Elith, J. (2018) A comparison of resampling methods for remote sensing classification and accuracy assessment. *Remote Sensing of Environment*, *208*, 145–153.

Macpherson, T., Nickling, W.G., Gillies, J.A. and Etyemezian, V. (2008) Dust emissions from undisturbed and disturbed supply-limited desert surfaces. *Journal of Geophysical Research: Earth Surface*, *113*(F2).

Madden, N.M., Southard, R.J. and Mitchell, J.P. (2010) Soil water and particle size distribution influence laboratory-generated PM10. *Atmospheric Environment*, *44*(6), 745–752.

Maghsood, F.F., Hashemi, H., Hosseini, S.H. and Berndtsson, R. (2020) Ground validation of GPM IMERG precipitation products over Iran. *Remote Sensing*, *12*(1), 48.

Magnus, G. (1844) Versuche über die Spannkräfte des Wasserdampfs. *Annual Review of Physical Chemistry, 61*, 225–247.

Maher, B.A., Prospero, J.M., Mackie, D., Gaiero, D., Hesse, P.P. and Balkanski, Y. (2010) Global connections between aeolian dust, climate and ocean biogeochemistry at the present day and at the last glacial maximum. *Earth-Science Reviews*, *99*(1-2), 61–97.

Mahowald, N.M., Bryant, R.G., del Corral, J. and Steinberger, L. (2003) Ephemeral lakes and desert dust sources. *Geophysical Research Letters*, *30*(2).

Mahowald, N.M., Jickells, T.D., Baker, A.R., Artaxo, P., Benitez-Nelson, C.R., Bergametti, G., Bond, T.C., Chen, Y., Cohen, D.D., Herut, B. and Kubilay, N. (2008) Global distribution of atmospheric phosphorus sources, concentrations and deposition rates, and anthropogenic impacts. *Global Biogeochemical Cycles*, *22*(4).

Mahowald, N.M., Lindsay, K., Rothenberg, D., Doney, S.C., Moore, J.K., Thornton, P., Randerson, J.T. and Jones, C.D. (2011). Desert dust and anthropogenic aerosol interactions in the Community Climate System Model coupled-carbon-climate model. *Biogeosciences*, *8*(2), 387–414.

Mahowald, N.M., Albani, S., Kok, J.F., Engelstaeder, S., Scanza, R., Ward, D.S. and Flanner, M.G. (2014) The size distribution of desert dust aerosols and its impact on the Earth system. *Aeolian Research*, *15*, 53–71.

Mahowald, N.M., Hamilton, D.S., Mackey, K.R., Moore, J.K., Baker, A.R., Scanza, R.A. and Zhang, Y. (2018) Aerosol trace metal leaching and impacts on marine microorganisms. *Nature communications*, *9*(1), 1–15.

Mahmoud, M.T., Mohammed, S.A., Hamouda, M.A. and Mohamed, M.M. (2021) Impact of topography and rainfall intensity on the accuracy of imerg precipitation estimates in an arid region. *Remote Sensing*, *13*(1), 13.

Malvern Panalytical (2022) ASD FieldSpec 4: The industry-leading portable device for field spectroscopy. Available: https://www.malvernpanalytical.com/en/products/product-range/asd-range/fieldspec-range.

Mann, G.W., Carslaw, K.S., Spracklen, D.V., Ridley, D.A., Manktelow, P.T., Chipperfield, M.P., Pickering, S.J. and Johnson, C.E. (2010) Description and evaluation of GLOMAP-mode: A modal global aerosol microphysics model for

the UKCA composition-climate model. *Geoscientific Model Development*, *3*(2), 519–551.

Marchese, F., Sannazzaro, F., Falconieri, A., Filizzola, C., Pergola, N. and Tramutoli, V. (2017) An enhanced satellite-based algorithm for detecting and tracking dust outbreaks by means of SEVIRI data. *Remote Sensing*, *9*(6), 537.

Marsham, J.H., Parker, D.J., Grams, C.M., Johnson, B.T., Grey, W.M. and Ross, A.N. (2008) Observations of mesoscale and boundary-layer scale circulations affecting dust transport and uplift over the Sahara. *Atmospheric Chemistry and Physics*, *8*(23), 6979–6993.

Marsham, J.H., Hobby, M., Allen, C.J.T., Banks, J.R., Bart, M., Brooks, B.J., Cavazos-Guerra, C., Engelstaedter, S., Gascoyne, M., Lima, A.R. and Martins, J.V. (2013) Meteorology and dust in the central Sahara: Observations from Fennec supersite-1 during the June 2011 Intensive Observation Period. *Journal of Geophysical Research: Atmospheres*, *118*(10), 4069–4089.

Marticorena, B. (2014) Dust Production Mechanisms. In: Knippertz, P. and Stuut, J. W. (Eds.) *Mineral Dust: A Key Player in the Earth System.* Dordrecht, Netherlands: Springer, 93–120.

Marticorena, B. and Bergametti, G. (1995) Modeling the atmospheric dust cycle: 1. Design of a soil-derived dust emission scheme. *Journal of Geophysical Research: Atmospheres*, *100*(D8), 16415–16430.

Marticorena, B., Chatenet, B., Rajot, J.L., Traoré, S., Coulibaly, M., Diallo, A., Koné, I., Maman, A., NDiaye, T. and Zakou, A. (2010) Temporal variability of mineral dust concentrations over West Africa: analyses of a pluriannual monitoring from the AMMA Sahelian Dust Transect. *Atmospheric Chemistry and Physics*, *10*(18), 8899–8915.

Marticorena, B., Chatenet, B., Rajot, J.L., Bergametti, G., Deroubaix, A., Vincent, J., Kouoi, A., Schmechtig, C., Coulibaly, M., Diallo, A. and Koné, I. (2017) Mineral dust over west and central Sahel: Seasonal patterns of dry and wet deposition fluxes from a pluriannual sampling (2006–2012). *Journal of Geophysical Research: Atmospheres*, *122*(2), 1338–1364.

Marx, S.K., May, J.H., Cohen, T., Kamber, B.S., McGowan, H.A. and Petherick, L. (2022) Dust emissions from Kati Thanda-Lake Eyre: a review. *Transactions of the Royal Society of South Australia*, *146*(1), 168–206.

Mateus, P., Mendes, V.B. and Plecha, S.M. (2021) HGPT2: an ERA5-based global model to estimate relative humidity. *Remote Sensing*, *13*(11), 2179.

McFeeters, S.K. (1996). The use of the Normalized Difference Water Index (NDWI) in the delineation of open water features. *International Journal of Remote Sensing*, *17*(7), 1425–1432.

McGowan, H.A. and Clark, A. (2008a) Identification of dust transport pathways from Lake Eyre, Australia using Hysplit. *Atmospheric Environment*, *42*(29), 6915–6925.

McGowan, H.A. and Clark, A. (2008b) A vertical profile of PM10 dust concentrations measured during a regional dust event identified by MODIS Terra, western Queensland, Australia. *Journal of Geophysical Research: Earth Surface*, *113*(F2).

McKenna Neuman, C. (2024) 'Laboratory wind tunnel simulation of several environmental controls on the production of dust from playa sediment collected from Owens Lake, CA.' [Webinar]. *Dust Alliance for North America (DANA) Webinar Series.* Online. 9 February.

McKenna Neuman, C. and Nickling, W.G. (1989) A theoretical and wind tunnel investigation of the effect of capillary water on the entrainment of sediment by wind. *Canadian Journal of Soil Science*, *69*(1), 79–96.

McLaurin, B.T., Goossens, D. and Buck, B.J. (2011) Combining surface mapping and process data to assess, predict, and manage dust emissions from natural and disturbed land surfaces. *Geosphere*, *7*(1), 260–275.

Mees, F. (1999) Distribution patterns of gypsum and kalistrontite in a dry lake basin of the southwestern Kalahari (Omongwa pan, Namibia). *Earth Surface Processes and Landforms: The Journal of the British Geomorphological Research Group*, *24*(8), 731–744.

Mees, F. and Singer, A. (2006) Surface crusts on soils/sediments of the southern Aral Sea basin, Uzbekistan. *Geoderma*, *136*(1-2), 152–159.

Mees, F. and Van Ranst, E. (2011) Euhedral sparitic calcite in buried surface horizons in lake basins, southwestern Kalahari, Namibia. *Geoderma*, *163*(1-2), 109–118.

Mei, L., Vandenbussche, S., Rozanov, V., Proestakis, E., Amiridis, V., Callewaert, S., Vountas, M. and Burrows, J.P. (2020) On the retrieval of aerosol optical depth over cryosphere using passive remote sensing. *Remote Sensing of Environment*, *241*, 111731.

Mendelsohn, J., Jarvis, A. and Robertson, T. (Eds.) (2013) *A profile and atlas of the Cuvelai-Etosha Basin.* Windhoek: RAISON & Gondwana Collection, 1–166.

Meng, X., Yao, F., Zhang, J., Liu, Q., Liu, Q., Shi, L. and Zhang, D. (2022) Impact of dust deposition on phytoplankton biomass in the Northwestern Pacific: A long-term study from 1998 to 2020. *Science of The Total Environment*, *813*, 152536.

Meque, A. and Abiodun, B.J. (2015) Simulating the link between ENSO and summer drought in Southern Africa using regional climate models. *Climate Dynamics*, *44*(7), 1881–1900.

Merchant, C.J., Embury, O., Le Borgne, P. and Bellec, B. (2006) Saharan dust in nighttime thermal imagery: Detection and reduction of related biases in retrieved sea surface temperature. *Remote Sensing of Environment*, *104*(1), 15–30.

Middleton, N.J. (2017) Desert dust hazards: A global review. *Aeolian Research*, *24*, 53–63.

Middleton, N.J. (2020) Health in dust belt cities and beyond—an essay by Nick Middleton. *bmj*, *371*.

Middleton, N.J. and Goudie, A.S. (2001) Saharan dust: sources and trajectories. *Transactions of the Institute of British Geographers*, *26*(2), 165–181.

Middleton, N.J. and Kang, U. (2017) Sand and dust storms: impact mitigation. *Sustainability*, *9*(6), 1053.

Milewski, R., Chabrillat, S. and Behling, R. (2017) Analyses of recent sediment surface dynamic of a Namibian Kalahari salt pan based on multitemporal Landsat and hyperspectral Hyperion data. *Remote Sensing*, *9*, 170.

Milewski, R., Chabrillat, S., Brell, M., Schleicher, A.M. and Guanter, L. (2019) Assessment of the 1.75 μm absorption feature for gypsum estimation using laboratory, air-and spaceborne hyperspectral sensors. *International Journal of Applied Earth Observation and Geoinformation*, *77*, 69–83.

Milewski, R., Chabrillat, S. and Bookhagen, B. (2020) Analyses of Namibian seasonal salt pan crust dynamics and climatic drivers using Landsat 8 time-series and ground data. *Remote Sensing*, *12*(3), 474.

Miller, R.M.G. (1997) The Owambo Basin of Northern Namibia. *Sedimentary Basins of the World, 3,* 237–268.

Miller, R.M.G., Pickford, M. and Senut, B. (2010) The geology, palaeontology and evolution of the Etosha Pan, Namibia: Implications for terminal Kalahari deposition. *South African Journal of Geology*, *113*(3), 307–334.

Miller, S.D. (2014) *System and method for atmospheric parameter enhancement*, United States Patent Application Publication, Pub no. US2014/0212061 A1.

Miller, S.D., Bankert, R.L., Solbrig, J.E., Forsythe, J.M., Noh, Y.J. and Grasso, L.D. (2017) A dynamic enhancement with background reduction algorithm: Overview and application to satellite-based dust storm detection. *Journal of Geophysical Research: Atmospheres*, *122*(23), 12–938.

Millington, A.C., Jones, A.R., Quarmby, N. and Townshend, J.R.G. (1987) Remote sensing of sediment transfer processes in playa basins. *Geological Society, London, Special Publications*, *35*(1), 369–381.

Millington, A. C., Drake, N. A., Townshend, J. R. G., Quarmby, N. A., Settle, J. J. and Reading, A. J. (1989) Monitoring salt playa dynamics using Thematic Mapper data. *IEEE Transactions on Geoscience and Remote Sensing, 27*(6), 754–761.

Mishra, M.K., Chauhan, P. and Sahay, A. (2015) Detection of Asian dust storms from geostationary satellite observations of the INSAT-3D imager. *International Journal of Remote Sensing*, *36*(18), 4668–4682.

Mishra, V., Limaye, A.S., Muench, R.E., Cherrington, E.A. and Markert, K.N. (2020) Evaluating the performance of high-resolution satellite imagery in detecting

ephemeral water bodies over West Africa. *International Journal of Applied Earth Observation and Geoinformation*, *93*, 102218.

Mohammadi, A., Costelloe, J.F. and Ryu, D. (2017) Application of time series of remotely sensed normalized difference water, vegetation and moisture indices in characterizing flood dynamics of large-scale arid zone floodplains. *Remote Sensing of Environment*, *190*, 70–82.

Moayeri, V., Miri, A., Shahriari, A., Rahdari, V. and Gill, T.E. (2023) A field study of the surface disturbance effects of animals and motor vehicles on aeolian sediment emission from a silty playa surface. *Environmental Research*, *216*, 114606.

Mona, L., Amiridis, V., Cuevas, E., Gkikas, A., Trippetta, S., Vandenbussche, S., Benedetti, A., Dagsson-Waldhauserova, P., Formenti, P., Haefele, A. and Kazadzis, S. (2023) Observing Mineral Dust in Northern Africa, the Middle East, and Europe: Current Capabilities and Challenges ahead for the Development of Dust Services. *Bulletin of the American Meteorological Society*, *104*(12), E2223–E2264.

Muhs, D.R., Prospero, J.M., Baddock, M.C. and Gill, T.E. (2014) Identifying sources of aeolian mineral dust: Present and past. *Mineral dust: A key player in the earth system*, 51–74.

Munday, C. and Washington, R. (2017) Circulation controls on southern African precipitation in coupled models: The role of the Angola low. *Journal of Geophysical Research: Atmospheres, 122*(2), 861–877.

Munkhtsetseg, E., Shinoda, M., Gillies, J.A., Kimura, R., King, J. and Nikolich, G. (2016) Relationships between soil moisture and dust emissions in a bare sandy soil of Mongolia. *Particuology*, *28*, 131–137.

Munkhtsetseg, E., Shinoda, M., Ishizuka, M., Mikami, M., Kimura, R. and Nikolich, G. (2017) A livestock trampling function for potential emission rate of wind-blown dust in a Mongolian temperate grassland. *Atmospheric Chemistry and Physics Discussions*, 1–27.

Muñoz-Sabater, J., Dutra, E., Agustí-Panareda, A., Albergel, C., Arduini, G., Balsamo, G., Boussetta, S., Choulga, M., Harrigan, S., Hersbach, H. and Martens, B. (2021) ERA5-Land: A state-of-the-art global reanalysis dataset for land applications. *Earth System Science Data*, *13*(9), 4349–4383.

Muñoz-Sabater, J., Balsamo, G., Buontempo, C., Burgess, S., Hersbach, H., Hodkinson, J., Mueller-Quintino, A., Radu, R., Rozum, I. and Villaume, S. (2023) *ERA5-Land: More than 7 decades of land surface consistency with timely updates* (No. EGU23-9774). Copernicus Meetings.

Murray, J.E., Brindley, H.E., Bryant, R.G., Russell, J.E., Jenkins, K.F. and Washington, R. (2016) Enhancing weak transient signals in SEVIRI false color imagery: Application to dust source detection in southern Africa. *Journal of Geophysical Research: Atmospheres*, *121*(17), 10199–10219.

Myhre, G., Berntsen, T.K., Haywood, J.M., Sundet, J.K., Holben, B.N., Johnsrud, M. and Stordal, F. (2003) Modeling the solar radiative impact of aerosols from biomass burning during the Southern African Regional Science Initiative (SAFARI-2000) experiment.*Journal of Geophysical Research: Atmospheres*, *108*(D13).

Nachshon, U., Shahraeeni, E., Or, D., Dragila, M. and Weisbrod, N. (2011) Infrared thermography of evaporative fluxes and dynamics of salt deposition on heterogeneous porous surfaces. *Water Resources Research*, *47*(12).

Nicholson, S.E. and Kim, J. (1997) The relationship of the El Niño–Southern oscillation to African rainfall. *International Journal of Climatology: A Journal of the Royal Meteorological Society*, *17*(2), 117–135.

Nicholson, S.E. and Selato, J.C. (2000) The influence of La Nina on African rainfall. *International Journal of Climatology: A Journal of the Royal Meteorological Society*, *20*(14), 1761–1776.

Nickling, W.G. (1984) The stabilizing role of bonding agents on the entrainment of sediment by wind. *Sedimentology*, *31*(1), 111–117.

Nickling, W.G. and Ecclestone, M. (1981) The effects of soluble salts on the threshold shear velocity of fine sand. *Sedimentology*, *28*(4), 505–510.

Nickling, W.G. and Gillies, J.A. (1989) Emission of dust from desert soils. In: Leinen, M. and Sarnthein, M. (Eds.) *Paleoclimatology and Paleometeorology: Modern and Past Patterns of Global Atmospheric Transport.* Alphen aan den Rijn, Netherlands: Kluwer, 133–165.

Nickling, W.G. and Gillies, J.A. (1993) Dust emission and transport in Mali, West Africa. *Sedimentology*, *40*(5), 859–868.

Nieke, J. and Rast, M. (2018) Towards the Copernicus Hyperspectral Imaging Mission for the Environment (CHIME). *IGARSS 2018 - IEEE International Geoscience and Remote Sensing Symposium*, Valencia, Spain, 157–159.

Nieke, J., Despoisse, L., Gabriele, A., Weber, H., Strese, H., Ghasemi, N., Gascon, F., Alonso, K., Boccia, V., Tsonevska, B. and Choukroun, P. (2023) The Copernicus Hyperspectral Imaging Mission for the Environment (CHIME): An overview of its mission, system and planning status. *Sensors, Systems, and Next-Generation Satellites XXVII*, *12729*, 21–40.

Nield, J.M., King, J., Wiggs, G.F.S., Leyland, J., Bryant, R.G., Chiverrell, R.C., Darby, S.E., Eckardt, F.D., Thomas, D.S., Vircavs, L.H. and Washington, R. (2013) Estimating aerodynamic roughness over complex surface terrain. *Journal of Geophysical Research: Atmospheres*, *118*(23), 12948–12961.

Nield, J.M., Bryant, R.G., Wiggs, G.F.S., King, J., Thomas, D.S., Eckardt, F.D. and Washington, R. (2015) The dynamism of salt crust patterns on playas. *Geology*, *43*(1), 31–34.

Nield, J.M., Wiggs, G.F.S., King, J., Bryant, R.G., Eckardt, F.D., Thomas, D.S. and Washington, R. (2016a) Climate–surface–pore-water interactions on a salt crusted playa: implications for crust pattern and surface roughness development measured using terrestrial laser scanning. *Earth Surface Processes and Landforms*, *41*(6), 738–753.

Nield, J.M., Neuman, C.M., O'Brien, P., Bryant, R.G. and Wiggs, G.F.S. (2016b) Evaporative sodium salt crust development and its wind tunnel derived transport dynamics under variable climatic conditions. *Aeolian Research*, *23*, 51–62.

Niemeyer, T.C., Gillette, D.A., DeLuisi, J.J., Kim, Y.J., Niemeyer, W.F., Ley, T., Gill, T.E. and Ono, D. (1999) Optical depth, size distribution and flux of dust from Owens Lake, California.*Earth Surface Processes and Landforms: The Journal of the British Geomorphological Research Group*, *24*(5), 463–479.

Nobakht, M., Shahgedanova, M. and White, K. (2021) New Inventory of Dust Emission Sources in Central Asia and Northwestern China Derived from MODIS Imagery using Dust Enhancement Technique. *Journal of Geophysical Research: Atmospheres*, e2020JD033382.

Ogilvie, A., Belaud, G., Massuel, S., Mulligan, M., Le Goulven, P. and Calvez, R. (2018) Surface water monitoring in small water bodies: potential and limits of

multi-sensor Landsat time series. *Hydrology and Earth System Sciences*, *22*(8), 4349.

Okin, G.S., Mahowald, N.M., Chadwick, O.A. and Artaxo, P. (2004) Impact of desert dust on the biogeochemistry of phosphorus in terrestrial ecosystems. *Global Biogeochemical Cycles*, *18*(2).

Ono, D., Kiddoo, P., Howard, C., Davis, G. and Richmond, K. (2011) Application of a combined measurement and modeling method to quantify windblown dust emissions from the exposed playa at Mono Lake, California. *Journal of the Air & Waste Management Association*, *61*(10), 1036–1045.

Oztas, T. and Fayetorbay, F. (2003) Effect of freezing and thawing processes on soil aggregate stability. *Catena*, *52*(1), 1–8.

Papi, R., Attarchi, S., Darvishi Boloorani, A. and Neysani Samany, N. (2022) Characterization of hydrologic sand and dust storm sources in the Middle East. *Sustainability*, *14*(22).

Parajuli, S.P., Yang, Z.L. and Kocurek, G. (2014) Mapping erodibility in dust source regions based on geomorphology, meteorology, and remote sensing. *Journal of Geophysical Research: Earth Surface*, *119*(9), 1977–1994.

Parajuli, S.P., Zobeck, T.M., Kocurek, G., Yang, Z.L. and Stenchikov, G.L. (2016) New insights into the wind-dust relationship in sandblasting and direct aerodynamic entrainment from wind tunnel experiments. *Journal of Geophysical Research: Atmospheres*, *121*(4), 1776–1792.

Parajuli, S.P. and Zender, C.S. (2017) Connecting geomorphology to dust emission through high-resolution mapping of global land cover and sediment supply. *Aeolian Research*, *27*, 47–65.

Parajuli, S.P., Stenchikov, G.L., Ukhov, A. and Kim, H. (2019) Dust emission modeling using a new high-resolution dust source function in WRF-Chem with implications for air quality. *Journal of Geophysical Research: Atmospheres*, *124*(17-18), 10109–10133.

Park, S.S., Kim, J., Lee, J., Lee, S., Kim, J.S., Chang, L.S. and Ou, S. (2014) Combined dust detection algorithm by using MODIS infrared channels over East Asia. *Remote sensing of environment*, *141*, 24–39.

Pavolonis, M.J., Sieglaff, J. and Cintineo, J. (2015) Spectrally Enhanced Cloud Objects—A generalized framework for automated detection of volcanic ash and dust clouds using passive satellite measurements: 1. Multispectral analysis.*Journal of Geophysical Research: Atmospheres*, *120*(15), 7813–7841.

Pelletier, J.D. (2006) Sensitivity of playa windblown-dust emissions to climatic and anthropogenic change. *Journal of Arid Environments*, *66*(1), 62–75.

Pelletier, J.D. and Cook, J.P. (2005) Deposition of playa windblown dust over geologic time scales. *Geology*, *33*(11), 909–912.

Peng, J., Liu, T., Huang, Y., Ling, Y., Li, Z., Bao, A., Chen, X., Kurban, A. and De Maeyer, P. (2021) Satellite-Based Precipitation Datasets Evaluation Using Gauge Observation and Hydrological Modeling in a Typical Arid Land Watershed of Central Asia.*Remote Sensing*, *13*(2), 221.

Penner, J.E., Charlson, R.J., Hales, J.M., Laulainen, N.S., Leifer, R., Novakov, T., Ogren, J., Radke, L.F., Schwartz, S.E. and Travis, L. (1994) Quantifying and minimizing uncertainty of climate forcing by anthropogenic aerosols. *Bulletin of the American Meteorological Society*, *75*(3), 375–400.

Peyghambari, S. and Zhang, Y. (2021) Hyperspectral remote sensing in lithological mapping, mineral exploration, and environmental geology: an updated review. *Journal of Applied Remote Sensing*, *15*(3), 031501.

Philippon, N., Rouault, M., Richard, Y. and Favre, A. (2012) The influence of ENSO on winter rainfall in South Africa. *International Journal of Climatology*, *32*(15), 2333–2347.

Pickford, M., Senut, B., Hipondoka, M., Person, A., Segalen, L., Plet, C., Jousse, H., Mein, P., Guérin, C., Morales, J. and Mourer-Chauviré, C. (2009) Mio-plio-pleistocene geology and palaeobiology of Etosha Pan, Namibia. *Communications of the geological Survey of namibia*, *14*, 95–139.

Piketh, S.J., Tyson, P.D. and Steffen, W. (2000) Aeolian transport from southern Africa and iron fertilization of marine biota in the South Indian Ocean.*South African Journal of Science*, *96*(5), 244–246.

Piketh, S.J., Swap, R.J., Maenhaut, W., Annegarn, H.J. and Formenti, P. (2002) Chemical evidence of long-range atmospheric transport over southern Africa. *Journal of Geophysical Research: Atmospheres*, *107*(D24), 7-1–7-13.

Pradhan, R.K. Markonis, Y., Godoy, M.R.V., Villalba-Pradas, A., Andreadis, K.M., Nikolopoulos, E.I., Papalexiou, S.M., Rahim, A., Tapiador, F.J. and Hanel, M. (2022) Review of GPM IMERG performance: A global perspective. *Remote Sensing of Environment, 26*(112754).

Preston-Whyte, R. A., Diab, R. D. and Sokolic, F. (1994) Thermo—Topographically induced winds in the boundary layer over the Etosha Pan. *South African Geographical Journal, 76*(2), 59–62.

Prospero, J.M., Ginoux, P., Torres, O., Nicholson, S.E. and Gill, T.E. (2002) Environmental characterization of global sources of atmospheric soil dust identified with the Nimbus 7 Total Ozone Mapping Spectrometer (TOMS) absorbing aerosol product. *Reviews of Geophysics*, *40*(1), 2-1–2-31.

Prospero, J.M., Delany, A.C., Delany, A.C. and Carlson, T.N. (2021) The discovery of African dust transport to the Western Hemisphere and the Saharan air layer: A history. *Bulletin of the American Meteorological Society*, 1–53.

Qiang, M., Chen, F., Zhang, J., Zu, R., Jin, M., Zhou, A. and Xiao, S. (2007) Grain size in sediments from Lake Sugan: a possible linkage to dust storm events at the northern margin of the Qinghai–Tibetan Plateau. *Environmental Geology*, *51*(7), 1229–1238.

Qu, J.J., Hao, X., Kafatos, M. and Wang, L. (2006) Asian dust storm monitoring combining Terra and Aqua MODIS SRB measurements. *IEEE Geoscience and remote sensing letters*, *3*(4), 484–486.

Querol, X., Tobías, A., Pérez, N., Karanasiou, A., Amato, F., Stafoggia, M., García-Pando, C.P., Ginoux, P., Forastiere, F., Gumy, S. and Mudu, P. (2019) Monitoring the impact of desert dust outbreaks for air quality for health studies. *Environment international*, *130*, 104867.

Quick, D.J. and Chadwick, O.A. (2011) Accumulation of salt-rich dust from Owens Lake playa in nearby alluvial soils. *Aeolian Research*, *3*(1), 23–29.

Radwin, M.H. and Bowen, B.B. (2021) Mapping mineralogy in evaporite basins through time using multispectral Landsat data: Examples from the Bonneville basin, Utah, USA. *Earth Surface Processes and Landforms*, *46*(6), 1160–1176.

Rahm, L. and Buch, M. (1997) Groundwater flow in the southern part of the Etosha basin indicated by the chemical composition of water. *Madoqua*, *1997*(1), 129–135.

Rajot, J.L., Formenti, P., Alfaro, S., Desboeufs, K., Chevaillier, S., Chatenet, B., Gaudichet, A., Journet, E., Marticorena, B., Triquet, S. and Maman, A. (2008) AMMA dust experiment: An overview of measurements performed during the dry season special observation period (SOP0) at the Banizoumbou (Niger) supersite. *Journal of Geophysical Research: Atmospheres*, *113*(D23).

Rashki, A., Kaskaoutis, D.G., Rautenbach, C.D., Eriksson, P.G., Qiang, M. and Gupta, P. (2012) Dust storms and their horizontal dust loading in the Sistan region, Iran. *Aeolian Research*, *5*, 51–62.

Rashki, A., Kaskaoutis, D.G., Goudie, A.S. and Kahn, R.A. (2013) Dryness of ephemeral lakes and consequences for dust activity: the case of the Hamoun drainage basin, southeastern Iran. *Science of the Total Environment*, *463*, 552–564.

Rashki, A., Arjmand, M. and Kaskaoutis, D.G. (2017) Assessment of dust activity and dust-plume pathways over Jazmurian Basin, southeast Iran. *Aeolian Research*, *24*, 145–160.

Rashki, A., Middleton, N.J. and Goudie, A.S. (2021) Dust storms in Iran–Distribution, causes, frequencies and impacts. *Aeolian Research*, *48*, 100655.

Rast, M. and Painter, T.H. (2019) Earth observation imaging spectroscopy for terrestrial systems: An overview of its history, techniques, and applications of its missions. *Surveys in Geophysics*, *40*(3), 303–331.

Ratnam, J.V., Behera, S.K., Masumoto, Y. and Yamagata, T. (2014) Remote effects of El Niño and Modoki events on the austral summer precipitation of southern Africa. *Journal of Climate*, *27*(10), 3802–3815.

Raupach, M.R., Gillette, D.A. and Leys, J.F. (1993) The effect of roughness elements on wind erosion threshold. *Journal of Geophysical Research: Atmospheres*, *98*(D2), 3023–3029.

Raupach, M.R. and Lu, H. (2004) Representation of land-surface processes in aeolian transport models. *Environmental Modelling & Software*, *19*(2), 93–112.

Ravi, S., D'Odorico, P., Breshears, D.D., Field, J.P., Goudie, A.S., Huxman, T.E., Li, J., Okin, G.S., Swap, R.J., Thomas, A.D. and Van Pelt, S. (2011) Aeolian processes and the biosphere. *Reviews of Geophysics*, *49*(3).

Rayner, N.A., Parker, D.E. and Horton, E.B. (2003) Hadley Centre for Climate Prediction and Research, Met Office, Bracknell, UK global analyses of sea surface temperature, sea ice, and night marine air temperature since the late nineteenth century. *Journal of Geophysical Research, 108*(D14), 4407.

Reason, C.J.C. (2001) Subtropical Indian Ocean SST dipole events and southern African rainfall. *Geophysical Research Letters*, *28*(11), 2225–2227.

Reason, C.J.C. (2002) Sensitivity of the southern African circulation to dipole sea-surface temperature patterns in the south Indian Ocean. *International Journal of Climatology: A Journal of the Royal Meteorological Society*, *22*(4), 377–393.

Reason, C.J.C. (2017) 'Climate of Southern Africa.' In: *Oxford Research Encyclopaedia of Climate Science.* Available: https://doi.org/10.1093/acrefore/9780190228620.013.513

Reason, C.J.C. and Rouault, M. (2002) ENSO-like decadal variability and South African rainfall. *Geophysical Research Letters*, *29*(13), 1638.

Reason, C.J.C. and Jagadheesha, D. (2005) A model investigation of recent ENSO impacts over southern Africa. *Meteorology and Atmospheric Physics*, *89*(1), 181–205.

Reason, C.J.C. and Smart, S. (2015) Tropical south east Atlantic warm events and associated rainfall anomalies over southern Africa. *Frontiers in Environmental Science*, *3*(24).

Reheis, M.C. (2006) A 16-year record of eolian dust in Southern Nevada and California, USA: Controls on dust generation and accumulation. *Journal of Arid Environments*, *67*(3), 487–520.

Reheis, M.C. and Urban, F.E. (2011) Regional and climatic controls on seasonal dust deposition in the southwestern US. *Aeolian Research*, *3*(1), 3–21.

Reynolds, R.L., Yount, J.C., Reheis, M., Goldstein, H., Chavez Jr, P., Fulton, R., Whitney, J., Fuller, C. and Forester, R.M. (2007) Dust emission from wet and dry playas in the Mojave Desert, USA. *Earth Surface Processes and Landforms: The Journal of the British Geomorphological Research Group*, *32*(12), 1811–1827.

Reynolds, R.L., Bogle, R., Vogel, J., Goldstein, H. and Yount, J. (2009) Dust emission at Franklin Lake Playa, Mojave Desert (USA): Response to meteorological and hydrologic changes 2005–2008. *Natural Resources and Environmental Issues*, *15*(18), 105–115.

Ridley, D.A., Heald, C.L. and Ford, B. (2012) North African dust export and deposition: A satellite and model perspective. *Journal of Geophysical Research: Atmospheres*, *117*(D2).

Rivera Rivera, N.I., Gill, T.E., Gebhart, K.A., Hand, J.L., Bleiweiss, M.P. and Fitzgerald, R.M. (2009) Wind modeling of Chihuahuan Desert dust outbreaks. *Atmospheric Environment*, *43*(2), 347–354.

Rivera Rivera, N.I., Gill, T.E., Bleiweiss, M.P. and Hand, J.L. (2010) Source characteristics of hazardous Chihuahuan Desert dust outbreaks. *Atmospheric environment*, *44*(20), 2457–2468.

Romano, F., Ricciardelli, E., Cimini, D., Di Paola, F. and Viggiano, M. (2013) Dust Detection and Optical Depth Retrieval Using MSG-SEVIRI Data. *Atmosphere*, *4*(1), 35–47.

Roney, J.A. and White, B.R. (2004) Definition and measurement of dust aeolian thresholds. *Journal of Geophysical Research: Earth Surface*, *109*(F1).

Roskovensky, J.K. and Liou, K.N. (2005) Differentiating airborne dust from cirrus clouds using MODIS data. *Geophysical Research Letters*, *32*(12), 1–5.

Rossow, W.B. and Garder, L.C. (1993) Cloud detection using satellite measurements of infrared and visible radiances for ISCCP. *Journal of climate*, *6*(12), 2341–2369.

Rouse, J., Haas, R., Schell, J. and Deering, D. (1973) Monitoring Vegetation Systems in the Great Plains with ERTS. *Third ERTS Symposium, NASA. Vol. 1,* 309–317.

Saidou Chaibou, A.A., Ma, X. and Sha, T. (2020) Dust radiative forcing and its impact on surface energy budget over West Africa. *Scientific reports*, *10*(1), 12236.

Saji, N.H., Goswami, B.N., Vinayachandran, P.N. and Yamagata, T. (1999) A dipole mode in the tropical Indian Ocean, *Nature, 401,* 360–363.

Saji, N.H. and Yamagata, T. (2003a) Structure of SST and surface wind variability during Indian Ocean Dipole Mode events: COADS observations. *Journal of Climate, 16,* 2735–2751.

Saji, N.H. and Yamagata, T. (2003b) Possible impacts of Indian Ocean dipole events on global climate. *Climate Research, 25,* 151–169.

Sannazzaro, F., Filizzola, C., Marchese, F., Corrado, R., Paciello, R., Mazzeo, G., Pergola, N. and Tramutoli, V. (2014) Identification of dust outbreaks on infrared MSG-SEVIRI data by using a Robust Satellite Technique (RST). *Acta Astronautica*, *93*, 64–70.

Sayer, A.M., Munchak, L.A., Hsu, N.C., Levy, R.C., Bettenhausen, C. and Jeong, M.J. (2014) MODIS Collection 6 aerosol products: Comparison between Aqua's e-Deep Blue, Dark Target, and "merged" data sets, and usage recommendations. *Journal of Geophysical Research: Atmospheres*, *119*(24), 13965–13989.

Schepanski, K. (2018) Transport of mineral dust and its impact on climate. *Geosciences*, *8*(5), 151.

Schepanski, K., Tegen, I., Laurent, B., Heinold, B. and Macke, A. (2007) A new Saharan dust source activation frequency map derived from MSG-SEVIRI IR-channels. *Geophysical Research Letters*, *34*(18).

Schepanski, K., Tegen, I., Todd, M.C., Heinold, B., Bönisch, G., Laurent, B. and Macke, A. (2009) Meteorological processes forcing Saharan dust emission inferred from MSG-SEVIRI observations of subdaily dust source activation and numerical models. *Journal of Geophysical Research: Atmospheres*, *114*(D10).

Schepanski, K., Tegen, I. and Macke, A. (2012) Comparison of satellite based observations of Saharan dust source areas. *Remote Sensing of Environment*, *123*, 90–97.

Schmit, T.J., Li, J., Li, J., Feltz, W.F., Gurka, J.J., Goldberg, M.D. and Schrab, K.J. (2008) The GOES-R Advanced Baseline Imager and the continuation of current sounder products. *Journal of Applied Meteorology and Climatology*, *47*(10), 2696–2711.

Settle, J.J. and Drake, N.A. (1993) Linear mixing and the estimation of ground cover proportions. *International Journal of Remote Sensing*, *14*(6), 1159–1177.

Shao, Y.P. (2001) A model for mineral dust emission. *Journal of Geophysical Research: Atmospheres*, *106*(D17), 20239–20254.

Shao, Y.P. (2004) Simplification of a dust emission scheme and comparison with data. *Journal of Geophysical Research: Atmospheres*, *109*(D10).

Shao, Y.P. (2008) *Physics and Modelling of Wind Erosion.* Heidelberg: Springer.

Shao, Y.P., Raupach, M.R. and Findlater, P.A. (1993) Effect of saltation bombardment on the entrainment of dust by wind. *Journal of Geophysical Research: Atmospheres*, *98*(D7), 12719–12726.

Shao, Y.P., Raupach, M.R. and Leys, J.F. (1996) A model for predicting aeolian sand drift and dust entrainment on scales from paddock to region. *Soil Research*, *34*(3), 309–342.

Shao, Y.P., Wyrwoll, K.H., Chappell, A., Huang, J., Lin, Z., McTainsh, G.H., Mikami, M., Tanaka, T.Y., Wang, X. and Yoon, S. (2011) Dust cycle: An emerging core theme in Earth system science. *Aeolian Research*, *2*(4), 181–204.

Sharratt, B.S. and Vaddella, V. (2014) Threshold friction velocity of crusted windblown soils in the Columbia Plateau. *Aeolian Research*, *15*, 227–234.

Shaw, P.A. and Bryant, R.G. (2011) Pans, playas and salt lakes. *Arid zone geomorphology: process, form and change in drylands*, 373–401.

Shawky, M., Moussa, A., Hassan, Q.K. and El-Sheimy, N. (2019) Performance assessment of sub- daily and daily precipitation estimates derived from GPM and GSMaP products over an arid environment. *Remote Sensing*, *11*(23), 2840.

She, L., Xue, Y., Yang, X., Guang, J., Li, Y., Che, Y., Fan, C. and Xie, Y. (2018) Dust detection and intensity estimation using Himawari-8/AHI observation. *Remote Sensing*, *10*(4), 490.

Shi, Z., Krom, M.D., Jickells, T.D., Bonneville, S., Carslaw, K.S., Mihalopoulos, N., Baker, A.R. and Benning, L.G. (2012) Impacts on iron solubility in the mineral dust by processes in the source region and the atmosphere: A review. *Aeolian Research*, *5*, 21–42.

Shi, L., Zhang, J., Zhang, D., Igbawua, T. and Liu, Y. (2020) Developing a dust storm detection method combining Support Vector Machine and satellite data in typical dust regions of Asia. *Advances in Space Research*, *65*(4), 1263-1278.

Shikangalah, R.N. (2020) The 2019 drought in Namibia: An overview. *Journal of Namibian Studies: History Politics Culture*, *27*, 37–58.

Singh, J., Noh, Y.J., Agrawal, S. and Tyagi, B. (2019) Dust detection and aerosol properties over Arabian sea using MODIS data. *Earth Systems and Environment*, *3*(1), 139–152.

Skiles, S.M., Mallia, D.V., Hallar, A.G., Lin, J.C., Lambert, A., Petersen, R. and Clark, S. (2018) Implications of a shrinking Great Salt Lake for dust on snow deposition

in the Wasatch Mountains, UT, as informed by a source to sink case study from the 13–14 April 2017 dust event. *Environmental Research Letters*, *13*(12), 124031.

Sokolik, I.N. (2002) The spectral radiative signature of wind-blown mineral dust: Implications for remote sensing in the thermal IR region. *Geophysical Research Letters*, *29*(24), 7-1–7-4.

Soltaninejad, A., Ranjbar, H., Honarmand, M. and Dargahi, S. (2018) Evaporite mineral mapping and determining their source rocks using remote sensing data in Sirjan playa, Kerman, Iran. *Carbonates and Evaporites*, *33*, 255–274.

Soti, V., Tran, A., Bailly, J.S., Puech, C., Seen, D.L. and Bégué, A. (2009) Assessing optical earth observation systems for mapping and monitoring temporary ponds in arid areas. *International Journal of Applied Earth Observation, 11*, 344–351.

Sow, M., Alfaro, S.C., Rajot, J.L. and Marticorena, B. (2009) Size resolved dust emission fluxes measured in Niger during 3 dust storms of the AMMA experiment. *Atmospheric Chemistry and Physics*, *9*(12), 3881–3891.

Stanelle, T., Bey, I., Raddatz, T., Reick, C. and Tegen, I. (2014) Anthropogenically induced changes in twentieth century mineral dust burden and the associated impact on radiative forcing. *Journal of Geophysical Research: Atmospheres*, *119*(23), 13–526.

Storelvmo, T. (2017) Aerosol effects on climate via mixed-phase and ice clouds. *Annual Review of Earth and Planetary Sciences*, *45*, 199–222.

Strong, C.L., Parsons, K., McTainsh, G.H. and Sheehan, A. (2011) Dust transporting wind systems in the lower Lake Eyre Basin, Australia: A preliminary study. *Aeolian Research*, *2*(4), 205–214.

Sun, F., Zhao, Y., Gong, P., Ma, R. and Dai, Y. (2014) Monitoring dynamic changes of global land cover types: fluctuations of major lakes in China every 8 days during 2000–2010. *Chinese Science Bulletin*, *59*(2), 171–189.

Sweeney, M.R., Etyemezian, V., Macpherson, T., Nickling, W., Gillies, J., Nikolich, G. and McDonald, E. (2008) Comparison of PI-SWERL with dust emission measurements from a straight-line field wind tunnel. *Journal of Geophysical Research: Earth Surface*, *113*(F1).

Sweeney, M.R., McDonald, E.V. and Etyemezian, V. (2011) Quantifying dust emissions from desert landforms, eastern Mojave Desert, USA. *Geomorphology*, *135*(1-2), 21–34.

Sweeney, M.R. and Mason, J.A. (2013) Mechanisms of dust emission from Pleistocene loess deposits, Nebraska, USA. *Journal of Geophysical Research: Earth Surface*, *118*(3), 1460–1471.

Sweeney, M.R., Zlotnik, V.A., Joeckel, R.M. and Stout, J.E. (2016) Geomorphic and hydrologic controls of dust emissions during drought from Yellow Lake playa, West Texas, USA. *Journal of Arid Environments*, *133*, 37–46.

Sweeney, M.R., Forman, S.L. and McDonald, E.V. (2022) Contemporary and future dust sources and emission fluxes from gypsum-and quartz-dominated eolian systems, New Mexico and Texas, USA. *Geology*, *50*(3), 356–360.

Sweeney, M.R., Lacey, T. and Forman, S.L. (2023) The role of abrasion and resident fines in dust production from aeolian sands as measured by the Portable in situ Wind Erosion Laboratory (PI-SWERL). *Aeolian Research*, *63*, 100889.

Tan, M.L. and Santo, H. (2018) Comparison of GPM IMERG, TMPA 3B42 and PERSIANN-CDR satellite precipitation products over Malaysia. *Atmospheric Research*, *202*, 63–76.

Tang, G., Clark, M.P., Papalexiou, S.M., Ma, Z. and Hong, Y. (2020) Have satellite precipitation products improved over last two decades? A comprehensive comparison of GPM IMERG with nine satellite and reanalysis datasets. *Remote Sensing of Environment, 240*(111697).

Tegen, I. and Fung, I. (1995) Contribution to the atmospheric mineral aerosol load from land surface modification. *Journal of Geophysical Research: Atmospheres*, *100*(D9), 18707–18726.

Tegen, I., Harrison, S.P., Kohfeld, K., Prentice, I.C., Coe, M. and Heimann, M. (2002) Impact of vegetation and preferential source areas on global dust aerosol: Results from a model study. *Journal of Geophysical Research: Atmospheres*, *107*(D21), AAC 14-1–14-27.

Tegen, I., Werner, M., Harrison, S.P. and Kohfeld, K.E. (2004) Relative importance of climate and land use in determining present and future global soil dust emission. *Geophysical Research Letters*, *31*(5).

Tegen, I., Schepanski, K. and Heinold, B. (2013) Comparing two years of Saharan dust source activation obtained by regional modelling and satellite observations. *Atmospheric Chemistry and Physics*, *13*(5), 2381–2390.

Tegen, I. and Schulz, M. (2014) 'Numerical dust models.' In: Knippertz, P. and Stuut, J.W. (Eds.) *Mineral Dust: A Key Player in the Earth System.* Dordrecht, Netherlands, Springer. 201–222.

Teller, J.T. and Last, W.M. (1990) Paleohydrological indicators in playas and salt lakes, with examples from Canada, Australia, and Africa. *Palaeogeography, Palaeoclimatology, Palaeoecology*, *76*(3-4), 215–240.

Tjemkes, S. A. (2005) On the conversion from radiances to equivalent brightness temperatures. Available: https://www-cdn.eumetsat.int/files/2020-04/pdf_ten_052556_rad2bright.pdf.

Tobías, A. and Stafoggia, M. (2020) Modeling desert dust exposures in epidemiologic short-term health effects studies. *Epidemiology*, *31*(6), 788.

Todd, M.C., Washington, R., Martins, J.V., Dubovik, O., Lizcano, G., M'bainayel, S. and Engelstaedter, S. (2007) Mineral dust emission from the Bodélé Depression, northern Chad, during BoDEx 2005. *Journal of Geophysical Research: Atmospheres*, *112*(D6).

Todd, M.C., Bou Karam, D., Cavazos, C., Bouet, C., Heinold, B., Baldasano, J.M., Cautenet, G., Koren, I., Perez, C., Solmon, F. and Tegen, I. (2008a) Quantifying uncertainty in estimates of mineral dust flux: An intercomparison of model performance over the Bodélé Depression, northern Chad. *Journal of Geophysical Research: Atmospheres*, *113*(D24).

Todd, M.C., Washington, R., Raghavan, S., Lizcano, G. and Knippertz, P. (2008b) Regional model simulations of the Bodélé low-level jet of northern Chad during the Bodélé Dust Experiment (BoDEx 2005). *Journal of Climate*, *21*(5), 995–1012.

Tollerud, H.J. and Fantle, M.S. (2014) The temporal variability of centimeter-scale surface roughness in a playa dust source: Synthetic aperture radar investigation of playa surface dynamics. *Remote sensing of environment*, *154*, 285–297.

Tong, D.Q., Gill, T.E., Sprigg, W.A., Van Pelt, R.S., Baklanov, A.A., Barker, B.M., Bell, J.E., Castillo, J., Gassó, S., Gaston, C.J. and Griffin, D.W. (2023) Health and safety effects of airborne soil dust in the Americas and beyond. *Reviews of Geophysics*, *61*(2), e2021RG000763.

Tramutoli, V. (2007) 'Robust satellite techniques (RST) for natural and environmental hazards monitoring and mitigation: Theory and applications.' In: *Proceedings of the 2007 International Workshop on the Analysis of Multi-Temporal Remote Sensing Images*. Leuven, Belgium, 18–20 July 2007. New York, NY, USA: IEEE.

Tramutoli, V., Filizzola, C., Marchese, F., Mazzeo, G., Paciello, R., Pergola, N., Pietrapertosa, C. and Sannazzaro, F. (2010) 'A Robust Satellite Technique (RST) for dust storm detection and monitoring: The case of 2009 Australian event.' In: *2010 IEEE International Geoscience and Remote Sensing Symposium*. Honolulu, Hawaii, 25 – 30 July 2010. New York, NY, USA: IEEE, 1707–1709.

Tramutoli, V., Marchese, F., Falconieri, A., Filizzola, C., Genzano, N., Hattori, K., Lisi, M., Liu, J.Y., Ouzounov, D., Parrot, M. and Pergola, N. (2019) Tropospheric and Ionospheric Anomalies Induced by Volcanic and Saharan Dust Events as Part of Geosphere Interaction Phenomena. *Geosciences*, *9*(4), 177.

Tuccella, P., Pitari, G., Colaiuda, V., Raparelli, E. and Curci, G. (2021) Present-day radiative effect from radiation-absorbing aerosols in snow. *Atmospheric Chemistry and Physics*, *21*(9), 6875–6893.

Tweed, S., Leblanc, M., Cartwright, I., Favreau, G. and Leduc, C. (2011) Arid zone groundwater recharge and salinisation processes; an example from the Lake Eyre Basin, Australia. *Journal of Hydrology*, *408*(3-4), 257–275.

Ukhov, A., Mostamandi, S., Da Silva, A., Flemming, J., Alshehri, Y., Shevchenko, I. and Stenchikov, G. (2020) Assessment of natural and anthropogenic aerosol air

pollution in the Middle East using MERRA-2, CAMS data assimilation products, and high-resolution WRF-Chem model simulations. *Atmospheric Chemistry and Physics*, *20*(15), 9281–9310.

Urban, F.E., Reynolds, R.L. and Fulton, R. (2009) The dynamic interaction of climate, vegetation, and dust emission, Mojave Desert, USA. *Arid environments and wind erosion*, 243–267.

Urban, F.E., Goldstein, H.L., Fulton, R. and Reynolds, R.L. (2018) Unseen dust emission and global dust abundance: Documenting dust emission from the Mojave Desert (USA) by daily remote camera imagery and wind-erosion measurements. *Journal of Geophysical Research: Atmospheres*, *123*(16), 8735–8753.

Vakkari, V., Beukes, J.P., Dal Maso, M., Aurela, M., Josipovic, M. and van Zyl, P.G. (2018) Major secondary aerosol formation in southern African open biomass burning plumes. *Nature Geoscience*, *11*(8), 580–583.

van der Meer, F. (2001) Spectral matching using pixel cross-correlograms for the analysis of LANDSAT TM data. *International Journal of Applied Earth Observation and Geoinformation, 3*(2), 197–202.

van der Meer, F. (2006) The effectiveness of spectral similarity measures for the analysis of hyperspectral imagery. *International journal of applied earth observation and geoinformation*, *8*(1), 3–17.

Vandenberghe, J. (2013) Grain size of fine-grained windblown sediment: A powerful proxy for process identification. *Earth-Science Reviews*, *121*, 18–30.

van Leeuwen, C.C.E., Fister, W., Vos, H.C., Cammeraat, L.H. and Kuhn, N.J. (2021) A cross-comparison of threshold friction velocities for PM10 emissions between a

traditional portable straight-line wind tunnel and PI-SWERL. *Aeolian Research*, *49*, 100661.

Van Pelt, R.S., Zobeck, T.M., Baddock, M.C. and Cox, J.J. (2010) Design, construction, and calibration of a portable boundary layer wind tunnel for field use. *Transactions of the ASABE*, *53*(5), 1413–1422.

Van Pelt, R.S. and Zobeck, T.M. (2013) Portable wind tunnels for fields testing of soils and natural surfaces. *Wind tunnels designs and their diverse engineering applications. InTech*, 59–73.

Van Pelt, R.S., Tatarko, J., Gill, T.E., Chang, C., Li, J., Eibedingil, I.G. and Mendez, M. (2020) Dust emission source characterization for visibility hazard assessment on Lordsburg Playa in Southwestern New Mexico, USA. *Geoenvironmental Disasters*, *7*, 1–12.

Van Pelt, R.S., Eibedingil, I.G., Gill, T.E., Tong, D.Q., Tatarko, J., Li, J., Chang, C. and Mendez, M. (2023) Characterizing a Hazardous Dust Source in the Chihuahuan Desert Using Ground-Based Measurements, Remote Sensing, and Modelling. *American Society of Agricultural and Biological Engineers – Soil Erosion Research Under a Changing Climate,* Aguadilla, Puerto Rico, USA, *8-13 January 2023*. Available: https://elibrary.asabe.org/abstract.asp?aid=53777

van Rensburg and Tortajada, C. (2021) An Assessment of the 2015–2017 Drought in Windhoek. *Frontiers in Climate, 3*(602962).

Varga, G. (2012) Spatio-temporal distribution of dust storms-a global coverage using NASA TOMS aerosol measurements. *Hungarian geographical bulletin*, *61*(4), 275–298.

Vickery, K.J., Eckardt, F.D. and Bryant, R.G. (2013) A sub-basin scale dust plume source frequency inventory for southern Africa, 2005–2008. *Geophysical Research Letters*, *40*(19), 5274–5279.

Vishkaee, F.A., Flamant, C., Cuesta, J., Flamant, P. and Khalesifard, H.R. (2011) Multiplatform observations of dust vertical distribution during transport over northwest Iran in the summertime. *Journal of Geophysical Research: Atmospheres*, *116*(D5).

Vishkaee, F.A., Flamant, C., Cuesta, J., Oolman, L., Flamant, P. and Khalesifard, H.R. (2012) Dust transport over Iraq and northwest Iran associated with winter Shamal: A case study. *Journal of Geophysical Research: Atmospheres*, *117*(D3).

Vivone, G. (2023) Multispectral and hyperspectral image fusion in remote sensing: A survey. *Information Fusion*, *89*, 405–417.

von Holdt, J.R.C., Eckardt, F.D. and Wiggs, G.F.S. (2017) Landsat identifies aeolian dust emission dynamics at the landform scale. *Remote Sensing of Environment*, *198*, 229–243.

von Holdt, J.R.C., Eckardt, F.D., Baddock, M.C. and Wiggs, G.F.S. (2019) Assessing landscape dust emission potential using combined ground-based measurements and remote sensing data. *Journal of Geophysical Research: Earth Surface*, *124*(5), 1080–1098.

von Holdt, J.R.C., Eckardt, F.D., Baddock, M.C., Hipondoka, M.H.T. and Wiggs, G.F.S. (2021) Influence of sampling approaches on physical and geochemical analysis of aeolian dust in source regions. *Aeolian Research*, *50*, 100684.

Vos, H.C., Fister, W., Eckardt, F.D., Palmer, A.R. and Kuhn, N.J. (2020) Physical crust formation on sandy soils and their potential to reduce dust emissions from croplands. *Land*, *9*(12), 503.

Vos, H.C., Fister, W., von Holdt, J.R., Eckardt, F.D., Palmer, A.R. and Kuhn, N.J. (2021) Assessing the PM10 emission potential of sandy, dryland soils in South Africa using the PI-SWERL. *Aeolian Research*, *53*, 100747.

Walker, A.L., Liu, M., Miller, S.D., Richardson, K.A. and Westphal, D.L. (2009) Development of a dust source database for mesoscale forecasting in southwest Asia. *Journal of Geophysical Research: Atmospheres*, *114*(D18).

Wang, X., Zhou, Z. and Dong, Z. (2006) Control of dust emissions by geomorphic conditions, wind environments and land use in northern China: An examination based on dust storm frequency from 1960 to 2003. *Geomorphology*, *81*(3-4), 292–308.

Wang, X., Ding, Y., Zhao, C. and Wang, J. (2019) Similarities and improvements of GPM IMERG upon TRMM 3B42 precipitation product under complex topographic and climatic conditions over Hexi region, Northeastern Tibetan Plateau. *Atmospheric Research*, *218*, 347–363.

Wang, Z., Chen, S., Liu, C., Chen, Y., Gong, Y. and Cheng, S. (2022) Dynamic Dust Source Regions and the Associated Natural and Anthropogenic Dust Emissions at the Global Scale. *Frontiers in Earth Science*, *10*, 802658.

Warren, J.K. (2010) Evaporites through time: Tectonic, climatic and eustatic controls in marine and nonmarine deposits. *Earth-Science Reviews*, *98*(3-4), 217–268.

Warren, J.K. (Ed.) (2016) *Evaporites: A geological compendium*. 2nd edn. Heidelberg: Springer.

Warren, A., Chappell, A., Todd, M.C., Bristow, C., Drake, N., Engelstaedter, S., Martins, V., M'bainayel, S. and Washington, R. (2007) Dust-raising in the dustiest place on earth. *Geomorphology*, *92*(1-2), 25–37.

Washington, R., Todd, M., Middleton, N.J. and Goudie, A.S. (2003) Dust-storm source areas determined by the total ozone monitoring spectrometer and surface observations. *Annals of the Association of American Geographers*, *93*(2), 297–313.

Washington, R. and Todd, M.C. (2005) Atmospheric controls on mineral dust emission from the Bodélé Depression, Chad: The role of the low level jet. *Geophysical Research Letters*, *32*(17).

Washington, R. and Preston, A. (2006) Extreme wet years over southern Africa: Role of Indian Ocean sea surface temperatures. *Journal of Geophysical Research: Atmospheres*, *111*(D15).

Washington, R., Todd, M.C., Lizcano, G., Tegen, I., Flamant, C., Koren, I., Ginoux, P., Engelstaedter, S., Bristow, C.S., Zender, C.S. and Goudie, A.S. (2006) Links between topography, wind, deflation, lakes and dust: The case of the Bodélé Depression, Chad. *Geophysical research letters*, *33*(9).

Watson, C.S., King, O., Miles, E.S. and Quincey, D.J. (2018) Optimising NDWI supraglacial pond classification on Himalayan debris-covered glaciers. *Remote Sensing of Environment*, *217*, 414–425.

Webb, N.P. and McGowan, H.A. (2009) Approaches to modelling land erodibility by wind. *Progress in Physical Geography*, *33*(5), 587–613.

Webb, N.P. and Strong, C.L. (2011) Soil erodibility dynamics and its representation for wind erosion and dust emission models. *Aeolian Research*, *3*(2), 165–179.

Webb, N.P. and Pierre, C. (2018) Quantifying anthropogenic dust emissions. *Earth's Future*, *6*(2), 286–295.

Webb, N.P., LeGrand, S.L., Cooper, B.F., Courtright, E.M., Edwards, B.L., Felt, C., Van Zee, J.W. and Ziegler, N.P. (2021) Size distribution of mineral dust emissions from sparsely vegetated and supply-limited dryland soils. *Journal of Geophysical Research: Atmospheres*, *126*(22), e2021JD035478.

White, K. and Eckardt, F.D. (2006) Geochemical mapping of carbonate sediments in the Makgadikgadi basin, Botswana using moderate resolution remote sensing data. *Earth Surface Processes and Landforms*, *31*(6), 665–681.

Wiggs, G.F.S., Baddock, M.C., Bryant, R.G., Thomas, D.S.G., Eckardt, F.D., Washington, R., Engelstaedter, S., von Holdt, J.R.C., Murray, J.E., Nield, J.M., Kötting, S. and Seely, M. (2018) 'Resolving aeolian dust emission dynamics from a globally significant source: combining field-based observations and remote sensing data at Etosha Pan, Namibia'. ICAR, Bordeaux, 25 – 29 June 2018.

Wiggs, G.F.S., Baddock, M.C., Thomas, D.S.G., Washington, R., Nield, J.M., Engelstaedter, S., Bryant, R.G., Eckardt, F.D., von Holdt, J.R.C. and Kötting, S. (2022) Quantifying mechanisms of aeolian dust emission: Field measurements at Etosha Pan, Namibia. *Journal of Geophysical Research: Earth Surface*, *127*(8), e2022JF006675.

Williams, C.A. (2010) 'Integration of remote sensing and modelling to understand carbon fluxes and climate interactions in Africa.' In: Hill, M.J. and Hanan, N.P. (Eds.) *Ecosystems Function in Global Savannas: Measurement and Modelling at Landscape to Global Scales,* Boca Raton, FL, USA, CRC Press. 327–345.

Wolfe, S.A. and Nickling, W.G. (1996) Shear stress partitioning in sparsely vegetated desert canopies. *Earth Surface Processes and Landforms*, *21*(7), 607–619.

Wolter, K. and Timlin, M.S. (2011) El Niño/Southern Oscillation behaviour since 1871 as diagnosed in an extended multivariate ENSO index (MEI.ext). *International Journal of Climatology, 31*(14), 1074–1087.

Wu, C., Lin, Z. and Liu, X. (2020) The global dust cycle and uncertainty in CMIP5 (Coupled Model Intercomparison Project phase 5) models. *Atmospheric Chemistry and Physics*, *20*(17), 10401–10425.

Xi, X. and Sokolik, I.N. (2016) Dust interannual variability and trend in Central Asia from 2000 to 2014 and their climatic linkages. *Journal of Geophysical Research: Atmospheres*, *120*(23), 12175–12197.

Xu, H. (2006) Modification of normalised difference water index (NDWI) to enhance open water features in remotely sensed imagery. *International journal of remote sensing*, *27*(14), 3025–3033.

Xu, Z., Chen, S., Lu, P., Wang, Z., Li, A., Zeng, Q. and Chen, L. (2022) Optimizing a standard spectral measurement protocol to enhance the quality of soil spectra: Exploration of key variables in lab-based VNIR-SWIR spectral measurement. *Remote Sensing*, *14*(7), 1558.

Yao, F., Wang, J., Wang, C. and Crétaux, J.F. (2019) Constructing long-term high-frequency time series of global lake and reservoir areas using Landsat imagery. *Remote Sensing of Environment*, *232*, 111210.

Yoshioka, M., Mahowald, N.M., Conley, A.J., Collins, W.D., Fillmore, D.W., Zender, C.S. and Coleman, D.B. (2007) Impact of desert dust radiative forcing on Sahel precipitation: Relative importance of dust compared to sea surface temperature variations, vegetation changes, and greenhouse gas warming. *Journal of Climate*, *20*(8), 1445–1467.

Yue, H., Li, Y., Qian, J. and Liu, Y. (2020) A new accuracy evaluation method for water body extraction. *International Journal of Remote Sensing*, *41*(19), 7311–7342.

Zander, P.D., Wienhues, G. and Grosjean, M. (2022) Scanning hyperspectral imaging for in situ biogeochemical analysis of lake sediment cores: Review of recent developments. *Journal of Imaging*, *8*(3), 58.

Zender, C.S., Bian, H. and Newman, D. (2003) Mineral Dust Entrainment and Deposition (DEAD) model: Description and 1990s dust climatology. *Journal of Geophysical Research: Atmospheres*, *108*(D14).

Zender, C.S. and Kwon, E.Y. (2005) Regional contrasts in dust emission responses to climate. *Journal of Geophysical Research: Atmospheres*, *110*(D13).

Zhang, B., Tsunekawa, A. and Tsubo, M. (2008) Contributions of sandy lands and stony deserts to long-distance dust emission in China and Mongolia during 2000–2006. *Global and Planetary Change*, *60*(3-4), 487–504.

Zhang, B., Tsunekawa, A. and Tsubo, M. (2015) Identification of dust hot spots from multi-resolution remotely sensed data in eastern China and Mongolia. *Water, Air, & Soil Pollution*, *226*(4), 1–18.

Zhang, F., Li, J., Zhang, B., Shen, Q., Ye, H., Wang, S. and Lu, Z. (2018) A simple automated dynamic threshold extraction method for the classification of large water bodies from landsat-8 OLI water index images. *International Journal of Remote Sensing*, *39*(11), 3429–3451.

Zhang, G., Xiao, Y., Xiang, M., Hong, C., Zhang, B.T., Liu, L., Shi, P. and Liu, J. (2021) Structure and morphological characteristics of polygonal salt crust, the West Juyan Lake, China. *Geosciences Journal*, 1–12.

Zhang, G., Li, L., Tang, W., Liu, L., Shi, P., Han, X. and Dai, J. (2023) Wind erosion from crusted playa surfaces by no saltation and with saltation: A comparison through laboratory wind tunnel experiments. *International Soil and Water Conservation Research*, *11*(3), 518–527.

Zhang, J., Guo, W., Zhou, B. and Okin, G.S. (2021) Drone-based remote sensing for research on wind erosion in drylands: Possible applications. *Remote Sensing, 13*(2), 283.

Zhang, P. and Shao, M.A. (2013) Temporal stability of surface soil moisture in a desert area of northwestern China. *Journal of Hydrology*, *505*, 91–101.

Zhao, A., Ryder, C.L. and Wilcox, L.J. (2022) How well do the CMIP6 models simulate dust aerosols? *Atmospheric Chemistry and Physics*, *22*(3), 2095–2119.

Zhao, F., Liu, H., Yin, Y., Hu, G. and Wu, X. (2011) Vegetation succession prevents dry lake beds from becoming dust sources in the semi-arid steppe region of China. *Earth Surface Processes and Landforms*, *36*(7), 864–871.

Zucca, C., Middleton, N., Kang, U. and Liniger, H. (2021) Shrinking water bodies as hotspots of sand and dust storms: The role of land degradation and sustainable soil and water management. *Catena*, *207*, 105669.

Zunckel, M., Held, G., Preston-Whyte, R. A. and Joubert, A. (1996a) Low-level wind maxima and the transport of pyrogenic products over southern Africa. *Journal of Geophysical Research: Atmospheres, 101*(19), 23745–23755.

Zunckel, M., Hong, Y., Brassel, K., and O'Beirne, S. (1996b) Characteristics of the nocturnal boundary layer: Okaukuejo, Namibia, during SAFARI-92. *Journal of Geophysical Research: Atmospheres, 101*(19), 23757–23766.

APPENDICES

Appendix 1: Supplementary Information for Chapter 4

Appendix 2: Supplementary Information for Chapter 6

Appendix 1: Supplementary Information for Chapter 4

A.1.1. Validation of catchment precipitation data

The accuracy of satellite-retrieved precipitation data was evaluated by statistical comparison against the ground-based observations data from the meteorological stations. The Pearson Correlation Coefficient (PCC) was computed for satellite-retrieved pixel estimates and measured monthly rainfall observations at corresponding meteorological stations. At the individual station level, significant moderate (Mannheim; $r = 0.58$, $p < 0.001$, $n = 116$) to very strong (Namacunde; $r = 0.99$, $p < 0.001$, $n = 63$) positive correlations were found between ground-based observation records and satellite-retrieved rainfall estimates (Figure 4.2, Chapter 4). Note, however, differences in PCC values may in part reflect inherent sample size variability, as determined by the availability of observation records across individual meteorological stations (Figure 4.2, Chapter 4) (Peng *et al.,* 2021).

For time-series values measured across all stations, there is an overall significant moderate-strong correlation between observed and satellite-retrieved rainfall estimates ($r = 0.83$, $p < 0.001$, $n = 1{,}336$) (Figure A1.1). However, the scatter plot displayed in Figure A1.1 shows that correlation coefficients are significant but reduced slightly when seasonal rainfall estimates are examined. Satellite-retrieved rainfall estimates are more closely correlated to observed rainfall records during the wet season (November – April) ($r = 0.71$, $p < 0.001$) than dry season (May – October) rainfall estimates (r

= 0.68, $p < 0.001$) (Figure A1.1). Nonetheless, outcomes of the accuracy assessment do correspond with similar studies that evaluate the performance of satellite precipitation products using rain gauge data in semi-arid desert environments (e.g., Lu *et al.,* 2018; Fang *et al.,* 2019; Mahmoud *et al.,* 2021), where correlation coefficients ranged between 0.63 – 0.9 for monthly precipitation estimates.

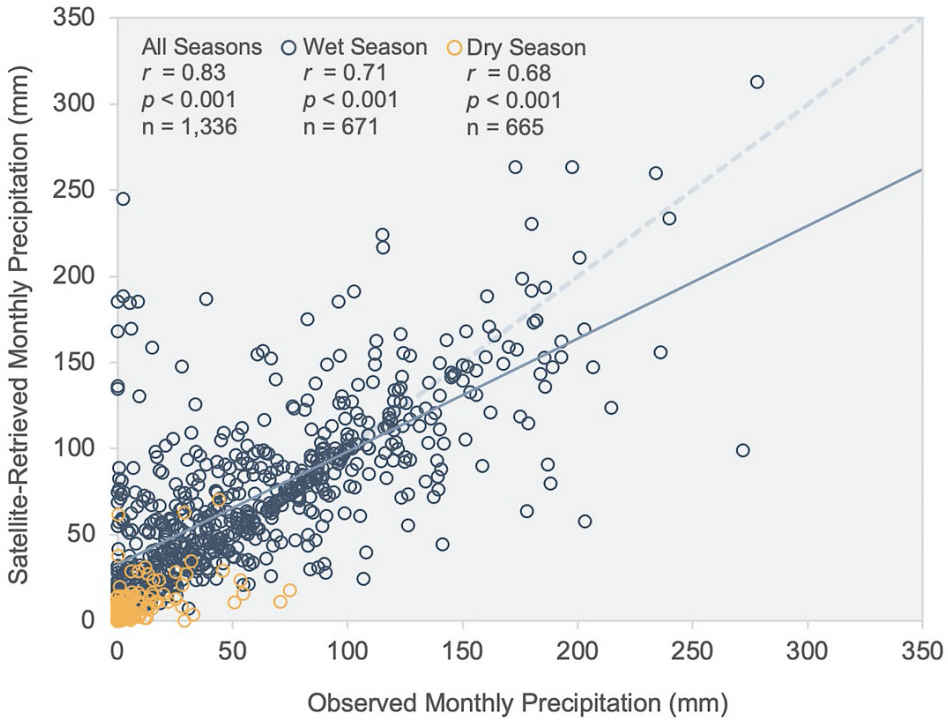


Figure A1.1. Scatterplot of observed monthly wet season (blue) and dry season (ochre) precipitation at meteorological stations and corresponding pixel values of TRMM/GPM-IMERG satellite-derived precipitation totals within the Cuvelai-Etosha Basin, where the dashed line represents 1:1 and the solid line represents the outcome of linear regression. Results indicate a tendency for the satellite-derived data to over-estimate low rainfall values observed in the region, particularly during the dry season.

Such variability in correlation coefficients may reflect the semi-arid climate context, characterised by unreliable precipitation and high spatiotemporal variability in rainfall events, which are sub-optimally captured by the satellite precipitation products (Tan and Santo, 2018). It can be seen in both Figure 4.2 (Chapter 4) and Figure A1.1 that

the satellite-derived rainfall products are inclined to provide an overestimate of light rainfall (< 50 mm) at the monthly scale, especially during the dry season, compared to the observed monthly accumulations from meteorological stations.

This finding may in part be a consequence of errors associated with the potential interruption of rain gauge measurements or false detection by the satellite sensors. However, it is also likely a function of the spatially and temporally localised nature of light rainfall events from convection-induced cloud formations in the semi-arid desert region (Engert, 1997). For such conditions, a rainfall event that partially affects a satellite pixel, and is thus added to its precipitation total, may not necessarily be observed by point-scale rain gauge measurements within that pixel. Conversely, the chance for this condition is reduced in wetter periods in the catchment, where uniform rainfall over a large area is common. This is in agreement with the findings of several other researchers who demonstrated that the satellite-based products overestimate light rainfall events in various arid and semi-arid regions (e.g., Guo *et al.,* 2016; Alsumaiti *et al.,* 2020; Maghsood *et al.,* 2020; Kawo *et al.,* 2021; Li, X. *et al.,* 2021).

Yet, a systematic method to provide data bias-correction of the TRMM and GPM-IMERG products in capturing light precipitation in arid and semi-arid climate contexts has yet to be established (Wang *et al.,* 2019). Nevertheless, given that the potential errors have been recognised and quantified, the satellite-derived monthly gridded precipitation data were deemed viable for the purpose of this study, since they enable

assessment of rainfall dynamics across the whole Cuvelai-Etosha catchment and for the entire research period, which would otherwise be unachievable with the limited observation record from meteorological stations.

A.1.2. Validation of pan surface flooding extents

To assess the accuracy of results of water body detection from MODIS data, the extent of water classified from Landsat imagery served as a validation source in this study. Owing to its long record of near-infrared data at high spatial resolution (30 m), Landsat offers a standard and widely used data source for evaluating MODIS-based surface water classifications (Klein *et al.,* 2014; Li *et al.,* 2015; Jing *et al.,* 2018; Herndon *et al.,* 2020).

The dynamic threshold density method was used to segment water bodies from Landsat 5 TM and 8 OLI NIR data derived following the same methodology as for the MODIS imagery (see section 4.2.2.). The water bodies detected from the 30 m Landsat images were resampled to the 500 m MODIS pixel size to perform a pixel-to-pixel comparison with MODIS water masks for the same acquisition date. It should be noted that pixel resampling may result in some classification error in water extent mapped from Landsat data, which may influence the accuracy assessment results (Lyons *et al.,* 2018). Mixed pixels from lake fringes and small water bodies detected in the 30 m resolution Landsat images may result in varying spectral response at 500 m resolution (Li *et al.,* 2015). A more accurate validation exercise could be conducted based on

comparison with manually collected validation samples (Herndon *et al.,* 2020). However, such approach is very time-consuming for large image time-series and therefore was not conducted in this research.

A total of 185 corresponding Landsat-MODIS binary water mask images were selected and compared to assess the accuracy of water body classifications across the study period. Confusion matrices were generated to evaluate the agreement and disagreement of the classification results (Congalton and Green, 2019). Three standard measurements, namely user's accuracy (defined as the number of correctly classified water pixels divided by the total number of classified water pixels in the MODIS detection results), producer's accuracy (total number of correctly classified water pixels divided by the total number of water pixels in the Landsat detection results), and overall accuracy (sum of all correctly classified water/non-water pixels divided by the total number of validation samples) were quantified to assess the accuracies of MODIS water body detection.

Table A1.1 details the monthly summaries of individual class accuracies (user's and producer's accuracy) and overall total accuracy for water body detection.

Table A1.1. The user's, producer's and overall accuracies of water body detection from MODIS time-series data. **Note:** n refers to the number of validation samples (MODIS-Landsat image pairings of flooding occurrence) compared for each month for the 2000–2022 period (n = 185 total image pairings analysed overall).

Month	User's Accuracy	Producer's Accuracy
January *(n = 14)*	0.94	0.82
February *(n = 19)*	0.92	0.75
March *(n = 24)*	0.90	0.89
April *(n = 31)*	0.92	0.92
May *(n = 24)*	0.96	0.87
June *(n = 14)*	0.98	0.86
July *(n = 12)*	0.96	0.93
August *(n = 12)*	0.97	0.92
September *(n = 11)*	0.97	0.90
October *(n = 8)*	0.98	0.92
November *(n = 7)*	0.99	0.94
December *(n = 9)*	0.92	0.78
Overall Accuracy *(n = 185)*	0.96	

An overall accuracy of 0.96 was obtained for this study (Table A1.1), which is adequate for the dynamic analysis of lake surface area (Li *et al.,* 2015). Due to the high concentration of salts and other dissolved particles, the spectral features of flood waters on Etosha Pan are likely to differ from clear water bodies in the infrared region and may vary considerably between time-steps (Herndon *et al.,* 2020). Hence, despite

utilising a dynamic threshold technique to mitigate these effects over time across the study period, the misclassification of water and non-water pixels can still occur based on simple threshold values (Zhang, F. *et al.,* 2018).

Individual class accuracies were moderate-high for validation samples in this study (Table A1.1). The detection results showed consistently lower producer's accuracies, suggesting that water body masks developed from MODIS data may underestimate the extent of water bodies during flooding events. This is demonstrated by comparison of a water mask derived from MODIS data (Figure A1.2a) with a water mask derived from Landsat data (Figure A1.2b) acquired for the same date (May 15, 2020). The occurrence of water at lake fringes and smaller water bodies displayed in the true-colour imagery (Figure A1.2c) were not extracted from the MODIS imagery (Figure A1.2d).

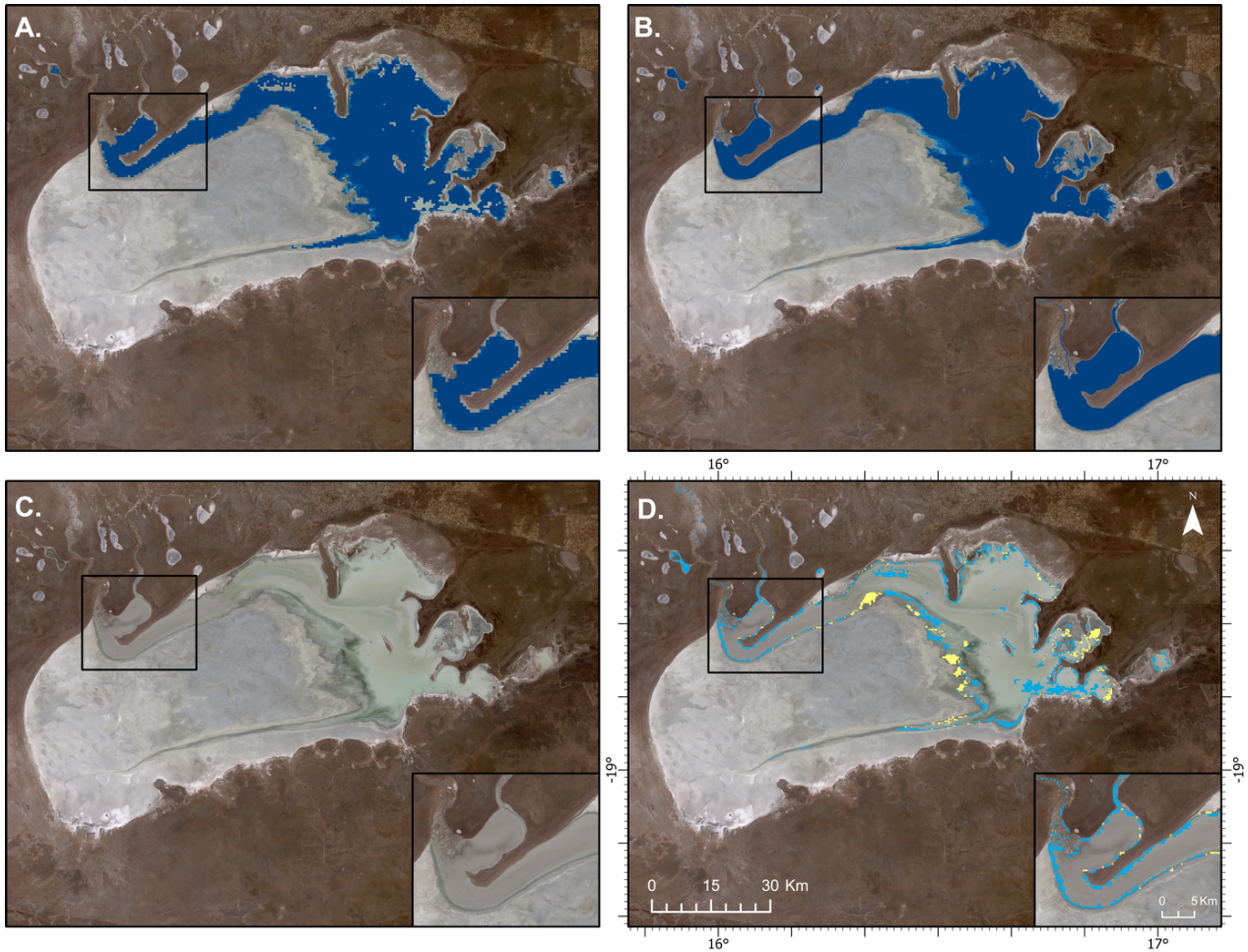


Figure A1.2. Comparison of surface flooding at Etosha Pan on 15 May 2020 displayed as a (a) water mask derived from MODIS data [425 km^2 (8.85% of total pan area) detected as surface water]; (b) water mask derived from Landsat data [427 km^2 (8.89% of total pan area) detected as surface water]; (c) true-colour Landsat 8 OLI image; and (d) water mask difference image, where light blue areas indicate pixels that were classified as water by Landsat and not MODIS [2 km^2 (0.04% of total pan area)] and yellow areas indicate pixels that were classified as water by MODIS and not Landsat [0.5 km^2 (0.01% of total pan area)]. In this example, a 99.5% agreement value was achieved between surface water detection results from MODIS and Landsat data.

Appendix 2: Supplementary Information for Chapter 6

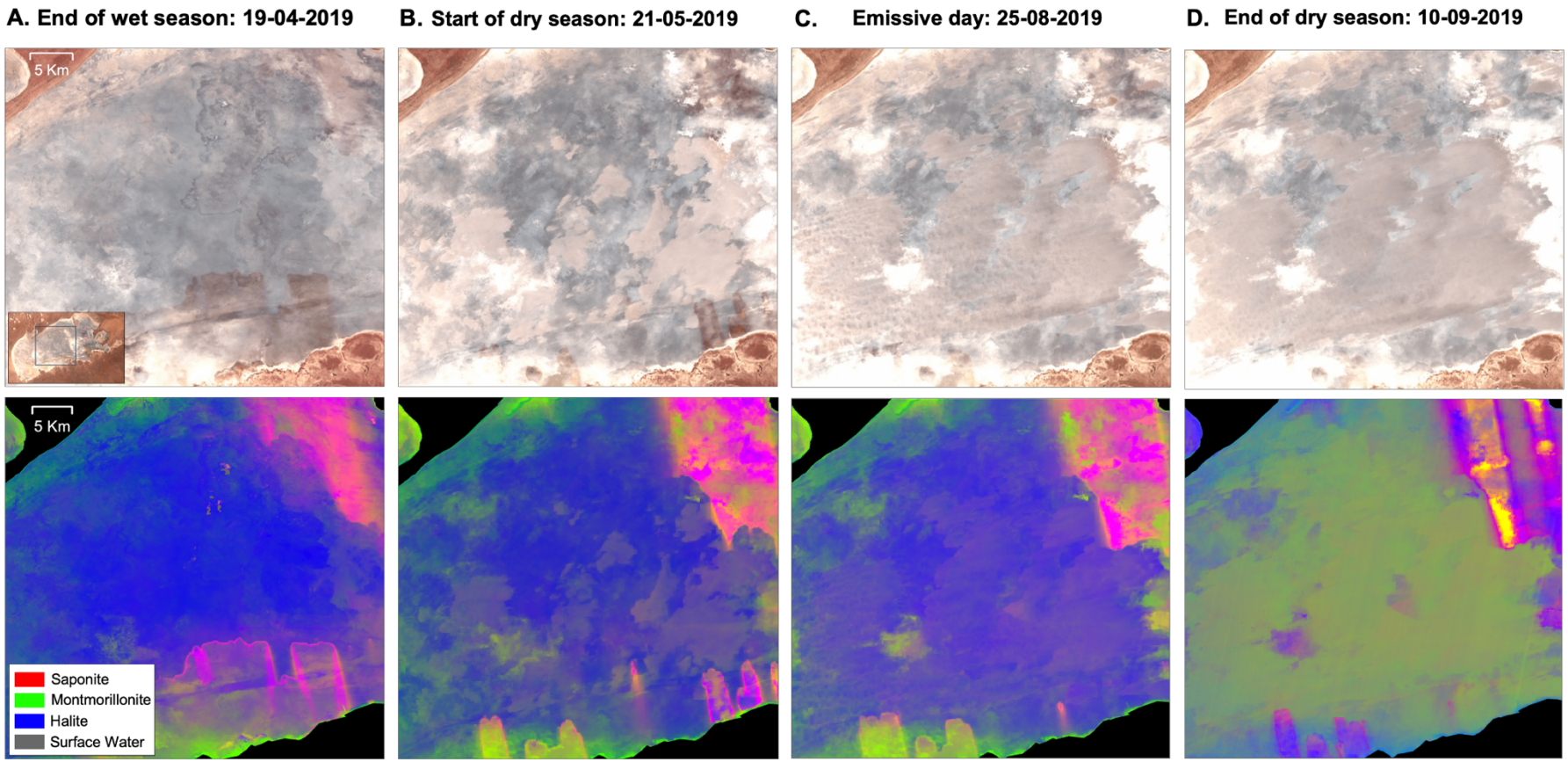


Figure A2.1. Temporal comparisons of Landsat 8-9 OLI false-colour composite (bands 5, 4, 3) images of surface change at Etosha Pan across the 2019 winter dry season showing the development of emissive 'hot-spot' surfaces and linear spectral unmixing model output RGB image composite maps for corresponding image dates, where RGB channels delineate estimates of relative mineral abundances (%) for (R) saponite, (G) montmorillonite and (B) halite minerals,

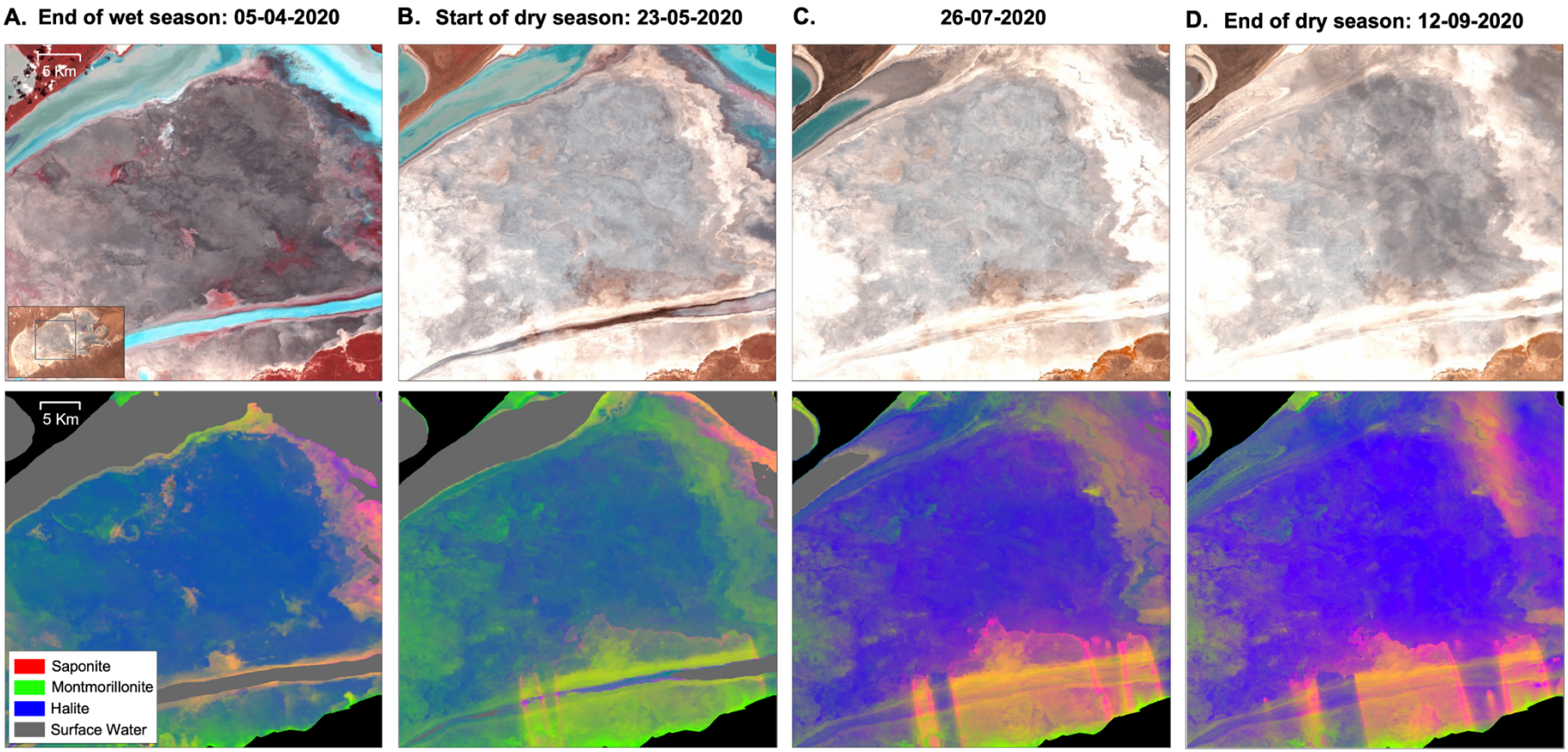


Figure A2.2. Temporal comparisons of Landsat 8-9 OLI false-colour composite (bands 5, 4, 3) images of surface change at Etosha Pan across the 2020 winter dry season and linear spectral unmixing model output RGB image composite maps for corresponding image dates, where RGB channels delineate estimates of relative mineral abundances (%) for (R) saponite, (G) montmorillonite and (B) halite minerals, respectively.

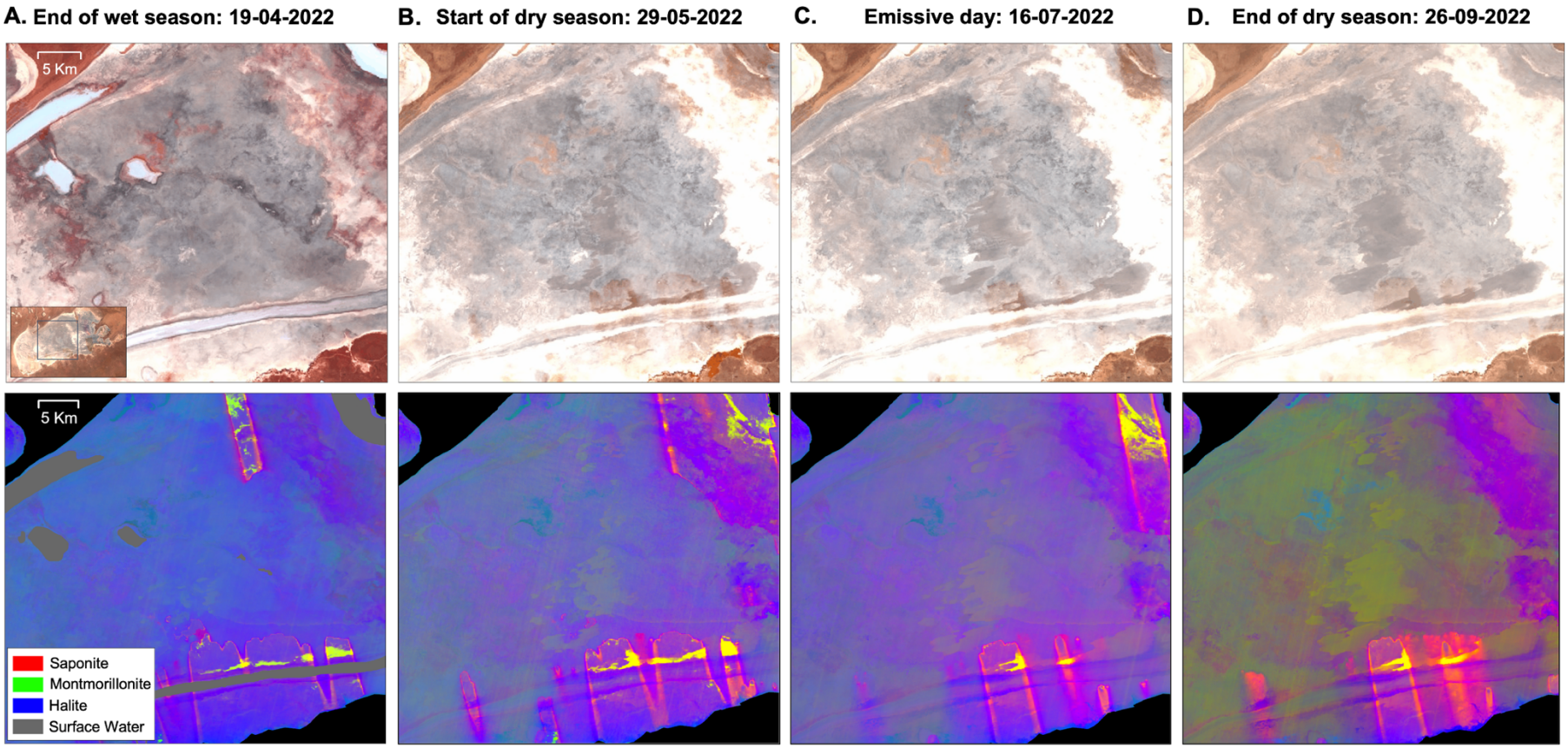


Figure A2.3. Temporal comparisons of Landsat 8-9 OLI false-colour composite (bands 5, 4, 3) images of surface change at Etosha Pan across the 2022 winter dry season showing the development of emissive 'hot-spot' surfaces and linear spectral unmixing model output RGB image composite maps for corresponding image dates, where RGB channels delineate estimates of relative mineral abundances (%) for (R) saponite, (G) montmorillonite and (B) halite minerals,